

Structure and Evolution of the Oceanic Lithosphere-Asthenosphere System from High-Resolution Surface-Wave Imaging

Joshua Berryman Russell

Submitted in partial fulfillment of the
requirements for the degree of
Doctor of Philosophy
under the Executive Committee
of the Graduate School of Arts and Sciences

COLUMBIA UNIVERSITY

2020

© 2020

Joshua Berryman Russell

All Rights Reserved

Abstract

Structure and Evolution of the Oceanic Lithosphere-Asthenosphere System from High-Resolution Surface-Wave Imaging

Joshua Berryman Russell

In this thesis, I investigate the seismic structure of oceanic lithosphere and asthenosphere with a particular focus on seismic anisotropy, using high-resolution surface waves recorded on ocean-bottom seismometers (OBS) in the Pacific and Atlantic Oceans. The NoMelt (~ 70 Ma) and YoungORCA¹ (~ 43 Ma) OBS experiments located in the central and south Pacific, respectively, provide a detailed picture of “typical” oceanic lithosphere and asthenosphere and offer an unprecedented opportunity to investigate the age dependence of oceanic upper mantle structure. The ENAM-CSE² OBS array located just offshore the Eastern U.S. captures the transition from continental rifting during Pangea to normal seafloor spreading, representing significantly slower spreading rates. Collectively, this work represents a diverse set of observations that improve our understanding of seafloor spreading, present-day mantle dynamics, and ocean basin evolution.

At NoMelt, which represents pristine relatively unaltered oceanic mantle, we observe strong azimuthal anisotropy in the lithosphere that correlates with corner-flow induced shear during seafloor spreading. We observe perhaps the first clear Love-wave azimuthal anisotropy that, in addition to co-located Rayleigh-wave and active source P_n constraints, provides a novel *in situ* estimate of the complete elastic tensor of the oceanic lithosphere. Comparing this observed anisotropy to a database of laboratory and naturally deformed olivine samples from the literature leads us to infer an alternative “D-type” fabric associated with grain-size sensitive deformation, rather than the commonly assumed A-type fabric. This has vast

¹Young OBS Research into Convecting Asthenosphere

²Eastern North American Margin Community Seismic Experiment

implications for our understanding of grain-scale deformation active at mid-ocean ridges and subsequent thermo-rheological evolution of the oceanic lithosphere.

At both NoMelt and YoungORCA we observe radial anisotropy in the lithosphere with $V_{SH} > V_{SV}$ indicating subhorizontal fabric, in contrast to some recent global models. We also observe azimuthal anisotropy in the lithosphere that parallels the fossil-spreading direction. Estimates of radial anisotropy in the crust at both locations are the first of their kind and suggest horizontal layering and/or shearing associated with the crustal accretion process. Both experiments show asthenospheric anisotropy that is significantly rotated from current-day absolute plate motion as well as rotated from one another, at odds with the typical expectation of plate-induced shearing. This observation is consistent with small-scale density- or pressure-driven convection beneath the Pacific basin that varies in orientation over a length scale of at most \sim 2000 km and likely shorter.

By directly comparing shear velocities at YoungORCA and NoMelt, we show that the half-space cooling model can account for most (\sim 75%) of the sublithospheric velocity difference between the two location when anelastic effects are accounted for. The unaccounted for \sim 25% velocity reduction at YoungORCA is consistent with lithospheric reheating, perhaps related to upwelling of hot mantle from small-scale convection or its proximity to the Marquesas hotspot.

While lithospheric anisotropy is parallel to the fossil-seafloor-spreading direction at both fast-spreading Pacific locations, it is perpendicular to spreading at the ENAM-CSE in the northwest Atlantic where spreading was ultra-slow to slow. Instead, anisotropy correlates with paleo absolute plate motion at the time of Pangea rifting \sim 180–195 Ma. We propose that ultra-slow-spreading environments, such as the early Atlantic, primarily record plate-motion modified fabric in the lithosphere rather than typical seafloor spreading fabric. Furthermore, slow shear velocities in the lithosphere may indicate that normal seafloor spreading did not initiate until \sim 170 Ma, 10–25 Myr after the initiation of continental rifting, revising previous estimates. Additionally, these slow velocities may shed new light on

melt extraction at ultra-slow spreading environments.

Table of Contents

List of Figures	viii
List of Tables	ix
Code Availability	xiii
Introduction	1
1 High-resolution constraints on Pacific upper mantle petrofabric inferred from surface-wave anisotropy	8
1.1 Introduction	9
1.2 A comprehensive model of seismic anisotropy	11
1.3 Anisotropy of the Pacific and the NoMelt Experiment	12
1.4 Data	15
1.4.1 High-frequency ambient-noise processing	15
1.4.2 Cross-spectral waveform fitting	16
1.4.3 1-D average phase velocities	18
1.5 Inversion methods	22
1.5.1 Radial anisotropy	22
1.5.2 Azimuthal anisotropy	27
1.6 Results	29

1.6.1	Radial anisotropy	29
1.6.2	Azimuthal anisotropy	31
1.7	Discussion	33
1.7.1	Comparison to petrofabrics	33
1.7.2	Comparison to previous Pacific studies	37
1.7.3	Constraints on mid-ocean ridge dynamics	46
1.7.4	Radial anisotropy in the crust	48
1.8	Conclusion	50
2	Seismic evidence for grain-size sensitive olivine deformation during mid-ocean ridge spreading	53
2.1	Introduction	54
2.2	Methods	56
2.2.1	Surface-wave inversion with P_n constraints	56
2.2.2	Constructing the orthorhombic elastic tensor	57
2.2.3	Olivine fabric database	57
2.2.4	Accounting for pyroxene in anisotropy calculations	59
2.2.5	Steady-state grain size calculation	60
2.3	A comprehensive elastic model of oceanic lithosphere	60
2.4	Strain accumulation in the shallow lithosphere	62
2.5	Inferring LPO fabric type	65
2.6	Implications for MOR conditions	68
3	Surface-wave constraints on upper mantle petrofabric and flow beneath ~43 Ma seafloor in the south Pacific	71

3.1	Introduction	72
3.2	Data and Methods	74
3.2.1	Tilt and compliance removal	75
3.2.2	Ambient-noise surface-wave dispersion	76
3.2.3	Teleseismic Rayleigh-wave dispersion	77
3.2.4	Inversion for shear velocity, radial and azimuthal anisotropy	80
3.3	Results	82
3.3.1	Shear velocity and radial anisotropy	82
3.3.2	Azimuthal anisotropy	83
3.4	Discussion	85
3.4.1	Comparison to previous studies in the Pacific	85
3.4.2	Anelastic predictions for half-space cooling: possible evidence for mantle reheating	89
3.4.3	Implications for mid-ocean ridge spreading fabric	92
3.4.4	Sublithospheric mantle flow	94
3.5	Conclusion	95
4	Lithosphere structure and seismic anisotropy offshore eastern North America: Implications for early seafloor spreading dynamics	97
4.1	Introduction	98
4.2	Data and Methods	101
4.2.1	Daily OBS tilt noise removal	101
4.2.2	Ambient noise processing	102
4.2.3	Interstation phase velocities	104

4.2.4	Phase velocity inversion	106
4.2.5	Inversion for shear velocity, V_S	110
4.3	Results	111
4.3.1	Phase velocity maps	111
4.3.2	Azimuthal anisotropy	112
4.3.3	3-D shear velocity model	118
4.4	Discussion	122
4.4.1	Margin-perpendicular structure and significance of the BSMA	122
4.4.2	Implications for the onset of normal seafloor spreading	124
4.4.3	Comparison to previous anisotropy observations	126
4.4.4	Interpretation of fossilized margin-parallel anisotropy	127
4.5	Conclusion	131
Concluding Remarks		133
Bibliography		135
Appendices		158
A	Chapter 1 Supplementary Material	159
B	Chapter 2 Supplementary Material	172
C	Chapter 3 Supplementary Material	179
D	Chapter 4 Supplementary Material	186
E	Sensitivity kernels	193
F	Equivalence of (G, B, H, E) and $(\delta V_{SV}, \delta V_{SH}, \delta V_{PH})$	198

G	Error propagation from (A, ψ) to (A_c, A_s)	202
H	Linear Radon Transform	203

List of Figures

1	Map showing OBS experiments used in this thesis	4
1.1	Map of the NoMelt array	13
1.2	Time-domain CCFs and cross-spectral power	17
1.3	Cross-spectral waveform fitting procedure	19
1.4	Rayleigh and Love azimuthal anisotropy measurements	21
1.5	Array average phase velocity dispersion	22
1.6	Sensitivity kernels	25
1.7	Starting crustal model	26
1.8	Radial anisotropy inversion results	30
1.9	Azimuthal anisotropy inversion results	33
1.10	Anisotropy comparison to petrofabrics	38
1.11	Shear velocity and radial anisotropy comparison to other studies	42
1.12	Schematic summary of crust and mantle structure	49
2.1	Schematic of olivine LPO types	55
2.2	Comprehensive elastic model and data fit	62
2.3	LPO strain evolution	64
2.4	Azimuthal vs. radial anisotropy strength for A-, D-, and E-type	66
2.5	Deformation mechanism map	69
3.1	Map of YoungORCA study region	75
3.2	Ambient-noise CCFs and Radon transform	78

3.3	Azimuthal anisotropy data	79
3.4	Shear velocity and radial anisotropy	83
3.5	Azimuthal anisotropy G and E	86
3.6	Comparison of shear velocity and anisotropy to NoMelt	89
3.7	Conductive cooling signature and evaluation of HSC model	93
4.1	Map of ENAM-CSE study region	99
4.2	SNR reduction from tilt corrections	103
4.3	Ambient noise EGFs	104
4.4	Cross-spectral waveform fitting example	105
4.5	Conversion of Line 1 V_P to V_S	108
4.6	2-D finite-frequency sensitivity kernels	109
4.7	V_S sensitivity kernels	112
4.8	Isotropic phase velocity maps	113
4.9	2-D azimuthal anisotropy maps	115
4.10	Anisotropy strength and azimuth from 2-D maps	116
4.11	Average 1-D azimuthal anisotropy	117
4.12	Comparison of data fit for 1-D and 2-D anisotropy	118
4.13	Representative V_S profiles from Monte Carlo inversion	120
4.14	Horizontal slices through 3-D V_S model	121
4.15	Average margin-perpendicular V_S structure	124
4.16	Comparison of anisotropy to paleo plate motions	129
A.1	2-D variations in Rayleigh phase velocity	164
A.2	2-D variations in Love phase velocity	165
A.3	Damp changes in radial anisotropy across Moho	167
A.4	Damp radial anisotropy in the crust	168
A.5	Damp radial anisotropy in the mantle	169

A.6	Summary of all radial anisotropy squeeze tests	170
B.1	Perple_X estimates of V_S and V_P	172
B.2	Generic orthopyroxene texture used in calculations	173
B.3	Anisotropy strength with orthopyroxene content	174
B.4	Effect of olivine content on LPO type	175
B.5	Effect of fabric dip on LPO type	176
B.6	Average strain evolution of <i>Hansen et al.</i> (2011, 2014) samples	177
C.1	Clock drift correction example	180
C.2	Summary of clock drift corrections	181
C.3	Sensitivity kernels: shallow V_P sensitivity	182
C.4	Map of spreading rates	183
D.1	Synthetic anisotropy tests: Input synthetic model	186
D.2	Synthetic anisotropy tests: Smooth model output	187
D.3	Synthetic anisotropy tests: Break at BSMA output	188
D.4	Synthetic anisotropy tests: Performance summary	189
D.5	Starting model phase velocity maps	190
D.6	Horizontal slices through reference V_S model	191
D.7	V_S uncertainties	192
F.1	Numerical tests $G/L = \delta V_{SV}/V_{SV}$	201

List of Tables

1.1 Components of the in situ elastic tensor	35
A.1 NoMelt OBS orientations	171
B.1 NoMelt elasticity tensor including P_n constraints	178
C.1 YoungORCA OBS orientations	184
C.2 YoungORCA OBS clock drift corrections	185

Acknowledgements

My time at Lamont has been shaped by many wonderful people who have supported and encouraged me and from whom I have learned so much. I feel fortunate to have been a part of the Lamont community.

First and foremost, I thank my advisor Jim Gaherty, who has allowed me the freedom to explore my interests and grow as a scientist, while always sharing new ideas and perspectives along the way and with a keen eye for improvement in my work. His advising style and overall approach to science exemplify the scientist that I hope to be.

Special thanks go to my committee members Göran Ekström and Spahr Webb for their patience and guidance throughout my time at Lamont. Göran's attention to detail and rigor as a scientist has greatly impacted me and my work, and Spahr has been an invaluable source of knowledge on OBS data, seismic noise, and instrumentation. Additional thanks to Anne Bécel and Hitoshi Kawakatsu for their thoughtful feedback on this thesis, which helped improve it greatly.

There are many others who I am indebted to for their open doors and instruction during my time at Lamont including Felix Waldhauser, Paul Richards, Donna Shillington, Alberto Malinverno, Roger Buck, Terry Plank, Jonny Kingslake, and Ryan Abernathey. Bill Menke is almost entirely responsible for my knowledge of inverse theory, and I will greatly miss our impromptu office chats. Some of my most enjoyable and enlightening conversations were with Ben Holtzman, whose ability to communicate ideas through drawings and animations is inspiring and whose data sonification class transformed my perspective on science communication. Meredith Nettles has been a wonderful mentor and advocate for the SGT graduate students and in many ways is the glue that holds the SGT community together. I would also like to thank the broader SGT community and everyone who attended the weekly

Seismogroup meetings and Record Readings—I have learned so much from all of you.

Thanks to my fellow graduate students and postdocs who made grad school a fun and rewarding experience: Kelvin Tian, Anna Barth, Emily Hopper, William Hawley, Lorelei Curtin, Chris Carchedi, Michelle Lee, Theresa Sawi, Genevieve Coffey, Rachel Marzen, Mike Howe, Andrew Hollyday, Natalie Accardo, Helen Janiszewski, Celia Eddy, Hannah Rabinowitz, Zach Eilon, Kira Olsen, Bar Oryan, Henry Towbin, Joyce Sim, and Samer Naif. Especially Dan Sousa and Dan Bishop for the many barbeques in Morningside Park and Lion’s Head outings. Special thanks to Josh Maurer and Yen Joe Tan for taking up birding with me and helping me maintain my sanity with many trips to Central Park over the years.

The work presented in this thesis would not have been possible without the seagoing data collection efforts of many people. In particular, thanks to the Scripps Institution of Oceanography engineers Sean McPeak, Mark Gibaud, and Ernie Aaron as well as the captain and crew of the R/V Kilo Moana who made the data collection possible for YoungORCA. Additional thanks to the science crews on the YoungORCA and OldORCA deployments who helped make some of my fondest memories from grad school and motivated my science in a new way.

Finally, I would like to thank my friends and family: Andrew Kinslow for starting me down this path all those years ago and Mom, Dad, Jess, and Ira for their unwavering support over the past five years.

I dedicate this dissertation to Mom, Dad, and Jess—my biggest cheerleaders.

Code availability

A variety of computer codes were used to generate the results contained within this dissertation. To promote reproducibility, they are hosted at <https://github.com/jbrussell>. This repository includes codes that were built from, strongly contributed to, or entirely developed by Ge Jin (ASWMS), Helen Janiszewski (ATaCR), Adrian Doran (DLOPy), James Connolly (Perple_X), Robert Herrmann (surf96), James Wookey (MSAT), Pei-ying (Patty) Lin and Natalie Accardo (MATnoise), and Benjamin Holtzman and Chris Havlin (VBRc). Without their willingness to openly share code, completion of this work would not have been possible in 5 years.

Introduction

Plate tectonics forms the foundational framework for understanding the evolution of our planet. The ocean basins represent the most fundamental expression of plate tectonics, accounting for \sim 70% of Earth's surface and encompassing the entire plate lifecycle from lithosphere formation at mid-ocean ridges (MORs), to its thickening and cooling with age, and finally its recycling at subduction zones. The underlying low viscosity asthenosphere interacts with the lithosphere both thermally and mechanically as they shear past one another. Together, these structures and interactions constitute the lithosphere-asthenosphere system.

Despite its importance for understanding plate tectonics, questions regarding the structure and thermochemical evolution of the oceanic lithosphere and asthenosphere remain unanswered. As asthenosphere passively upwells at the MOR and undergoes decompression melting forming the crust, a depleted and possibly dry lithosphere is left behind, defining its compositional origin (*Gaherty et al.*, 1999, *Hirth and Kohlstedt*, 1996). A thermal definition of the lithosphere is suggested by seafloor depth and heat flow data, which indicate a conductively cooling plate that thickens with age following a half-space cooling (HSC) model (e.g. *Parker and Oldenburg*, 1973) at ages <70 Ma and a plate cooling model at older ages (e.g. *McKenzie et al.*, 2005, *Parsons and Sclater*, 1977, *Stein and Stein*, 1992). The physical mechanism leading to this deviation from HSC at older seafloor ages is debated but may indicate reheating of the lithosphere via small-scale convection (SSC) (e.g. *Haxby and Weissel*, 1986, *Huang and Zhong*, 2005, *Parsons and McKenzie*, 1978, *Richter and Parsons*, 1975). The ubiquitously observed low-velocity zone (LVZ) beneath the oceanic plates (*Gaherty et al.*, 1996, *Nettles and Dziewoński*, 2008, *Nishimura and Forsyth*, 1989, *Takeo et al.*, 2018) suggests a low viscosity region (*Lin et al.*, 2016) that may decouple lithospheric

motions from the underlying convecting asthenosphere. However, global-scale tomographic models of asthenospheric azimuthal anisotropy, which act as a proxy for present-day mantle shear deformation, largely indicate that they are well coupled at the plate scale (*Beghein et al.*, 2014, *Burgos et al.*, 2014, *Debayle and Ricard*, 2013, *Montagner and Tanimoto*, 1991, *Smith et al.*, 2004).

Seismic anisotropy of olivine, the dominant mantle mineral, provides insight into both present and past mantle flow. The shearing of olivine-rich mantle in the dislocation creep regime produces a lattice-preferred orientation (LPO) with the seismically fast crystallographic a-axis aligning parallel to shear (e.g. *Zhang and Karato*, 1995, *Zhang et al.*, 2000), which leads to an observable azimuthal dependence of seismic wavespeed (e.g. *Forsyth*, 1975, *Hess*, 1964, *Morris et al.*, 1969, *Raitt et al.*, 1969). In general, the lithosphere records fossilized LPO associated with corner-flow deformation near the ridge (e.g. *Blackman and Kendall*, 2002a, *Blackman et al.*, 1996, 2017, *Kaminski and Ribe*, 2002), while asthenosphere LPO largely reflects present-day shear deformation associated with absolute plate motion (*Debayle and Ricard*, 2013, *Montagner and Tanimoto*, 1991, *Smith et al.*, 2004). However, this simplified view has recently been challenged by high-resolution ocean-bottom seismic observations, which show fabric that is significantly rotated from fossil spreading in the lithosphere (*Takeo et al.*, 2016, *Toomey et al.*, 2007) and rotated from absolute plate motion in the asthenosphere (*Lin et al.*, 2016, *Takeo et al.*, 2016, 2018). One of the clearest observations of this asthenospheric misalignment is seen at the NoMelt experiment in the central Pacific (*Lin et al.*, 2016), where Chapters 1 and 2 are focused.

Direct constraints on oceanic lithosphere anisotropy and composition come from field samples of abyssal peridotites and ophiolites (*Ben-Ismail and Mainprice*, 1998, *Michibayashi et al.*, 2006, 2016, *Peselnick and Nicolas*, 1978). These samples represent both pristine and reworked oceanic lithosphere, such as those from the Josephine shear zone (*Hansen and Warren*, 2015, *Skemer et al.*, 2010, *Warren et al.*, 2008), and generally display strong anisotropy compared to mantle tomographic models. Laboratory deformation experiments

on olivine further probe the various deformation styles expected to occur in the upper mantle, and in recent years, have uncovered alternative olivine LPO types that may be sensitive to stress, grain size, and water content (*Bystricky et al.*, 2000, *Jung and Karato*, 2001, *Jung et al.*, 2006, *Karato et al.*, 2008, *Katayama et al.*, 2004). These alternative olivine LPO types form under slip systems other than the commonly assumed A-type [100](010). While this complicates the interpretation of seismic anisotropy observations, it also holds the potential for a deeper understanding of the deformation state of the mantle if LPO type can be determined *in situ*. Such an integration of seismic observations, natural petrofabrics, and laboratory olivine deformation experiments has yet to be achieved, owing largely to the vast differences in length scale³.

In this thesis, I utilize new high-resolution data from ocean-bottom seismometer (OBS) arrays located in the Pacific and Atlantic oceans, in order to image shear velocity and seismic anisotropy of the lithosphere-asthenosphere system (Figure 1). Targets include “typical” relatively pristine upper mantle structure beneath the open ocean in the Pacific basin at ages of \sim 70 Ma (*Lin et al.*, 2016, *Ma et al.*, 2020, *Mark et al.*, 2019, *Russell et al.*, 2019a, *Yang et al.*, 2020) and \sim 43 Ma (*Russell et al.*, 2019b) as well as seafloor just offshore the Eastern U.S. that recorded the latest stages of rifting and onset of normal seafloor spreading (*Bécel et al.*, 2020, *Lynner and Bodmer*, 2017, *Lynner and Porritt*, 2017, *Lynner et al.*, 2020, *Shuck et al.*, 2019). These locations represent a range of seafloor ages as well as spreading rates, allowing us to investigate their effects on oceanic upper mantle structure. Surface waves generated from teleseismic earthquakes provide excellent depth resolution of elastic shear structure in the upper \sim 300 km of the mantle. In addition, ocean-noise generated high-frequency Rayleigh and Love waves are sensitive to both azimuthal and radial anisotropy in the lithosphere, allowing us to resolve these parameters over significantly shorter length scales than typical global tomographic models.

In Chapter 1, I present a new high-resolution model of shear velocity and radial and

³A length-scale difference of \sim 10⁹ assuming a seismic wavelength on the order of \sim 100 km and laboratory LPO texture measurements of \sim 100 μm .

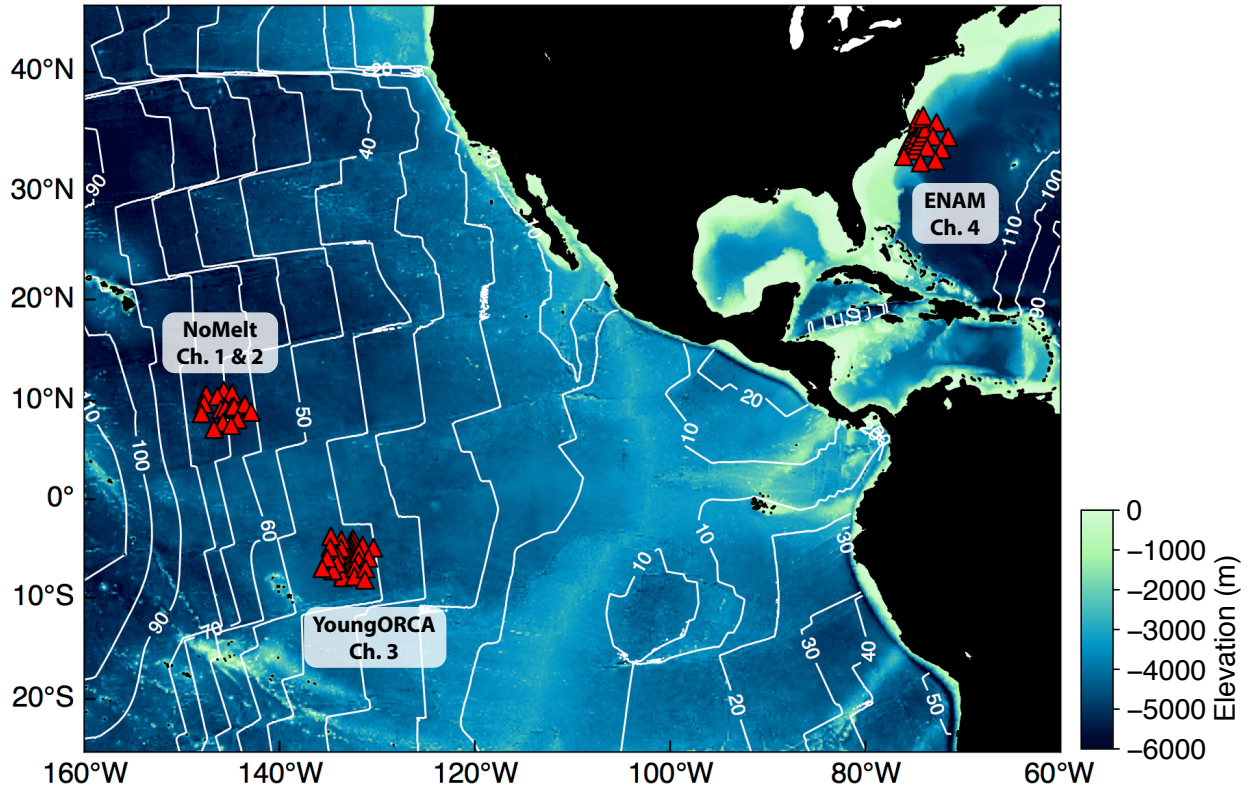


Figure 1: Map showing the locations of the three OBS experiments utilized in this dissertation. Red triangles indicate broadband ocean bottom seismometers (OBS) and white contours show seafloor age. Chapters 1 and 2 take place at the ~70 Ma NoMelt array in the central Pacific, Chapter 3 at the ~43 Ma Young OBS Research into Convecting Asthenosphere (YoungORCA) experiment, and Chapter 4 at the Eastern North American Margin (ENAM).

azimuthal anisotropy of ~ 70 Ma oceanic lithosphere using ambient-noise Rayleigh and Love waves measured at the NoMelt OBS array. We present perhaps the first clearly observed Love-wave 2θ and 4θ azimuthal anisotropy⁴ in addition to Rayleigh 2θ anisotropy, providing an *in situ* estimate of the complete shear elastic structure. Observed anisotropy is consistent with predictions for horizontally aligned orthorhombic olivine with an a-axis parallel to fossil-spreading down to ~ 80 –90 km depth. We argue that the base of this strongly anisotropic layer marks the dehydration boundary originally formed at or near the MOR. An extensive set of sensitivity tests (Appendix A.4) demonstrate that the data require radial anisotropy in both the crust and mantle with $V_{SH} > V_{SV}$, counter to some recent global models. The

⁴That is, phase velocities vary as a function of $\cos(2\theta) + \cos(4\theta)$, where θ is propagation azimuth.

crustal observation is the first of its type and indicates horizontal fabric related to layering and/or shearing during crustal accretion, consistent with previously observed lower-crustal dipping reflectors in the Pacific (e.g. *Bécel et al.*, 2015, *Kodaira et al.*, 2014). Finally, we compare our *in situ* elastic tensor with peridotites from the literature and find excellent agreement, suggesting extremely coherent olivine LPO over the 600×400 km NoMelt footprint.

Chapter 2 builds on these results by explicitly incorporating compressional velocity and anisotropy constraints from P_n refraction tomography at NoMelt (*Mark et al.*, 2019), yielding a complete elastic tensor for the upper ~ 7 km of the lithospheric mantle. This provides an unprecedented opportunity to directly compare our *in situ* estimate of anisotropy with natural and laboratory deformed olivine fabrics from the literature. We compare radial and azimuthal anisotropy for a database of 32 natural samples and 91 laboratory samples of various LPO type⁵ and find excellent agreement with the D-type fabrics, which are characterized by girdled intermediate and slow crystallographic axes. In addition we are able to place bounds on shear strain accumulation in the lithosphere of 300–400%. Our results suggests that D-type LPO may be more pervasive in the oceanic lithosphere than previously thought. Based on this observation, we argue that deformation via grain-size sensitive dislocation-accommodated grain boundary sliding (disGBS) dominates at the MOR environment rather than grain-size insensitive dislocation creep. Such non-Newtonian deformation impacts solid-state convection, melt extraction, and thermo-rheological evolution of the lithosphere (*Turner et al.*, 2017), informing our understanding of seafloor spreading processes.

In Chapter 3, we move ~ 2100 km southeast to the ~ 43 Ma YoungORCA⁶ array, where the tools developed in Chapter 1 are applied, and we include longer period Rayleigh waves that constrain shear velocity and azimuthal anisotropy to ~ 300 km depth. We observe a 35–

⁵A-, E-, and D-type, each with their fast a-axis parallel to shear but variable orientation of the intermediate and slow axes.

⁶Young OBS Research into Convecting Asthenosphere

40 km thin lithosphere defined by fast velocities (>4.6 km/s) and anisotropy that parallels fossil spreading. In the asthenosphere, anisotropy is significantly rotated from the plate motion direction, indicating a decoupling from the lithosphere and influence of pressure- or density-driven SSC. The resulting models of shear velocity and radial and azimuthal anisotropy are comparable in resolution to those obtained at NoMelt and separated in age by \sim 30 Myr, providing an exceptional opportunity to investigate their age dependence. We define a cooling proxy as the ratio of old to young seafloor, which effectively cancels commonalities such as composition and grain size, and find that the HSC model (*Parker and Oldenburg, 1973*) explains the majority of observations when anelastic effects are included (*Jackson and Faul, 2010*). An unaccounted for \sim 1% velocity reduction from 40–100 km depth at YoungORCA is consistent with reheating of the sublithospheric mantle and/or SSC.

Chapter 4 extends our study of the oceanic lithosphere to the passive margin offshore the Eastern U.S. where the earliest stages of seafloor spreading are preserved. The Eastern North American Margin (ENAM) was formed \sim 200 Ma during the breakup of supercontinent Pangea and records the transition from continental breakup to the onset of normal seafloor spreading. In contrast to the fast-spreading Pacific, this region represents ultra-slow spreading for which relatively few observations exist of lithospheric anisotropy, thus informing our understanding of the spreading-rate dependence of LPO formation. We utilize ambient-noise Rayleigh waves to constrain azimuthal anisotropy and shear velocity of the crust and lithospheric mantle. A striking low velocity lid that is in accord with thinned continental lithosphere and/or trapped melts during ultra-slow spreading extends \sim 200 km eastward from the margin and terminates at the Blake Spur Magnetic Anomaly (BSMA). If the slow lid is attributed to continental lithosphere, then the BSMA likely marks the completion of continental breakup and onset of normal seafloor spreading at \sim 170 Ma, 10–25 Myr after the initiation of rifting. Alternatively, the low velocities could indicate trapped gabbroic melts frozen into the lithosphere during spreading. In addition, fossil-spreading perpendic-

ular azimuthal anisotropy is observed in the lithosphere that approximately correlates with absolute plate motion (APM) at the time of spreading, and we hypothesize that lithosphere formed at slow-spreading ridges may record APM-modified olivine fabric rather than typical fossil-spreading fabric found in fast-spreading lithosphere.

Collectively, this thesis demonstrates the suitability of surface waves for probing Earth's upper-mantle elastic properties, and especially seismic anisotropy. It also highlights the value of high-resolution OBS deployments, especially those which incorporate multiple co-located geophysical data types, for elucidating the detailed structure and evolution of the ocean basins. This work represents a step forward in our ability to integrate observations at the seismic length scale with those at the laboratory and hand-sample scale, bridging that observational gap and informing our understanding of seafloor spreading processes in unprecedented detail.

1 | High-resolution constraints on Pacific upper mantle petrofabric inferred from surface-wave anisotropy

CO-AUTHORS: JAMES B. GAHERTY, PEI-YING (PATTY) LIN, DANIEL LIZARRALDE, JOHN A. COLLINS, GREG HIRTH, AND ROB L. EVANS.

This chapter has been published:

Russell, J. B., Gaherty, J. B., Lin, P.-Y. P., Lizarralde, D., Collins, J. A., Hirth, G., Evans, R. L. (2019). High-resolution constraints on Pacific upper mantle petrofabric inferred from surface-wave anisotropy. Journal of Geophysical Research: Solid Earth, 124, 631–657. <https://doi.org/10.1029/2018JB016598>

Abstract

Lithospheric seismic anisotropy illuminates mid-ocean ridge dynamics and the thermal evolution of oceanic plates. We utilize short-period (5–7.5 s) ambient-noise surface waves and 15–150 s Rayleigh waves measured across the NoMelt ocean-bottom array to invert for the complete radial and azimuthal anisotropy in the upper ~35 km of ~70-Ma Pacific lithospheric mantle. Strong azimuthal variations in Rayleigh- and Love-wave velocity are observed, including the first clearly measured Love-wave 2θ and 4θ variations. Inversion of averaged dispersion requires radial anisotropy in the shallow mantle (2–3%) and lower crust (4–5%), with horizontal velocities (V_{SH}) faster than vertical velocities (V_{SV}). Azimuthal anisotropy is strong in the mantle, with 4.5–6% 2θ variation in V_{SV} with fast propagation parallel to the fossil-spreading direction (FSD), and 2–2.5% 4θ variation in V_{SH} with a fast direction 45° from FSD. The relative behavior of 2θ , 4θ , and radial anisotropy in the mantle are consistent with ophiolite petrofabrics, linking outcrop and surface-wave length scales. V_{SV} remains fast parallel to FSD to ~80 km depth where the direction changes, suggesting spreading-dominated deformation at the ridge. The transition at ~80 km perhaps marks the dehydration boundary and base

of the lithosphere. Azimuthal anisotropy strength increases from the Moho to \sim 30 km depth, consistent with flow models of passive upwelling at the ridge. Strong azimuthal anisotropy suggests extremely coherent olivine fabric. Weaker radial anisotropy implies slightly non-horizontal fabric, or the presence of alternative (so-called E-type) peridotite fabric. Presence of radial anisotropy in the crust suggests subhorizontal layering and/or shearing during crustal accretion.

1.1 Introduction

Seafloor spreading at mid-ocean ridges offers perhaps the most direct observational window into deformation associated with convection in Earth's mantle. Solid-state shear deformation from the upward-and-outward trajectory of corner flow induces strong fabric in olivine-rich mantle rocks that can be readily observed at the hand and outcrop scale in ophiolites (e.g. *Ben-Ismail and Mainprice*, 1998, *Nicolas and Christensen*, 1987, *Peselnick and Nicolas*, 1978), and indirectly inferred from measurements of azimuthal seismic anisotropy in oceanic lithosphere at scales ranging from a ridge segment to an entire plate (e.g. *Forsyth*, 1975, *Hess*, 1964, *Morris et al.*, 1969, *Raitt et al.*, 1969). In particular, the [100] (*a*-) axes of olivine crystals, and the faster seismic wavespeeds, both tend to align with the paleo-spreading direction in the shallow mantle lithosphere. The strong correspondence between this character of seismic anisotropy observed in ophiolites and seismic observations from oceanic lithosphere, and that predicted in laboratory studies of simple shear in olivine (e.g. *Karato et al.*, 2008, *Zhang and Karato*, 1995) and reproduced in modeling of polycrystalline materials (e.g. *Kaminski and Ribe*, 2001, 2002, *Ribe*, 1989) provides strong confidence that seismic anisotropy can be used to infer shear deformation and thus mantle flow. This correspondence is one of the key observations that underpins the widely applied practice of using seismic anisotropy to map flow direction in the upper mantle (e.g. see *Long and Silver*, 2009, *Savage*, 1999, for reviews).

In detail, observations suggest significant complexity in the apparent relationship be-

tween deformation processes and seismic anisotropy. Early refraction experiments in the Pacific recorded slight misalignment between the fast propagation direction of P_n and paleo-spreading direction (e.g. *Keen and Barrett*, 1971, *Morris et al.*, 1969). These early findings are corroborated by a growing body of seismic observations from the oceanic lithosphere documenting variations in anisotropic fabric that appear to depend on seafloor-spreading rate (e.g. *Gaherty et al.*, 2004), differences in relative versus absolute plate motion at the ridge (e.g. *Takeo et al.*, 2016, *Toomey et al.*, 2007, *Vanderbeek and Toomey*, 2017), and/or the nature of upwelling beneath the ridge (e.g. *Delorey et al.*, 2007, *Gaherty*, 2001). In the oldest reaches of the Pacific, the lithospheric anisotropy varies over relatively short length scales and does not always correlate with the direction of seafloor spreading (e.g. *Shintaku et al.*, 2014, *Takeo et al.*, 2016, 2018). These observations suggest a rich diversity of dynamic processes beneath mid-ocean ridges that go well beyond the simple symmetrical-spreading models explored to date (e.g. *Blackman and Kendall*, 2002a, *Blackman et al.*, 1996, 2017).

Observations of seismic anisotropy produced by a given fabric take different forms depending on the type of seismic data being analyzed. The alignment of olivine's fast [100] axis parallel to spreading should produce measurable wavespeed perturbations to horizontally propagating seismic waves depending on: (1) the propagation direction of the wave relative to the olivine [100] axis (azimuthal anisotropy); and (2) the shear-wave polarization angle relative to the fabric plane (radial anisotropy). In the ocean basins, the former is generally measured on P- and S-waves traveling subhorizontally in the shallow mantle, and on Rayleigh waves from earthquakes and ambient noise. The latter is observed as a discrepancy between the azimuthally averaged velocity of Rayleigh and Love waves relative to an isotropic model, which can be modeled as the difference in shear velocities (V_{SV} and V_{SH}) experienced by horizontally propagating, vertically and horizontally polarized shear waves, respectively (e.g. *Anderson and Dziewonski*, 1982). For a given underlying olivine fabric, the two types of anisotropy can be related to one another in a predictable way, and should be consistent. However, most observations of anisotropy only quantify a small subset of the

possible anisotropic parameters, and little attention is generally paid to whether anisotropy models derived from different subsets of data sampling the same region are consistent with a common peridotite fabric. As a result, the observations are used to qualitatively assess mid-ocean ridge models, rather than provide quantitative constraints on deformation and flow.

In this study, we provide the first high-resolution constraints on a complete parameterization of shear-wave anisotropy (including Love waves) in the oceanic lithosphere. We utilize short-period (5–7.5 s) ambient-noise surface-wave observations in conjunction with previously measured 15–150 s Rayleigh waves (*Lin et al.*, 2016) recorded on an array of ocean-bottom seismometers (OBS) deployed on 70 Ma seafloor in the central Pacific. Strong azimuthal and radial anisotropy are observed in both Rayleigh- and Love-wave phase velocities, including perhaps the first clearly observed 2θ and 4θ variations in Love-wave velocities. Although radial and azimuthal anisotropy have been previously observed in the Pacific, this study is one of the first to explicitly solve for and interpret together both types of anisotropy within a relatively small footprint. The resulting shear-anisotropy model is compared to observed petrofabrics from oceanic environments, and discussed in the context of improving models of mid-ocean ridge dynamics.

1.2 A comprehensive model of seismic anisotropy

The lattice-preferred orientation (LPO) of olivine produces observable seismic body- and surface-wave anisotropy that can be used to infer past and present deformation patterns in the mantle (*Mainprice*, 2015). For weak anisotropy appropriate for olivine, 13 elastic parameters are required to fully model anisotropy observed in surface waves (see Appendix A.1). In practice, these parameters are often separated into the azimuthally averaged components that control radial anisotropy, and those that control the azimuthal variations relative to these averages. Our analysis incorporates the full set of 13 parameters, as defined by *Montagner and Nataf* (1986) and fully described in Appendix A.1. Here we summarize the

dominant shear-velocity components that are the focus of our analysis.

To first order, Rayleigh waves are sensitive to the horizontally propagating vertically polarized shear wavespeed V_{SV} (or the parameter L), and Love waves are dominantly sensitive to V_{SH} (or the parameter N). Radial anisotropy ($\xi = V_{SH}^2/V_{SV}^2$) is constrained by azimuthally averaged Rayleigh- and Love-wave velocities and is a proxy for the degree that the underlying fabric is organized with fast axes that are predominantly subhorizontal ($\xi > 1$) or subvertical ($\xi < 1$) (e.g. *Anderson and Dziewonski*, 1982). If the LPO fabric is organized laterally over seismic length scales, then azimuthal anisotropy also occurs, where V_{SV} displays a 2θ variability described by a peak-to-peak amplitude (parameter G) and fast direction of propagation (Ψ_G). Similarly, V_{SH} displays a 4θ azimuthal variability controlled by parameters E and Ψ_E . Anisotropic fabric of this form results in Rayleigh waves with a 2θ azimuthal variability and Love waves with both a 2θ and 4θ variability (*Montagner and Nataf*, 1986).

In this study, we model the full azimuthal variability of Rayleigh- and Love-wave velocities to constrain radial (ξ) and azimuthal anisotropy (G, Ψ_G, E, Ψ_E) at NoMelt (Figure 1.1), including the first observations of 2θ and 4θ Love-wave anisotropy and E in the lithosphere. We utilize additional scaling relations derived from oceanic peridotites from the literature as well as scaling between P- and S-wavespeeds to solve for the remaining 7 elastic parameters, resulting in the first local-scale estimate of the complete in situ anisotropic fabric of oceanic lithosphere.

1.3 Anisotropy of the Pacific and the NoMelt Experiment

The Pacific is especially well-suited for investigating plate evolution and mid-ocean ridge (MOR) processes due to its broad range of plate ages, excellent distribution of seismic sources, and the recent proliferation of onshore and offshore data. Radial and azimuthal anisotropy have been extensively studied in the Pacific upper mantle at regional (*Forsyth*, 1975, *Forsyth et al.*, 1998, *Gaherty et al.*, 1996, *Lin et al.*, 2016, *Nishimura and Forsyth*, 1989, *Takeo et al.*,

2013, 2014, 2016, 2018, *Tan and Helmberger*, 2007, *Weeraratne et al.*, 2007) and global scales (*Beghein et al.*, 2014, *Debayle and Ricard*, 2013, *Ekström and Dziewonski*, 1998, *French and Romanowicz*, 2014, *Montagner*, 2002, *Montagner and Tanimoto*, 1990, 1991, *Moulik and Ekström*, 2014, *Nettles and Dziewoński*, 2008, *Schaeffer et al.*, 2016, *Yuan and Beghein*, 2013), providing a comprehensive picture of the upper mantle LPO and flow field.

Surface-wave observations of azimuthal anisotropy predominantly show fast propagation directions approximately parallel to the fossil-spreading direction (FSD) in the lithosphere (*Beghein et al.*, 2014, *Forsyth*, 1975, *Lin et al.*, 2016, *Montagner*, 2002, *Schaeffer et al.*, 2016,

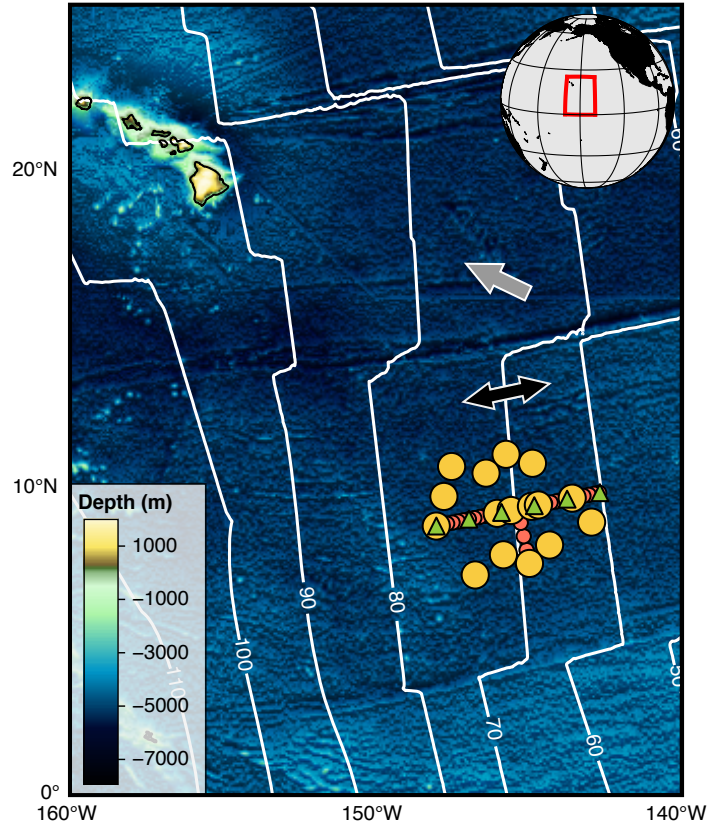


Figure 1.1: The 600×400 km NoMelt array consisting of 16 broadband OBS (large yellow circles), 34 short period OBS (smaller red circles), and 6 magnetotelluric (MT) instruments (green triangles) (*Sarafian et al.*, 2015). Solid white lines show ocean floor isochrons in increments of 10 Ma (*Müller et al.*, 2008). The grey arrow shows the absolute plate motion (APM) direction (*Argus and Gordon*, 1991) and the black double-headed arrow shows the fossil-spreading direction (FSD) in the NoMelt region.

Takeo et al., 2014) and approximately parallel to absolute plate motion (APM) direction in the asthenosphere (*Beghein et al.*, 2014, *Nishimura and Forsyth*, 1989, *Schaeffer et al.*, 2016, *Takeo et al.*, 2016). Furthermore, mantle-refracted P_n waves propagate through the uppermost lithosphere with a fast direction parallel to the FSD (*Hess*, 1964, *Raitt et al.*, 1969). This FSD parallel anisotropy in the lithosphere suggests quasi-horizontal alignment of olivine [100] crystallographic axes and is consistent with strain localization due to corner flow at the MOR during plate formation (*Blackman and Kendall*, 2002a).

The strength of azimuthal anisotropy in the lithosphere is less well-constrained however, appearing weaker than the asthenosphere in some models (*Beghein et al.*, 2014, *Schaeffer et al.*, 2016, *Yuan and Beghein*, 2013) and stronger in others (*Lin et al.*, 2016, *Nishimura and Forsyth*, 1989, *Rychert and Harmon*, 2017, *Takeo et al.*, 2016, 2018). Observations of radial anisotropy in the low velocity zone (LVZ) beneath the Pacific plate show $\xi > 1$, suggesting horizontal fabric interpreted as low-viscosity channels of flow (*Beghein et al.*, 2014, *Nettles and Dziewoński*, 2008). However, the strength and even the sign of lithospheric radial anisotropy vary widely between models (see section 1.7.2). The lack of agreement between models of lithosphere anisotropy (both radial and azimuthal) can perhaps be attributed to poor shallow resolution and lateral smearing inherent in plate-scale models, thus emphasizing the need for new high-resolution, local-scale measurements.

The NoMelt array, situated on 70 Ma lithosphere, was designed to provide high-resolution surface-wave constraints over a relatively undeformed region in the Pacific basin in order to better understand the first-order lithosphere-asthenosphere structure (Figure 1.1). Previously, *Lin et al.* (2016) utilized Rayleigh waves from teleseismic earthquakes (20–150 s) and ambient noise (10–20 s) to characterize V_{SV} and azimuthal anisotropy (G) down to ~ 300 km depth beneath NoMelt. In the lithosphere, they observe Ψ_G parallel to the FSD ($\sim 78^\circ$), consistent with previous studies and with new active-source constraints on P-wave anisotropy just beneath the Moho at NoMelt (*Mark et al.*, 2019). However, the direction of anisotropy in the asthenosphere was neither parallel to FSD nor APM, suggesting secondary local-scale

deformation processes that overprint the simple plate motion signal observed in many global and plate-scale models.

Our study utilizes high-frequency (5–7.5 s) Rayleigh and Love waves to provide updated high-resolution constraints on G as well as new constraints on B , H , E , and ξ in the upper \sim 30 km of the mantle to produce a complete anisotropic model of the oceanic lithosphere beneath NoMelt. In particular, we focus on the lithospheric strengths and directions of G , E , and ξ , providing quantitative estimates that are consistent with peridotite samples and predictions of LPO fabric formed at ridges.

1.4 Data

1.4.1 High-frequency ambient-noise processing

Twelve months of continuous data were collected on 16 high signal-to-noise, three-component broadband OBS instruments from January–December 2012. We follow the data processing procedures outlined in *Bensen et al.* (2007). The data are downsampled to 1 Hz and the daily mean and trends are removed. The horizontal H1 and H2 components are then rotated to the radial and transverse orientations for each station pair. OBS orientations and their 4σ uncertainties are determined using the DLOPy method (*Doran and Laske*, 2017) with earthquakes $>$ M7.0 (Table A.1). To minimize the influence of earthquakes on the noise spectra, we use a one-bit normalization procedure where the amplitude of each point in the time series is normalized by its absolute value such that a point is either -1 if negative or +1 if positive. Finally, the daily spectra are whitened to enhance localization of signals in the time domain.

Cross-correlations between station pairs are calculated in the frequency domain for each day of data on all three components (vertical, radial, transverse) to extract the coherent ambient noise wavefield. Each station component is cross-correlated with the same component of a nearby station. To maximize signal-to-noise, each day of data is split into 15

three-hour segments with 50% overlap between neighboring segments. The 15 individual cross-spectra are then stacked together yielding a single daily cross-spectrum for each of the three components. These daily traces are then stacked over the entire year producing the final year-averaged cross-spectra.

The power spectral density (PSD) and time-domain empirical Green's functions (EGF) for the year-averaged cross-spectra are shown in Figure 1.2 for both vertical and transverse components. Rayleigh waves are recorded on the vertical component and Love waves on the transverse component. Comparing the cross-spectral PSDs of the two components (Figure 1.2a, b), we see a similar peak at 5–7.5 s period on both components, but the typical primary microseism peak at \sim 20 s is absent on the transverse component. In the time domain, the 5–7.5 s signal manifests itself as two distinct mode branches on the vertical component (Figure 1.2c). The slower traveling wave is the fundamental mode Rayleigh wave (S_0) traveling through the water column at \sim 1.5 km/s, and the faster traveling wave is the first overtone Rayleigh wave (S_1) traveling through the solid earth. On the transverse component, this frequency band contains only the fundamental mode Love wave (T_0) traveling at a similar group velocity to the first overtone Rayleigh wave. In order to isolate the S_1 and T_0 mode branches and improve signal-to-noise, we apply a 2.2–5.5 km/s group-velocity cosine-tapered window to both the vertical and transverse components, shown by the grey shaded regions in Figure 1.2c, d.

1.4.2 Cross-spectral waveform fitting

Phase velocities are measured from the windowed data using the cross-spectral formulation of *Aki* (1957). For a homogeneous noise source and interstation distances much longer than the wavelength of the waves being measured, the real parts of the vertical (Z) and transverse (T) cross-spectra, ρ , take the functional form (*Aki*, 1957, *Cox*, 1973):

$$\rho^{Z,T}(\omega, r) = AJ_0\left(\frac{\omega r}{c^{R,L}(\omega)}\right), \quad (1.1)$$

where $c(\omega)$ is the interstation phase velocity of Rayleigh (R) or Love (L) waves at frequency ω , r is the interstation distance, J_0 is the Bessel function of order zero, and A is an amplitude prefactor. Equation (1.1) is only valid for Love waves when r is much larger than the wavelength of the waves being measured, which is true for this study. Previous studies have included amplitude information, A , to extract dispersion from multiple mode branches (*Nishida et al.*, 2008, *Takeo et al.*, 2013, 2014, 2016, 2018). However, we have chosen to

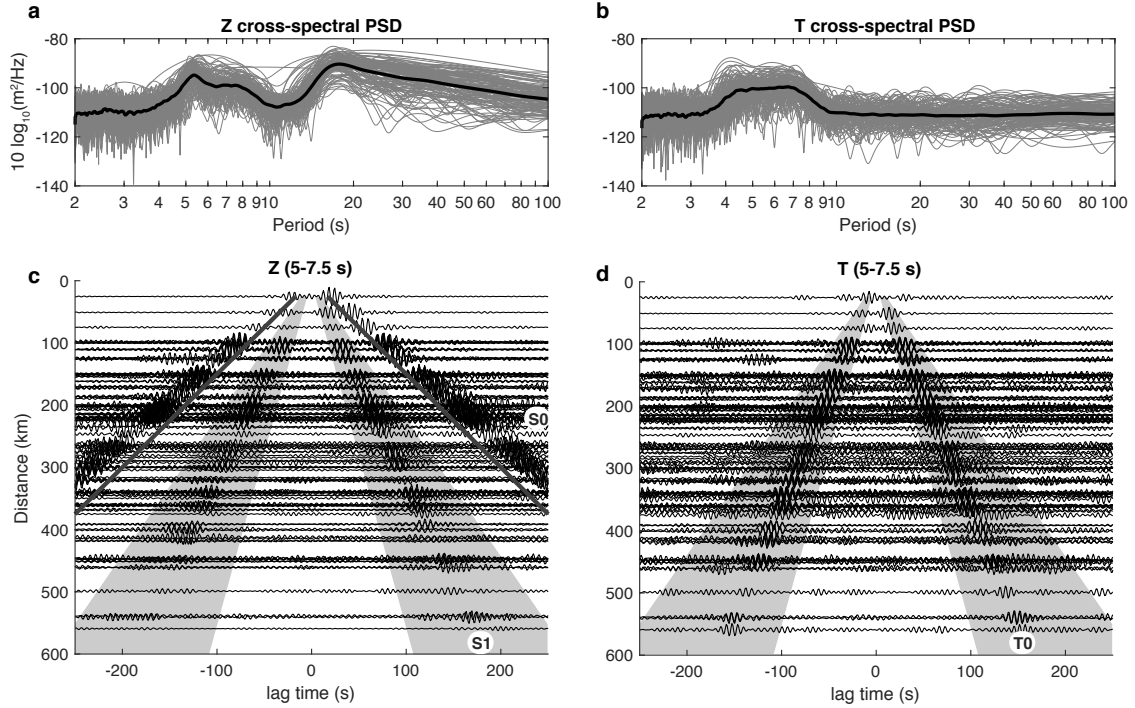


Figure 1.2: Cross-spectral power spectral density (PSD) and empirical Green's functions (EGF) for Rayleigh and Love waves. (a) Average PSD calculated from the year-averaged cross spectra for Rayleigh waves on the vertical component. The primary microseism peaks at 20 s and the secondary microseism at 5–7.5 s. Station pair PSDs are shown by thin grey lines and their mean in black. (b) Same as (a) but for Love waves on the transverse component. Note that only the secondary microseism peak (5–7.5 s) appears for the transverse component. (c) Vertical component EGFs bandpass filtered at 5–7.5 s period with the 2.2–5.5 km/s group-velocity window shaded in grey. The fundamental mode Rayleigh wave (S0) travels through the water column at these frequencies (~ 1.5 km/s, grey line) and arrives outside the chosen group-velocity window. The first overtone Rayleigh wave (S1) arrives within the window. (d) same as (b) but for the transverse component showing the fundamental mode Love wave (T0).

reduce the number of free parameters by letting $A = 1$, measuring dispersion for a single mode branch on each component, which is justified by our relatively tight group velocity window (Figure 1.2). Interstation phase velocities are extracted from 4–10 s period by fitting a Bessel function to the observed cross-spectra for each station pair (Figure 1.3) using the method of *Menke and Jin* (2015). Due to the decrease in signal at periods <5 s and >7.5 s (Figure 1.2a, b) as well as possible Love-wave overtone interference at >7.5 s (Figure 1.5), this study utilizes the period range 5–7.5 s.

The fitting is performed on each station pair using a nonlinear least-squares algorithm where the starting dispersion model is taken from *Lin et al.* (2016). The inversion is performed twice for each station pair. After the first inversion, the resulting dispersion curves for every station pair are weighted based on the misfit of each Bessel function and averaged together, yielding a single average dispersion curve. This average curve is then used as the starting model for the second iteration of the inversion. This procedure greatly reduces the degree of cycle skipping in the final Bessel function fits and is more convenient than performing a gridsearch to determine a suitable starting model. Examples of typical Bessel fits and their corresponding dispersion curves are shown in Figure 1.3 for long ($r = 540$ km) and short ($r = 98$ km) interstation distances. For short interstation distances, there are fewer zero-crossings in the Bessel function, and therefore the resulting dispersion curve is less well-constrained. To ensure high quality phase velocity measurements, only interstation distances ≥ 200 km are used in this study.

1.4.3 1-D average phase velocities

We measure interstation phase-velocity dispersion of S1 and T0 mode branches for each station pair at 5–7.5 s, providing excellent azimuthal coverage within the array footprint. The collection of phase-velocity measurements are used to solve for the average (1-D) phase velocity, and an azimuthal variation relative to this average, for each wave type at each frequency. This 1-D approach is justified given the relatively small lateral variations in

phase velocity ($<1\%$) for both Rayleigh and Love waves at 5–7.5 s period (see Figure A.1–A.2). In general, the azimuthal variability of phase velocity c , is given by (Montagner and Nataf, 1986):

$$c(\omega, \theta) = c_0(\omega) \left[1 + A_{c2}(\omega) \cos(2\theta) + A_{s2}(\omega) \sin(2\theta) + A_{c4}(\omega) \cos(4\theta) + A_{s4}(\omega) \sin(4\theta) \right], \quad (1.2)$$

where ω is the angular frequency of the wave, θ is the wave-propagation azimuth measured clockwise from north, and $A_i(\omega) = (\delta c/c)_i$ are the zero-to-peak amplitudes describing the

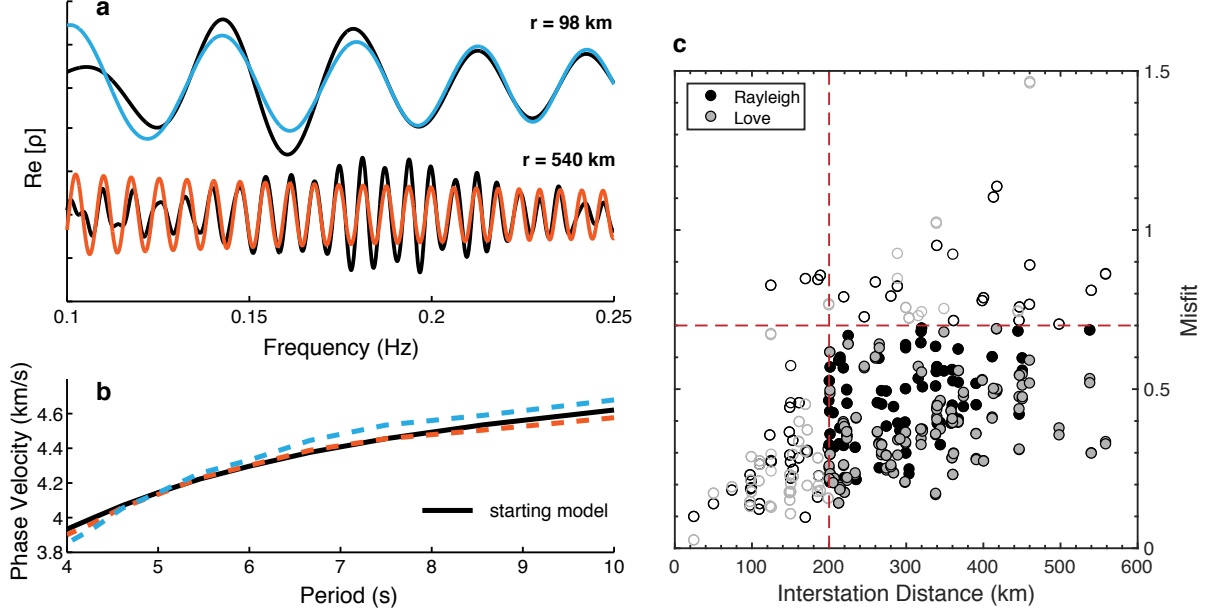


Figure 1.3: (a) An example of the Bessel function fitting procedure on the transverse component for extracting interstation Love-wave phase velocities. The real part of the cross-spectra, $\rho(\omega, r)$, for two stations separated by 98 km and 540 km are plotted in black. The corresponding synthetic Bessel function fits using equation (1.1) are plotted in color. (b) Comparison of the starting phase velocity model, $c(\omega)$, in black and the final models dashed in color. Longer interstation distances have more zero crossings, thus providing a better constraint on phase velocity. (c) Misfit between the observed (ρ_{obs}) and predicted (ρ_{pre}) cross-spectra where misfit is defined as $\sum_{\omega}(\rho_{obs} - \rho_{pre})^2 / \sum_{\omega} \rho_{pre}^2$. To ensure the highest quality measurements, we use interstation distance and misfit cutoffs of 200 km and 0.7, respectively, shown by the red dashed lines. Open circles depict measurements which do not meet these standards.

azimuthal dependence of phase velocity. The term $c_0(\omega)$ is the isotropic phase velocity, which is independent of azimuth and captures radial anisotropy.

For Rayleigh waves, the 4θ terms A_{c4}^R and A_{s4}^R are nearly zero (*Montagner and Nataf*, 1986) (see Figure A.1) and therefore, the azimuthal dependence can be approximated as:

$$c^R(\omega, \theta) = c_0^R(\omega) \left[1 + A_{c2}^R(\omega) \cos(2\theta) + A_{s2}^R(\omega) \sin(2\theta) \right], \quad (1.3)$$

or in terms of an amplitude A_2^R and fast direction ψ_2^R :

$$c^R(\omega, \theta) = c_0^R \left[1 + A_2^R \cos 2(\theta - \psi_2^R) \right], \quad (1.4)$$

where $A_2^R = \sqrt{(A_{c2}^R)^2 + (A_{s2}^R)^2}$ and $\psi_2^R = 0.5 \arctan(A_{s2}^R/A_{c2}^R)$. Love waves, on the other hand, require both 2θ and 4θ components to fully describe their azimuthal variation and therefore the equation for the azimuthal dependence of Love waves is given by:

$$\begin{aligned} c^L(\omega, \theta) &= c_0^L(\omega) \left[1 + A_{c2}^L(\omega) \cos(2\theta) + A_{s2}^L(\omega) \sin(2\theta) \right. \\ &\quad \left. + A_{c4}^L(\omega) \cos(4\theta) + A_{s4}^L(\omega) \sin(4\theta) \right] \\ &= c_0^L \left[1 + A_2^L \cos 2(\theta - \psi_2^L) + A_4^L \cos 4(\theta - \psi_4^L) \right]. \end{aligned} \quad (1.5)$$

Sinusoidal functions are fit to the data using equations (1.3–1.5), resulting in the amplitude (strength) and direction of azimuthal variations in phase velocity (Figure 1.4) as well as the isotropic phase velocities (Figure 1.5). Strong azimuthal anisotropy from 5–7.5 s is observed with peak-to-peak amplitudes ranging from 2%–4% for Rayleigh- 2θ and 0.5%–1% for both Love- 2θ and Love- 4θ (Figure 1.4 and Figure 1.9a). The Rayleigh- 2θ fast direction aligns parallel to the FSD. Additionally, the Love- 2θ and -4θ fast directions approximately align with FSD+90° and FSD+45°, respectively. These inferred fast directions for Rayleigh and Love waves are consistent with predictions from *Montagner and Nataf* (1986) assuming FSD parallel anisotropic fabric. While Rayleigh and Love waves are both sensitive to the

mantle, crust, and sediments at these periods (Figure 1.6a, b), the data clearly show a dominant signal consistent with strong mantle anisotropy oriented parallel to paleo-spreading, as observed previously at longer periods (*Lin et al.*, 2016).

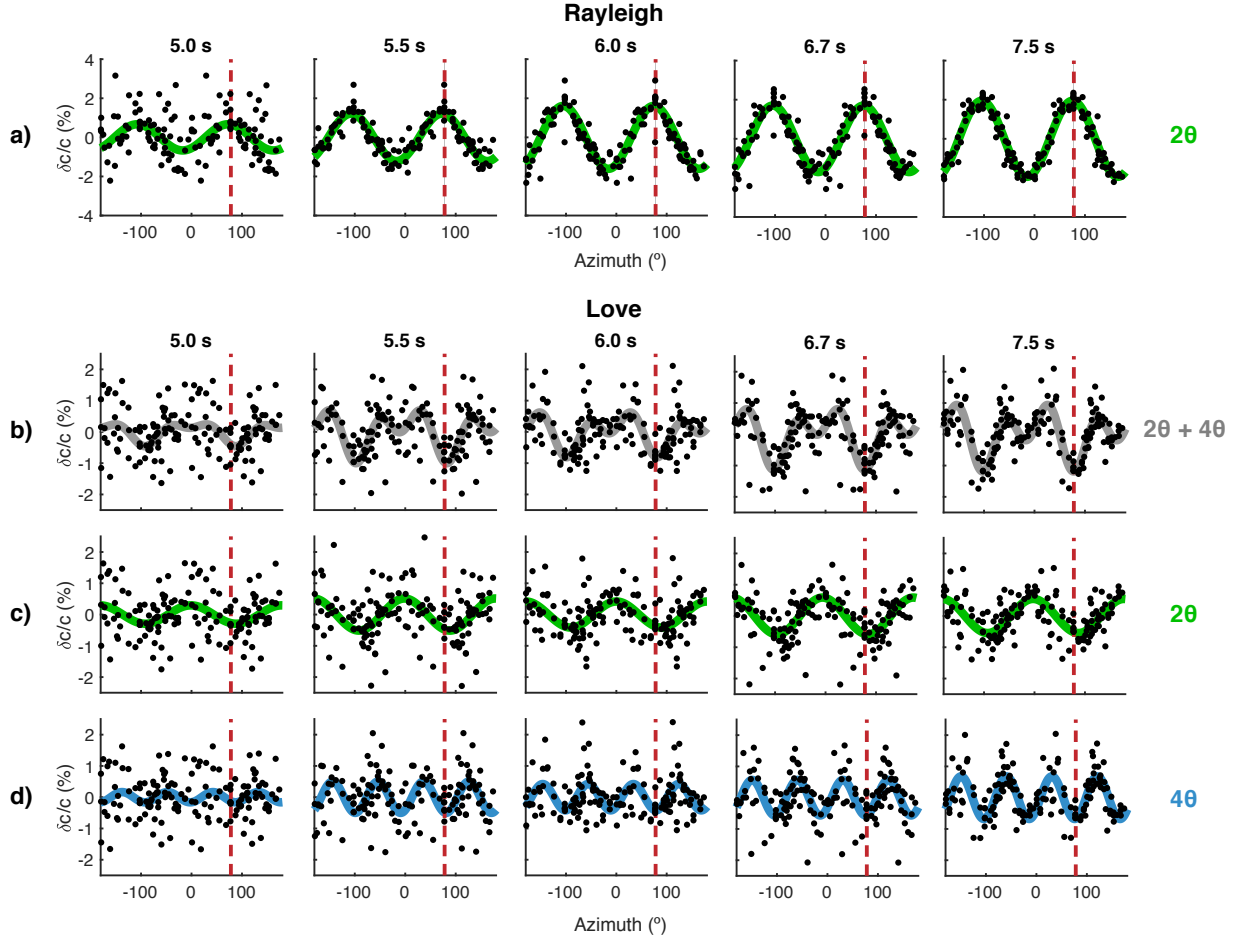


Figure 1.4: Azimuthal variation of phase velocity residuals relative to their isotropic values (see Figure 1.5 for the isotropic velocities, c_0) where 2θ , 4θ , and $2\theta + 4\theta$ sinusoidal fits are shown in green, blue, and grey, respectively. (a) Rayleigh wave 2θ ; (b) Love wave $2\theta + 4\theta$; (c) Love wave 2θ only (4θ prediction subtracted from the observations); (d) Love wave 4θ only (2θ prediction subtracted from the observations). The fossil-spreading direction (78°) is denoted by a red dashed line in each plot. To ensure high quality data, only measurements from stations separated by ≥ 200 km are used. See Figure 1.9a, b for the anisotropy parameters (A, ψ) corresponding to each sinusoidal fit.

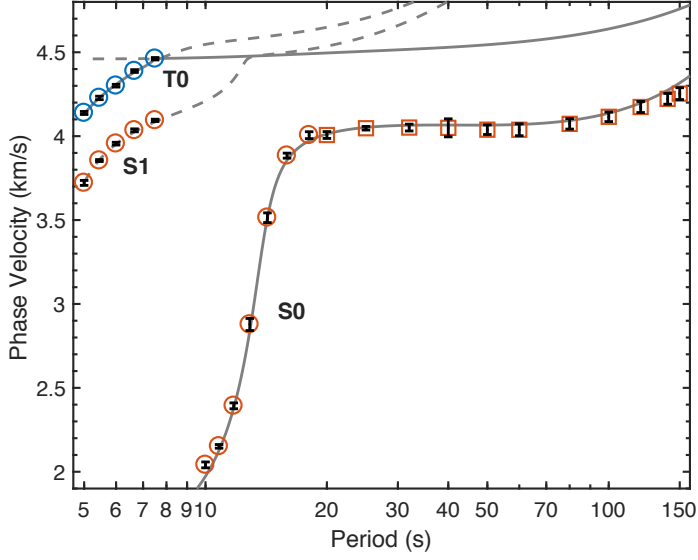


Figure 1.5: Isotropic phase velocity measurements, c_0 , for the fundamental mode (S0) and first overtone Rayleigh waves (S1) in red and fundamental mode Love (T0) in blue. Measurements from 10–150 s are from *Lin et al.* (2016) and are included in the modeling for completeness. Ambient noise and teleseismic measurements are shown as circles and squares, respectively. Grey lines show the predictions of the preferred model from this study (model 3 in Figure 1.8) where the solid and dashed lines depict fundamental mode and first overtone predictions, respectively. Predicted phase velocities are corrected for physical dispersion using a reference frequency of 35 mHz (see Supporting Information for anelastic Q model).

1.5 Inversion methods

1.5.1 Radial anisotropy

Isotropic phase velocity measurements for both Rayleigh and Love waves at 5–7.5 s (Figure 1.5) are used to constrain radial anisotropy in the upper \sim 35 km of the lithosphere. The inverse problem is parameterized in terms of the wavespeeds of horizontally propagating vertically and horizontally polarized S-waves (V_{SV} , V_{SH}) and vertically and horizontally propagating P-waves (V_{PV} , V_{PH}) as well as η , which influences P-SV propagation at angles intermediate to vertical and horizontal but lacks a precise physical meaning (*Kawakatsu, 2016a,b*). We choose to use the traditional η parameterization defined by *Anderson (1961)* instead of the newly defined η_κ , which has a clear physical meaning describing departures

from the elliptic condition (*Kawakatsu*, 2016a,b) but is yet to be applied to an inversion for Earth structure. Since η is poorly constrained by surface-wave data, we prescribe a character similar to that of PREM, whereby a linear gradient is imposed starting from 0.9 at the Moho to 1.0 at 200 km depth and is 1.0 elsewhere in the crust and upper mantle (*Dziewonski and Anderson*, 1981). The precise character of η beneath NoMelt may differ slightly from this assumption but is unlikely to have a significant effect on the resulting model. The equation linking observed isotropic phase velocities with the desired model parameters is expressed as:

$$\begin{aligned}\delta c(\omega) &= \frac{c^2(\omega)}{U(\omega)} \int_a^0 \sum_i K_i(\omega, r) \delta m_i(r) dr \\ &= \frac{c^2}{U} \int_a^0 \left(K_{PV} \delta V_{PV}(r) + K_{PH} \delta V_{PH}(r) + K_{SV} \delta V_{SV}(r) \right. \\ &\quad \left. + K_{SH} \delta V_{SH}(r) + K_\eta \delta \eta(r) \right) dr ,\end{aligned}\quad (1.6)$$

where $\delta c(\omega) = c_0(\omega) - c^{pre}(\omega)$ is the residual between observed and predicted isotropic phase velocity for a given model iteration, $U(\omega)$ is group velocity, $K_m(\omega, r) = \omega^{-1} \cdot \partial \omega / \partial m$ are the eigenfrequency Fréchet derivatives for each model parameter (Figure 1.6a, b), and $\delta m = m - m_0^j$ are the model perturbations away from the starting model m_0 at iteration j . In matrix form, equation (1.6) becomes:

$$\mathbf{K}' (\mathbf{m} - \mathbf{m}_0) = \delta \mathbf{c} ,\quad (1.7)$$

where $\mathbf{K}' = \mathbf{K} c^2 / U$ is the matrix of phase-velocity sensitivity kernels and \mathbf{m}_0 is the starting model from the previous iteration. In order to solve directly for \mathbf{m} , equation (1.7) can be rearranged:

$$\mathbf{K}' \mathbf{m} = \delta \mathbf{c}' ,\quad (1.8)$$

where $\delta\mathbf{c}' = \delta\mathbf{c} + \mathbf{K}'\mathbf{m}_0$. Equation (1.8) allows for the straightforward implementation of constraint equations of the form $\mathbf{H}\mathbf{m} = \mathbf{h}$, applied directly to \mathbf{m} as opposed to the model perturbations, $\delta\mathbf{m}$. Therefore, we have (Menke, 2012):

$$\begin{pmatrix} \mathbf{W}_e^{1/2} \mathbf{K}' \\ \mathbf{W}_\varepsilon^{1/2} \mathbf{H} \end{pmatrix} \mathbf{m} = \begin{pmatrix} \mathbf{W}_e^{1/2} \delta\mathbf{c}' \\ \mathbf{W}_\varepsilon^{1/2} \mathbf{h} \end{pmatrix}, \quad (1.9)$$

where \mathbf{W}_e is a diagonal weighting matrix containing uncertainties in isotropic phase velocity, σ^{-2} , obtained from bootstrapping the sinusoidal fitting parameters in equations (1.3–1.5), and \mathbf{W}_ε contains damping parameters for each constraint equation. Finally, the least-squares solution which minimizes the misfit function $\Phi = (\delta\mathbf{c}' - \mathbf{K}'\mathbf{m})^T \mathbf{W}_e (\delta\mathbf{c}' - \mathbf{K}'\mathbf{m}) + (\mathbf{h} - \mathbf{H}\mathbf{m})^T \mathbf{W}_\varepsilon (\mathbf{h} - \mathbf{H}\mathbf{m})$ is given by:

$$\mathbf{m} = \left(\mathbf{K}'^T \mathbf{W}_e \mathbf{K}' + \mathbf{H}^T \mathbf{W}_\varepsilon \mathbf{H} \right)^{-1} \left(\mathbf{K}'^T \mathbf{W}_e \delta\mathbf{c}' + \mathbf{H}^T \mathbf{W}_\varepsilon \mathbf{h} \right). \quad (1.10)$$

The inverse problem is solved iteratively by calculating \mathbf{m} , updating \mathbf{m}_0 , and recalculating $\delta\mathbf{c}$ until the model converges and the change in misfit Φ is small from one iteration to the next. Sensitivity kernels and predicted phase-velocity dispersion, c^{pre} , are calculated at each iteration using MINEOS with a physical dispersion correction using an assumed Q model (Supplemental Dataset S1) and a reference frequency of 0.035 Hz. Due to the small array size relative to lateral velocity variations, we invert all available data for a single 1-D velocity profile representative of the entire NoMelt study region.

Inversions for mantle velocity structure are dependent on the starting crustal velocity model (Figure 1.6a, b). We use the average NoMelt P-wave refraction model as the isotropic starting crustal V_{PV} and V_{PH} (Lizarralde *et al.*, 2012) and convert to V_S using V_P/V_S of 1.85 from Brocher (2005). The starting crustal velocity model is shown in Figure 1.7 along with crust1.0 (Laske *et al.*, 2013) and Lin *et al.* (2016) for comparison. We use a single sediment layer of 250 m thickness inferred from the refraction model and assign to it a

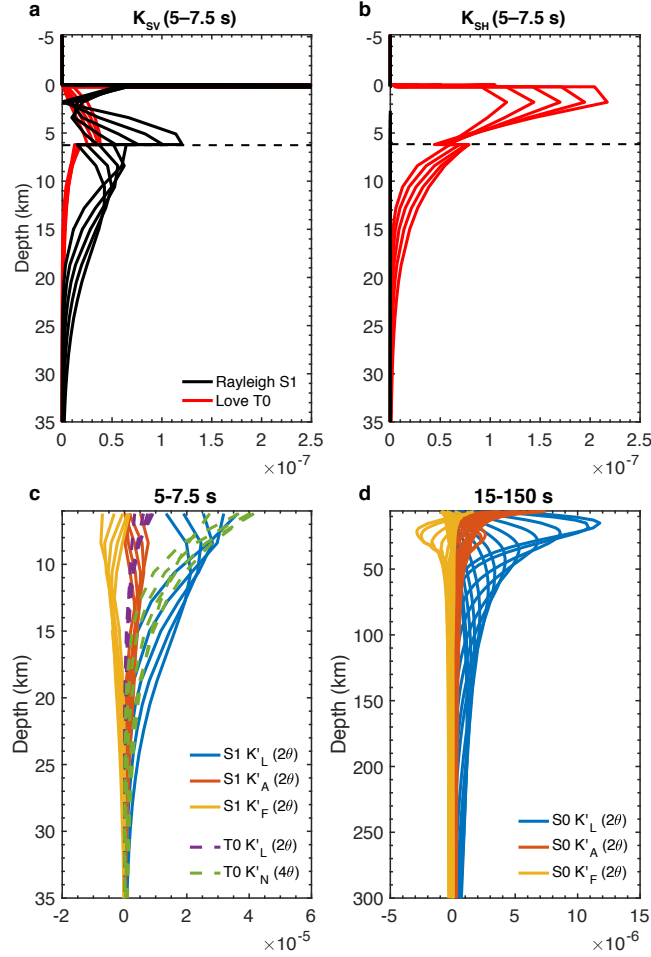


Figure 1.6: Phase velocity sensitivity kernels used in the radial and azimuthal anisotropy inversions. (a) V_{SV} model sensitivity to the first overtone Rayleigh (black solid) and fundamental mode Love waves (red) from 5–7 s. The Moho is marked by the black dashed line. (b) same as (a) but for V_{SH} sensitivity. (c) Sensitivity to G (K_L), B (K_A), H (K_F), and E (K_N) from 5–7.5 s. Solid and dashed lines represent first overtone Rayleigh and fundamental mode Love-wave sensitivities, respectively. (d) same as (c) but for fundamental mode Rayleigh-wave sensitivity to G , B , and H from 15–150 s.

constant shear velocity of 250 m/s (Ruan *et al.*, 2014), which remains fixed throughout the inversion. Because V_{PV} and V_{PH} are difficult to resolve independently with surface-wave data, we instead allow V_{SV} and V_{SH} to vary and impose a constraint requiring the corresponding components of V_P to vary proportionally. The amount that V_P varies with V_S is determined by V_P/V_S of the starting model and remains fixed throughout the inversion.

Additional damping towards the starting model ensures stability between iterations.

Borehole constraints show $V_{PH} \approx V_{PV}$ in the upper ~ 1.5 km (layer 2) of the oceanic crust (*Swift et al.*, 1998); therefore, we require the upper 1.5 km of the crust to remain isotropic ($\xi = 1$) throughout the inversion. Variations of ξ with depth in the lower crust and mantle are not well-resolved by our dataset due to the narrow bandwidth of the high-frequency measurements and poor depth sensitivity of Love waves. Therefore, layers of constant radial anisotropy are enforced in the lower crust and mantle, respectively by starting with an isotropic model and requiring constant $\partial\xi/\partial r$ within each layer (see appendix A.3). This constraint effectively reduces the number of model parameters such that additional smoothing is not required.

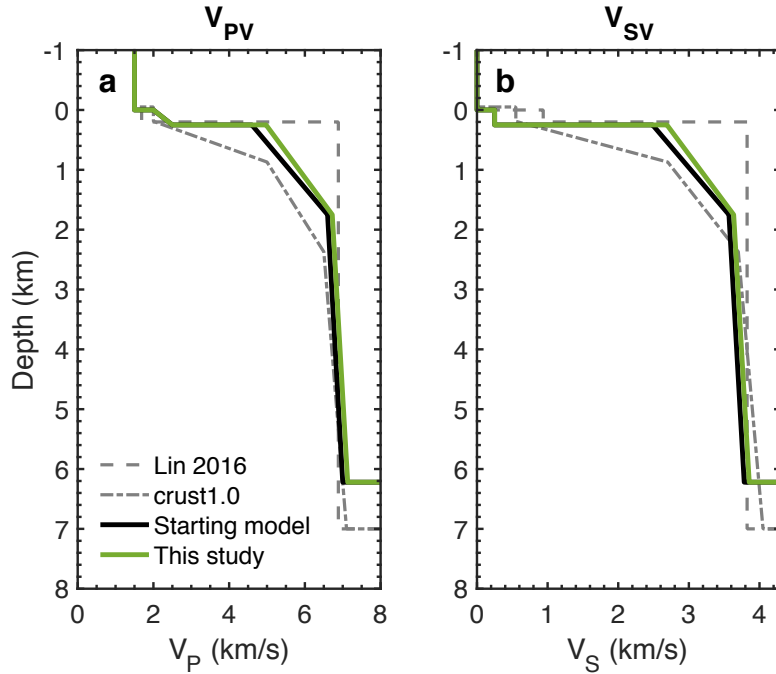


Figure 1.7: The radially isotropic ($V_{SH} = V_{SV}$, $V_{PH} = V_{PV}$) starting crustal model for (a) V_P and (b) V_S derived from the NoMelt P-wave refraction study is shown in black. Velocity models from crust1.0 (*Laske et al.*, 2013) and *Lin et al.* (2016) are shown for comparison. The final preferred model (V_{PV} , V_{SV}) of this study is shown in green (same as model 3 in Figure 1.8).

1.5.2 Azimuthal anisotropy

The azimuthal variations of Rayleigh- (5–150 s) and Love-wave (5–7.5 s) phase velocities are inverted for depth-dependent anisotropy parameters $G_{c,s}$, $B_{c,s}$, and $H_{c,s}$ from the Moho down to 400 km depth and $E_{c,s}$ from the Moho to 35 km depth (\sim 30 km depth beneath the Moho) following the formulation of *Montagner and Nataf* (1986). They show that the phase velocity sensitivities of the azimuthally anisotropic depth parameters equal the sensitivities of the corresponding transversely isotropic Love parameters. Thus, the Rayleigh- 2θ , Love- 2θ , and Love- 4θ cosine and sine amplitude components are written in terms of the 4 desired anisotropic depth functions as:

$$A_{c2,s2}^R(\omega) = \frac{c}{U} \int \left(L K_L^R \frac{G_{c,s}}{L}(r) + A K_A^R \frac{B_{c,s}}{A}(r) + F K_F^R \frac{H_{c,s}}{F}(r) \right) dr, \quad (1.11)$$

$$A_{c2,s2}^L(\omega) = \frac{c}{U} \int \left(-L K_L^L \frac{G_{c,s}}{L}(r) \right) dr, \quad (1.12)$$

$$A_{c4,s4}^L(\omega) = \frac{c}{U} \int \left(-N K_N^L \frac{E_{c,s}}{N}(r) \right) dr, \quad (1.13)$$

where K_A , K_L , K_F , and K_N are eigenfrequency Fréchet derivatives of the corresponding Love parameters which depend on frequency ω and radius r . The preferred model from the radial anisotropy inversion (model 3 in Figure 1.8) is used to calculate the Fréchet derivatives and elastic constants. In matrix form, equations (11–13) become:

$$\begin{pmatrix} \mathbf{A}_{c2,s2}^R(\omega) \\ \mathbf{A}_{c2,s2}^L(\omega) \end{pmatrix} = \begin{pmatrix} \mathbf{K}'_L^R(\omega, r) & \mathbf{K}'_A^R(\omega, r) & \mathbf{K}'_F^R(\omega, r) \\ \mathbf{K}'_L^L(\omega, r) & \mathbf{0} & \mathbf{0} \end{pmatrix} \begin{pmatrix} \mathbf{G}_{c,s}/\mathbf{L}(r) \\ \mathbf{B}_{c,s}/\mathbf{A}(r) \\ \mathbf{H}_{c,s}/\mathbf{F}(r) \end{pmatrix}, \quad (1.14)$$

$$\mathbf{A}_{c4,s4}^L(\omega) = \mathbf{K}'_N^L(\omega, r) \mathbf{E}_{c,s}/\mathbf{N}(r), \quad (1.15)$$

where boldface variables are vectors and $\mathbf{K}'_j = (c/U) \int \mathbf{K}_j dr$ are matrices containing the scaled sensitivity kernels (Figure 1.6c, d).

Rayleigh waves are weakly sensitive to $B_{c,s}$ and $H_{c,s}$ which depend mostly on V_{PH} and η , respectively. Therefore, we use peridotites from the literature (i.e. *Ben-Ismail and Mainprice, 1998, Peselnick and Nicolas, 1978*) to enforce scaling relations between $B_{c,s}$, $H_{c,s}$, and $G_{c,s}$. The elastic tensors are rotated such that their inferred shear planes are horizontal (i.e. horizontal [100] crystallographic axes), and ratios G/L , B/A , and H/F are calculated from equations (A.12–A.17). This yields approximate scaling relations of $B_{c,s}/A = 1.25 G_{c,s}/L$ and $H_{c,s}/F = 0.11 G_{c,s}/L$, which are used as prior constraints in the inversion. Equations (1.14–1.15) are inverted using standard damped-weighted least-squares with second derivative smoothing and a priori constraints forcing G , B , and H to zero below 300 km. The inversions are carried out using the cosine and sine representation of the anisotropy depth functions with the corresponding strengths and directions defined by equations (A.8–A.11).

In order to evaluate confidence in the final models, a balanced bootstrap resampling algorithm is used (*Davison et al., 1986*). Balanced resampling of M data over N iterations involves randomly selecting M points from the full dataset allowing for repetition and requiring that every datum is eventually selected N times. This method ensures even sampling over the entire dataset with every point represented an equal number of times, reducing variance in bias and providing robust uncertainty estimates with fewer iterations compared to uniform resampling approaches (*Hung et al., 2011*). We perform 2,000 iterations of balanced resampling and calculate 68% (σ) and 95% (2σ) confidence bounds from the subset of final models which fit the full dataset with reduced chi-squared less than 1.25 (1,424 models for G and 1,958 models for E).

1.6 Results

1.6.1 Radial anisotropy

Azimuthally averaged high-frequency Love- and Rayleigh-wave dispersion are fit by introducing radial anisotropy in the lower crust and upper ~ 30 km of the mantle. We compare three models where we have allowed anisotropy to appear in different parts of the model in order to evaluate where, if at all, anisotropy is required by the data (Figure 1.8). In model 1, anisotropy is allowed only in the lower crust, while the mantle is forced to be isotropic ($\xi = 1$). Model 2 contains anisotropy in the mantle with isotropy enforced in the crust. In model 3, anisotropy is allowed in both the crust and mantle.

The resulting suite of inverse models is shown in Figure 1.8. Love-wave dispersion is fit best by models with radial anisotropy in the mantle with $\xi > 1$ ($V_{SH} > V_{SV}$) (Figure 1.8, models 2 and 3). Rayleigh waves are best fit by models with stronger crustal anisotropy with $\xi > 1$ (Figure 1.8, models 1 and 3). In particular, forcing the mantle to be isotropic (model 1) underpredicts Love-wave velocities at periods > 6 s. An isotropic crust (model 2) overpredicts Rayleigh-wave velocities < 6 s and underpredicts them > 6 s. Figure 1.8g shows large reduced- χ^2 misfit for Love waves in model 1 and Rayleigh waves in model 2 resulting in large total misfits for both models (χ^2 much greater than 1).

In order to evaluate model significance, we test the null hypothesis that the data are sufficiently described by the model using a chi-square test for goodness of fit with. The black dashed line in Figure 1.8g indicates a significance level (p -value) of 0.05. Models with a high χ^2 misfit that plot above this line have $p < 0.05$, meaning that the null hypothesis, and thus the model, can be rejected with greater than 95% confidence (or in other words, there is less than a 5% chance that the model does sufficiently describe the data but that a statistically improbable departure of χ^2 has occurred). Models plotting below this line have $p > 0.05$, and thus the null hypothesis cannot be rejected. Model 3, which has a low misfit ($\chi^2 = 1.48$) and is within the 95% confidence limit of model acceptance ($p = 0.14$), is our

preferred model (see Figures S3—S6 for the comprehensive exploration of the model space).

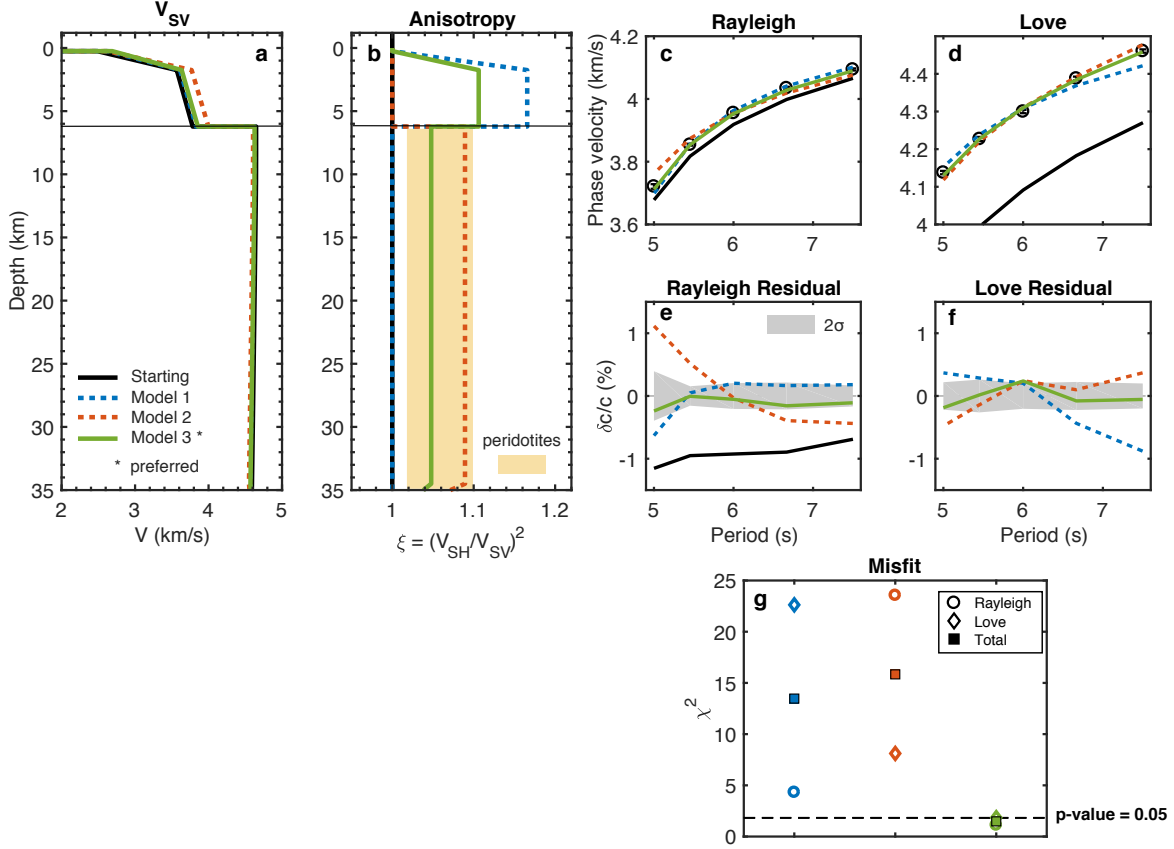


Figure 1.8: Radial anisotropy squeeze test: (a) V_{SV} and (b) radial anisotropy ξ of the starting model in black, plotted against Model 1 (anisotropic lower crust), Model 2 (anisotropic mantle), and Model 3 (anisotropic crust and mantle). The thin black line marks the Moho and the orange bar shows ranges of ξ measured from peridotites from the Antalya ophiolite complex (lower bound) (*Peselnick and Nicolas, 1978*) and from fast-spreading environments (upper bound) (*Ben-Ismail and Mainprice, 1998*). (c,d) Calculated and observed Rayleigh- and Love-wave dispersion. (e,f) Rayleigh and Love phase velocity residuals with the 2σ measurement error shaded in grey, where negative values indicate phase velocities that are underpredicted. Love-wave residuals of the starting model range from -4% to -6% (beyond figure axis). (g) Reduced chi-square misfit of phase velocities for each model, defined as $\chi^2 = N^{-1} \sum_i^N (c_i^{obs} - c_i^{pre})^2 / \sigma_i^2$. Models plotted above the black dashed line have a p -value less than 0.05 and can be rejected with greater than 95% confidence. Model 3 (green solid) fits the Rayleigh- and Love-wave measurements to within 2σ , yielding the lowest overall misfit ($\chi^2 \approx 1$) and therefore, is our preferred model.

Model 3 in Figure 1.8 consists of radial anisotropy with $V_{SH} > V_{SV}$ by $\sim 2.4\%$ ($\xi \sim 1.05$)

in the mantle and $\sim 5.2\%$ ($\xi \sim 1.1$) in the crust. It fits both Rayleigh and Love dispersion data to within the 2σ error bounds and produces the lowest total misfit. The depth extent of radial anisotropy in the mantle is not well resolved by the dataset due to the decay of V_S sensitivity with depth below the Moho (Figure 1.6a, b) and therefore, we favor a simple model with single layers of anisotropy in the crust and upper ~ 30 km of the mantle. Due to the loss of sensitivity with depth, we cannot rule out models with anisotropy confined to the upper 10–15 km of the mantle. Our model agrees well with the range of $\xi = N/L$ calculated from oceanic petrofabrics of *Peselnick and Nicolas* (1978) and *Ben-Ismail and Mainprice* (1998), as indicated by the orange bar in Figure 1.8b (see section 1.7.1). Rayleigh and Love wave data cannot be simultaneously satisfied by radial anisotropy only in the crust or only in the mantle. Instead, the data require both the crust and uppermost mantle to be radially anisotropic with $\xi > 1$.

1.6.2 Azimuthal anisotropy

Figure 1.9 shows strength and azimuth of G and E in the upper mantle, which control 2θ and 4θ variations in phase velocity, respectively. B and H are constrained using the scaling relations from peridotites mentioned previously, and we find B/A of $\sim 6\%$ directly beneath the Moho, which agrees well with P_n anisotropy of 6.2% observed at NoMelt (*Mark et al.*, 2019). Deeper estimates of B/A agree well with oceanic peridotites (section 1.7.1). Since B and H are simply scalar multiples of G/L , we simplify the remainder of the discussion by focusing only on features of G and E .

The strength of G increases with depth in the uppermost mantle lithosphere from $\sim 4.5\%$ at the Moho (~ 6 km) to $\sim 6\%$ at ~ 30 km depth, resulting in a positive gradient of 0.06–0.08 %/km. This increase in G strength with depth in the uppermost mantle is required by the high-frequency data and was not previously resolved by *Lin et al.* (2016). In contrast, E strength is not required to increase with depth, and we observe a relatively constant strength of 2–2.5% from the Moho down to 35 km depth. These magnitudes of G and E

strength are consistent with petrofabrics from *Peselnick and Nicolas* (1978) and *Ben-Ismail and Mainprice* (1998) (thick bars in Figure 1.9c; see section 1.7.1). Estimates from BIM98 coincide with our seismic observations of G/L from \sim 15–35 km depth and E/N from the Moho to 35 km depth to within the 68% confidence contours. Below \sim 35 km depth, G strength decreases, reaching a minimum of \sim 2% at \sim 135 km depth, which corresponds with the low velocity zone (Figure 1.11). This feature was previously seen by *Lin et al.* (2016) and interpreted as relatively weak fabric development within the center of a low viscosity asthenospheric channel with non-Newtonian rheology. Finally, there is a secondary peak in G strength of \sim 3% at 210–240 km depth that *Lin et al.* (2016) interpreted as strong fabric development at the base of an asthenospheric channel due to pressure- and/or buoyancy-driven flow.

We also solve for Ψ_G and Ψ_E in the upper 300 km and 35 km respectively. In the lithosphere, Ψ_G is parallel to the fossil-spreading direction to within \sim 7° and Ψ_E is 45° rotated from fossil spreading to within \sim 5°. The direction of G remains parallel to the FSD down to 80–90 km depth before rotating clockwise down to 150–160 km depth, approaching but never reaching the APM direction. Deeper in the model, anisotropy rotates back counterclockwise and is neither parallel to FSD nor APM, as observed previously (*Lin et al.*, 2016).

Although the model presented here fits the Rayleigh- 2θ and Love- 4θ data to within measurement error, the Love- 2θ measurements are not well fit (Figure 1.9a, b). In particular, the G model predicts a Love- 2θ direction that is 10°–15° counterclockwise from the true measurements. Additionally, the strength of the Love- 2θ component is underestimated by a factor of 2–4. Since these are some of the first robust in situ measurements of the full Love- $2\theta/-4\theta$ behavior, further modeling efforts are required to fully understand the source of these discrepancies (see section 1.7.2.3).

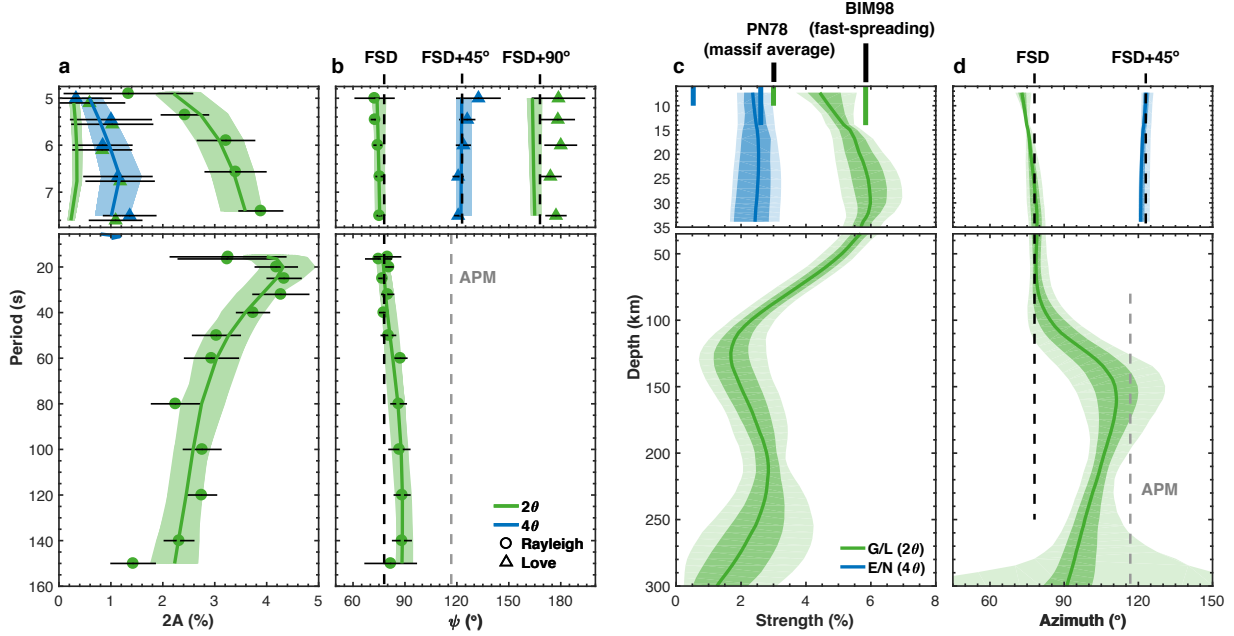


Figure 1.9: NoMelt azimuthal anisotropy data fit (a, b) and model (c, d). Measurements from 15–150 s are from *Lin et al.* (2016). Top panels have expanded scale to highlight short-period data and upper-lithosphere models. (a) Peak-to-peak amplitudes of azimuthal anisotropy, $2A$, measured for each mode branch from Figure 1.4. 2θ and 4θ measurements are represented by green and blue symbols, respectively and their 2σ errors by black solid bars. Rayleigh measurements are represented by circles and Love measurements by triangles. Thick solid lines show the median model predictions resulting from 2,000 bootstrap iterations, and shading represents the range of model predictions. (b) same as (a) but for fast directions, ψ . The black dashed lines represent fast directions predicted for each wave type from *Montagner and Nataf* (1986) assuming olivine alignment parallel to the fossil-spreading direction (FSD) of 78° . The grey dashed line represents absolute plate motion (APM). (c) Strength of anisotropy parameters G/L and E/N are shown in green and blue. Petrofabric estimates from *Peselnick and Nicolas* (1978) (Mesozoic ophiolites; labeled PN78) and *Ben-Ismail and Mainprice* (1998) (fast-spreading peridotites; BIM98) are shown by short and long bars, respectively. The solid lines are the median model values obtained from bootstrapping, and light and dark shading depict the 95% and 68% confidence bounds, respectively. (d) same as (c) but for anisotropy azimuth, Ψ .

1.7 Discussion

1.7.1 Comparison to petrofabrics

Elastic properties of peridotites gathered in the field provide direct constraints on upper mantle fabric, and because they have traveled to the surface, these samples are thought to

be most representative of shallow mantle lithosphere. However, many seismic models constructed from global datasets have relatively poor shallow resolution, making direct comparisons with natural samples unfeasible. Our model provides some of the first high-resolution constraints on shear-wave anisotropy of the lithosphere, allowing for direct comparisons with peridotites. Although measurements on petrofabrics may be performed at different P–T conditions than occur in the mantle, the anisotropic components depend only on relative differences in elements of the elastic tensor (*Ben-Ismail and Mainprice*, 1998), and to first order, direct comparisons with our model can be made without the need for pressure and temperature corrections.

We compare the anisotropic structure observed at NoMelt with elastic tensors (C_{ij}) representing average oceanic upper mantle from two petrofabric studies: (1) an average of 72 olivine aggregates of peridotites from fast-spreading environments by *Ben-Ismail and Mainprice* (1998) (BIM98) and (2) an outcrop-scale massif average of the Antalya ophiolite complex representative of Mesozoic uppermost oceanic mantle by *Peselnick and Nicolas* (1978) (PN78), as well as the single harzburgite sample used to construct that average. The averaging procedures between the two studies are quite different. BIM98 determine the structural fabric (lineation direction and pole to foliation plane) for each of the 72 samples and orient them in a consistent framework before averaging them together. In contrast, PN78 utilize ultrasonic measurements from cores of a single harzburgite sample in addition to 100 field observations of the structural fabric as it appears today to reconstruct a massif average C_{ij} for the Antalya ophiolite complex. Since the integrity of the PN78 massif average relies heavily on the single harzburgite sample used to construct the average, we include it also in our comparisons.

The anisotropic elasticity tensor, C_{ij} , is calculated for the NoMelt model at 30 km depth containing all 13 elements in equation (A.23). The resulting C_{ij} is oriented with its *SV* fast axis ([100]) in the direction of fossil spreading, rotated $\sim 78^\circ$ clockwise from x_1 and within the horizontal x_1 – x_2 plane. For ease of comparison with BIM98 and PN78, we rotate the

Table 1.1: C_{ij} constructed at 30 km depth beneath NoMelt and rotated into the (x'_1, x'_2, x'_3) coordinate system with C_{45} , C_{16} , C_{26} , and C_{36} minimized (see main text; rotation angle is 78.3°). x'_1 is parallel to the [100] crystallographic axis and x'_3 vertical. Units are GPa and the lower diagonal terms have been omitted ($C_{ij} = C_{ji}$).

i	j	1	2	3	4	5	6
1		271.6149	101.6837	101.2700	0	0	-0.1902
2		–	233.9946	99.9429	0	0	0.3918
3		–	–	239.5542	0	0	0.0071
4		–	–	–	66.1769	0.0452	0
5		–	–	–	–	74.6177	0
6		–	–	–	–	–	71.9655

coordinate system about x_3 to form a new system (x'_1, x'_2, x'_3) in which the [100] crystallographic axis is aligned parallel to x'_1 (Table 1.1; see Figure 1.10 for diagram of coordinate system). This is achieved by rotating the x_1 – x_2 coordinate axes clockwise about x_3 until the C_{ij} elements associated with G_s , B_s , H_s , and E_s are minimized (i.e. minimizing the function $\lambda = \sqrt{C_{45}^2 + C_{36}^2 + C_{16}^2 + C_{26}^2}$). The optimal rotation occurs at $\sim 78.3^\circ$ and is the inferred FSD at 30 km depth beneath NoMelt. Equations (A.20–A.22) are solved along all azimuths in the horizontal x'_1 – x'_2 plane, yielding the velocities and polarizations of 3 orthogonal waves: the quasi P-wave (V_{qP}), quasi-horizontal S-wave (V_{qSH}) polarized approximately in the x'_1 – x'_2 plane, and quasi-vertical S-wave (V_{qSV}) polarized approximately in the x'_1 – x'_3 plane (Crampin, 1981).

Figure 1.10 shows the predicted azimuthal (δV_{qP} , δV_{qSV} , δV_{qSH}) and apparent radial (V_{qSH}^2/V_{qSV}^2) anisotropy for each C_{ij} . Each tensor is oriented such that its shear plane is horizontal (x'_1 – x'_2 plane) with shear in the direction of x'_1 . The NoMelt P-wave anisotropy, δV_{qP} , is $\sim 1.25 \delta V_{qSV}$ as a result of the scaling enforced between B and G in the inversion. For NoMelt, we predict V_{qSV} anisotropy of $\sim 6\%$ peak-to-peak with a fast direction in the x'_1 ([100]) direction, in agreement with G/L (Figure 1.9). Similarly, we predict peak-to-peak

V_{qSH} anisotropy of $\sim 2.5\%$ with a fast direction 45° rotated from the x'_1 direction, consistent with E/N . For radial anisotropy (the azimuthal average of the squared wavespeed ratio), we calculate $\xi \sim 1.05$ or $V_{qSH} > V_{qSV}$ by $\sim 2.4\%$ (black arrow in Figure 1.10d).

In general, the mantle anisotropy measured in situ at NoMelt agrees with the petrofabrics that represent average oceanic upper mantle. The peak-to-peak amplitude and fast directions of P- and S-wave azimuthal anisotropy at NoMelt agree extremely well with BIM98, including the 4θ signal for δV_{qSH} . The BIM98 average displays very strong anisotropy since each of the 72 samples was rotated to its optimal orientation before being averaged, implying that the fabric at NoMelt is exceptionally coherent. Radial anisotropy at NoMelt is significantly weaker than BIM98 however, and agrees more closely with the PN78 harzburgite sample. The PN78 massif average shows weaker radial and azimuthal anisotropy than what we observe and has a $4\theta \delta V_{SH}$ signal that is $\sim 45^\circ$ rotated.

One way to explain the relatively weak radial anisotropy and strong azimuthal anisotropy that we observe is by an LPO fabric other than perfectly horizontal A-type (*Karato et al.*, 2008). Horizontal shearing to produce an A-type fabric results in horizontal [100] (fast) axes parallel to the shear direction and vertical [010] (slow) axes perpendicular to the shear plane (i.e. activation of the [100](010) slip system), producing relatively strong radial anisotropy and weaker azimuthal anisotropy. However, the same deformation in an E-type regime activates the [100](001) slip system producing subhorizontal alignment of both [100] and [010] with vertical [001] (intermediate) axes, resulting in strong azimuthal anisotropy and relatively weak radial anisotropy, similar to what we observe. Weak radial anisotropy can also result from A-type fabric that has been rotated about x_2 such that the [100] axis is tilted from the horizontal plane. The PN78 harzburgite is an example of such a fabric with [100] rotated $\sim 20^\circ$ out of the foliation plane and agrees with the radial anisotropy that we observe quite well, although E/N is overestimated. Such rotated fabrics are commonly observed in natural (*Warren et al.*, 2008, *Webber et al.*, 2010) and laboratory (*Skemer et al.*, 2011, *Zhang and Karato*, 1995) olivine samples as well as in numerical models of fabric

development (*Blackman and Kendall*, 2002a,b, *Blackman et al.*, 2017, *Kaminski and Ribe*, 2001) and may be linked to deformation history or pre-existing LPO fabrics (*Skemer et al.*, 2012). Forward calculations suggest that BIM98 fabric with the fast direction rotated $\sim 25^\circ$ from the horizontal plane produces azimuthal and radial anisotropy that are very similar to the NoMelt model. We prefer this interpretation given that E-type fabric implies higher stress and/or water conditions than typically expected for a mid-ocean ridge environment (e.g. *Jung et al.*, 2006, *Karato et al.*, 2008).

We have no need for alternative mechanisms for anisotropy such as diking, layering, or other shape-preferred orientations (e.g. *Backus*, 1962, *Holtzman and Kendall*, 2010). Laminate structures proposed to explain high-frequency scattered phases (P_n and S_n) in western Pacific lithosphere (*Kennett and Furumura*, 2013, *Kennett et al.*, 2014, *Shito et al.*, 2013, 2015) would produce strong apparent radial anisotropy with $\xi > 1$ and weak (negligible) azimuthal anisotropy, the opposite of that observed here. If such structures are present in the NoMelt region, either the velocity heterogeneity must be weak enough to produce relatively minor contributions to radial anisotropy, or they must exist below ~ 30 km depth.

1.7.2 Comparison to previous Pacific studies

Efforts to model seismic anisotropy in the Pacific basin range in scale from global surface-wave studies to active-source refraction experiments. Long-period surface waves that traverse the plate are broadly sensitive to both the lithosphere and asthenosphere, providing a plate-scale view of seismic anisotropy and mantle flow, while active-source experiments utilizing P_n waves sample the local lithospheric structure just beneath the Moho. Although complementary, these two types of observations lack the overlapping sensitivities (both laterally and in depth) required to constrain the complete anisotropic structure. Furthermore, agreement between recent global and regional models of radial and azimuthal anisotropy is relatively poor, especially at lithospheric depths. Local-scale broadband OBS array deployments like NoMelt bridge the gap between these existing datasets by providing local, high-frequency

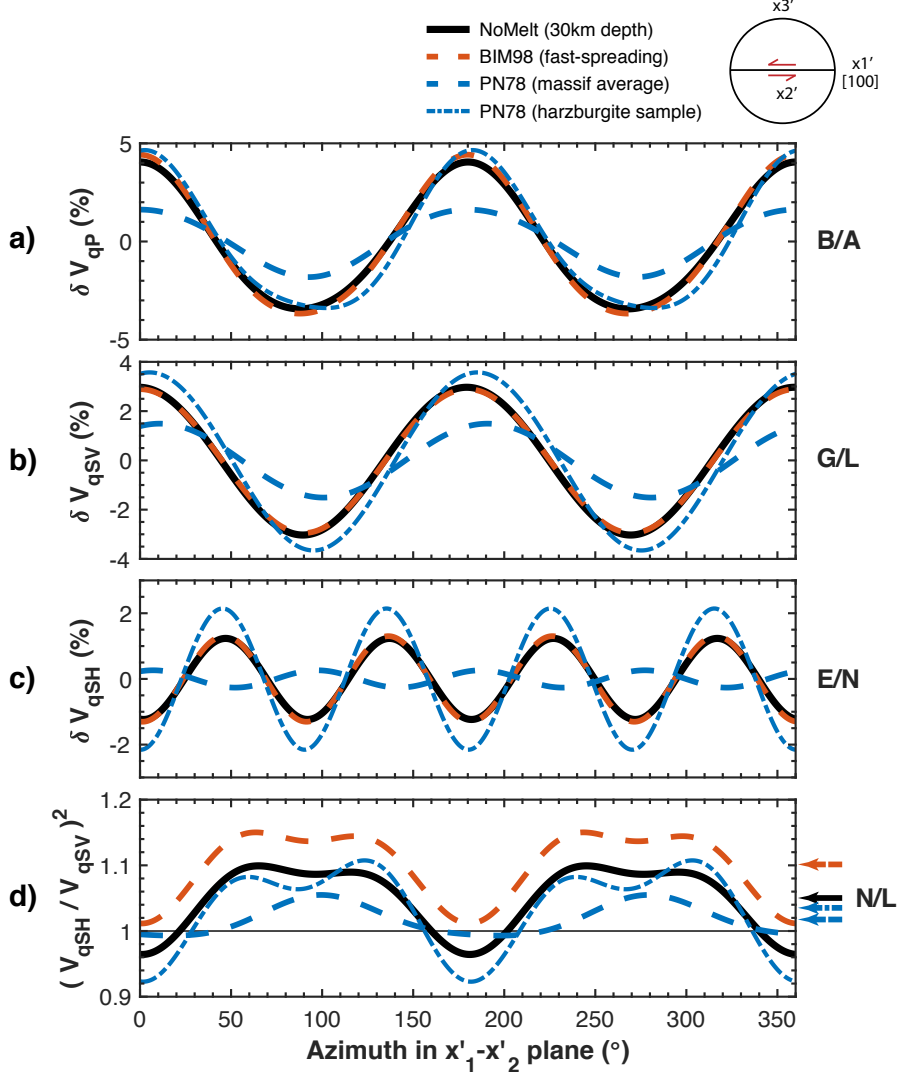


Figure 1.10: Azimuthal anisotropy is calculated from the NoMelt C_{ij} at 30 km depth (Table 1.1) and compared to BIM98 (*Ben-Ismail and Mainprice, 1998*) and PN78 (*Peselnick and Nicolas, 1978*) for (a) δV_{qP} , (b) δV_{qSV} , (c) δV_{qSH} , and (d) $(V_{qSH}/V_{qSV})^2$. The peak-to-peak variations in (a), (b), and (c) correspond to *B/A*, *G/L*, and *E/N*, respectively. The azimuthal average of (d) corresponds to ξ and is shown as an arrow at the right of the plot for each tensor. All tensors are oriented such that the shear plane is defined by $x'_1-x'_2$ with shear in the x'_1 direction. The NoMelt tensor has been rotated counter-clockwise about the x_3 (vertical) axis by 78.3° such that the fast [100] axis is along x'_1 . Zero azimuth is parallel to x'_1 .

surface wave constraints on shear anisotropy in the shallow lithosphere. Here, we compare our results with previous Pacific models of seismic anisotropy that range from global- to regional-scale focusing primarily on lithospheric anisotropy.

1.7.2.1 Global and plate-scale models

The fast propagation direction of Rayleigh-waves, Ψ_G , is a proxy for the direction of shear strain in the mantle and is typically thought to be parallel to the fossil-spreading direction in the oceanic lithosphere (*Nicolas and Christensen*, 1987). While many seismic observations in the Pacific support this notion (e.g. *Beghein et al.*, 2014, *Debayle and Ricard*, 2013, *Eddy et al.*, 2019, *Forsyth*, 1975, *Forsyth et al.*, 1998, *Hess*, 1964, *Lin et al.*, 2016, *Nishimura and Forsyth*, 1989, *Raitt et al.*, 1969, *Smith et al.*, 2004, *Weeraratne et al.*, 2007), other observations of fast wavespeeds rotated from fossil spreading in the lithosphere challenge this simple model of spreading-controlled fabric (*Keen and Barrett*, 1971, *Morris et al.*, 1969, *Shintaku et al.*, 2014, *Takeo et al.*, 2016, 2018, *Toomey et al.*, 2007, *Vanderbeek and Toomey*, 2017). Additionally, some global studies suggest that the correlation between Ψ_G and fossil spreading breaks down for older aged seafloor (*Debayle and Ricard*, 2013), perhaps due to reheating processes at >80 Ma (*Becker et al.*, 2014). *Becker et al.* (2014) observe a spreading-rate dependence, where fast-spreading plates (>5 cm/yr) display more coherent fossil-spreading parallel fabric compared to slower spreading. They also note that variations in Ψ_G between different seismic models are often greater than variations between seismic models and geodynamic models, suggesting the need for higher-resolution seismic constraints. Our broadband Rayleigh-wave measurements (5–150 s) require Ψ_G parallel to fossil spreading within the lithosphere down to 80–90 km depth, followed by a rotation towards, but not parallel to, the plate-motion direction, perhaps signifying the transition to asthenospheric flow marking the approximate depth to the lithosphere–asthenosphere boundary (LAB) beneath NoMelt.

Estimates of the strength of G and its depth dependence vary widely between studies of different scales. Global studies using Rayleigh-waves that traverse the basin observe stronger G in the asthenosphere relative to the lithosphere (*Beghein et al.*, 2014, *Burgos et al.*, 2014, *Debayle and Ricard*, 2013, *Schaeffer et al.*, 2016, *Yuan and Beghein*, 2013), typically ranging in the lithosphere from 1–2% and from 3–3.5% in the asthenosphere, significantly weaker than oceanic petrofabrics (Figure 1.10). However, regional studies using data which average

over smaller regions of the plate tend toward stronger anisotropy in the lithosphere relative to the asthenosphere (*Lin et al.*, 2016, *Nishimura and Forsyth*, 1989, *Rychert and Harmon*, 2017, *Takeo et al.*, 2016) as well as stronger anisotropy overall. We invert for all 6 parameters (G , Ψ_G , B , Ψ_B , H , Ψ_H) controlling 2θ Rayleigh-wave variations and observe strong G in the lithosphere of 4–6% that weakens into the asthenosphere (2–3%), generally in agreement with other regional-scale studies but \sim 2–3 times stronger in the lithosphere than global studies. We also observe a positive gradient in G with depth in the lithosphere that is constrained by the short-period data, not previously seen by *Lin et al.* (2016). Although evidence of a positive lithospheric gradient in G can perhaps be seen in some studies (e.g. *Nishimura and Forsyth*, 1989, *Rychert and Harmon*, 2017, *Yuan and Beghein*, 2014), it has not been interpreted. We discuss this gradient in relation to numerical models of fabric formation at the mid-ocean ridge in section 1.7.3.

Several factors contribute to variations in G strength. The strength of azimuthal anisotropy has been shown to vary with spreading rate (*Gaherty et al.*, 2004, *Song and Kim*, 2012) as well as plate age (*Eddy et al.*, 2019, *Smith et al.*, 2004), and the direction of the anisotropy can vary rapidly due to abrupt changes in spreading history. It is widely observed that the fossil-spreading history of the Pacific is complex, resulting in relatively short-wavelength changes in fast direction. These variations are difficult to resolve tomographically, and the resulting models are likely to underestimate the strength of the fabric (e.g. *Nishimura and Forsyth*, 1989). In contrast, anisotropy induced by APM is highly coherent and smooth over the scale of the Pacific basin, and its strength is likely to be well resolved by large-scale models. Our result suggests that at the local scale, mantle deformation in the ocean basins is dominated by flow associated with seafloor spreading, and that subsequent deformation in the asthenosphere, including shear induced by APM, are secondary processes in comparison.

Our preferred model of radial anisotropy shows $\xi > 1$ in both the lower crust and lithospheric mantle. Figure 1.11 compares isotropic shear velocity and radial anisotropy for several recent regional and global models roughly within the NoMelt footprint. While V_{SV}

estimates agree relatively well at most depths, ξ does not, particularly in the lithosphere. Global models tend to show $\xi < 1$ (*Beghein et al.*, 2014, *Burgos et al.*, 2014, *Kustowski et al.*, 2008, *Moulik and Ekström*, 2014, *Nettles and Dziewoński*, 2008) in the lithosphere, at odds with our results and suggesting vertical fabric rather than horizontal. $\xi < 1$ has been observed in regions of upwelling such as beneath the EPR (e.g. *Kustowski et al.*, 2008, *Panning and Romanowicz*, 2006) and is interpreted as vertical flow. However, it is more difficult to explain vertical fabric recorded in the oceanic lithosphere far from the ridge. Our results are instead consistent with regional models which show $\xi > 1$ in the lithosphere (*Forsyth*, 1975, *Gaherty et al.*, 1996, *Nishimura and Forsyth*, 1989, *Rychert and Harmon*, 2017, *Takeo et al.*, 2013, *Tan and Helmberger*, 2007), indicating horizontal fabric consistent with numerical predictions of strain induced by corner flow at the ridge (e.g. *Blackman and Kendall*, 2002a). Some global models do observe $\xi > 1$ in the lithosphere (*Dziewonski and Anderson*, 1981, *French and Romanowicz*, 2014, *Panning and Romanowicz*, 2006), in agreement with our results. Our observations of ξ in the lithosphere are significantly weaker than observed previously (Figure 1.11b), perhaps due to the requirement of anisotropy in the crust.

The importance of accurate shallow estimates of radial and azimuthal anisotropy and their depth dependence has become increasingly clear. The relative strengths of ξ and G may help differentiate between different LPO fabric types, which reflect in situ temperature, stress, and water content (*Jung and Karato*, 2001, *Karato et al.*, 2008). For example, typical A-type fabric should produce strong ξ and relatively weak G , while E-type should exhibit weaker ξ relative to G . Additionally, the maximum of the gradient in radial anisotropy with depth ($\partial\xi/\partial r$) as well as the maximum gradient in fast-direction rotation ($\partial\Psi_G/\partial r$) have previously been used as proxies for depth to the LAB or G-discontinuity (e.g. *Beghein et al.*, 2014, *Burgos et al.*, 2014). However, the practice of using such depth derivatives of elastic parameters from global models to infer physical properties of the mantle should be performed with caution, and regional constraints should be utilized where possible (e.g. *Kawakatsu and Utada*, 2017, *Takeo et al.*, 2018).

The relatively strong radial and azimuthal anisotropy observed in the lithosphere at NoMelt and other regional-scale studies compared to recent global studies is perhaps due to differences in sensitivities of the datasets used. Longer period surface waves have broad depth sensitivity that will necessarily smear shallow and/or thin layers of anisotropy. Thus, strong fabric that is shallow and/or has a fast direction rotated from the layers beneath it may appear weaker to longer period waves. Additionally, plate-scale studies utilizing Rayleigh waves that traverse large transects of the basin inherently average over heterogeneities that vary over short length-scales. This may result in weaker estimates of G , especially if Ψ_G also varies appreciably. These depth and lateral limitations call for higher frequency surface-wave constraints measured over smaller regions of the plate.

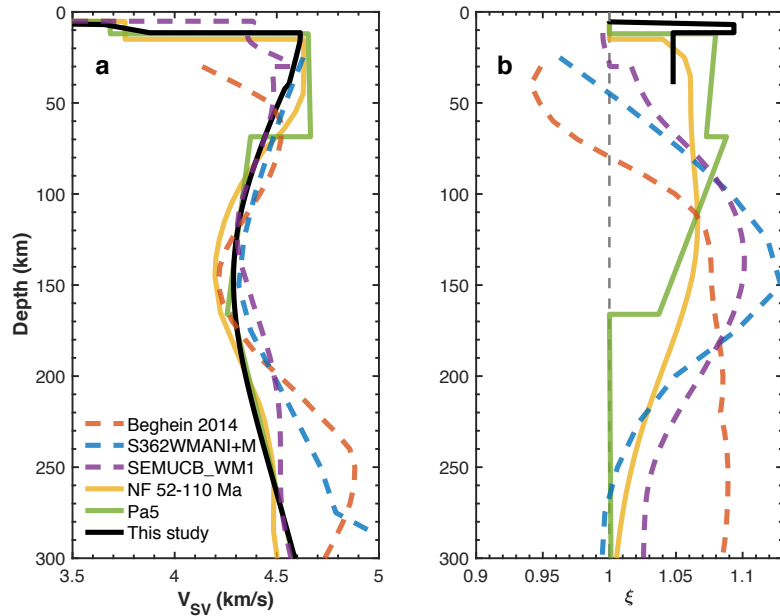


Figure 1.11: (a) Vertical shear velocity (V_{SV}) and (b) radial anisotropy (ξ) are compared for several regional and global models, each roughly within the NoMelt footprint. Regional models are shown as solid lines with *Nishimura and Forsyth* (1989) in yellow, *Gaherty et al.* (1996) in green, and the preferred model from this study in black (Figure 1.8, model 3). Dashed lines depict global models with *Beghein et al.* (2014) in red, *Moulik and Ekström* (2014) in blue, and *French and Romanowicz* (2014) in purple.

1.7.2.2 Ocean-bottom array studies

In an effort to image upper mantle anisotropy in more detail, several other array-scale OBS surface-wave investigations have been carried out in various regions of the Pacific ranging in seafloor age from young (20–30 Ma; Shikoku basin) (*Takeo et al.*, 2013) to intermediate (60 Ma; TIARES project SE of Tahiti) (*Takeo et al.*, 2016) to old (130–160 Ma; PLATE and NOMan projects in the NW Pacific) (*Takeo et al.*, 2014, 2018). These studies utilize similar array-based techniques to model short-period surface-waves overlapping in sensitivity with our study and provide complementary constraints on both radial and azimuthal anisotropy that can be compared with our results. In detail, considerable heterogeneity exists in both radial and azimuthal anisotropy for different regions of the Pacific basin.

Strong radial anisotropy is observed in some areas of the Pacific, while others require none at all. Beneath the Shikoku basin, *Takeo et al.* (2013) observe a constant layer of anisotropy from the Moho to 220 km depth with V_{SH} faster than V_{SV} by 4–5% ($\xi = 1.083$ to 1.1052). In contrast, an isotropic uppermost mantle (upper 25 km) sufficiently explains Rayleigh- and Love-wave observations from 3–40 s period beneath the PLATE experiment (*Takeo et al.*, 2014). Our preferred model requires strong radial anisotropy in the lower crust with V_{SH} faster than V_{SV} by ~5.2% ($\xi = 1.11$) and relatively weak anisotropy of ~2.4% ($\xi = 1.05$) in the upper ~30 km of the mantle. This strong crustal anisotropy suggests horizontal fabric that has not been previously required by Pacific models but is consistent with proposed mechanisms of crustal accretion (see section 1.7.4). Our ability to resolve radial anisotropy in the crust is perhaps due to the relatively small lateral variations in crustal thickness across the NoMelt region, the small footprint and dense station spacing, and/or the accurate crustal starting model constrained by the P_n refraction study (*Lizarralde et al.*, 2012). The radial anisotropy observed in the lithosphere beneath NoMelt is significantly weaker than in previous models (Figure 1.11b), perhaps due to our improved sensitivity to the crust. Forcing the crust to be isotropic produces ~4.4% ($\xi = 1.09$) radial anisotropy in the uppermost mantle, closer to previous models; however, the Rayleigh waves are not well

fit in this case (model 2; Figure 1.8e). We are unable to constrain the depth dependence of ξ due to the limited depth-resolution of Love waves in the period band of 5–7.5 s (Figure 1.6b), and thus, longer period teleseismic Love-wave measurements are required.

Azimuthal anisotropy in the lithosphere also varies considerably in strength and direction across these focused regions of the Pacific basin. We find a positive gradient with depth in the lithosphere with a peak of $\sim 6\% G/L$ at ~ 30 km depth with a fast direction parallel to the FSD. In comparison, *Takeo et al.* (2014) observe stronger Rayleigh-wave anisotropy of 7% (assumed P-wave anisotropy B/A of 9%) from the Moho to 60 km depth with a fast direction parallel to the FSD. Their single-layer model does not include H and underpredicts peak-to-peak amplitudes shorter than 6 s by 1–2%, suggesting a shallow layer of even stronger anisotropy. Beneath the TIARES region, *Takeo et al.* (2016) invert for G without accounting for B and H and find significantly weaker Rayleigh-wave anisotropy of $\sim 3.5\%$ in the lithosphere, which decreases to $\sim 2\%$ in the asthenosphere. Notably, the fast direction of anisotropy in the lithosphere is rotated 50° – 55° from fossil spreading, parallel to the direction of ancient plate motion prior to 43 Ma with a spreading rate of 2–3 cm/yr. Their resolution tests are unable to recover structure shallower than 20 km depth, suggesting that if fossil-spreading parallel fabric does in fact exist, it must be embedded in the upper 20 km of the mantle. We observe Ψ_G parallel to fossil spreading from the Moho down to 80–90 km depth, significantly deeper for similarly aged lithosphere. This difference in fabric direction is perhaps related to the faster spreading rates inferred at NoMelt (~ 4.4 cm/yr) relative to TIARES (see section 1.7.3) (*Müller et al.*, 2008). At the Noman region, *Takeo et al.* (2018) also observe significant Ψ_G rotation ($\sim 70^\circ$) away from fossil spreading at ~ 140 Ma lithosphere, perhaps associated with the complex triple paleo-ridge configuration. Less prominent rotations away from the spreading direction have also been observed in P_n refraction studies at the East Pacific Rise ($\sim 10^\circ$) (*Toomey et al.*, 2007), Juan de Fuca ridge ($\sim 18^\circ$) (*Vanderbeek and Toomey*, 2017), as well as old seafloor in the western Pacific (10 – 15°) (*Shintaku et al.*, 2014), suggesting that modification of lithospheric fabric by underlying mantle flow is

perhaps not uncommon.

1.7.2.3 Love-wave anisotropy constraints

Previous observations of 4θ Love-wave anisotropy are scarce and comprised primarily of higher-mode datasets with broad depth sensitivities and very little discussion of their directional and amplitude variations (*Montagner and Tanimoto*, 1990, 1991, *Trampert and Heijst*, 2002, *Visser et al.*, 2008). Observations in the Pacific of 4θ variations in P_n (*Mark et al.*, 2019, *Shintaku et al.*, 2014) show fast directions quasi-parallel (and perpendicular) to fossil spreading, consistent with Love-wave fast directions rotated by 45° relative to fossil spreading in the shallow mantle. Our Love- 4θ measurements are characterized by a peak-to-peak strength of 0.5–1.5% and a fast direction 45° rotated from FSD, in agreement with P_n anisotropy. Only two previous studies, that we are aware of, have inverted Love- 4θ measurements for E (*Trampert and Heijst*, 2002, *Yuan and Beghein*, 2014); both are global inversions which restrict their interpretations of E strength to the deep upper mantle and transition zone and do not interpret Ψ_E beyond noting disagreement between studies. We provide the first high-resolution estimates of E in the lithosphere with a strength of 2–2.5% and a direction 45° rotated from fossil spreading, in agreement with petrofabrics (Figure 1.9, 1.10c).

In an anisotropic medium, the 2θ Love-wave variations should be small in magnitude compared to the 4θ variations (*Montagner and Nataf*, 1986). For this reason, Love- 2θ is often thought to be negligible and has only been observed in a few previous studies (*Forsyth*, 1975, *Montagner and Tanimoto*, 1990, 1991, *Visser et al.*, 2008). Rayleigh-Love coupling was speculated to cause this stronger-than-expected Love- 2θ signal observed in some studies (*Montagner and Tanimoto*, 1990, 1991, *Visser et al.*, 2008) and has been shown to produce strong Love-wave sensitivity to B and H in near-source regions (*Sieminski et al.*, 2007). However, previous studies invariably find ψ_2^L parallel to FSD (and therefore, parallel to ψ_2^R), perpendicular to predictions by *Montagner and Nataf* (1986) and *Montagner and Anderson* (1989) for an anisotropic medium with orthorhombic symmetry. We observe the

first high-resolution Love- 2θ signal with a fast direction that is perpendicular to FSD, in agreement with petrologic predictions. However, its strength is comparable to that of the Love- 4θ component, which is stronger than predicted and not fit by our model. We observe this strong 2θ component even when allowing for 2-D variations in isotropic phase velocity, suggesting that this signal is not due to unaccounted-for 2-D isotropic structure (Figure A.2). Rayleigh-Love coupling (Love-wave sensitivity to B and H) may account for our unusually strong Love- 2θ observations, but further investigation into coupling effects on Love-wave anisotropy at short periods is required.

1.7.3 Constraints on mid-ocean ridge dynamics

As young oceanic lithosphere forms and cools away from the ridge, the mantle flow history is recorded in the LPO fabric of the lithosphere (*Nicolas and Christensen*, 1987). Therefore, observations of present-day radial and azimuthal anisotropy in the lithosphere are important for understanding ridge dynamics at the time of plate formation and in particular, for distinguishing between two end-member ridge processes (*Blackman et al.*, 1996): (1) passive upwelling and (2) buoyancy driven upwelling. Observations of $V_{SV} > V_{SH}$ in the upper \sim 100 km of the mantle beneath the Reykjanes Ridge have been used to infer hotspot-induced buoyant upwelling (*Gaherty*, 2001), although alternative interpretation in terms of 3-D flow have been proposed (*Delorey et al.*, 2007). This interpretation is consistent with numerical models of such buoyancy driven upwelling at slow-spreading ridges, which predict primarily vertical off-axis fabrics associated with the downgoing limb of cooler mantle material, extending from the Moho down to 40–50 km depth (*Blackman and Kendall*, 2002a, *Blackman et al.*, 1996). Conversely, numerical flow models of passive upwelling at fast-spreading ridges produce primarily horizontal lithospheric fabrics that are oriented in the direction of spreading and increase in strength with depth in the lithosphere (*Blackman and Kendall*, 2002a,b, *Blackman et al.*, 1996, 2017).

Radial and azimuthal anisotropy observed at NoMelt are consistent with features of the

passive upwelling model. We observe $\xi > 1$ as well as G and E directions parallel to FSD and FSD+45°, respectively, which are all consistent with horizontal lithospheric fabric that formed due to corner flow at the ridge. Furthermore, our observations of a positive gradient in G from the Moho to ~30 km depth is consistent with numerical flow models of passive spreading that predict a positive gradient in LPO strength within the upper 20–80 km of the mantle (*Blackman and Kendall*, 2002a, *Blackman et al.*, 1996, 2017). The depth dependent LPO strength predicted by flow models is a result of the positive temperature gradient, which reduces viscosities leading to higher strain and enhanced fabric alignment with depth.

Although the strength of G varies within in the lithosphere, Ψ_G remains parallel to fossil spreading down to 80–90 km depth. One interpretation is that this depth marks the dehydration boundary above which volatiles were extracted to form the dry, rigid lithosphere locking in the spreading-parallel fabric. Below 80–90 km depth, we observe the transition from the seismically fast lid to the LVZ (Figure 1.11a), a minimum in G , and a rotation in Ψ_G away from fossil spreading. Together, these observations are consistent with the transition from lithosphere to the weaker asthenosphere with a rotated fabric that underlies the dehydration boundary. This interpretation agrees with the high electrical resistivities ($> 10^3 \Omega\text{m}$) observed in the upper ~80 km beneath NoMelt attributed to dehydrated lithosphere (*Sarafian et al.*, 2015).

In contrast to our observations of FSD-parallel fabric throughout the lithosphere, departures in the fast direction away from fossil spreading have been observed at the East Pacific Rise (*Toomey et al.*, 2007), Juan de Fuca ridge (*Vanderbeek and Toomey*, 2017), and in the south (*Takeo et al.*, 2016) and NW Pacific (*Shintaku et al.*, 2014, *Takeo et al.*, 2018). Rotations ranging from 9°–70° have been observed at depths of 4–60 km beneath the Moho. These rotations have been attributed to spreading-oblique flow at the base of the plate that reorganizes and overprints the spreading-parallel signal before being incorporated into the LPO fabric as the lithosphere cools (e.g. *Toomey et al.*, 2007). According to plate reconstructions by *Seton et al.* (2012), Pacific plate motion 60–80 Ma was to the NW with spreading

oriented approximately E-W at the ridge. Therefore, an ancient plate motion signal would manifest as a clockwise rotation in lithospheric Ψ_G (and Ψ_E) at NoMelt, similar to that observed by *Takeo et al.* (2016) at TIARES. Although the ancient apparent plate motions were similar in the two regions, the half-spreading rate is relatively fast (~ 4.4 cm/yr) at NoMelt and slow (2–3 cm/yr) at TIARES (*Müller et al.*, 2008, *Takeo et al.*, 2016). The difference in fast direction between these regions may reflect that lithosphere fabric records the FSD if spreading rate is large relative to absolute plate velocity, while fabric is dominated by absolute plate motion if spreading rate is slow. This suggests spreading rate may play an important role in determining not only the strength of anisotropy in the lithosphere (e.g. *Gaherty et al.*, 2004, *Song and Kim*, 2012), but also its direction relative to spreading. The LPO fabric inferred from the strength and direction of G and E observed in the lithosphere at NoMelt will help improve future models of mid-ocean ridge dynamics.

1.7.4 Radial anisotropy in the crust

Strong radial anisotropy is required in the lower crust with $V_{SH} \sim 5.2\%$ faster than V_{SV} , suggesting layered horizontal crustal fabrics and/or shear. Radial anisotropy in the crust has not been observed in previous surface-wave studies, perhaps due to the lack of high-frequency data with strong sensitivity to the crust; however, it is required by our dataset in order to simultaneously fit the high-frequency Rayleigh- and Love-wave dispersion to within the error bounds of the data (Figure 1.8e–g; Figure A.3–A.6). Forcing the crust to be isotropic produces Rayleigh-wave velocities that are overpredicted at the shorter periods and underpredicted at longer periods, resulting in large overall data misfit ($\chi^2 \approx 17$). Furthermore, allowing for a more complex mantle structure with additional layers of anisotropy does not significantly change its strength in the crust, suggesting that it is not an artifact of underparameterization but is truly a robust feature of our model.

Anisotropy with $V_{SH} > V_{SV}$ may be consistent with crustal accretion processes including the “gabbro glacier” model (e.g. *Morgan and Chen*, 1993) where accretion occurs through

ductile flow from a mid-crustal magma lens and the “sheeted sill” model (e.g. *Boudier et al.*, 1996) where sills are injected throughout the crust at the ridge, if these processes produce significant vertical variations in either isotropic velocities or anisotropic fabric. Horizontal crustal fabrics have been observed at the Samail ophiolite, where plagioclase in the lower crust is characterized by a strong foliation ([010] axis vertical) and weak lineation ([100] axis girdle in horizontal plane) indicating horizontal strain via compaction (*Van Tongeren et al.*,

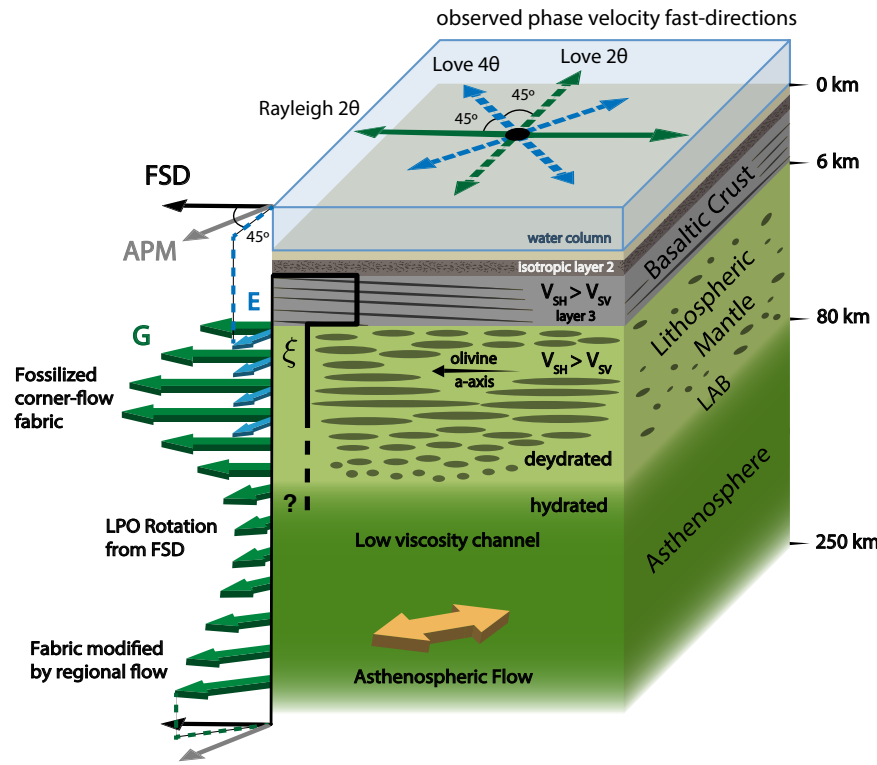


Figure 1.12: Interpretation of the crust and upper mantle beneath NoMelt. Observed Rayleigh- 2θ and Love- 2θ and - 4θ variations in phase velocity are shown with fast directions parallel to FSD, FSD+ 90° , and FSD+ 45° , respectively. Olivine a-axes are subhorizontal with LPO strength increasing from the Moho to ~ 30 km depth, consistent with numerical flow models of passive upwelling. G is parallel to fossil spreading from the Moho down to 80–90 km depth where it rotates to a direction intermediate to FSD and APM, perhaps marking the depth at which dehydration occurred at the ridge, thus locking in lithosphere LPO and forming the LAB. The rotation and minimum in G below 80 km suggests a low viscosity decoupling zone beneath the plate. Deeper in the asthenosphere, G reflects the asthenospheric flow pattern which is not parallel to plate motion, suggesting deformation associated with regional flow dominates. Strong horizontal fabric ($V_{SH} > V_{SV}$) is observed in the lower crust (layer 3), consistent with both the “gabbro glacier” and “sheeted sill” models of crustal accretion involving horizontal layering and/or shearing.

2015). A fabric of this character should produce radial anisotropy with $V_{SH} > V_{SV}$ and weak to no azimuthal anisotropy, similar to what we observe.

Further evidence for quasi-horizontal fabrics in the lower crust comes from lower crustal reflectors observed in the northwest Pacific dipping toward the paleo-ridge axis at 20°–25° (*Kodaira et al.*, 2014, *Reston et al.*, 1999) and south of the Alaska Peninsula with dips of 10°–30° (*Bécel et al.*, 2015). These dipping reflectors typically extend from the Moho to the top of layer 3 and are thought to originate from shear zones in the ductile lower crust during accretion, requiring differential motion between the crust and mantle (*Bécel et al.*, 2015, *Kodaira et al.*, 2014). In both scenarios, the accretion and/or shearing process produce short-wavelength velocity variations that are large enough to reflect high-frequency seismic energy and produce apparent surface-wave radial anisotropy through Backus averaging (*Backus*, 1962). Our observation of $\xi \sim 1.1$ suggests root-mean-square shear-velocity variations of approximately 16% (*Gee and Jordan*, 1988), consistent with intracrustal reflectors that are comparable to the brightness of the Moho (*Bécel et al.*, 2015). Our results are inconsistent with vertical diking and/or vertical cracks, which should produce fast V_{SV} relative to V_{SH} ($\xi < 1$) as well as crack-parallel (ridge-parallel) Rayleigh-wave fast directions (*Hudson*, 1981, *Thomsen*, 1995), neither of which we observe.

1.8 Conclusion

We use high-frequency ambient-noise Rayleigh and Love waves (5–7.5 s) in addition to previously analyzed 15–150 s Rayleigh waves recorded on the NoMelt array to provide high-resolution, *in situ* constraints on seismic anisotropy parameters ξ , G , and E for the upper ~30 km of the mantle (Figure 2.1). We measure the full azimuthal variability of surface waves including Rayleigh- 2θ behavior, and for the first time, Love- 2θ and - 4θ variability. The data require radial anisotropy with $\xi > 1$ in the uppermost Pacific lithosphere and crust, in contrast to recent global models that show $\xi < 1$ throughout the lithosphere. G is stronger in the lithosphere than the asthenosphere, reaching a peak of ~6% at ~30 km

depth and has a direction parallel to the FSD down to 80–90 km depth, perhaps marking the depth to the dehydration boundary and LAB. We provide the first high-resolution estimates of E parallel to FSD+45° with a strength of 2–2.5% down to 35 km depth. Our in situ surface wave constraints on ξ , G , and E agree in magnitude and direction with oceanic petro-fabric observations, suggesting extremely coherent LPO fabric within the NoMelt footprint and bridging the gap between surface-wave and outcrop length scales. Furthermore, strong azimuthal anisotropy and relatively weak radial anisotropy in the lithosphere at NoMelt indicate either E-type LPO fabric or A-type fabric with its fast axis rotated slightly out of the horizontal plane. Observations of G and E azimuths, the increase in strength of G with depth, and $\xi > 1$ in the upper ~30 km of the mantle are consistent with numerical flow model predictions of LPO fabric produced by corner flow at the passively upwelling ridge. Strong radial anisotropy in the lower crust with $\xi > 1$ suggests horizontal layering consistent with either the gabbro glacier and sheeted sill models of crustal accretion.

Acknowledgements

We thank the captain, crew, and engineers of the R/V *Marcus G. Langseth* for making the data collection possible. OBS were provided by Scripps Institution of Oceanography via the Ocean Bottom Seismograph Instrument Pool (<http://www.obsip.org>), which is funded by the National Science Foundation. All waveform data used in this study are archived at the IRIS Data Management Center (<http://www.iris.edu>) with network code ZA for 2011–2013, and all OBS orientations are included in Table A.1. The 1-D transversely isotropic and azimuthally anisotropic models and their uncertainties from this study can be found in the supporting information. This work was supported by NSF grants OCE-0928270 and OCE-1538229 (J.B. Gaherty), EAR-1361487 (G. Hirth), and OCE-0938663 (D. Lizarralde, J.A. Collins, and R.L. Evans) as well as an NSF Graduate Research Fellowship DGE-16-44869 to J.B. Russell. The authors thank the editor as well as reviewers Donald Forsyth, Hitoshi Kawakatsu, and Thorsten Becker for their constructive comments, which significantly

improved this manuscript. J.B. Russell thanks Natalie J. Accardo for kindly sharing codes and expertise that contributed greatly to the analysis.

Seismic evidence for grain-size sensitive 2 | olivine deformation during mid-ocean ridge spreading

CO-AUTHORS: JAMES B. GAHERTY, HANNAH F. MARK, GREG HIRTH, LARS N. HANSEN, DANIEL LIZARRALDE, JOHN A. COLLINS, AND ROB L. EVANS.

Abstract

Seismic anisotropy of the oceanic lithosphere offers a window into mid-ocean ridge (MOR) processes, lithosphere evolution, and the state of Earth's upper mantle. Natural and laboratory olivine samples deformed under various conditions exhibit a range of lattice-preferred orientations (LPOs) that provide a direct link between seismic observables and upper mantle conditions. However, interpreting seismic anisotropy in the context of laboratory LPO data has proven challenging due to incomplete seismic constraints and vast differences in length scale. Here, we bridge this gap by estimating the complete orthorhombic elastic tensor of unperturbed \sim 70 Ma Pacific lithosphere directly beneath the Moho using high-resolution ocean-bottom seismic observations sensitive to compressional- and shear-wavespeed anisotropy. We then utilize a compilation of natural and laboratory petrofabrics from the literature to infer LPO type and shear strain accumulated within the shallow lithosphere. Our findings indicate an alternative (D-type) LPO and strain accumulation of 300–400% in the oceanic lithosphere, challenging conventional assumptions of the prevalence of A-type LPO and suggesting D-type may be more ubiquitous in oceanic lithosphere than previously thought. We infer that MOR seafloor spreading occurs through deformation by grain-size sensitive dislocation-accommodated grain boundary sliding (dis-GBS), rather than grain-size insensitive dislocation creep. This study represents a first

in situ estimate of LPO type and strain accumulation in the oceanic lithosphere that will inform future geodynamic modeling of LPO evolution in ocean basins.

2.1 Introduction

Observations of seismic anisotropy in the ocean basins provide unparalleled insight into Earth's mantle circulation patterns, including the plate-tectonic process of seafloor spreading (*Forsyth*, 1975, *Gaherty et al.*, 2004, *Hess*, 1964, *Lin et al.*, 2016, *Mark et al.*, 2019, *Montagner and Tanimoto*, 1991, *Nishimura and Forsyth*, 1989, *Takeo et al.*, 2018, *Toomey et al.*, 2007). Based on olivine lattice-preferred orientation (LPO) observed in peridotites sampled from ophiolites and oceanic settings (*Ben-Ismail and Mainprice*, 1998, *Michibayashi et al.*, 2006, *Peselnick and Nicolas*, 1978, *Skemer et al.*, 2010, *Warren et al.*, 2008) and in deformation experiments on olivine (*Bystricky et al.*, 2000, *Zhang and Karato*, 1995, *Zhang et al.*, 2000), upper-mantle anisotropy has historically been interpreted as evidence that deformation associated with mantle convection and plate tectonics occurs via dislocation creep in an olivine-rich upper mantle (*Karato and Wu*, 1993). This inference in turn constrains key physical parameters such as grain size, and more generally, the rheology of the upper mantle (*Hirth and Kohlstedt*, 2003). Subsequent advances in laboratory deformation experiments on olivine have complicated this interpretation, illuminating several olivine slip systems and associated LPO fabric types that are strongly dependent on mantle conditions such as stress, volatile content, and partial melting (*Bystricky et al.*, 2000, *Jung and Karato*, 2001, *Jung et al.*, 2006, *Katayama et al.*, 2004) (Figure 2.1). Several of these slip systems have anisotropic signatures that are difficult to distinguish using traditional seismic observations, leading to renewed ambiguity on physical state and deformation processes during seafloor spreading (*Karato et al.*, 2008).

Here, we combine a unique high-resolution estimate of seismic anisotropy in Pacific lithosphere with a database of 123 laboratory and naturally deformed olivine petrofabrics from the literature to directly constrain olivine fabric type and associated deformation mechanism

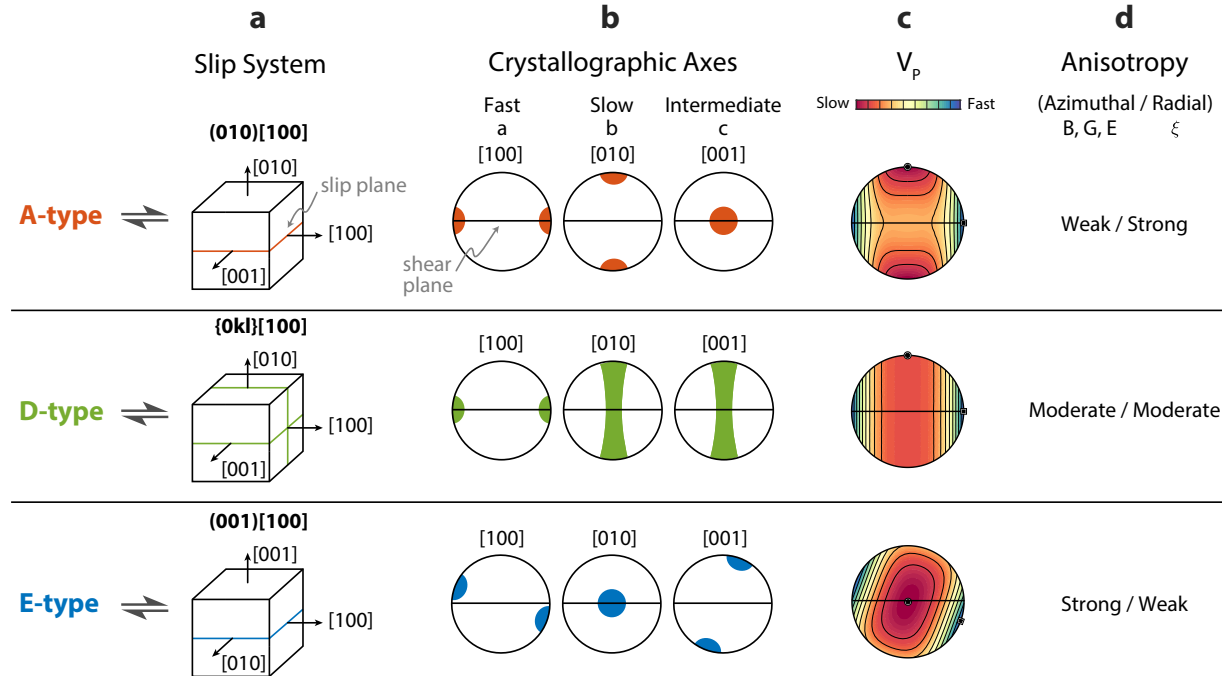


Figure 2.1: **Summary of the most commonly observed LPO types.** Schematic showing the **a** slip systems, **b** crystallographic orientations, **c** V_p , and **d** relative strengths of radial and azimuthal anisotropy for A-, D-, and E-type fabrics. Note the qualitative differences in V_p between the three fabric types arising from the relative orientations of [100], [010], and [001]. Variations in the slow [010] and intermediate [001] axes result in measurable differences in seismic anisotropy. Azimuthal anisotropy is sensitive to the two crystallographic axes in the horizontal plane, and radial anisotropy is sensitive to the difference between the azimuthally averaged horizontal axes and the vertically oriented axis.

and to quantify shear strain associated with seafloor spreading. The new seismic model combines a co-located set of compressional and shear anisotropy observations (*Mark et al., 2019, Russell et al., 2019a*), resulting in an exceptionally complete *in situ* estimate of peridotite elasticity in the oceanic lithosphere. The fabric database includes 91 laboratory deformed olivine samples from direct shear (*Jung and Karato, 2001, Jung et al., 2006, Katayama et al., 2004, Zhang and Karato, 1995*) and high-strain torsion (*Bystricky et al., 2000, Hansen et al., 2014, 2016*) experiments as well as 32 natural peridotite samples from diverse settings including ophiolites (*Ben-Ismail and Mainprice, 1998, Michibayashi et al., 2006, Peselnick and Nicolas, 1978, Skemer et al., 2010, Warren et al., 2008*), volcanic arcs (*Mehl et al., 2003*), and xenoliths and kimberlites from continental cratons (*Ben-Ismail et al., 2001, Satsukawa*

et al., 2010). This database includes the three most common types of olivine LPO (as shown in Figure 2.1), A-, E-, and D-type, each with their fast [100] crystallographic axis oriented sub-parallel to the shear direction and variable orientation of the slow [010] and intermediate [001] axes. The collection of laboratory and field petrofabric observations provide a framework for quantitative interpretation of the *in situ* elasticity tensor in terms of degree of strain, composition, LPO type, and deformation mechanism.

2.2 Methods

2.2.1 Surface-wave inversion with P_n constraints

We solve for the shear and compressional velocities and anisotropy beneath the NoMelt array to 400 km depth as in *Russell et al.* (2019a) but only focus here on the upper ~ 7 km of the mantle where both P and S constraints exist. Previously measured anisotropic Rayleigh- (5–150 s) and Love-wave (5–7.5 s) phase velocities from *Russell et al.* (2019a) are inverted, while simultaneously satisfying V_P constraints in the upper ~ 7 km of the mantle from *Mark et al.* (2019) (“Weighted data, with gradients” in their Table 1). The inversion is carried out in two steps following *Russell et al.* (2019a):

(1) Invert for seismic velocities $V_{SV} = \sqrt{L/\rho}$, $V_{SH} = \sqrt{N/\rho}$, $V_{PV} = \sqrt{C/\rho}$, and $V_{PH} = \sqrt{A/\rho}$ with $\eta = F/(A - 2L)$ fixed to PREM values (*Dziewonski and Anderson*, 1981) and V_{PH} in the upper 7 km of the mantle fixed to values from *Mark et al.* (2019). V_{PV} is scaled such that $\phi^{-1} = (V_{PH}/V_{PV})^2$ remains equal to $\xi = (V_{SH}/V_{SV})^2$.

(2) Invert for azimuthal anisotropy magnitude and direction of G/L , B/A , H/F , and E/N from the azimuthal anisotropy of Rayleigh and Love waves (see *Russell et al.* (2019a) Appendix). The 2θ and 4θ dependence of P_n provides independent constraints on the magnitude and azimuth of B and E , respectively via

$$\rho V_{Pn}(\theta)^2 = A + B_c \cos(2\theta) + B_s \sin(2\theta) + E_c \cos(4\theta) + E_s \sin(4\theta) \quad (2.1)$$

and enters the surface-wave inversion simply as prior constraints on B and E . Below ~ 7 km beneath the Moho, where P_n constraints terminate, and for the parameter H , we follow the general scaling approach described in *Russell et al.* (2019a) whereby B and H scale directly with G . For this study, the direct B and G constraints in the upper 7 km provide an empirical B/G scaling of ~ 1.5 that is applied throughout the model. Additionally, an H/G scaling of -0.11 is applied based on ophiolite samples (*Ben-Ismail and Mainprice*, 1998, *Peselnick and Nicolas*, 1978).

2.2.2 Constructing the orthorhombic elastic tensor

A general elastic tensor is described by 21 independent elastic parameters. This is simplified to only 9 parameters ($A, C, F, L, N, G, B, H, E$) if orthorhombic symmetry is assumed and the three orthogonal crystallographic axes ([100], [010], [001]) are oriented along the principle directions (i.e., in the principle coordinate system). In this configuration, any crystallographic axis may be oriented along any of three principle directions. This requirement is relaxed for the two horizontal directions in order to allow for arbitrary orientations of azimuthal anisotropy in the horizontal plane, resulting in an elastic tensor with 13 parameters (*Montagner and Nataf*, 1986). As one axis is assumed to be vertical, dipping fabrics are not resolvable. This elastic tensor is given by A.23.

Although we solve for all 13 parameters of the tensor in the upper 7 km of the mantle, only 9 are independently determined by our observations ($V_{SV}, V_{SH}, V_{PH}, G_{c,s}, B_{c,s}, E_{c,s}$). The remaining four terms ($C_{13}, C_{23}, C_{33}, C_{36}$) that result from scaling assumptions do not contribute to the quantitative comparisons between the *in situ* tensor and observed and laboratory petrofabrics in Figures 2.3 and 2.4.

2.2.3 Olivine fabric database

We have compiled a database of the elastic properties of 123 published olivine fabrics that includes 91 laboratory deformed olivine samples from direct shear (*Jung and Karato*,

2001, *Jung et al.*, 2006, *Katayama et al.*, 2004, *Zhang and Karato*, 1995) and high-strain torsion (*Bystricky et al.*, 2000, *Hansen et al.*, 2014, 2016) experiments as well as 32 natural peridotite samples from diverse settings including ophiolites (*Ben-Ismail and Mainprice*, 1998, *Michibayashi et al.*, 2006, *Peselnick and Nicolas*, 1978, *Skemer et al.*, 2010, *Warren et al.*, 2008), volcanic arcs (*Mehl et al.*, 2003), and xenoliths and kimberlites from continental cratons (*Ben-Ismail et al.*, 2001, *Satsukawa et al.*, 2010). Of these samples, 12 have been identified as A-type, 6 E-type, and 25 D-type, by the authors based on the orientations of their crystallographic axes. The methods employed by authors to calculate bulk seismic properties from individual crystallographic orientations generally follow a similar procedure and nearly ubiquitously assume 100% olivine and use the single-crystal olivine tensor of *Abramson et al.* (1997). For one harzburgite sample from the Oman ophiolite, the seismic properties were measured directly using ultrasonics, and therefore, contributions from other phases are inherently included (*Peselnick and Nicolas*, 1978). The temperature and pressure at which the elastic calculations are carried out can vary slightly between studies but has negligible effect on seismic anisotropy (*Ben-Ismail and Mainprice*, 1998).

For all samples considered, the orientation of the elastic tensor with respect to the shear plane and shear direction were determined. Upon comparing to the seismic model, all samples in the database were oriented in the seismic reference frame: shear plane parallel to the X - Y plane defined by Earth's surface and shear direction parallel to the the X -axis defined by the fossil-spreading direction (FSD). The Z -axis is oriented perpendicular to the Earth's surface (i.e., perpendicular to the shear plane).

Estimates of shear strain associated with deformation are routinely measured for laboratory samples and range from undeformed ($\gamma \sim 0$) to $\gamma \sim 18.7$ in our dataset, but such estimates are rarely available for natural rocks. One exception is the Josephine shear zone in southwestern Oregon (*Hansen and Warren*, 2015, *Warren et al.*, 2008), which has pre-existing foliations that provide passive strain markers that imply highly strained peridotites up to $\gamma \sim 20$ (*Skemer et al.*, 2010).

2.2.4 Accounting for pyroxene in anisotropy calculations

Secondary phases in addition to olivine in a given sample act to reduce the bulk strength of seismic anisotropy, yet most values reported for laboratory and natural petrofabrics assume pure olivine. In order to directly compare them against our *in situ* estimate, which inherently includes bulk chemistry, we approximate the influence of secondary phases on seismic anisotropy following *Hansen et al.* (2014). Mineral physics calculations using the tool Perple_X (*Connolly*, 2009) suggest ~60 vol.% olivine in the shallow lithosphere for a standard depleted mid-ocean ridge basalt (MORB) mantle composition (*Hacker*, 2008) and a half-space cooling temperature profile for 70 Ma (see supplementary Figure B.1). Invoking the simplifying assumption that the remaining 40% by volume can be approximated by orthopyroxene, a composite elastic tensor is constructed for each sample by taking the Voigt average between the olivine tensor and an orthopyroxene texture from *Hansen et al.* (2014) (see supplementary Figure B.2). As shown in Figure 2.3, this acts to reduce the overall strength of the fabric without having a large effect on the fast azimuth. For the natural samples from *Hansen and Warren* (2015) in Figure 2.3, dunite samples are used for the 100% olivine case, while harzburgite samples with 40% orthopyroxene added are used for the 60% olivine case.

For some samples used in Figure 2.4 in which anisotropy data was pulled from tables rather than calculated from an elastic tensor, an empirical scaling was applied to account for pyroxene. Considering only well-developed fabrics with $\gamma > 2$ from the laboratory data of *Hansen et al.* (2014, 2016), fabric strength was calculated with orthopyroxene content ranging from 0% to 100% by volume for each sample and was fit with a linear function (see supplementary Figure B.3). The relationship between pyroxene content and anisotropy magnitude reduction is nearly -1:1 and provides a straightforward way to scale anisotropy magnitude.

2.2.5 Steady-state grain size calculation

Steady-state grain size (d_{ss}) is estimated as a function of stress (σ) following a previously published grain-size-variable, non-newtonian creep model at a mid-ocean ridge (*Turner et al.*, 2017). In the model, grain-size evolution follows the wattmeter of *Austin and Evans* (2007):

$$\dot{d} = \frac{K_g}{p} d^{1-p} \exp\left(-\frac{E_g + \bar{P}V_g}{RT}\right) - \psi d^2 \sigma : \dot{\varepsilon} \quad (2.2)$$

where K_g and E_g are the grain growth prefactor and activation energy, respectively. The first term on the right-hand side represents grain growth by material diffusion between grains, and the second term represents grain-size reduction through dynamic recrystallization, scaled by a prefactor, ψ . We follow *Turner et al.* (2017) and assume a grain growth exponent $p = 5$, which may be appropriate when a minor pinning phase such as pyroxene is present (*Hiraga et al.*, 2010). Assuming deformation occurs via disGBS, $\dot{\varepsilon} = A_{GBS} \sigma^n d^{-m} \exp(-(E_{GBS} + PV_{GBS})/RT)$. Setting equation 2.2 equal to zero and solving for grain size yields the steady-state solution:

$$d_{ss} = \left[\frac{K_g}{p\psi A_{GBS} \sigma^{n+1}} \exp\left(\frac{(E_{GBS} - E_g) + (PV_{GBS} - PV_g)}{RT}\right) \right]^{\frac{1}{1+p-m}} \quad (2.3)$$

All parameter values can be found in Table 1 of *Turner et al.* (2017). disGBS flow law parameters from *Hansen et al.* (2011) are used. The resulting steady-state grain size variation with stress at $T = 1250^\circ\text{C}$ is shown in Figure 2.5.

2.3 A comprehensive elastic model of oceanic lithosphere

The NoMelt geophysical experiment in the central Pacific provides unique co-located compressional- and shear-wave constraints on *in situ* lithosphere petrofabric over a 600×400 km footprint with average seafloor age of ~ 70 Ma. It comprised a refraction survey that constrained V_{PH} and its azimuthal anisotropy in the upper ~ 7 km of the mantle (*Mark et al.*,

2019), and a broadband OBS deployment that resolved the complete V_S structure via observations of both Rayleigh-wave (*Lin et al.*, 2016) and Love-wave azimuthal anisotropy (*Russell et al.*, 2019a) in the upper 40-km of the lithosphere. Employing V_P constraints from the refraction tomography of *Mark et al.* (2019), we invert previously measured high-frequency (5–7.5 s) ambient noise Rayleigh- and Love-wave phase velocities for all 13 elastic parameters that describe the orthorhombic elastic tensor following *Montagner and Nataf* (1986) (see Methods).

The resulting model is shown in Figure 2.2, and here we focus on the upper \sim 7 km beneath the Moho where P- and S-constraints coincide. Azimuthal anisotropy increases with depth beneath the Moho for both G (V_{SV}) and B (V_{PH}), but remains relatively constant for E (V_{SH}) largely due to the lack of depth sensitivity for Love waves (*Russell et al.*, 2019a). Anisotropy fast azimuths Ψ_G and Ψ_B are sub-parallel to the fossil-spreading direction (FSD), and Ψ_E is rotated by 45° , as predicted for orthorhombic olivine (*Montagner and Nataf*, 1986). In detail, while Ψ_G and Ψ_B are each consistent with FSD within error, they differ from one another by 5–10° degrees. This subtle mismatch is likely attributed to the different depth sensitivities of P_n and surface waves: the refraction imaging is primarily sensitive to the shallowest \sim 7 km of the mantle, while the surface waves integrate across the upper \sim 20 km.

From the 13 elastic parameters, we construct the equivalent orthorhombic elastic tensor at each depth and average the upper 7 km to produce a single representative fabric (Figure 2.2c). The V_P pole figure indirectly expresses the relative orientations of the three crystallographic axes. The well-defined maximum parallel to the FSD indicates a sub-horizontal, clustered [100] fast axis. The girdled slow and intermediate directions indicate dispersed [010] and [001] axes perpendicular to the inferred shear direction, characteristic of D-type olivine fabric (Figure 2.1b).

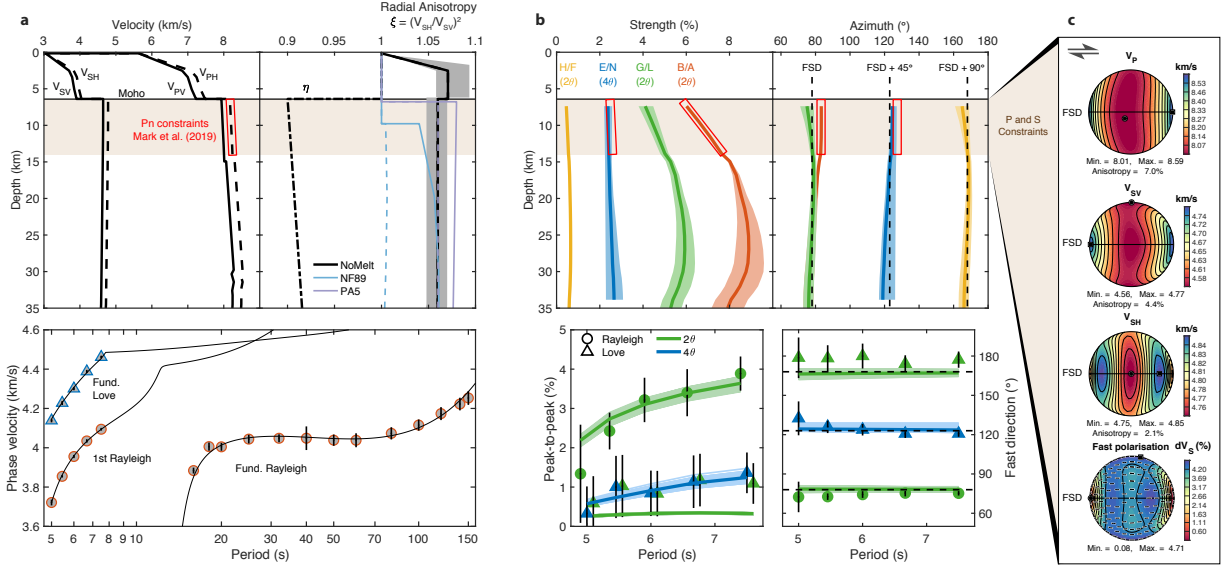


Figure 2.2: Comprehensive elastic model and data fit for the NoMelt region. **a**, V_P , V_S , and Radial anisotropy model and data fit (modified from *Russell et al.*, 2019a). Grey shading for NoMelt radial anisotropy captures the range of models that fit the data, with the best fit model shown in black. Brown shading indicates where both V_P (*Mark et al.*, 2019) and V_S constraints exist in the upper ~ 7 km of the mantle. NF89, *Nishimura and Forsyth* (1989) 52–110 Ma region; PA5, *Gaherty et al.* (1996). **b**, Azimuthal anisotropy strength and azimuth. Model uncertainties of two standard deviations from bootstrapping are shaded. Data fit and range of bootstrap model fits are shown in the lower panels. **c**, Velocity calculations for the average elastic tensor for the upper ~ 7 km of the lithospheric mantle. The horizontal black line denotes the horizontal plane with the fossil-spreading direction (FSD) to the east and west. Maxima and minima are denoted by a square and circle, respectively. $dV_S = 200(V_{SH} - V_{SV})/(V_{SH} + V_{SV})$

2.4 Strain accumulation in the shallow lithosphere

Olivine LPO strength, and in turn the magnitude of seismic anisotropy, increase with shear strain (*Hansen et al.*, 2014, 2016). Our NoMelt model provides four independent estimates of the magnitude of seismic anisotropy, and three independent estimates of anisotropic directions, that can be directly compared to olivine LPO formed as a function of strain (Figure 2.3). We compare to samples deformed in laboratory torsion experiments (*Hansen et al.*, 2014, 2016) as well as samples deformed naturally at the Josephine shear zone (*Hansen and Warren*, 2015, *Warren et al.*, 2008) for which strain has been determined (see Methods for details of the fabric dataset). The seismic model represents a harzburgitic oceanic litho-

sphere, so it is not surprising that a direct comparison to pure olivine fabrics fails to find a range of shear strains compatible with the model; the high strains required to match the fast directions correspond to anisotropy magnitudes that are approximately twice that which we observe. Incorporating the effect of composition on the sample fabrics by accounting for the presence of pyroxene helps to resolve this discrepancy. For each sample, we approximate the contributions from pyroxene by mixing each pure olivine elastic tensor with an appropriately oriented orthopyroxene texture following *Hansen et al.* (2014) (see Methods for details). We assume a nominal harzburgite composition of 60% olivine and 40% orthopyroxene by volume, which represents the lower bound of olivine content in abyssal peridotites observed globally (*Warren*, 2016). This composition is also consistent with the average lithospheric P and S velocities in the NoMelt model, as compared to Perple_X calculations (*Connolly*, 2009) for a typical depleted mid-ocean ridge basalt (see supplementary Figure B.1). Compared to the pure olivine estimates, the mixture systematically decreases the strength of anisotropy due to orthopyroxene's weaker single-crystal anisotropy and LPO compared to olivine (Figure B.2), while fast azimuths are largely unaffected.

The overall agreement between NoMelt anisotropy and the laboratory torsion data for 60% olivine is remarkable given the vast difference in length scale of the measurements (~9 orders of magnitude). Anisotropy strength at NoMelt is consistent with laboratory samples for shear strains ranging from 2–4, and fast directions indicate $\gamma > 3$. Our inferred strain ranging from 3–4 is on the upper end of that expected during corner flow at the ridge. The angle between the fast V_P axis and shear plane are small (10°) for $\gamma > 1.5$ (Figure 2.3e), implying a sub-horizontal [100] crystallographic axis, in agreement with previous work (*Skemer et al.*, 2012). This suggests a horizontal fabric at NoMelt, though we are unable to directly constrain fabric dip with our dataset consisting only of horizontally propagating waves.

The strain evolution of natural samples are more scattered and show clear differences from the experimental samples. For a given strain and olivine content, the magnitude of anisotropy of the natural fabrics is consistently weaker. This is perhaps unsurprising given

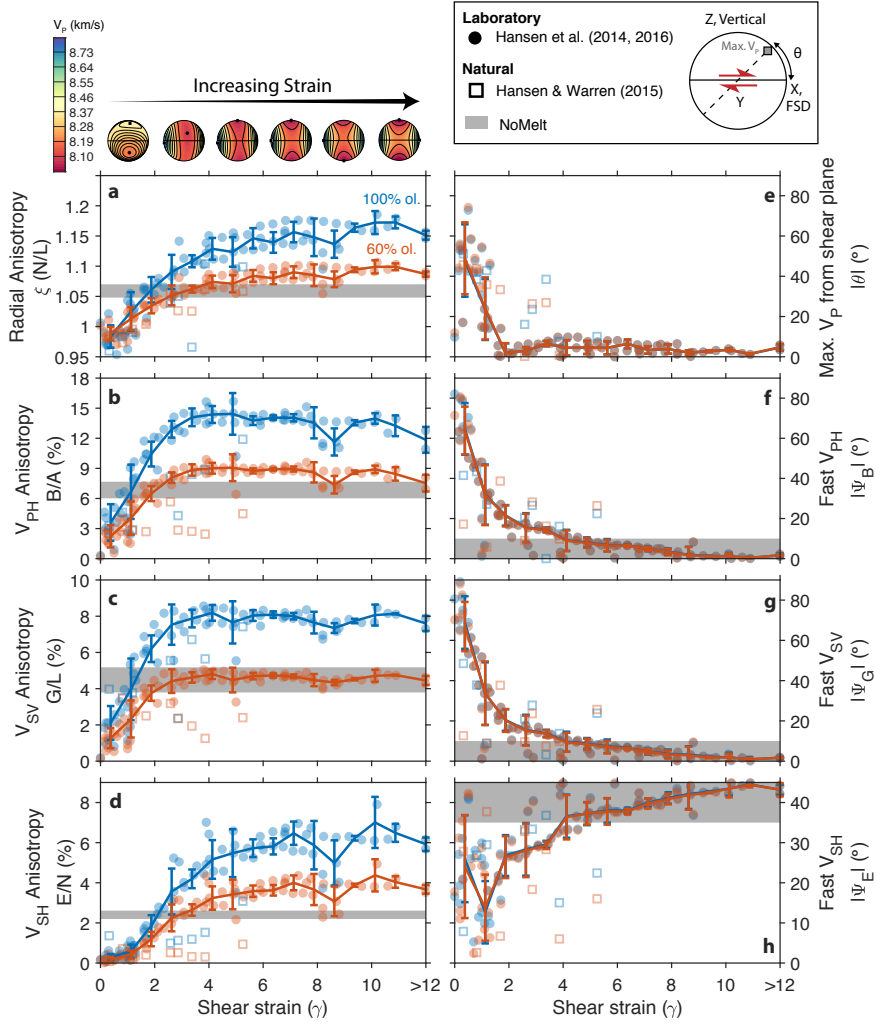


Figure 2.3: NoMelt anisotropy compared with olivine petrofabric data as a function of shear strain and pyroxene content. Anisotropy strength (**a–d**) and fast azimuth with respect to the shear direction or FSD (**f–h**) for laboratory (solid circles) (*Hansen et al.*, 2014, 2016) and natural samples (open squares) (*Hansen and Warren*, 2015). The NoMelt seismic model for the upper ~ 7 km of the lithospheric mantle is shown in grey with a width that represents the full range of values in that depth range. NoMelt FSD uncertainty is $\sim 10^\circ$. **e** Magnitude of the angle between maximum V_P and the shear plane; seismic model does not constrain this parameter. Calculations for (blue) pure olivine and (red) 60% olivine, 40% orthopyroxene are shown (see Methods for details on the inclusion of orthopyroxene). Error bars show median and standard deviation for laboratory data binned by strain with bin width $\gamma = 0.75$. V_P surfaces are shown above **a** for laboratory samples averaged by increments of $\gamma = 2$ (See also Figure B.6). All samples oriented consistent with the seismic reference frame: shear plane parallel to Earth's surface and shear direction parallel to the FSD.

the differences in scale between natural shear zones, such as at the Josephine ophiolite, and laboratory torsion experiments. In addition, the anisotropy fast directions of the natural samples fail to consistently rotate into the shear direction with increasing strain, remaining misaligned by $\sim 25^\circ$ at $\gamma = 5.25$ (Figure 2.3f–h). The relatively weak and misaligned anisotropy of the highly strained Josephine samples is likely attributed to the presence of a pre-existing LPO upon entering the shear zone, which prolongs fabric development and misalignment of [100] with respect to the shear direction (*Skemer et al.*, 2012, *Warren et al.*, 2008). That NoMelt anisotropy is stronger than even the most highly strained natural sample ($\gamma = 5.25$) for 60% olivine, highlights the remarkably coherent lithosphere LPO across the 600×400 km NoMelt footprint (*Russell et al.*, 2019a). In addition, any pre-existing vertical LPO associated with upwelling at the ridge was likely weak in comparison to corner flow and overprinted.

The strain evolution of LPO from D-type at intermediate strains to A-type at high strains was previously identified by *Hansen et al.* (2014). This LPO evolution is reflected in the average V_P surfaces shown above Figure 2.3a. The inferred shear strain at NoMelt of 3–4 based on strength and direction of anisotropy fit with experiment samples corresponds to fabrics with girdled slow and intermediate V_P directions on average, consistent with D-type LPO in the NoMelt lithosphere.

2.5 Inferring LPO fabric type

We further evaluate LPO fabric type by comparing the relative magnitudes of azimuthal and radial anisotropy, which provides a good discriminant if the orientation of the sample with respect to the shear plane is known (*Karato*, 2008, *Karato et al.*, 2008) (Figure 2.1). In Figure 2.4, we compare the strength of NoMelt anisotropy with that calculated for A-, D-, and E-type olivine fabrics from both natural settings (*Ben-Ismail and Mainprice*, 1998, *Ben-Ismail et al.*, 2001, *Karato*, 2008, *Mehl et al.*, 2003, *Michibayashi et al.*, 2006, *Peselnick and Nicolas*, 1978, *Satsukawa et al.*, 2010, *Skemer et al.*, 2010, *Warren et al.*, 2008) and

laboratory deformation experiments (*Bystricky et al.*, 2000, *Jung and Karato*, 2001, *Jung et al.*, 2006, *Katayama et al.*, 2004, *Zhang et al.*, 2000). For most samples, fabric type was characterized by the original authors.

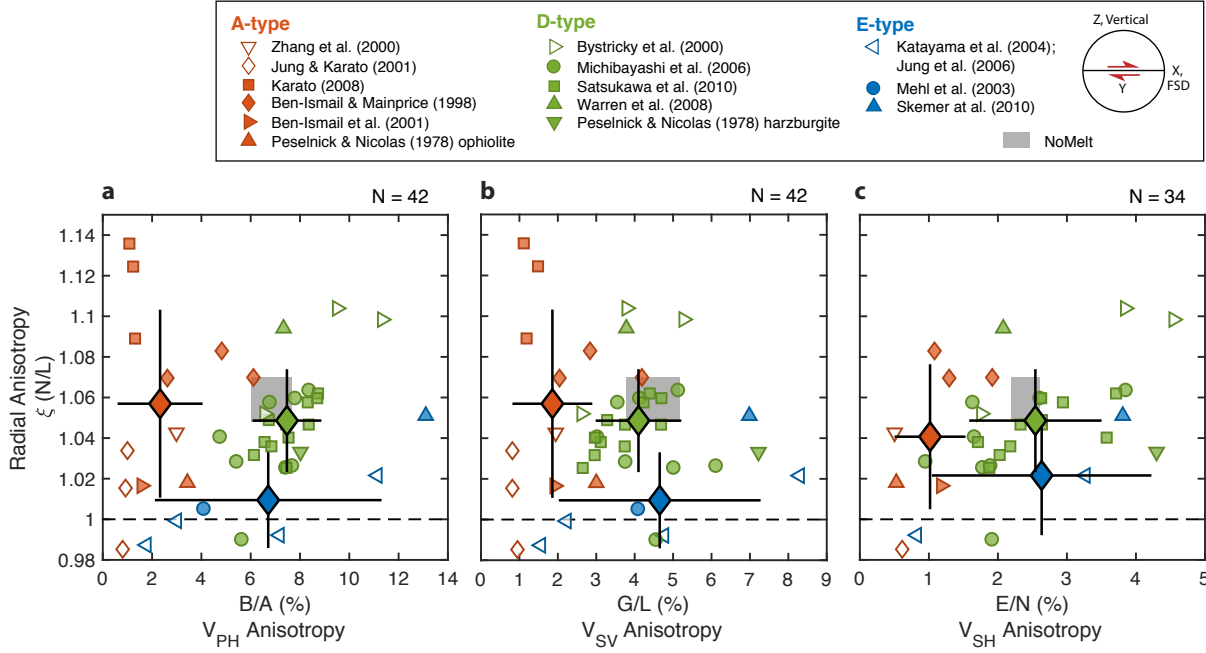


Figure 2.4: i

Inference] Anisotropy of A-, D-, and E-type olivine LPO. Radial anisotropy compared to **a** V_{PH} , **b** V_{SV} , and **c** V_{SH} azimuthal anisotropy for three fabric types compared to the NoMelt model, shown in grey. Open and closed symbols denote laboratory and natural samples, respectively. The large filled diamonds show the mean and one standard deviation for each fabric type. Effects of orthopyroxene are included assuming a composition of 75% olivine and 25% orthopyroxene by volume. No correction is applied to the samples from *Peselnick and Nicolas* (1978), which were derived ultrasonically and therefore already include the bulk chemistry. Note that **c** contains fewer data points than **a** and **b** due to unreported V_{SH} anisotropy values for some studies.

To first order, samples with A-type LPO tend to exhibit strong radial anisotropy relative to azimuthal, whereas the opposite is true for E-type. NoMelt displays moderate radial and azimuthal anisotropy most similar to the samples with D-type LPO. This result holds regardless of the olivine content assumed (see supplementary Figure B.4), though we find that a composition of 75% olivine and 25% orthopyroxene provides the best overall fit to the seismic observations. As the D-type LPO data in Figure 2.4 represent mostly natural

samples, the higher olivine content required to match the seismic model is consistent with Figure 2.3, which showed that natural samples underestimate anisotropy strength for 60% olivine and 40% orthopyroxene. A harzburgite composition with 75% olivine is consistent with abyssal peridotites from fast-spreading MORs, which tend to have higher olivine content (70–95%) compared to slow spreading (*Dick and Natland*, 1996, *Niu and Hékinian*, 1997, *Warren*, 2016).

Scatter between samples of the same fabric type in Figure 2.4 is likely attributed to differences in shear strain, with low strain samples exhibiting weaker anisotropy, as demonstrated in Figure 2.3a–d. At lower shear strains (and in the presence of a pre-existing LPO fabric) the [100] axis is likely to be dipping with respect to the shear plane (*Skemer et al.*, 2012) (Figure 2.3e), resulting in weaker radial and azimuthal anisotropy. Therefore, dipping fabrics in Figure 2.4 will tend to skew towards the origin, which does not change the overall inference of D-type fabric (Figure B.5). In other cases, scatter may be attributed to samples that straddle the boundary between two LPO types, such as the peridotite averages of *Ben-Ismail and Mainprice* (1998), which are composed of both A-type and D-type samples.

Although A-type LPO is typically considered the most prevalent type in the upper-mantle, D-type is also commonly observed in nature (Figure 2.4), yet the conditions under which they form are still debated. D-type fabrics have been produced in laboratory experiments on fine-grained olivine aggregates deformed under dry, high stress conditions (*Bystricky et al.*, 2000, *Carter and Ave'Lallement*, 1970, *Jung et al.*, 2006); such stresses are unlikely to be present during ridge corner flow or in the asthenosphere. Alternatively, there is increasing evidence that D-type fabrics form under a range of natural conditions through grain-size sensitive dislocation-accommodated grain boundary sliding (disGBS). In ophiolites, A- and D-type fabrics have been observed in course-grained dunites and finer-grained harzburgites, respectively, suggesting pyroxene may play a role in D-type fabric formation by limiting olivine grain size and promoting deformation by disGBS (*Braun*, 2004, *Warren et al.*, 2008). Recalibrated olivine flow laws suggest that disGBS may be active at a range

of stresses and grain sizes that are appropriate for upper-mantle deformation (*Hansen et al.*, 2011). MOR geodynamic modeling that incorporates grain-size evolution and mixed deformation processes (diffusion, dislocation creep, and disGBS) suggest that shallow, near-ridge deformation is dominated by disGBS (*Turner et al.*, 2015).

2.6 Implications for MOR conditions

The strong correspondence between observed anisotropic fast directions and the direction of fossil seafloor spreading implies that the NoMelt *in situ* elasticity tensor represents the upper ~ 7 km of mantle deformed by corner flow during spreading. We interpret the inferred D-type fabric as observational evidence of deformation via grain-size sensitive disGBS, rather than grain-size insensitive dislocation creep (*Braun*, 2004, *Hansen et al.*, 2011, *Warren et al.*, 2008). The stress and grain-size parameters suggested by geodynamic modeling (*Turner et al.*, 2015, 2017) provide plausible mantle conditions appropriate for NoMelt lithosphere during its formation ~ 70 Ma, and those parameters sit within a disGBS regime (Figure 2.5). For reasonable grain sizes (1–10 mm) and strain rates ($10^{-14.5}$ – $10^{-12.5}$ s $^{-1}$), inferred stress is relatively low (0.2–1.5 MPa). This hypothesis provides an alternative to the notion that D-type fabric forms only at high stress (*Jung et al.*, 2006, *Karato et al.*, 2008), which was concluded from laboratory experiments with small grain sizes deformed under high strain rates unrepresentative of mantle conditions.

Grain-size piezometers calibrated on laboratory olivine data provide an estimate of minimum grain size achieved through dynamic recrystallization, assuming a steady state is reached (*Hirth and Kohlstedt*, 2015, *Karato et al.*, 1980). Extrapolated to MOR conditions, these piezometers predict large grain sizes up to ~ 100 mm that fall well within the dislocation-creep regime but are larger than expected to occur in the mantle (Figure 2.5). That piezometers calibrated on pure olivine samples overpredict grain sizes may indicate that grain-size pinning via secondary phases such as pyroxene is an important process in the mantle. The wattmeter – a grain-size evolution model based on the balance between rates

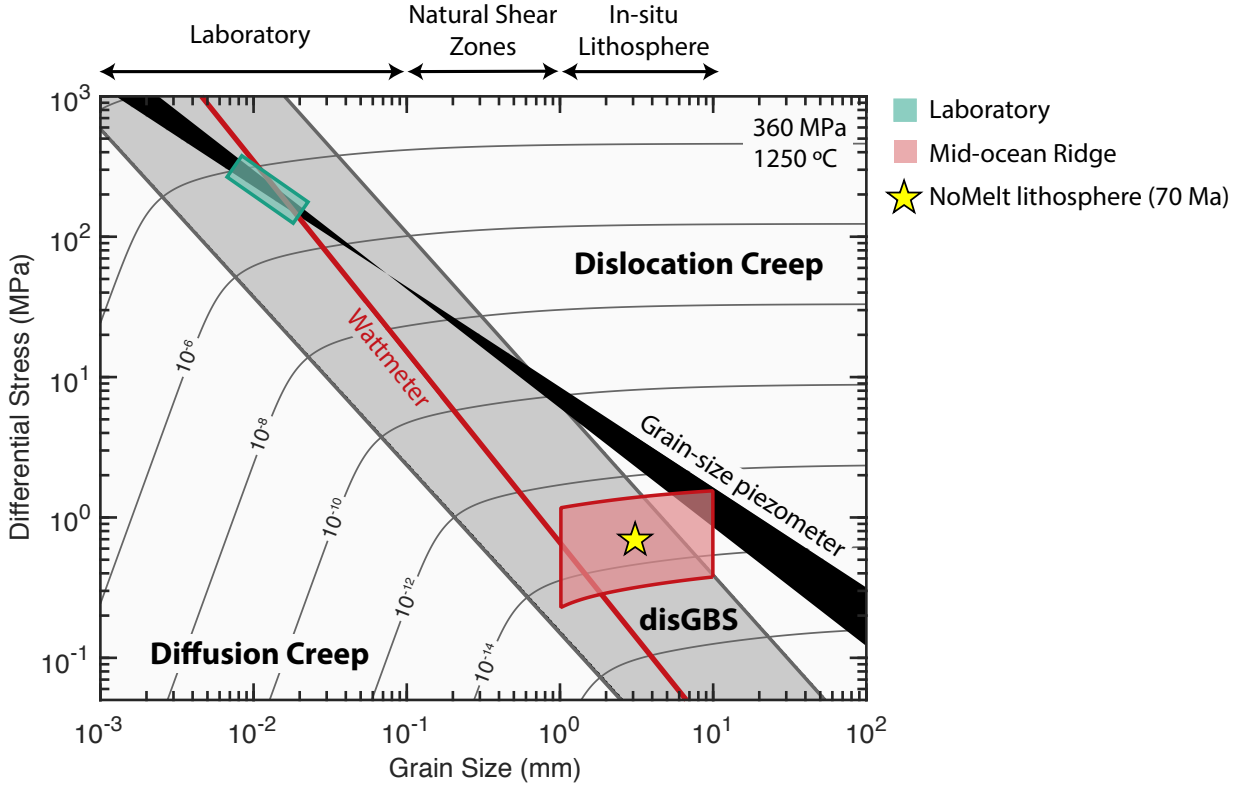


Figure 2.5: **Deformation mechanism map at mid-ocean ridge conditions.** Strain rate calculated as a function of differential shear stress and grain size using the olivine flow laws of Hansen *et al.* (2011) at a temperature of 1250°C and pressure of 360 MPa. These conditions represent the shallow mantle during formation of the sub-moho fabric at the ridge. Approximate grain sizes (1–10 mm) and strain rates ($10^{-14.5}$ – $10^{-12.5}$ s $^{-1}$) from a geodynamic model at a MOR (Turner *et al.*, 2017) are shaded in red and indicate deformation primarily via dislocation-accommodated grain boundary sliding (disGBS). The yellow star represents approximate conditions during shallow NoMelt fabric formation 70 Ma. The red line shows a grain-size wattmeter from Austin and Evans (2007) for the same parameters used in Turner *et al.* (2017) (see Methods for details), which coincides with the disGBS regime. For comparison, in black is a grain-size piezometer derived from experimental data (Hirth and Kohlstedt, 2015, Karato *et al.*, 1980) that suggests larger-than-expected grain sizes for reasonable strain rates at MOR conditions.

of grain growth and reduction (Austin and Evans, 2007) – yields more realistic grain sizes at mantle conditions when disGBS flow laws are used in addition to a grain growth exponent that accounts for olivine grain-size pinning (see Methods for details). Thus, the wattmeter may be a more appropriate scaling relation than laboratory-calibrated piezometers for understanding grain sizes at mantle conditions.

Observations implying shallow deformation via grain-size sensitive disGBS with high strain accumulation ($\gamma = 3\text{--}4$) and sub-horizontal [100] axis will inform new geodynamic modeling efforts of MOR dynamics and associated fabric development. Models that assume dislocation creep often contain relatively weak anisotropy in the shallow lithosphere with a dipping [100] axis and are characteristically A-type fabric (*Blackman et al.*, 1996, 2017), in contrast to what we infer. Deformation via disGBS implies complex non-Newtonian and grain-size dependent rheologies that impact solid-state convection streamlines, melt extraction, and thermal and rheological evolution of the lithosphere and asthenosphere (*Turner et al.*, 2017). It has been shown that girdled D-type LPO can be formed by relaxing strain compatibility constraints in viscoplastic self-consistent models (*Tommasi et al.*, 2000), but generally alternative LPO types are not considered. Our *in situ* characterization of LPO type in oceanic lithosphere provides a new target for geodynamic models that will improve understanding of MOR dynamics and fabric development.

Acknowledgements

We thank Haemyeong Jung, Katsuyoshi Michibayashi, Misha Bystricky, Jessica Warren, and Philip Skemer who provided fabric data used in this study. This work is supported by the NSF under Grant No. DGE-16-44869, OCE-0928270, and OCE-1538229. Seismic data can be accessed through the IRIS Data Management Center (www.iris.edu) under network code ZA. Elastic tensors were plotted using the MSAT software (<https://geophysics.gly.bris.ac.uk/MSAT/>).

Surface-wave constraints on upper mantle

3 | petrofabric and flow beneath \sim 43 Ma seafloor

in the south Pacific

CO-AUTHORS: JAMES B. GAHERTY, ZACHARY EILON, DONALD W. FORSYTH,
GÖRAN EKSTRÖM

Abstract

The age dependence of oceanic upper mantle structure provides insights into the thermal evolution of the lithosphere-asthenosphere system and mantle convection. We utilize high-resolution Rayleigh- (5–150 s) and Love-wave (5–7 s) phase velocities from ambient noise and teleseismic earthquakes measured at \sim 43 Ma seafloor in the south Pacific to image shear velocity and azimuthal anisotropy to 300 km depth and radial anisotropy of the crust and uppermost mantle lithosphere. Fast shear velocities (>4.6 km/s) and azimuthal anisotropy parallel to the fossil-spreading direction (FSD) define a \sim 35–40 km thickness lithosphere. In the lithospheric mantle, azimuthal anisotropy (3–3.5%) with fast axis parallel to the FSD and radial anisotropy with $V_{SH} > V_{SV}$ by \sim 2% indicates horizontally aligned olivine associated with corner flow at the mid-ocean ridge (MOR). Strong radial anisotropy (\sim 5.5%) is also observed in the lower crust, consistent with horizontal layering or shearing during accretion. Below \sim 35 km depth, azimuthal anisotropy rotates to and overshoots absolute plate motion (APM) by \sim 30° below \sim 150 km depth. When a simple layered parameterization is enforced on the model, no layer displays anisotropy aligned with APM. These models suggest that anisotropic fabric below the lithosphere is controlled by pressure- or density-driven flow in the asthenosphere, rather than shear at the base of the plate. We find that half-space cooling (HSC) accounts for most (\sim 75%) of the sublithospheric shear velocity difference compared

to the \sim 30 Myr older NoMelt experiment when anelastic effects are included. However, an additional unaccounted for \sim 1% velocity difference from 40–100 km depth can be explained by reheated sublithospheric mantle possibly accompanied by a small amount of melt (<0.5%) at YoungORCA, consistent with the presence of small-scale convection.

3.1 Introduction

Structure and evolution of the oceanic lithosphere-asthenosphere system is one of the most fundamental and well studied components of plate tectonics. To first order, the oceanic lithosphere conductively cools following a half-space cooling (HSC) model (e.g. *Korenaga and Korenaga*, 2008, *Parker and Oldenburg*, 1973) to \sim 70 Myr and a plate-cooling model (PCM) at older ages (e.g. *McKenzie et al.*, 2005, *Stein and Stein*, 1992). These simple models can explain the age-dependence of seafloor depth and heat flow observations (*Parsons and Sclater*, 1977, *Stein and Stein*, 1992, *Turcotte and Schubert*, 2014) as well as seismic velocities to first order (*Faul and Jackson*, 2005). As the lithosphere forms near the mid-ocean ridge (MOR), shear deformation associated with corner flow produces a lattice-preferred orientation (LPO) of olivine crystals with fast a-axes that align parallel to the fossil-spreading direction (FSD) (e.g. *Blackman and Kendall*, 2002a, *Blackman et al.*, 1996, 2017, *Kaminski and Ribe*, 2002). This fabric is frozen into the lithosphere and transported as the plate cools, retaining a record of paleo deformation conditions near the MOR. This olivine LPO in the lithosphere produces azimuthal anisotropy of seismic wavespeed that has been extensively documented at length scales ranging from local active source P_n observations (e.g. *Hess*, 1964, *Morris et al.*, 1969, *Raitt et al.*, 1969) to plate-scale surface wave tomographic models (e.g. *Forsyth*, 1975, *Nishimura and Forsyth*, 1989, *Smith et al.*, 2004). Relative motion of the rigid lithosphere over the weaker asthenosphere leads to shearing of the asthenospheric mantle and formation of olivine LPO that, on a broad scale, aligns with the absolute plate motion (APM) direction beneath much of the Pacific basin (e.g. *Beghein et al.*, 2014, *Burgos et al.*, 2014, *Debayle and Ricard*, 2013, *Montagner and Tanimoto*, 1991, *Smith et al.*, 2004).

This conventional understanding of oceanic mantle processes is challenged by new high-resolution ocean bottom seismometer (OBS) array observations that more accurately capture short-wavelength variations in seismic structure and have illuminated new complexities at various seafloor ages throughout the Pacific basin. In particular, there is mounting evidence that perturbations to the system due to sublithospheric small-scale convection (SSC) (e.g. *Haxby and Weissel*, 1986, *Richter and Parsons*, 1975) may be more ubiquitous than previously thought. For instance, at the farthest reaches of the Pacific at 130–140 Ma seafloor, variations in asthenospheric shear velocities observed over a distance of ~1000 km could not be simultaneously explained by either the PCM or HSC model (*Takeo et al.*, 2018). Departures from HSC associated with off-axis volcanism have also been observed at young seafloor near the MOR (*Weeraratne et al.*, 2007). Further evidence for pressure- or density-driven SSC is indicated by asthenospheric azimuthal anisotropy that deviates significantly from APM (*Becker et al.*, 2014, *Lin et al.*, 2016, *Takeo et al.*, 2018). In addition, a growing number of studies have observed lithospheric anisotropy that is misaligned from the FSD by 10–90° (e.g. *Shinohara et al.*, 2008, *Shintaku et al.*, 2014, *Takeo et al.*, 2016, 2018, *Vanderbeek and Toomey*, 2017) indicating complexity during fabric formation near the ridge.

To investigate these processes in more detail, the Young OBS Research into Convecting Asthenosphere (YoungORCA) broadband array was deployed at ~43 Ma seafloor in the south Pacific, ~750 km northeast of the Marquesas islands (Figure 3.1). The site was chosen based on its relatively pristine gravity signature with possible evidence of short-wavelength lineations reminiscent of those originally observed by *Haxby and Weissel* (1986). Additionally, YoungORCA is situated ~2100 km southeast of the ~70 Ma NoMelt experiment of comparable size and data quality (*Lin et al.*, 2016), providing an opportunity to investigate the age-dependent structure of the oceanic mantle in unprecedented detail. As NoMelt displays extremely coherent azimuthal anisotropy (*Mark et al.*, 2019, *Russell et al.*, 2019a) that is thought to represent typical, unperturbed oceanic lithosphere, it also serves as a benchmark with which to compare.

In this study, we present high-resolution observations of shear velocity, radial anisotropy, and azimuthal anisotropy beneath the \sim 43 Ma YoungORCA array. We measure Rayleigh- (5–150 s) and Love-wave (5–7 s) phase velocities and anisotropy from teleseismic earthquakes and ambient noise, providing one of the few observations of Love-wave 4θ anisotropy. The resulting model of shear velocity and anisotropy is interpreted in the context of the previous NoMelt experiment (*Lin et al.*, 2016, *Russell et al.*, 2019a) in order to evaluate their age-dependence and to investigate whether HSC can explain the \sim 30 Myr age difference. We find evidence for a deviation from HSC consistent with reheating of the YoungORCA lithosphere and possible SSC.

3.2 Data and Methods

We use data from 30 broadband OBS from the YoungORCA experiment deployed from April 2018 to May 2019 to measure teleseismic and ambient-noise Rayleigh and Love wave phase velocities. OBS positions on the seafloor were determined to within \sim 5 m using the OBSrange software package (*Russell et al.*, 2019b). Based on these locations, average water depth in the region is \sim 4625 m. Orientations of the horizontal channels were successfully determined for 20 of the 30 OBS via the Doran–Laske–Orientation–Python (DLOPy) tool (*Doran and Laske*, 2017) using Rayleigh wave arrivals from earthquakes with magnitudes greater than Mw 7.0. Of the 30 recovered stations, 8 experienced a battery failure, and therefore clock drift was not known. We measure and correct clock drift following *Hable et al.* (2018) (see supplementary material for details). Instrument errors resulting in poor or unusable data (Supplemental information) appeared more commonly on the BHZ, BH1, and BH2 channels, and therefore we make additional use of the differential pressure gauges (DPGs) where possible in this study.

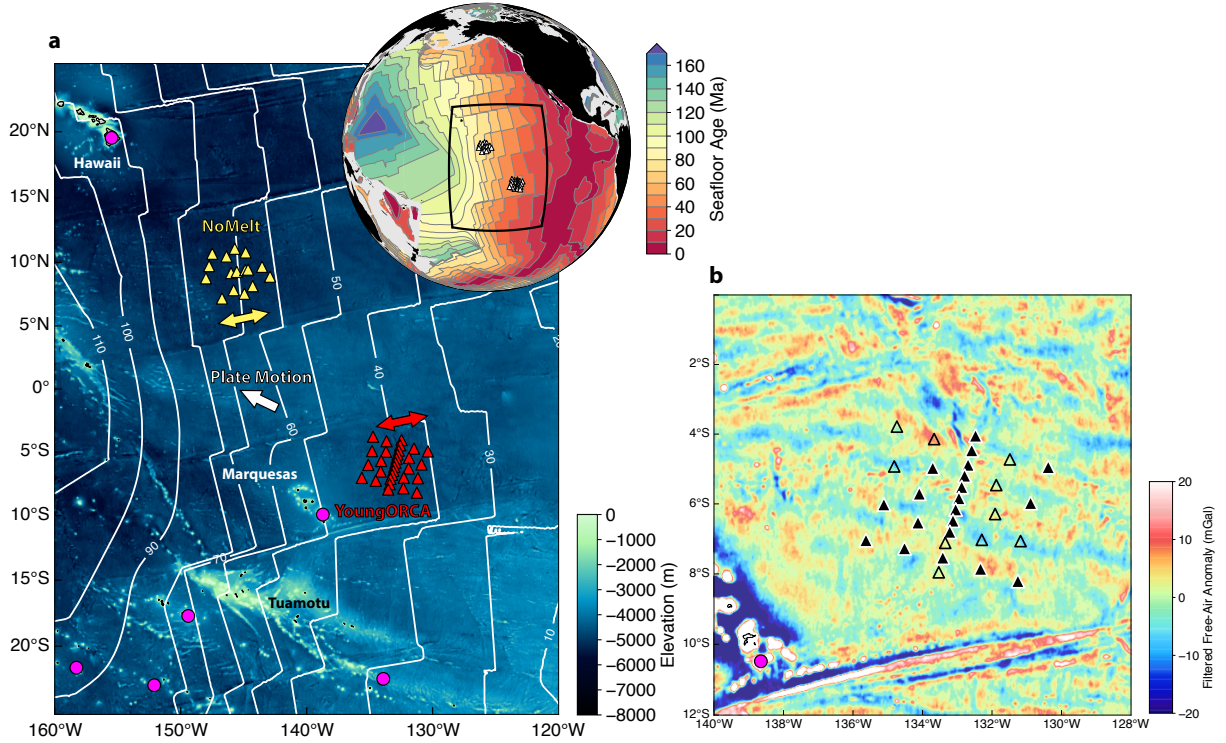


Figure 3.1: (a) Map of the study region showing the YoungORCA (~ 43 Ma) OBS array in red and NoMelt (~ 70 Ma) in yellow. Seafloor age is shown by white contours in increments of 10 Myr (Müller *et al.*, 2008). The white arrow shows present-day absolute plate motion (APM) (Argus and Gordon, 1991), and double-headed arrows show the approximate fossil-spreading direction (FSD) at each array based on seafloor fractures. Magenta circles mark hotspot locations. (b) Zoom in to YoungORCA showing the free-air gravity anomaly after removing long wavelength variations defined by a Gaussian smoothing filter with $\sigma = 0.5^\circ$. Open triangles denote OBS for which an orientation could not be determined, and therefore only the vertical and pressure channels were used.

3.2.1 Tilt and compliance removal

Prior to ambient-noise and teleseismic surface-wave analyses, we remove coherent horizontal and pressure energy (i.e., tilt and compliance) from the vertical channels using the Automated Tilt and Compliance Removal (ATaCR) software (Janiszewski *et al.*, 2019), which employs the methods detailed in Crawford and Webb (2000). For ambient-noise analysis, removing daily coherent pressure from the vertical channels amplifies the higher-mode Rayleigh-wave energy in the 3–10 s secondary microseism band (Bowden *et al.*, 2016, Yang *et al.*, 2020). We remove daily tilt followed by compliance at all frequencies for each 24 hour

seismogram. Removal of tilt and compliance also greatly improves the signal-to-noise ratio (SNR) of teleseismic Rayleigh waves at periods >50 s (*Crawford and Webb*, 2000). Therefore, we apply the same technique to remove tilt and compliance from each event trace using transfer functions calculated from the 24 hours prior to the earthquake.

3.2.2 Ambient-noise surface-wave dispersion

Ambient noise cross-correlation analysis is performed to extract interstation Rayleigh- and Love-wave phase velocity dispersion from 3–25 s period. In general, we follow the procedures outlined in detail in *Russell et al.* (2019a). Here, we summarize the approach.

Our preprocessing approach is similar to that of *Bensen et al.* (2007). After deconvolving instrument response to displacement and downsampling to 1 Hz, daily cross-correlations functions (CCFs) are calculated using 3 hour windows with 50% overlap. We do not apply time-domain normalization or spectral whitening prior to CCF calculation. Daily frequency-domain CCF cross-spectra are normalized to produce cross-coherence spectra prior to stacking. This procedure is performed for transverse-transverse (T-T), pressure-pressure (P-P), and tilt- and compliance-removed vertical-vertical (Z-Z corrected) station pairs (Figure 3.2).

Array-average phase velocity dispersion is extracted from the CCFs using the high-resolution linear Radon transform (LRT) (e.g. *Luo et al.*, 2008, 2015, *Schultz and Jeffrey Gu*, 2013, *Yang et al.*, 2020). The LRT effectively converts from distance-time to frequency-phase slowness space. We find stable results by solving the inverse problem using the conjugate guided gradient with model and residual weighting as described by *Ji* (2006). The resulting Radon panel for each component is shown in Figure 3.2d–f. Phase velocities are extracted along the curves of maximum energy with uncertainties estimated by the 0.9 contour. The P-P panel displays fundamental-mode Rayleigh wave energy (0S) from 3–25 s period. First- and second-overtone Rayleigh waves (1S, 2S) are shown on the corrected Z-Z panel from 4–11 s and 3–3.5 s, respectively. The T-T panel show clear Love-wave energy from 3–11 s, where at the shortest periods (<6.5 s), phase velocities are consistent with the fundamental

mode (0T), but the mode content is less certain for periods greater than 7–8 s (denoted xT) due to the crossover of the 0T and ≥ 1 T mode branches (e.g. *Russell et al.*, 2019a).

Interstation phase velocity dispersion is measured using the cross-spectral waveform fitting technique of *Menke and Jin* (2015), which is based on the zero-crossing approach of *Aki* (1957). We follow the general Bessel fitting procedure from *Russell et al.* (2019a) but make use of the average dispersion results from the LRT as the starting dispersion model. From the interstation phase velocity measurements, c , we reinvert for 1-D isotropic phase velocity (c_0) in addition to azimuthal anisotropy of the form:

$$c(\omega, \theta) = c_0(\omega) \left[1 + A_2(\omega) \cos 2(\theta - \psi_2(\omega)) + A_4(\omega) \cos 4(\theta - \psi_4(\omega)) \right] \quad (3.1)$$

where θ is propagation azimuth and A and ψ are the amplitude and fast azimuth of anisotropy, respectively. For Rayleigh waves, $A_4 \approx 0$ (*Montagner and Nataf*, 1986) and we solve only for the 2θ variations, while Love waves display both 2θ and 4θ anisotropy (*Russell et al.*, 2019a). The resulting sinusoidal fits to the data for T-T, Z-Z, and P-P are shown in Figure 3.3a–c.

3.2.3 Teleseismic Rayleigh-wave dispersion

We utilize the the Automated Surface-Wave Measurement System (ASWMS) of *Jin and Gaherty* (2015) to extract array-average Rayleigh-wave phase velocity dispersion and azimuthal anisotropy at 16–150 s period after *Lin et al.* (2016). The ASWMS tool employs a cross-correlation based technique to measure intra-array phase-delay times. Using tilt and compliance removed vertical seismograms and DPG data from 132 teleseismic earthquakes with magnitudes greater than M_W5.5 (Figure 3.3d), we apply the ASWMS in three overlapping frequency bands for the vertical channel (12–27, 20–100, and 70–150 s) and one for the DPG (20–50 s). We use a ray-theoretic framework to simultaneously invert delay times from all earthquakes for 1-D isotropic phase velocity and 2θ azimuthal anisotropy at each frequency of interest. Resulting measurements for the vertical and pressure channels are

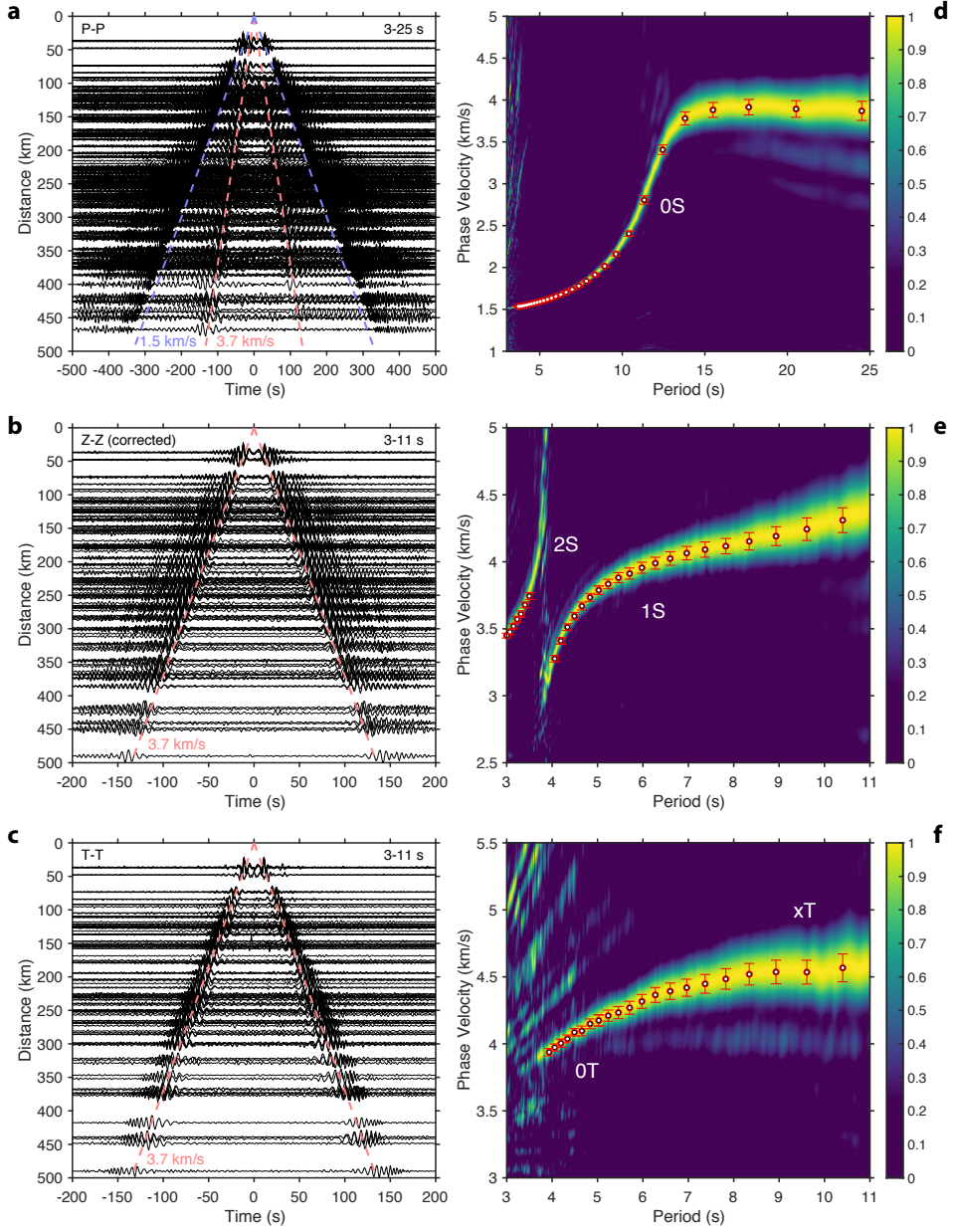


Figure 3.2: Ambient noise observations and array-averaged Rayleigh and Love dispersion measurements. Bandpass filtered ambient noise CCFs for (a) pressure (3–25 s Rayleigh fundamental mode: 0S), (b) vertical (3–11 s Rayleigh first and second overtones: 1S, 2S), and (c) transverse (3–11 s Love fundamental and overtones: 0T, xT) component pairs. Daily tilt and compliance were removed prior to calculation of the Z-Z pairs, amplifying the higher-mode Rayleigh waves. Group velocities of 3.7 km/s and 1.5 km/s are indicated by pink and blue dashed lines, respectively. (d–f) Linear Radon transform (LRT) panels showing phase velocity dispersion for the data shown in a–c. Picked measurements are shown in red.

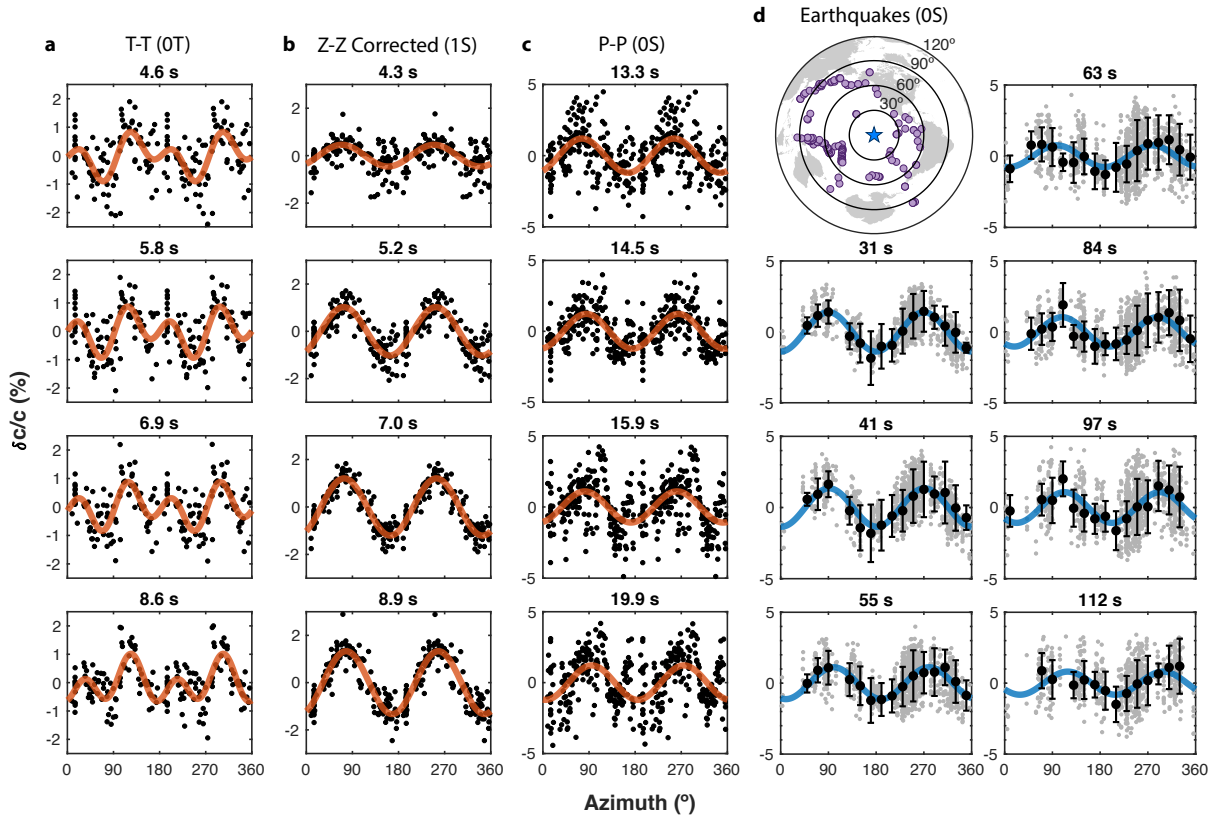


Figure 3.3: Array-averaged azimuthal anisotropy of Love and Rayleigh waves. (a) Love-wave anisotropy with interstation phase velocity residuals in black and best fit $2\theta + 4\theta$ model in orange. (b,c) same as a) but for 2θ anisotropy of Rayleigh first overtone and fundamental mode, respectively. (d) Anisotropy of interstation Rayleigh-wave phase velocity (grey points) measured from 132 earthquakes of $M_w 5.5$ and greater, shown in the inset map. Black symbols show residuals averaged in 20° azimuthal bins and one standard deviation. The 2θ fit to the binned averages is shown in blue. Strength and fast azimuth fitting parameters are shown in Figure 3.4c,d.

compared for consistency and averaged. We take a conservative approach to quality control and consider only measurements with a waveform coherence >0.8 and require input waveform SNR >5 . In order to evaluate possible bias due to uneven azimuthal distribution of earthquakes, we also estimate anisotropy for data averaged in 20° azimuthal bins (Figure 3.3d). The resulting strength and azimuth of anisotropy agrees with the unbinned measurements to within uncertainty, and we take their average as the final estimates. Reported uncertainties include contributions from the formal uncertainties associated with the inversion procedure as well as any scatter between the overlapping frequency band estimates, between vertical

channel and DPG estimates, and between the binned and unbinned estimates.

3.2.4 Inversion for shear velocity, radial and azimuthal anisotropy

Array-averaged isotropic phase velocities and anisotropy are inverted for depth dependent shear velocity, radial anisotropy, and azimuthal anisotropy in two steps following *Russell et al.* (2019a). The general procedure and scaling assumptions are outlined here.

First, isotropic Rayleigh- (5–150 s) and Love-wave (5–7 s) phase velocities are jointly inverted for the transversely isotropic (TI) structure. We solve for V_{SV} (wavespeed of horizontally propagating vertically polarized shear waves) and V_{SH} (wavespeed of horizontally propagating horizontally polarized shear waves) in the crust and upper ~ 25 km of the mantle, providing an estimate of radial anisotropy, $\xi = (V_{SH}/V_{SV})^2$. The Voigt averaged NoMelt model is used as the starting model after adjusting water depth to match the average at YoungORCA (4625 m). The crust in this starting model is based off refraction tomography results at NoMelt, and we assume a similar crustal structure at YoungORCA. We enforce layers of constant ξ in the crust and mantle, respectively, due to poor depth sensitivity of the 5–7 s Love waves to V_{SH} (*Russell et al.*, 2019a) and assume an isotropic upper (~ 1.5 km) crust (*Swift et al.*, 1998). As Rayleigh-wave measurements extend to 150 s period, we solve for V_{SV} down to 300 km depth. Compressional velocities V_{PV} and V_{PH} are scaled by V_{SV} and V_{SH} by preserving the starting model V_P/V_S and enforcing $\phi^{-1} = (V_{PH}/V_{PV})^2 = \xi$. We do not invert phase velocity measurements < 5 s primarily due to limitations in speed and stability of the MINEOS normal-mode based code for calculating perturbation kernels and phase velocities at such short periods. Physical dispersion effects due to seismic attenuation are applied to the eigenfrequencies assuming the Q_μ structure of *Ma et al.* (2020) and a reference frequency of 35 mHz.

Second, azimuthal anisotropy of Rayleigh (5–150 s) and Love waves (5–7 s) are inverted for the strength and azimuth of anisotropic parameters G and E following *Montagner and Nataf* (1986), using perturbation kernels calculated from the radially anisotropic model.

The parameters G and Ψ_G describe the strength and fast azimuth of V_{SV} anisotropy, respectively, and are constrained from the Moho to 300 km by the strength and azimuth of the 2θ azimuthal variations of Rayleigh and Love waves. Parameters E and Ψ_E reflect the 4θ anisotropy of V_{SH} and are solved from the Moho to 25 km depth. Historically, E has been poorly constrained as it is sensitive primarily to the 4θ azimuthal dependence of Love waves, which has rarely been observed in nature (*Russell et al.*, 2019a). In addition, Rayleigh waves have considerable sensitivity to parameters B (2θ anisotropy of V_{PH}) and H (2θ dependence of the anisotropic parameter η) (Figure C.3). As they are poorly resolved by Rayleigh waves, we scale them directly with G by enforcing $B = 1.25G$ and $H = 0.11G$, respectively, based on peridotite fabrics (*Ben-Ismail and Mainprice*, 1998). We apply additional norm damping below 300 km that linearly increases with depth such that no anisotropy is contained in the model below ~ 360 km depth.

We estimate uncertainties for G and E via 1000 bootstrap iterations. For each iteration, we invert surface-wave anisotropy data randomly selected from a Gaussian distribution with mean equal to the original data and standard deviation defined by their $1-\sigma$ uncertainties. The median and middle 68th percentile of the resulting model ensemble with acceptable misfit ($\chi^2 \leq 2$) is taken as the final model and $1-\sigma$ uncertainty region, respectively.

In addition to a smooth parameterization of G , we also solve for a simplified layered parameterization that allows for large discontinuities in anisotropy amplitude and direction. The layer boundaries are determined from the resolution matrix of the smooth inversion, which includes contributions from regularization. As the trace of the resolution matrix approximates the effective number of resolvable model parameters, we take its cumulative sum and assign layer boundaries at depths corresponding to the integer values. This yields a layered model with boundaries at 35, 80, and 300 km depth.

In order to more reliably compare the YoungORCA and NoMelt shear velocity profiles directly, we reinvert the NoMelt dispersion observations from *Lin et al.* (2016) and *Russell et al.* (2019a) to provide an improved degree of fit to the data comparable to that of Youn-

gORCA. The updated NoMelt model is similar to that of *Russell et al.* (2019a) in the upper 100 km but is slower from 150 to 350 km depth. The largest difference occurs at \sim 230 km depth where the updated model is \sim 3% slower than previously reported, better fitting the longer period (>60 s) Rayleigh dispersion observations.

3.3 Results

3.3.1 Shear velocity and radial anisotropy

Shear velocity (V_{SV}) and radial anisotropy (ξ) modeling results are shown in Figure 3.4. A thin lithospheric lid defined by velocities >4.5 km/s extends to \sim 35–40 km depth, where a sharp negative gradient in shear velocities occurs. This transition approximately marks the base of the lithosphere. Asthenospheric velocities decrease from \sim 4.4 km/s at \sim 50 km depth to \sim 4.2 km/s at 150 km. Below \sim 150–200 km depth, shear velocities do not deviate from the NoMelt starting model. Crust and uppermost mantle V_{SV} agrees well with that observed at the NoMelt array (Figure 3.4b) (*Russell et al.*, 2019a).

Radial anisotropy, ξ , is observed in the lower crust and uppermost lithospheric mantle with $V_{SH} > V_{SV}$. Anisotropy is strong in the crust ($\xi \sim 1.125$) and relatively weak in the mantle ($\xi \sim 1.038$). Similar to previous results at the NoMelt array (*Russell et al.*, 2019a), we find that radial anisotropy is required in both the crust and mantle. Forcing the model to be isotropic or restricting radial anisotropy to either the crust or mantle (but not both) results in a poor fit to the high-frequency Love waves. In comparison to NoMelt, radial anisotropy is stronger in the crust and slightly weaker in the mantle. Values of ξ in the mantle at YoungORCA and NoMelt approximately bracket the range observed in the 20–52 Ma average region 3 of *Nishimura and Forsyth* (1989) ($\xi \sim 1.04$ –1.055).

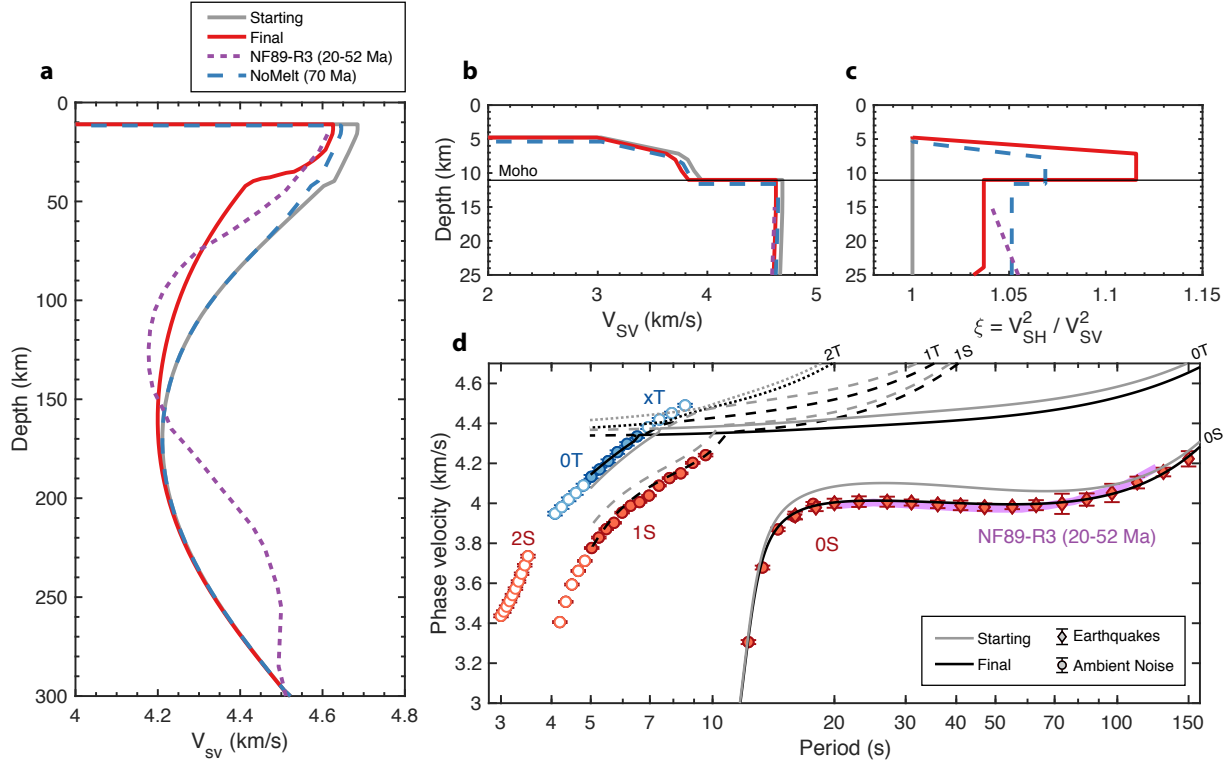


Figure 3.4: 1-D shear velocity and radial anisotropy at YoungORCA. (a) V_{SV} for YoungORCA in red, NoMelt in blue (*Lin et al., 2016, Russell et al., 2019a*), and the 20-52 Ma average of *Nishimura and Forsyth* (1989) in purple. (b,c) V_{SV} and radial anisotropy, ξ , for the crust and uppermost lithosphere. (d) Rayleigh (red) and Love (blue) phase velocities with data fits of the starting and final model shown in grey and black, respectively. Symbol type differentiates ambient-noise (circles) and earthquake (diamonds) measurements. Open symbols are not included in the inversion.

3.3.2 Azimuthal anisotropy

Surface-wave anisotropy fitting parameters are shown in Figure 3.5c,d. Rayleigh-wave anisotropy is characterized by 2θ anisotropy with a fast azimuth that is parallel to the FSD from 5–10 s period and linearly rotates towards APM for periods greater than ~ 15 s, reaching APM at ~ 80 s and surpassing it slightly at 130–150 s. Peak-to-peak amplitudes increase from 2% to 2.7% at 5–10 s period and remain relatively constant at $\sim 2.5\%$ from 15–50 s period. Amplitudes decrease to $\sim 2\%$ at 55–110 s and further reduce to $\sim 1\%$ at periods > 130 s.

We observe 2θ and 4θ Love-wave anisotropy over a limited frequency band (5–6.5 s

period) that is sensitive only to the shallow lithospheric mantle. Love 4θ anisotropy (1–1.25%) has a fast azimuth rotated from the FSD by $\sim 45^\circ$ in agreement with predictions for horizontally aligned orthorhombic olivine with fast a-axis parallel to the FSD (*Montagner and Nataf*, 1986). In contrast, Love 2θ anisotropy is rotated ~ 20 – 25° from its predicted direction of FSD+ 90° for orthorhombic olivine, inconsistent with the Love 4θ and Rayleigh 2θ anisotropy. Additionally, the amplitude of Love 2θ anisotropy (0.8–1%) is a factor of ~ 4 stronger than what is implied by the Rayleigh-wave anisotropy. A similar underprediction of Love 2θ anisotropy was also observed at the NoMelt experiment (*Russell et al.*, 2019a).

Rayleigh- and Love-wave anisotropy is inverted for depth dependent anisotropic parameters G ($2\theta V_{SV}$ anisotropy) and E ($4\theta V_{SH}$ anisotropy). In the shallow lithosphere (Moho to 35 km depth), G is parallel to the FSD to within 10° in both the smooth and layered models. From 35–120 km depth, the smooth model gradually rotates clockwise towards APM, while the layered model's 35–80 km layer falls between FSD and APM. In this depth range, G amplitude decreases from ~ 3.4 – 2.5% . Below 120 km depth in the asthenosphere, G continues to rotate clockwise surpassing APM by $\sim 35^\circ$ at 250 km depth with an amplitude of $\sim 2.2\%$. The layered model contains a single asthenospheric layer greater than 80 km depth with fast azimuth rotated $\sim 15^\circ$ clockwise from APM with an amplitude of $\sim 2\%$.

Seismic parameter E is resolved from the Moho to 25 km depth (upper ~ 10 km of the mantle). It is characterized by a fast azimuth that is parallel to FSD+ 45° to within 5° , which is less than the uncertainty on the local FSD estimated from fracture zones. We observe E amplitudes of $3.4\% \pm 0.2\%$, which is stronger than that observed previously at NoMelt by $\sim 1\%$ (*Russell et al.*, 2019a). Due to the limited frequency range of Love-wave observations, we do not attempt to resolve depth dependence of E .

3.3.2.1 Sensitivity to shallow V_{PH} anisotropy

It is well known that fundamental mode Rayleigh waves are highly sensitive to compressional velocities in the presence of TI (*Anderson and Dziewonski*, 1982). More recently,

Kawakatsu et al. (2015) and *Kawakatsu* (2016a,b) proposed a new and more intuitive definition of the fifth TI parameter η (renamed η_κ), which recasts the parameter set such that Rayleigh-wave sensitivity to V_{PH} and V_{PV} is largely reduced compared to that previously shown by *Anderson and Dziewonski* (1982). However, shallow sensitivity to V_{PH} remains strong regardless of the choice of η (*Kawakatsu*, 2020).

In turn, Rayleigh-wave anisotropy is sensitive to the anisotropic parameter B , which describes the 2θ anisotropy of V_{PH} . Rayleigh sensitivity kernels in Figure C.3 show that sensitivity to B is often comparable to G , and for longer periods that sample asthenospheric G (80 s), lithospheric sensitivity to B constitutes a significant fraction of the total sensitivity. Given the long history of refraction tomography experiments in the Pacific (*Hess*, 1964, *Morris et al.*, 1969, *Raitt et al.*, 1969) corroborated by more recent observations (e.g. *Mark et al.*, 2019, *Shintaku et al.*, 2014, *Toomey et al.*, 2007, *Vanderbeek and Toomey*, 2017), it is well-documented that lithospheric V_{PH} anisotropy is ubiquitous in the oceanic lithosphere and stronger than V_{SV} anisotropy by a factor of ~ 1.2 – 1.7 (*Mark et al.*, 2019, *Russell et al.*, 2019a, *Takeo et al.*, 2016). Therefore, failure to account for strong lithospheric B will result in biased estimates of G amplitude and azimuth, particularly in the asthenosphere. As lithospheric fabric is typically oriented sub-parallel to the FSD, failure to account for B will tend to bias asthenospheric G estimates towards the FSD. In this study, we include the effects of B (and H) through prior scaling relations based on peridotites in order to avoid these potential biases.

3.4 Discussion

3.4.1 Comparison to previous studies in the Pacific

Recent proliferation of high-resolution OBS arrays at a range of seafloor ages and locations in the Pacific basin provides insight into key plate tectonic processes such as seafloor spreading, thermal evolution of the lithosphere, and present-day mantle dynamics (e.g. *Lin*

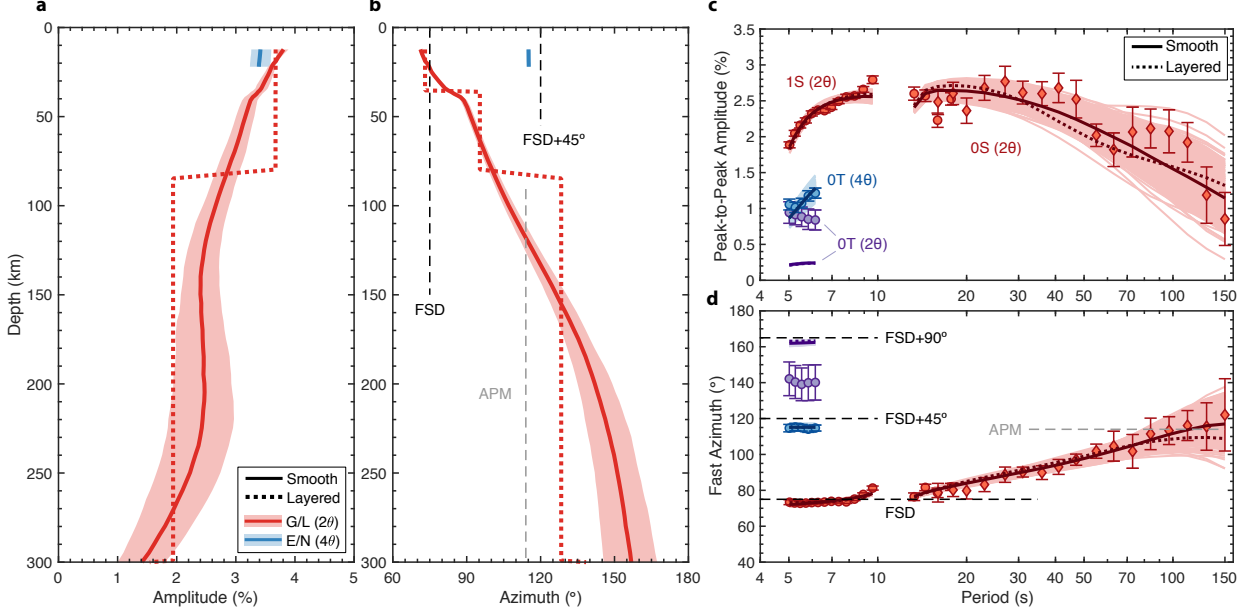


Figure 3.5: Azimuthal anisotropy (G/L , E/N) amplitude (a) and fast azimuth (b) for the smooth (solid) and layered (broken) inversion parameterizations. The shaded region shows $1-\sigma$ bootstrap uncertainties for the smooth model. (c,d) Anisotropy data and model fits for Rayleigh 2θ (red) and Love 2θ (blue) and 4θ (purple). Heavy smooth and broken lines show the median model fits for the smooth and layered models, respectively. Light lines show individual bootstrap model fits. Symbol types are as in Figure 3.4d. FSD – fossil-spreading direction; APM – absolute plate motion

et al., 2016, *Takeo et al.*, 2013, 2014, 2016, 2018, *Weeraratne et al.*, 2007, *Yang et al.*, 2020).

We directly compare our V_{SV} , ξ , and G models with recent observations at the older ~ 70 Ma NoMelt array (*Lin et al.*, 2016, *Russell et al.*, 2019a), ~ 2100 km northwest of YoungORCA (Figure 3.1). The YoungORCA and NoMelt datasets are of comparable resolution and separated in age by ~ 30 Myr, providing an unprecedented opportunity to investigate age-dependent properties of upper mantle shear velocity and anisotropy structure. In addition, these two arrays approximate the age-averaged regions 3 (20–52 Ma) and 4 (52–110 Ma) of *Nishimura and Forsyth* (1989) (hereafter referred to as NF89-R3 and NF89-R4). The NF89 profiles consist of regional average V_{SV} and ξ based on carefully selected 20–125 s pure-path dispersion observations and likely represent length scales intermediate between local-scale OBS array studies and the broader scale Pacific structure in global models.

Figure 3.6 shows shear velocities at YoungORCA, NoMelt, and NF89-R3 and R4. In

general, the character of V_{SV} at YoungORCA and NoMelt is remarkably similar to that of NF89-R3 and R4. In the shallow lithosphere, all four profiles have similar shear velocities that fall between 4.6 and 4.65 km/s. Thinner lithosphere is indicated by the shallower negative velocity gradients at NF89-R3 and YoungORCA, consistent with their younger ages. YoungORCA and NoMelt are nearly identical below \sim 170 km depth, and the same is true for R3 and R4. However, in this depth range the NF89 models are consistently faster than the array-based models. Overall, the YoungORCA and NoMelt profiles are generally smoother and less oscillatory compared to NF89: the NF89 models are faster at depths of 40–75 km, slower from 75–150 km, and faster again from 170–300 km depth. The low-velocity zone (LVZ) of NF89 is shallower, ranging from 100–150 km, while at YoungORCA and NoMelt it represents a broader region from \sim 125–200 km. These differences are likely due in part to the different starting models and regularization choices, although YoungORCA and NoMelt better explain the >125 s Rayleigh-wave phase velocities.

Radial anisotropy at NoMelt and YoungORCA are constrained only in the crust and shallow lithospheric mantle, while NF89 models extend from the Moho to 300 km depth (Figure 3.4). In the shallow mantle, all four models require $V_{SH} > V_{SV}$ ($\xi > 1$), consistent with horizontal olivine LPO fabric formed at the fast-spreading ridge (e.g. *Blackman and Kendall*, 2002a, *Blackman et al.*, 2017). Similar $\xi > 1$ anisotropy has also been observed in the lithosphere at other locations in the Pacific (*Gaherty et al.*, 1996, *Takeo et al.*, 2013, *Tan and Helmberger*, 2007). Radial anisotropy in the mantle at YoungORCA is slightly weaker than NoMelt, but both estimates are within the range of the NF89 profiles, which increase from \sim 1.04 to \sim 1.055 in the upper 10 km of the mantle.

In the lower crust, both YoungORCA and NoMelt require radial anisotropy with $V_{SH} > V_{SV}$, indicating the presence of quasi-horizontal layering that may be consistent with lower-crustal dipping reflectors previously observed in the Pacific (*Bécel et al.*, 2015, *Kodaira et al.*, 2014, *Reston et al.*, 1999). Our observations are also in agreement with plagioclase LPO found in lower crustal gabbros at the Samail ophiolite, which exhibit a strong horizontal

foliation (vertical [010] crystallographic axes) with a weak lineation (girdled [100] crystallographic axes aligned in the horizontal plane) indicating compaction dominated deformation (*Van Tongeren et al.*, 2015). This has been interpreted as evidence for the “sheeted sill” model of crustal accretion (e.g. *Kelemen et al.*, 1997, *Korenaga and Kelemen*, 1998) rather than the “gabbro glacier” model, which predicts a strong lineation along the spreading direction associated with ductile shearing (e.g. *Henstock et al.*, 1993, *Morgan*, 1993, *Quick and Denlinger*, 1993). The sheeted sill model should produce strong radial anisotropy with $V_{SH} > V_{SV}$ in the lower crust but no azimuthal anisotropy, similar to what we infer. However, distinguishing between these two end-member models of crustal accretion using surface-wave dispersion alone is challenging given the relatively limited depth sensitivity within the crust.

Azimuthal anisotropy, G , at YoungORCA shows distinct differences compared to that estimated at NoMelt (Figure 3.6b,c). While both locations show FSD-parallel fabric in the shallow lithosphere, G is weaker at YoungORCA by a factor of ~ 1.4 with fast azimuths parallel to the FSD to only ~ 35 km depth, in contrast to NoMelt, where FSD-parallel fabric extends to 80–90 km depth. In the asthenosphere, fabric at the two locations is significantly rotated both from APM and from one another. YoungORCA is rotated clockwise by 15–30° relative to APM, while NoMelt is rotate counterclockwise by $\sim 20^\circ$. Asthenospheric anisotropy differs from one another by 30–35° in the layered models, while the smooth models differ by up to $\sim 60^\circ$ below ~ 250 km depth. A similar misalignment of asthenospheric anisotropy relative to APM was observed in the northwest Pacific at two locations separated by ~ 1000 km at 130–140 Ma seafloor (*Takeo et al.*, 2018). G azimuths in the smooth models are both closest to one another as well as closest to the APM direction at depths of 120–150 km, approximately coinciding with the LVZ.

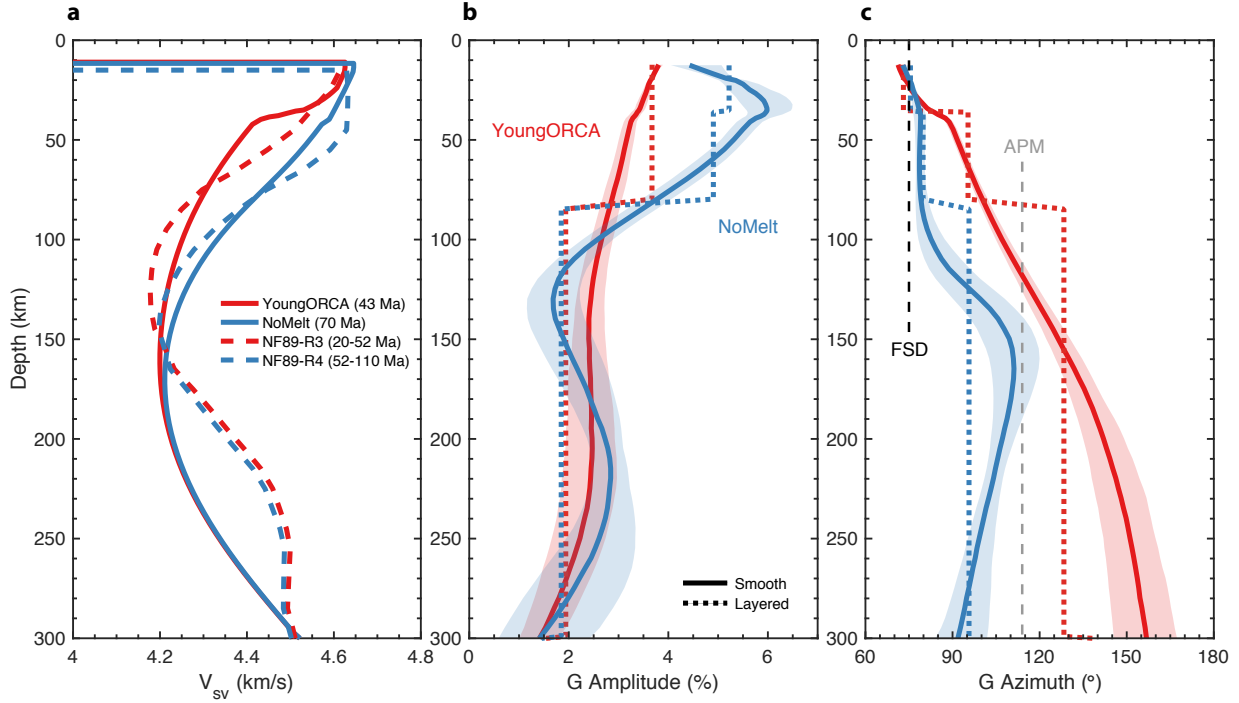


Figure 3.6: Comparison of shear velocity (a) and azimuthal anisotropy (b,c) at ~ 43 Ma and ~ 70 Ma seafloor. Younger seafloor models are shown in red and older in blue. NoMelt anisotropy and $1-\sigma$ uncertainties are from *Russell et al. (2019a)*. The FSD and APM directions at NoMelt are similar to those at YoungORCA. NF89 – (*Nishimura and Forsyth, 1989*)

3.4.2 Anelastic predictions for half-space cooling: possible evidence for mantle reheating

We evaluate whether a simple half-space cooling (HSC) model can explain the differences in shear velocities observed at YoungORCA and NoMelt separated in age by ~ 30 Myr (Figure 3.7). Temperature profiles are estimated for 43 Ma and 70 Ma seafloor assuming a mantle potential temperature of $T_P = 1350^\circ\text{C}$ and an adiabatic temperature gradient of 0.348°/km . Unrelaxed (anharmonic) shear velocities (V_S) are calculated using Perple_X (*Connolly, 2009*) and solution models of *Stixrude and Lithgow-Bertelloni (2011)* for a depleted mid-ocean ridge basalt (MORB) mantle composition (*Hacker, 2008*). We estimate temperature and pressure dependent anelastic effects following the extended Burgers model of *Jackson and Faul (2010)* using the Very Broadband Rheology calculator (VBRc) (*Havlin*

et al., 2020, Holtzman *et al.*, 2019) and assume a grain size of 1 cm and a frequency of 0.01 Hz. In this model, the attenuation spectrum is composed of two anelastic components, which we investigate separately: (1) the ubiquitously observed high-temperature background (HTB) characterized by an Arrhenius dependence on temperature (Faul and Jackson, 2005, McCarthy and Takei, 2011, McCarthy *et al.*, 2011, Sundberg and Cooper, 2010) and (2) an absorption peak that occurs at higher temperatures but is generally less well resolved in laboratory experiments and with an origin that is still debated (e.g. Faul and Jackson, 2015, 2005, Jackson and Faul, 2010, Takei, 2017, Yamauchi and Takei, 2016). We evaluate the effects of the HTB term alone as well as with the contribution of the absorption peak (HTB + peak).

In order to directly compare seismic observations at YoungORCA and NoMelt with predictions of Jackson and Faul (2010), we convert V_{SV} to V_S by assuming a ξ structure that is consistent with the lithospheric observations and follows the general character of Nishimura and Forsyth (1989). At each location, we approximate ξ in the upper mantle by extending the constant lithospheric values from Figure 3.4c to 150 km depth and assume a linear gradient from 150–300 km depth that transitions to isotropic structure ($\xi = 1$) below 300 km.

We define a conductive cooling signature as the ratio of shear velocities at older seafloor ages to those at younger ages (Figure 3.7c). For a given pair of shear velocity profiles, this metric effectively cancels the age-independent commonalities to first order that may otherwise be poorly constrained, such as composition, grain size, and absolute mantle potential temperature, and instead, amplifies the age-dependent differences. The cooling signatures of NoMelt/YoungORCA and NF89-R4/R3 are comparable to one another and peak at 1.36–1.4 from 40–90 km depth indicating a large (\sim 3.6–4%) velocity difference associated with age-thickening lithosphere. The change in unrelaxed shear velocities due to the \sim 30 Myr age difference accounts for only \sim 1.5% of this velocity change. Inclusion of the HTB anelastic mechanism further increases the velocity difference to \sim 1.8% at \sim 70 km depth, but still significantly underpredicts the observations. The prediction that includes both the HTB

and absorption peak term (HTB + peak) produces a cooling signature that most resembles the observations, with a peak of ~ 1.03 at 50–60 km depth, but still underpredicts the observations by $\sim 1\%$.

Our observations indicate that while the anelastic absorption peak term alone is unable to completely explain the observations, it is an important mechanism to consider when evaluating predictions of shear velocity. The anelastic peak as defined by *Jackson and Faul* (2010) is attributed to elastically accommodated grain boundary sliding (EAGBS) that may be sensitive to the presence of melt (*Faul and Jackson*, 2005, *Faul et al.*, 2004, *Sundberg and Cooper*, 2010) or water content (*ichiro Karato*, 2012, *Karato and Park*, 2019, *Olugboji et al.*, 2013) but has also been observed in experiments on melt-free borneol and attributed to subsolidus premelting (*Yamauchi and Takei*, 2016). Our result is consistent with a previous study at NoMelt that required both the HTB and EAGBS peak in order to jointly fit shear velocity (V_S) and seismic attenuation (Q_μ^{-1}) (*Ma et al.*, 2020).

The anelastic predictions for the conductive cooling signature underestimate the observations by $\sim 1\%$ from 40–100 km depth, suggesting that an additional factor is required to explain the velocity differences at YoungORCA and NoMelt. Perhaps the simplest way to decrease predicted velocities at YoungORCA to match the observations is by allowing the mantle potential temperature to be hotter there. Elevated mantle temperatures are conceivable considering the proximity to the South Pacific Superswell (*Adam and Bonneville*, 2005) and Marquesas hotspot ~ 750 km away (Figure 3.1). An increase in T_P of 100°C at YoungORCA relative to NoMelt is enough to explain the observations from 40–100 km depth, though this also produces slower velocities below 150 km, which is not seen in the models (magenta dashed line in Figure 3.7c). Rather, we suggest that only the sublithospheric mantle in the upper ~ 40 –100 km below YoungORCA has been reheated, possibly indicating small-scale convection.

A temperature increase may also lead to partial melting from 40–100 km depth beneath YoungORCA, further contributing to the deviation from HSC predictions. Such evidence for

melt in the vicinity is suggested by enhanced reflectivity from \sim 50–70 km depth (Schmerr, 2012). Introduction of only 0.5% melt by volume from 40–100 km to the nominal case ($T_P = 1350^\circ\text{C}$) is also able to explain the observations (orange dashed line in Figure 3.7c). Given that temperature and melt effects on velocity trade off, this can be thought of as an upper limit of melt allowed at YoungORCA. However, temperatures at depths <80 km are far colder than melting temperatures even for a damp solidus with 200 ppm of H_2O and a hotter mantle T_P of 1450°C (Figure 3.7a), meaning that melt is unlikely to remain stable at these depths. Although we cannot necessarily rule out an additional contribution from melt at YoungORCA, a modest increase in temperature alone is able to explain the observations.

While other factors such as grain size and composition also contribute to shear velocity estimates, it is unlikely that their lateral variations are large enough to account for the misfit in the predicted cooling signature in Figure 3.7c. These quantities would be required to vary considerably over a length scale of only \sim 2100 km. Instead, we argue that the simplest way to reduce velocities at YoungORCA relative to HSC predictions is via a modest temperature increase, which may be accompanied by as much as \sim 0.5% melt.

3.4.3 Implications for mid-ocean ridge spreading fabric

The lithospheric anisotropy that we observe at YoungORCA is consistent with olivine LPO frozen into the lithosphere near the MOR during seafloor spreading. Radial anisotropy with $V_{SH} > V_{SV}$ and azimuthal anisotropy G oriented parallel to the FSD (and E oriented parallel to FSD+ 45°) indicate horizontal alignment of orthorhombic olivine a-axes via corner flow at the fast-spreading MOR (Blackman and Kendall, 2002a, Blackman *et al.*, 2017). The depth extent of this anisotropic layer coincides with fast shear velocities (>4.6 km/s) indicative of lithospheric mantle. However, that the FSD-parallel fabric extends to only \sim 35 km depth is inconsistent with the lithosphere dehydration hypothesis that was previously invoked at NoMelt to explain the FSD-parallel anisotropy down to 80–90 km depth (Russell *et al.*, 2019a). This hypothesis posits that spreading-parallel fabric is locked in near the MOR

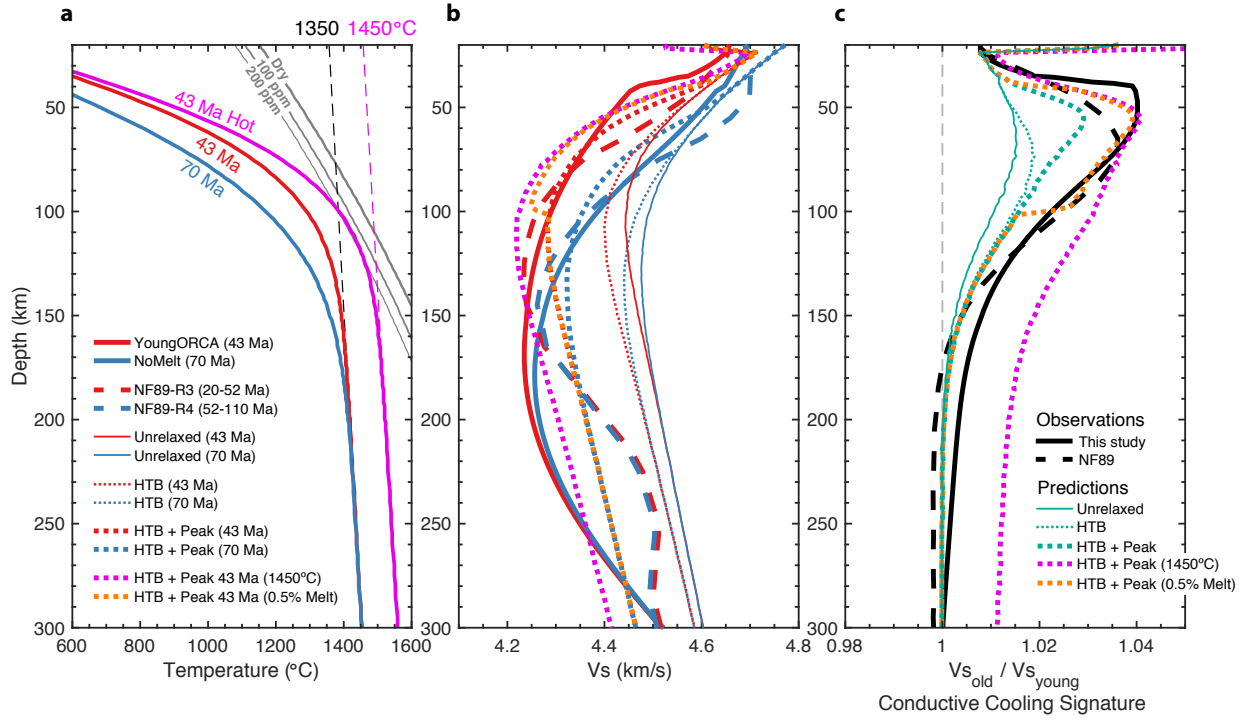


Figure 3.7: Conductive cooling signature of shear velocities in the Pacific compared to anelastic laboratory predictions for half-space cooling. (a) Temperature profiles at 43 Ma (red) and 70 Ma (blue) for a half-space cooling (HSC) model with mantle potential temperature $T_P = 1350^{\circ}\text{C}$. The magenta geotherm shows 43 Ma HSC for $T_P = 1450^{\circ}\text{C}$. Grey lines show solidi calculated via Katz *et al.* (2003) for the dry case as well as 100 ppm and 200 ppm H_2O added. (b) Observed shear velocity models compared with anelastic predictions. Unrelaxed shear velocities are calculated using Perple_X (Connolly, 2009) for a depleted mid-ocean ridge basalt mantle composition (Hacker, 2008) and temperature profiles from a). Additional anelastic components – high-temperature background (HTB; thin dotted) and the absorption peak (HTB + Peak; thick dotted) – are estimated using the parameterization of Jackson and Faul (2010) assuming a grain size of 1 cm and a frequency of 0.01 Hz. Profiles for a hot geotherm ($T_P = 1450^{\circ}\text{C}$; magenta) and 0.5% melt by volume (orange) are also shown. (c) Conductive cooling signatures are shown as the ratio of old to young shear velocity profiles. Observed cooling signatures (black) are 0.5–1% stronger than anelastic predictions (teal) at ~40–100 km depth. A temperature increase (magenta) and/or small amount of melt (orange) can explain the observations from ~40–100 km depth.

during dehydration of the lithosphere (rather than being progressively accumulated during plate cooling) and predicts an age-independent thickness for the FSD-parallel anisotropic layer (Gaherty *et al.*, 1999). Instead, the comparison of YoungORCA and NoMelt suggests a thickening of this layer with age.

It is possible that the thin FSD-parallel fabric at YoungORCA is the result of reheating or

thermochemical erosion of the originally thicker, unperturbed dehydrated lithosphere due to elevated mantle potential temperatures or small-scale convection and perhaps the presence of melt at the base of the lithosphere. Elevated mantle temperatures could effectively weaken the pristine LPO fabric emplaced at the ridge, allowing it to be overprinted below \sim 40 km depth. This would be consistent with the elevated mantle temperatures invoked to reconcile shear velocity predictions from 40–100 km depth in Section 3.4.2.

Another possibility is that YoungORCA lithosphere represents anomalous fabric associated with a complicated spreading history, as evidenced by the complex abyssal hill faulting orientations that vary by \sim 25° from north to south across the array as well as the abrupt changes in spreading rate inferred from the seafloor age contours. The estimated half spreading rates at YoungORCA are ultra fast (12–13 cm/yr), while rates are only 4–5 cm/yr at NoMelt (Figure C.4) (*Müller et al.*, 2008). Spreading rates increase by \sim 1 cm/yr from south to north within the YoungORCA footprint, and the region is flanked on the east and west by more typical spreading rates of \sim 4 cm/yr. Taken altogether, these observations indicate that YoungORCA crust and lithosphere likely formed during a period of anomalous spreading. Such a complex spreading history may have produced short-wavelength variations in olivine LPO orientation (on the order of seismic wavelengths) that could explain the relatively weak lithospheric anisotropy at YoungORCA compared to NoMelt. However, neither the clear, simple first-overtone Rayleigh 2θ anisotropy nor the distinct Love 4θ anisotropy (Figure 3.3) show evidence of strong intra-array lateral variations in LPO, at least in the upper 35 km where their sensitivities are strongest.

3.4.4 Sublithospheric mantle flow

Asthenospheric fabric at YoungORCA is rotated clockwise significantly from present-day APM below at least \sim 150 km depth, suggesting that flow within and just below the LVZ is largely decoupled from shear deformation imparted by the motion of the overlying plate. This is in contrast to the broader plate-scale observations in global models of largely

APM-parallel anisotropy beneath the base of the Pacific plate (e.g. *Beghein et al.*, 2014, *Burgos et al.*, 2014). The 30–60° difference in G orientation below this depth as compared to NoMelt represents lateral heterogeneity of asthenospheric flow on a length scale of ∼2100 km, compatible with previous observations in the northwest Pacific that found similar heterogeneity over a distance of ∼1000 km (*Takeo et al.*, 2018). Similar to *Takeo et al.* (2018), we note that the orientation of asthenospheric anisotropy averaged between YoungORCA and NoMelt yields approximately APM, perhaps explaining in part why plate-scale observations that average over large swaths of the plate tend to observe largely APM-parallel anisotropy beneath the plate.

The smooth transition from FSD-parallel anisotropy at ∼35 km depth to approximately APM-parallel by 120 km indicates a broad zone of accommodation from plate shearing. That there is no clear evidence at YoungORCA for a layer of pure-APM anisotropy is consistent with the presence of APM-oblique pressure or density driven flow beneath the plate similar to that previously inferred at NoMelt (*Lin et al.*, 2016).

3.5 Conclusion

We invert high-resolution Rayleigh- (5–150 s) and Love-wave (5–7 s) phase velocities for 1-D shear velocity, radial anisotropy, and azimuthal anisotropy beneath the ∼43 Ma YoungORCA array in the south Pacific, providing new insights into oceanic lithosphere–asthenosphere structure and evolution. Shear velocities >4.6 km/s and azimuthal anisotropy parallel to the FSD define a ∼35–40 km thin lithosphere. Observations of radial anisotropy with $V_{SH} > V_{SV}$ and azimuthal anisotropy G parallel to the FSD to ∼35 km depth (and E parallel to the FSD+45°) are consistent with horizontally aligned orthorhombic olivine formed via corner flow at the fast-spreading MOR.

The majority of the difference in shear velocities between YoungORCA and the ∼30 Myr older NoMelt array can be explained by HSC if both the HTB and EAGBS anelastic mechanisms are included. The remaining unaccounted for ∼1% V_S difference at 40–100 km depth is

consistent with elevated mantle temperatures that might be accompanied by a small amount of melt (<0.5%) at YoungORCA, perhaps owing to its proximity to the Marquesas hotspot \sim 750 km to the southwest. Relatively weak and thin lithospheric anisotropy compared to NoMelt is also consistent with a thermal perturbation that may have disrupted the original pristine spreading-related olivine LPO below 40 km or could be related to anomalous seafloor spreading \sim 43 Ma. Asthenospheric anisotropy is rotated \sim 30° clockwise from APM below \sim 150 km depth, consistent with the presence of pressure or density-driven small-scale convection. Taken together, our results suggest evidence for elevated mantle temperatures and potential reheating of the lithosphere associated with small-scale convective processes beneath the YoungORCA array.

Acknowledgements

The authors thank the captain, crew, and engineers of the R/V Kilo Moana who made the experiment possible as well as the Scripps Institution of Oceanography (SIO) engineers aboard the vessel who provided the OBS instrumentation and whose expertise contributed greatly to the success of the YoungORCA deployment and recovery. We are especially indebted to Sean McPeak at the SIO for his colossal data-recovery efforts that provided data from 12 of the 30 OBS, without which this study would not have been possible. This work was supported by the National Science Foundation (NSF) Grant Number OCE-1658214.

Lithosphere structure and seismic anisotropy 4 | offshore eastern North America: Implications for early seafloor spreading dynamics

CO-AUTHORS: JAMES B. GAHERTY

Abstract

The breakup of supercontinent Pangea occurred \sim 200 Ma forming the Eastern North American Margin (ENAM). Yet, precise timing of the completion of breakup and onset of seafloor spreading remains poorly constrained. Using broadband ocean-bottom seismometers (OBS) from the ENAM Community Seismic Experiment, we measure ambient-noise Rayleigh wave phase velocities for the offshore region from 12–32 s period and invert for 2-D phase velocity maps and azimuthal anisotropy (17–32 s) sensitive to the lithosphere. Incorporating previous detailed constraints on crustal structure, we construct a shear velocity model for the crust and upper \sim 60 km of the mantle beneath the ENAM-CSE. A low-velocity lid (4.4–4.55 km/s) is revealed in the upper 15 km of the mantle that extends \sim 200 km from the margin and terminates at the Blake Spur Magnetic Anomaly (BSMA). This feature is consistent with either thinned continental lithosphere overlying nominal oceanic lithosphere as previously proposed and/or evidence for trapped melts associated with ultra-slow spreading. East of the BSMA, velocities are fast (>4.6 km/s) and characteristic of typical oceanic mantle lithosphere. If the lower velocities west of BSMA are attributed to continental lithosphere, they suggest that the BSMA marks the completion of continental breakup and onset of normal seafloor spreading \sim 170 Ma. If instead trapped melts are responsible for the slow velocities, this sheds a new light on melt extraction processes in ultra-slow spreading environments. In addition, we report margin-parallel azimuthal anisotropy in the lithosphere that correlates with absolute plate mo-

tion (APM) at the time of spreading. We hypothesize that lithosphere formed at slow-spreading ridges may record APM-modified olivine fabric rather than typical fossil-spreading fabric.

4.1 Introduction

The Eastern North American Margin (ENAM) is a passive volcanic margin that formed during the breakup of supercontinent Pangea \sim 200 Ma (*Withjack et al.*, 1998). The breakup initiated at approximately 235 Ma with crustal extension that is recorded in a sequence of rift basins along the length of the margin (*Withjack et al.*, 2012), and it occurred alongside an outburst of volcanism known as the Central Atlantic Magmatic Province (CAMP) that is dated to 200 ± 4 Ma (*Marzoli et al.*, 2011) and characterized by a large volume ($\sim 1 \times 10^6$ km 3) of flood basalts (*McHone*, 2003) emplaced during a short period (<1 Myr) (*Olsen et al.*, 2003). Though the precise temporal and tectonic relationship between CAMP magmatism and rifting is debated (*McHone*, 2000), it is thought that normal seafloor spreading and opening of the Atlantic basin began sometime between \sim 200-170 Ma.

Insights into the transition from continental rifting to seafloor spreading are contained in the crust and mantle signature offshore ENAM. The offshore region is characterized by two positive polarity magnetic anomalies separated by the Inner Magnetic Quite Zone (IMQZ) that lacks well defined magnetic lineations (Figure 4.1). The higher amplitude East Coast Magnetic Anomaly (ECMA) occurs just seaward of the continental shelf and has generally been interpreted as marking the transition to oceanic crust (e.g. *Kelemen and Holbrook*, 1995, *Klitgord et al.*, 1988, *Lynner and Porritt*, 2017). ECMA emplacement ages range from 175–200 Ma (*Benson*, 2003, *Klitgord and Schouten*, 1986, *Labails et al.*, 2010), though recent revised estimates of \sim 195 Ma have been proposed based on the African conjugate to the ECMA as well as salt deposits off Nova Scotia and Morocco (*Labails et al.*, 2010, *Sahabi et al.*, 2004). Approximately 200 km seaward of the ECMA is the lower amplitude Blake Spur Magnetic Anomaly (BSMA). The age of the BSMA is estimated at \sim 170 Ma, but its precise origin and significance are still debated (*Greene et al.*, 2017).

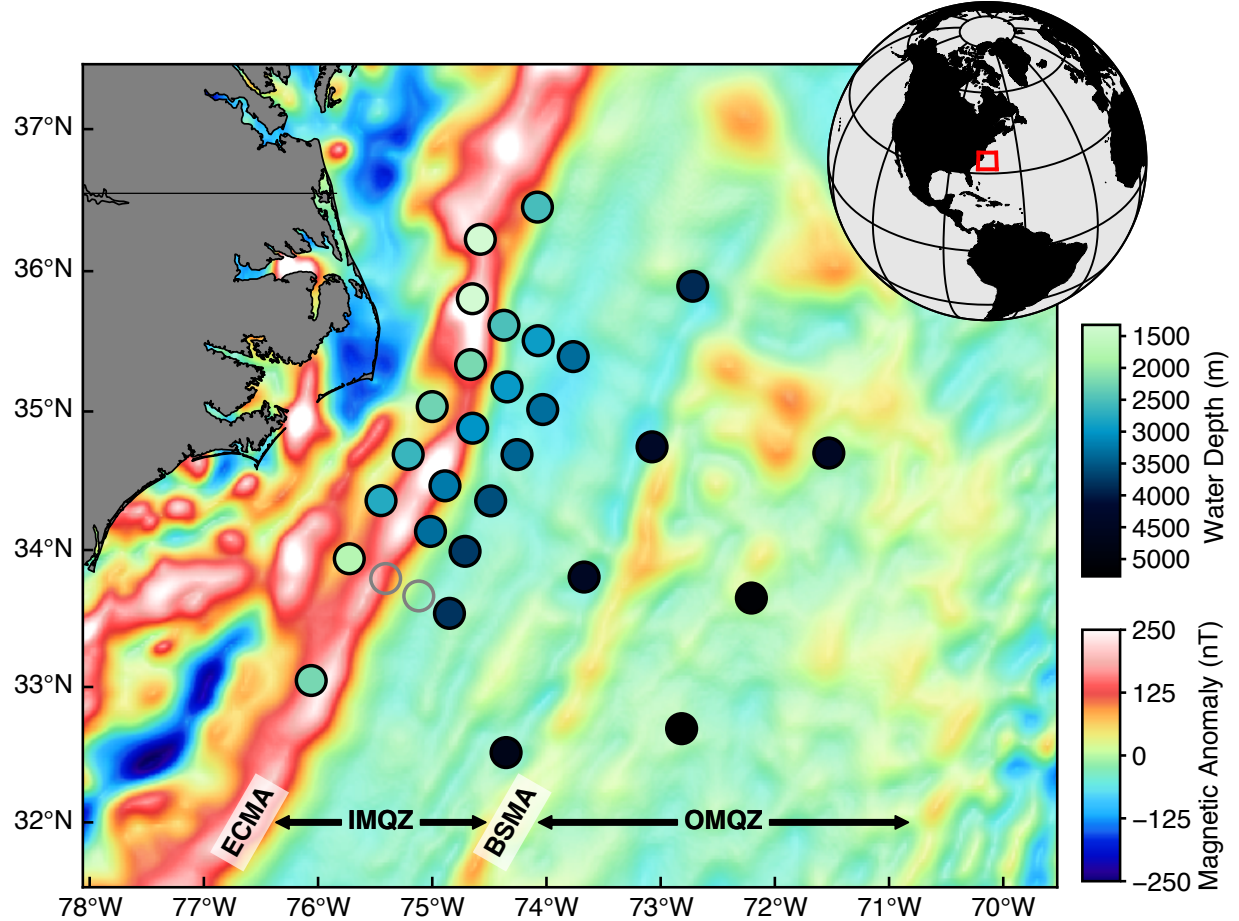


Figure 4.1: Magnetic anomalies of the ENAM-CSE region with broadband OBS shown as circles and colored by water depth. Open circles denote stations with poor data quality. East Coast Magnetic Anomaly (ECMA); Blake Spur Magnetic Anomaly (BSMA); Inner Magnetic Quiet Zone (IMQZ); Outer Magnetic Quiet Zone (OMQZ)

Recent work offshore ENAM has challenged the notion that the ECMA marks the completion of continental breakup and onset of seafloor spreading, and instead, it has been proposed that the BSMA marks this important transition (*Bécel et al.*, 2020, *Shuck et al.*, 2019). Using data collected during The ENAM Community Seismic Experiment (ENAM-CSE) that extends farther offshore than ever before, detailed crustal imaging shows thin proto-oceanic crust with higher lower crustal velocities and rougher basement topography west of the BSMA compared to the east, consistent with deeper melting and ultra-slow spreading rates (~ 0.65 cm/yr half-spreading) (*Bécel et al.*, 2020, *Shuck et al.*, 2019). This interpretation predicts a 15–20 km thick continental mantle lithosphere underlying the oceanic crust west

of the BSMA and normal oceanic lithosphere east of the BSMA; however, previous shear-velocity imaging in the region shows little evidence for a distinct change in mantle velocities across the BSMA (*Lynner and Porritt*, 2017).

Additional insights into dynamics associated with continental rifting and seafloor spreading may be preserved in the olivine lattice-preferred orientation (LPO) in the lithospheric mantle, which acts as a record of past mantle flow. The fast a-axis of olivine crystals tend to align parallel to the direction of shearing in the mantle, forming an LPO (*Karato et al.*, 2008, *Zhang and Karato*, 1995). In models of mid-ocean ridges (MOR), corner flow near the ridge aligns olivine LPO parallel to the spreading direction and is frozen-in as the lithosphere cools (e.g. *Blackman and Kendall*, 2002a, *Blackman et al.*, 1996, *Kaminski and Ribe*, 2001, 2002, *Ribe*, 1989). This frozen-in LPO leads to the azimuthal anisotropy of seismic waves routinely observed in the Pacific lithosphere, with a fast azimuth parallel to the fossil-spreading direction (FSD) (e.g. *Forsyth*, 1975, *Hess*, 1964, *Morris et al.*, 1969, *Raitt et al.*, 1969, *Russell et al.*, 2019a). Seismic anisotropy of the deeper asthenosphere reflects present-day mantle deformation and at large length scales broadly aligns sub-parallel to absolute plate motion (APM) beneath the ocean basins (*Beghein et al.*, 2014, *Nishimura and Forsyth*, 1989, *Schaeffer et al.*, 2016), with deviations associated with smaller-scale convective processes observed at smaller length scales (e.g. *Becker et al.*, 2014, *Lin et al.*, 2016).

Previous seismic anisotropy observations at the ENAM-CSE from shear-wave splitting show margin-parallel fast axes, significantly rotated from current-day APM, that is interpreted as present-day asthenospheric flow along the margin (*Lynner and Bodmer*, 2017). In addition, preliminary comparison of sub-Moho V_P along crossing margin-parallel and margin-perpendicular refraction lines in the region suggests a margin-parallel fast direction in the lithosphere that is approximately perpendicular to the FSD (*Shuck and Van Averdonk*, 2016). However, these observations are limited to two locations in the ENAM-CSE footprint where the refraction lines intersect.

In this study, we use ambient-noise Rayleigh waves to construct a shear velocity model of

the offshore ENAM-CSE region that incorporates recent crustal constraints from refraction tomography (*Shuck et al.*, 2019). Our model reveals relatively low-velocity mantle lithosphere extending \sim 200 km seaward that we interpret in the context of the detailed crustal architecture, providing further evidence for a prolonged breakup prior to seafloor spreading. We also report margin-parallel Rayleigh-wave anisotropy in the lithosphere, perpendicular to typical expectations for seafloor spreading, and offer an alternative perspective on lithosphere fabric formed at slow-spreading ridges.

4.2 Data and Methods

The Eastern North American Margin Community Seismic Experiment (ENAM-CSE) consisted of onshore-offshore active source reflection and refraction as well as a one year broadband ocean-bottom seismometer (OBS) deployment (*Lynner et al.*, 2020). We use continuous seismic data from 28 broadband OBS deployed during the ENAM-CSE from April 2014–May 2015. Water depth in the study region ranges from \sim 1300 m near the shelf to \sim 5200 m on the eastern-most edge of the array. Instrument response is deconvolved to displacement, and seismograms are downsampled to 1 Hz prior to processing.

4.2.1 Daily OBS tilt noise removal

We observe exceptionally strong horizontal noise on the vertical channels (i.e., tilt noise) at ENAM at periods >10 s (Figure 4.2a), presumably due to the strong Gulf Stream current that flows northeastward along the coast. We remove this coherent horizontal energy from the vertical channels for each 24 hour segment of the continuous data using the Automated Tilt and Compliance Removal (ATaCR) software (*Janiszewski et al.*, 2019), which implements the techniques developed by *Crawford and Webb* (2000). We do not remove pressure coherence from the vertical channel, as this has been shown to degrade the desired fundamental-mode primary microseism (*Bowden et al.*, 2016).

It is not common practice to remove daily tilt noise prior to performing ambient-noise

tomography, but we find that tilt removal improves the overall signal-to-noise ratio (SNR) of vertical component empirical Green's functions (EGFs) (See Section 4.2.2) by a factor of ~ 2 on average, and by an order of magnitude for some station pairs (Figure 4.2b). The largest SNR improvements occur for station pairs with shallower average water depth (Figure 4.2d). Similar ambient noise improvements were reported after tilt and compliance corrections at the shallow water stations at the Cascadia Initiative (*Tian and Ritzwoller, 2017*).

4.2.2 Ambient noise processing

Ambient noise EGFs are constructed from tilt-removed seismograms following the general procedure of *Bensen et al.* (2007) (Figure 4.3); however, we do not apply time-domain normalization or spectral whitening. Daily displacement seismograms are split into 15 3-hour segments with 50% overlap. Normalized coherence cross-spectra are calculated between the vertical channels for stations i and j and time window k :

$$\rho_{ijk}(\omega) = \frac{U_{ik}(\omega)U_{jk}^*(\omega)}{\sqrt{U_{ik}(\omega)U_{ik}^*(\omega)U_{jk}(\omega)U_{jk}^*(\omega)}} \quad (4.1)$$

where $U(\omega)$ is the vertical component displacement spectra at frequency ω and $U^*(\omega)$ its complex conjugate. These coherence spectra are summed over the entire duration of the deployment for each station pair, resulting in a final stacked spectrum, $\rho_{ij}(\omega) = \sum_k \rho_{ijk}(\omega)$. By utilizing the coherence spectrum rather than the unnormalized cross-correlation spectrum and relatively short time windows, any windows containing anomalous signals such as large earthquakes have little influence on the final stacked spectrum, precluding the need for time-domain normalization or other alteration of the original high-quality waveforms. We find that a typical one-bit normalization and spectral whitening procedure (e.g. *Bensen et al., 2007*) degrades signal-to-noise ratio in the 15–40 s period band by more than an order of magnitude.

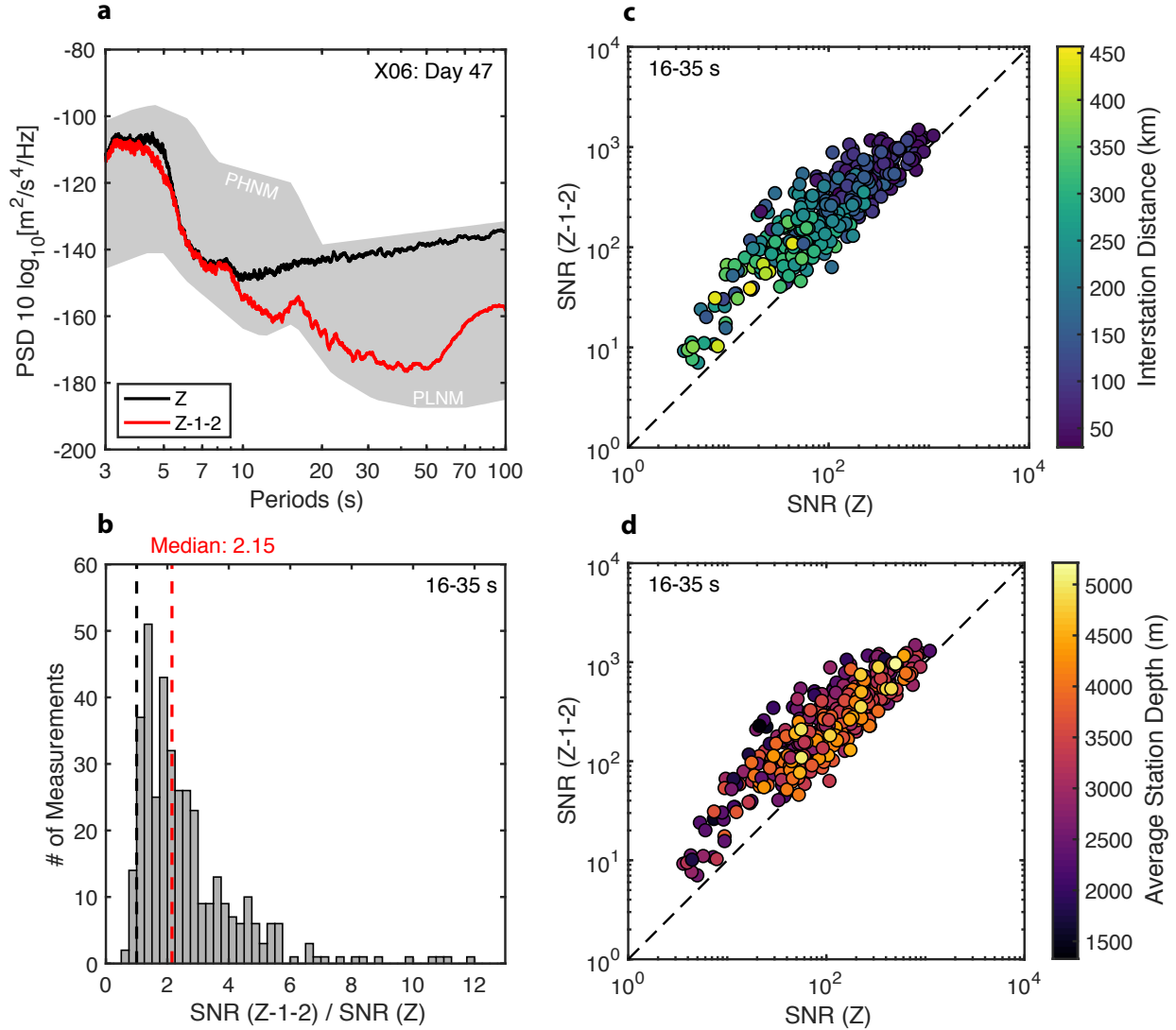


Figure 4.2: Ambient noise empirical Green's function (EGF) signal-to-noise ratio (SNR) improvement from daily tilt corrections. (a) Example 24 hour smoothed spectra for station X06 on day 47 of the deployment. The raw vertical channel (Z) and tilt-corrected vertical (Z-1-2) are shown. The grey region is bounded below by the Peterson low noise model (PLNM) and above by the high noise model (PHNM) (Peterson, 1993). The primary microseism peak at ~ 16 s period is visible only after the tilt correction is applied. (b) Histogram of tilt-corrected SNR values relative to raw values for all EGFs filtered from 16–35 s period. The red dashed line shows the median value of 2.15 and the black dashed line marks a value of 1 (i.e., no improvement). (c) Comparison of SNR values for each EGF, where the one-to-one line is dashed in black and points are colored by interstation distance. (d) Same as c) but colored by average station water depth. $\text{SNR} = \text{RMS}(\text{signal})^2 / \text{RMS}(\text{noise})^2$, where *signal* is defined as any arrival with group velocity greater than 1.5 km/s.

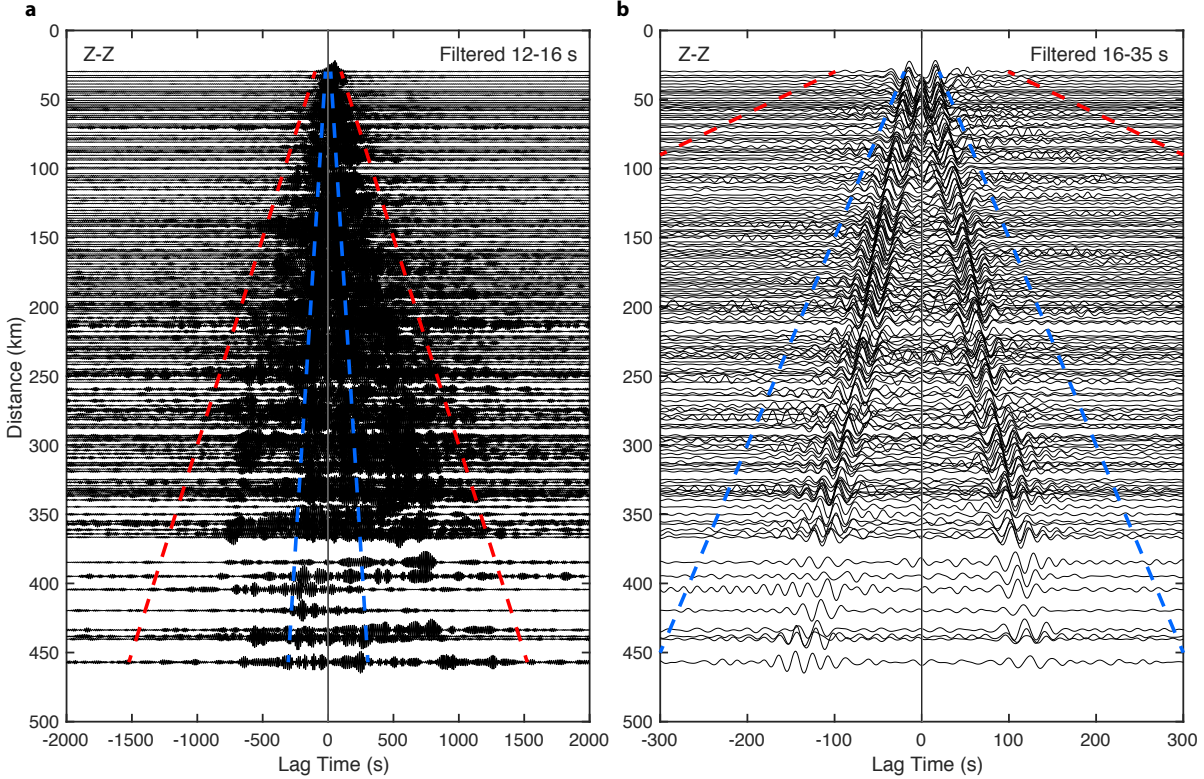


Figure 4.3: Vertical component ambient noise empirical Green's functions (EGFs) showing Rayleigh wave energy filtered from (a) 12–16 s and (b) 16–35 s period. Dashed blue and red lines indicate group velocities of 1.5 km/s and 0.3 km/s, respectively.

4.2.3 Interstation phase velocities

Interstation phase velocities are estimated from the stacked coherence spectra using Aki's spectral formulation, whereby the real part of the cross-spectra takes the form (Aki, 1957):

$$\bar{\rho}(\omega, r) = J_0 \left(\frac{\omega r}{c(\omega)} \right) \quad (4.2)$$

where r is station separation, c is phase velocity, and J_0 is the Bessel function. Phase velocity dispersion is estimated at each zero crossing following Ekström *et al.* (2009) and then interpolated to a uniform frequency axis. In theory, this process identifies an infinite number of possible dispersion curves, and we select the one with 25–30 s velocities that are closest to a nominal mantle velocity of 3.9 km/s (Figure 4.4c). We then discard dispersion curves that are not smooth or do not decrease with increasing frequency. In order to minimize noise

in the cross-spectrum prior to the zero-crossing analysis, we apply a cosine-taper window in the time domain defined by a minimum group velocity threshold of 0.3 km/s (that is, energy corresponding to group velocities < 0.3 km/s is zeroed). Additional smoothing is applied to \bar{p} for periods > 17 s to eliminate the occurrence of spurious zero crossings, particularly for large r . Dispersion measurements for r less than one wavelength are discarded.

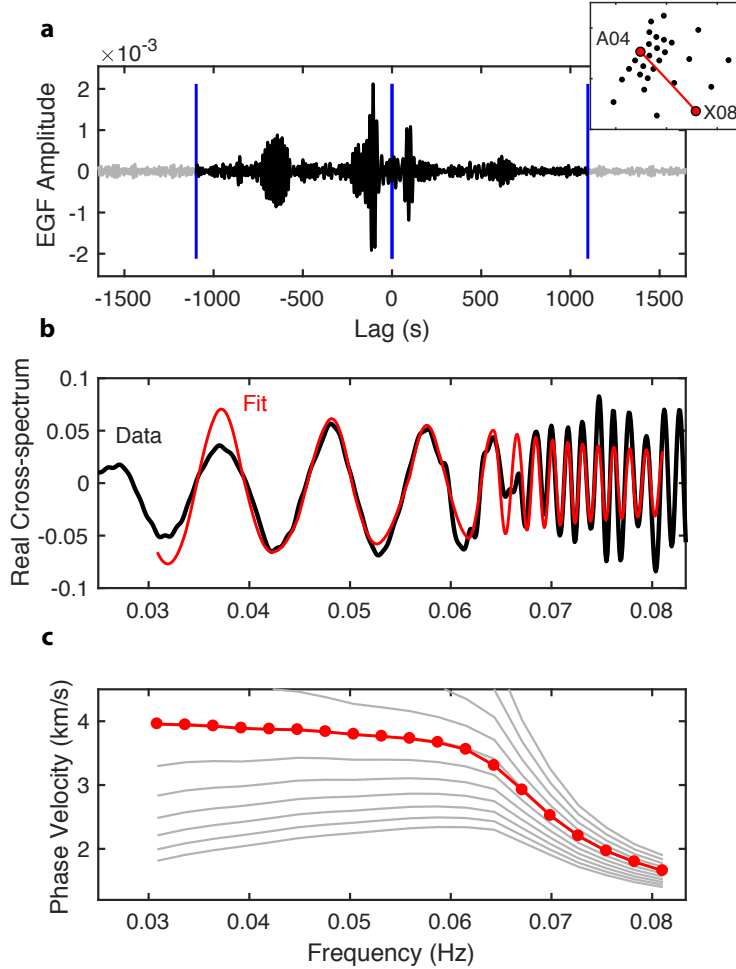


Figure 4.4: Demonstration of the cross-spectral zero-crossing analysis for phase velocity extraction from station pair A04–X08. (a) EGF cross-correlation in the time domain with station A04 and X08 indicated in red in the inset map separated by 330 km distance. The vertical blue lines mark the 0.3 km/s group velocity window applied prior to dispersion analysis. (b) Real part of the EGF cross-spectrum formed by taking the Fourier transform of a). The data are shown in black and the fit determined from the zero-crossing analysis in red. (c) Interstation dispersion curve extracted from the zero crossings of b). Grey lines show possible dispersion curves. The red points mark the final interpolated dispersion measurements selected based on a nominal mantle velocity of 3.9 km/s.

4.2.4 Phase velocity inversion

Interstation Rayleigh-wave phase velocities are inverted for 2-D phase velocity maps from 12–32 s period and azimuthal anisotropy from 17–32 s for the offshore ENAM region. We solve first for phase slowness maps $s(\mathbf{x})$ on a $0.1^\circ \times 0.1^\circ$ grid and take the reciprocal to obtain maps of phase velocity $c(\mathbf{x})$. Anisotropy terms are solved on a coarser $0.5^\circ \times 0.5^\circ$ grid. A perturbation in phase delay time $\delta\tau_{ij}$ between stations i and j due to a perturbation in phase slowness $\delta s(\mathbf{x})$ is given by

$$\delta\tau_{ij} = \iint_{\Omega} K_{ij}(\mathbf{x}, \omega) \delta s(\mathbf{x}) d\mathbf{x} - \int_i^j [A_c(\mathbf{x}, \omega) \cos(2\theta_{ij}) + A_s(\mathbf{x}, \omega) \sin(2\theta_{ij})] d\mathbf{r} \quad (4.3)$$

where θ_{ij} is propagation azimuth and r_{ij} is the great-circle distance between the stations. Coefficients A_c and A_s describe the frequency-dependent azimuthal anisotropy within the array footprint with magnitude $A = \sqrt{A_c^2 + A_s^2}$ and fast azimuth $\psi = 0.5 \tan^{-1}(A_s/A_c)$. The 2-D finite-frequency sensitivity kernel $K_{ij} = \partial\tau/\partial s$ is given by (*Lin and Ritzwoller, 2010*)

$$K_{ij}(\mathbf{x}, \omega) = \frac{2c_0}{\omega} \sqrt{\frac{r_{ij}}{8\pi |\mathbf{x} - \mathbf{x}_j| |\mathbf{x} - \mathbf{x}_i|}} \cos \left(\omega [\tau_i(\mathbf{x}_j) - \tau_i(\mathbf{x}) - \tau_j^\dagger(\mathbf{x})] + \frac{\pi}{2} \right) \quad (4.4)$$

where $\tau_i(\mathbf{x})$ is the phase delay surface due to an impulse at station i , and $\tau_j^\dagger(\mathbf{x})$ is the adjoint phase delay field due an impulse at station j . Reference velocity c_0 is taken as the average of all interstation dispersion measurements at frequency ω . To ensure that the kernel density matches the ray-theoretic value, the kernel is normalized such that

$$r_{ij} \iint_{\Omega} K_{ij}(\mathbf{x}, \omega) d\mathbf{x} = \frac{r_{ij}}{c_0} = \tau_0 \quad (4.5)$$

This formulation of the kernel, termed the “empirical” kernel by *Lin and Ritzwoller (2010)*, accounts for both finite-frequency effects and off-great-circle propagation caused by

lateral velocity gradients along the ray path. In theory, the quantities $\tau_i(\mathbf{x})$ and $\tau_j^\dagger(\mathbf{x})$ can be determined empirically for each station by fitting a smooth surface to the interstation phase delays measured at all other stations across the array. In practice however, this is challenging due to uneven data distribution and presence of noise in the phase delay measurements.

We take a “semi-empirical” approach and approximate $\tau(\mathbf{x})$ numerically via spectral-element method (SEM) simulations by propagating S-waves through a realistic phase velocity map at each frequency of interest for an impulse centered at each station. The input synthetic phase velocity maps are constructed from the 2-D V_P model along Line 1 from *Shuck et al.* (2019) after converting to V_S assuming $V_P/V_S = 1.85$ (Figure 4.5) and extrapolating phase velocities to the full ENAM footprint via constant depth contours. Example finite-frequency kernels are shown in Figure 4.6 for 13 s and 20 s period.

Equation (4.4) gives the sensitivity kernel at an instantaneous frequency ω and contains all Fresnel zones, but in practice each phase velocity measurement is made over a finite bandwidth $[\omega - \Delta\omega/2, \omega + \Delta\omega/2]$. We approximate finite-bandwidth kernels by forming a Gaussian weighted average of instantaneous kernels centered on ω with a half width of 10%. This effectively limits the spatial extent of the kernel to the first several Fresnel zones.

Phase slowness maps and anisotropy are inverted via eq. (4.3) using a linearized iterative least squares approach (*Menke, 2012*), and the final model is obtained after two iterations. Perturbations to the starting homogeneous, isotropic phase slowness model are regularized using wavelength-weighted second derivative smoothing and norm damping towards the starting model. At periods less than 17 s, anisotropy terms are damped to zero, as variations in phases velocity associated with anisotropy are swamped by the large variations associated with water depth. Sensitivity kernels are updated upon the second iteration to account for off-great-circle propagation associated with lateral gradients in slowness.

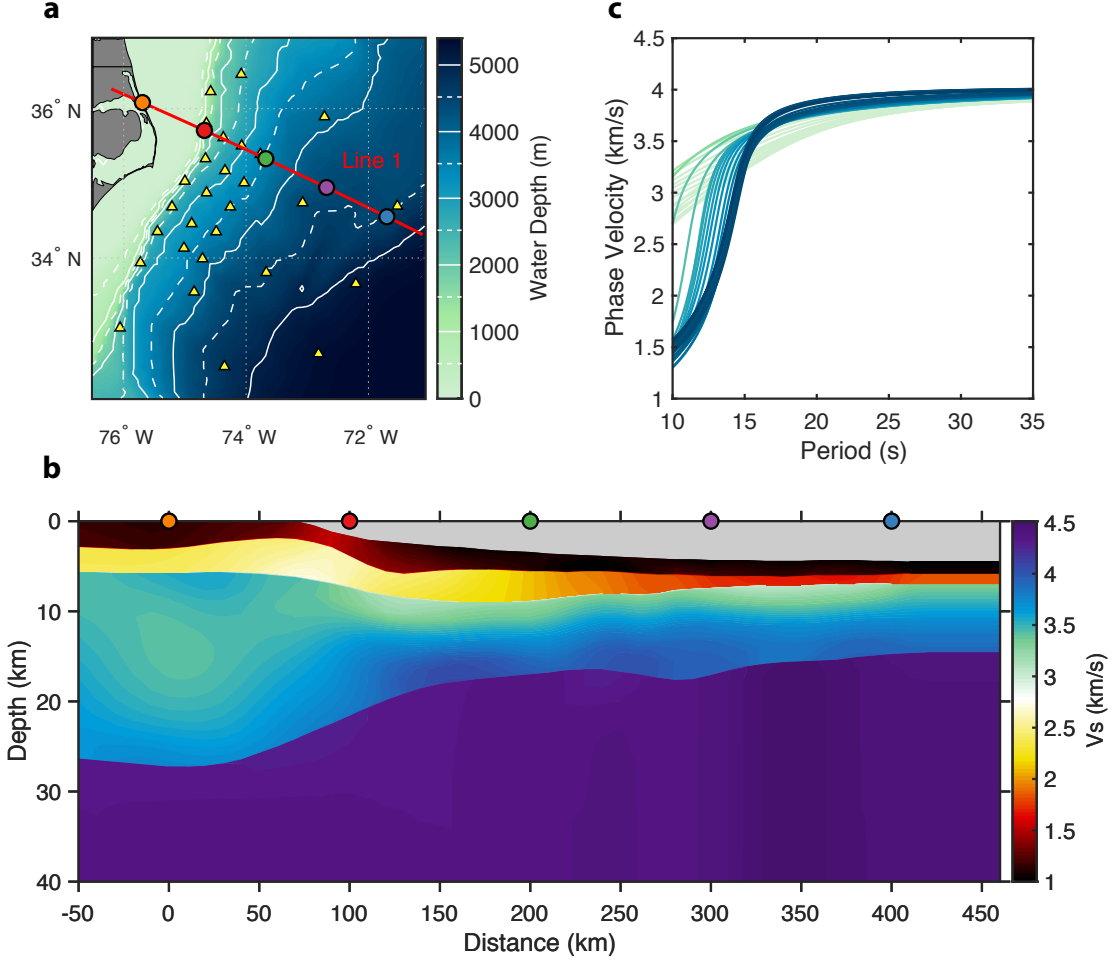


Figure 4.5: (a) Map of the ENAM region showing Line 1 from *Shuck et al. (2019)* in red. Broadband OBS are shown by yellow triangles. White contours show water depth with 500 m change between dashed and solid lines. Colored circles correspond to those in b). (b) Shear velocity V_S along Line 1 converted from V_P assuming $V_P/V_S = 1.85$. (c) Line 1 phase velocities calculated from b) and colored by water depth as in a).

4.2.4.1 Off-great-circle propagation

Water depth across ENAM increases by nearly 4000 m from west to east, leading to a drastic difference in short period Rayleigh-wave sensitivity across the array that is strongly controlled by water depth (Figure 4.7). A 13 s Rayleigh wave that primarily samples the eastern-most edge of the array where water is deep (4000–5000 m) will travel slower than a 13 s wave sampling shallow water near the shelf. This strong lateral velocity gradient at short periods steers energy towards the faster shallow-water regions leading to off-great-

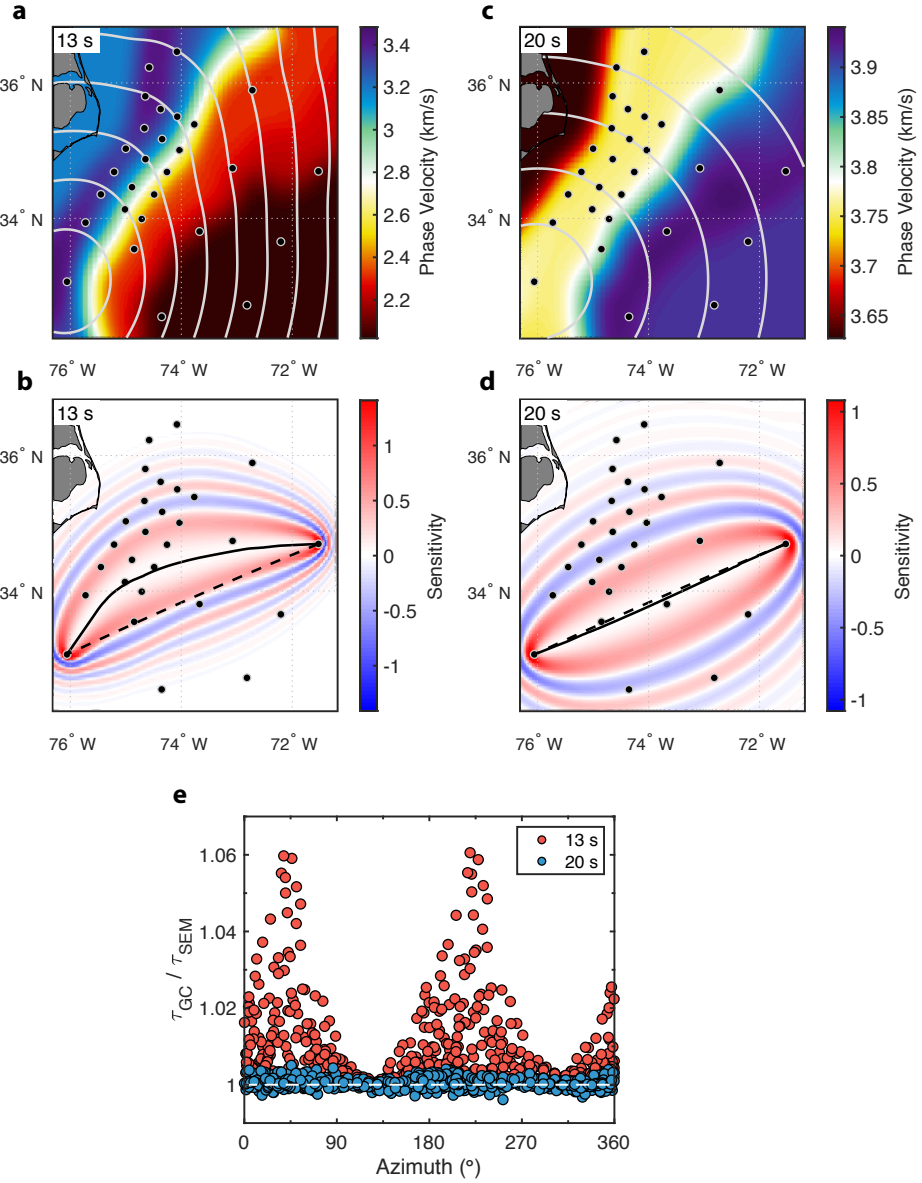


Figure 4.6: Finite-frequency sensitivity kernels and importance of off-great-circle propagation. (a) Synthetic phase velocity map at 13 s period after Gaussian smoothing ($\sigma = 0.2^\circ$). Grey contours show S-wave phase delay at 25 second intervals due to an impulse at station X10 modeled using the spectral element method (SEM) (i.e., $\tau(\mathbf{x})$ in eq.(4.4)). Note the strong wavefield distortion due to large lateral velocity gradients associated with changes in water depth. (b) Finite-frequency sensitivity kernel for station pair X10-X04. The dashed and solid black lines show the great circle (GC) and SEM ray paths, respectively. (c,d) same as a), b) but for 20 s period. The SEM ray path is nearly coincident with the GC. (e) Apparent azimuthal anisotropy of GC phase delays (τ_{GC}) relative to SEM phase delays (τ_{SEM}) for all station pairs with $r > 100$ km at 13 s (red) and 20 s (blue).

circle propagation (Figure 4.6). If great-circle paths are assumed, as is routinely done in surface-wave tomography studies, an apparent 2θ azimuthal anisotropy signal is produced, where waves that travel parallel to the margin appear faster on average than waves that travel perpendicular to the margin (Figure 4.6e). Left unaccounted for, this off-great-circle propagation can result in (1) apparent 2θ azimuthal anisotropy with a fast axis parallel to the margin and (2) biased fast isotropic velocities, on average. We avoid these biases by using semi-empirical finite-frequency kernels that account for off-great-circle propagation and by limiting anisotropy measurements to periods greater than 17 s, where the anisotropy bias is negligible (Figure 4.6e).

4.2.5 Inversion for shear velocity, V_S

The single-frequency phase velocity maps are subsampled to a $0.25^\circ \times 0.25^\circ$ grid and combined to produce a dispersion curve at each grid point in the model. Each dispersion curve is individually inverted for a 1-D depth dependent shear velocity (V_S) profile, and all profiles are ultimately combined to produce the final 3-D V_S model. The starting 3-D V_S model for the inversion is constructed from the 2-D crustal V_P model along line 1 from *Shuck et al.* (2019) assuming $V_P/V_S = 1.85$ and an oceanic mantle structure (*Russell et al.*, 2019a). As seismic structure mostly varies perpendicular to the margin (*Shuck et al.*, 2019) (i.e., with water depth), the 2-D line is extrapolated to the entire 3-D ENAM region along contours of constant water depth.

Each 1-D inversion aims to solve for V_S while minimizing dispersion misfit via a standard linearized iterative least-squares approach (*Menke*, 2012). The perturbation kernels and forward estimates of phase velocity are calculated for a layered Earth model extending to 250 km using the SURF96 software (*Herrmann*, 2013) (Figure 4.7). The inversion is regularized with norm damping towards the starting model, second derivative smoothing, and a constraint that seeks to preserve layer gradients in the crust and mantle (*Russell et al.*, 2019a). These constraints are broken across prescribed sediment and Moho boundaries to

allow for discontinuities. Compressional velocities (V_P) and density are held fixed. A linear increase in damping toward the reference model is applied below 50 km such that the reference model is exactly maintained by ~ 100 km depth. A total of 10 iterations are performed: iterations 1–9 maintain the same kernel, and dispersion is predicted via perturbation theory using the kernels; upon iteration 10, the kernels and predicted dispersion are recalculated.

In order to evaluate starting model dependence, a Monte Carlo approach is used. At each grid point, the starting model sediment, crust, and mantle V_S and layer thicknesses are randomly perturbed by drawing from a zero-mean normal distribution with standard deviation of 10% of the reference values for the crust and mantle and 25% for the sediments. This process is repeated 100 times for each grid point and the median and middle 68th percentile of the ensemble of final models with $\chi^2 \leq 1.25$ are taken as the preferred V_S and associated 1- σ uncertainties.

4.3 Results

4.3.1 Phase velocity maps

Figure 4.8 shows isotropic phase velocity maps for periods ranging from 13–32 s. The dashed grey boundary shows the resolving limit defined by a value of 0.1 on the diagonals of the frequency-averaged resolution matrix. At 13 s period (Figure 4.8a), Rayleigh wave velocities decrease from west to east due to the increasing water depth. At longer periods this general trend reverses, and velocities increase eastward as a result of the transition from thick continental crust in the west to thinner oceanic crust (and increased mantle sensitivity) in the east. This same character is seen in the synthetic phase velocity maps in Figure 4.6a,c (see also Figure D.5). Similar to the synthetic maps, variations parallel to the margin are smooth and relatively minor, suggesting that the measurements are largely 2-D and primarily controlled by structure associated with the continent-to-ocean transition. At the longest periods (27–32 s), the highest velocities (>4.1 km/s) are observed east of the

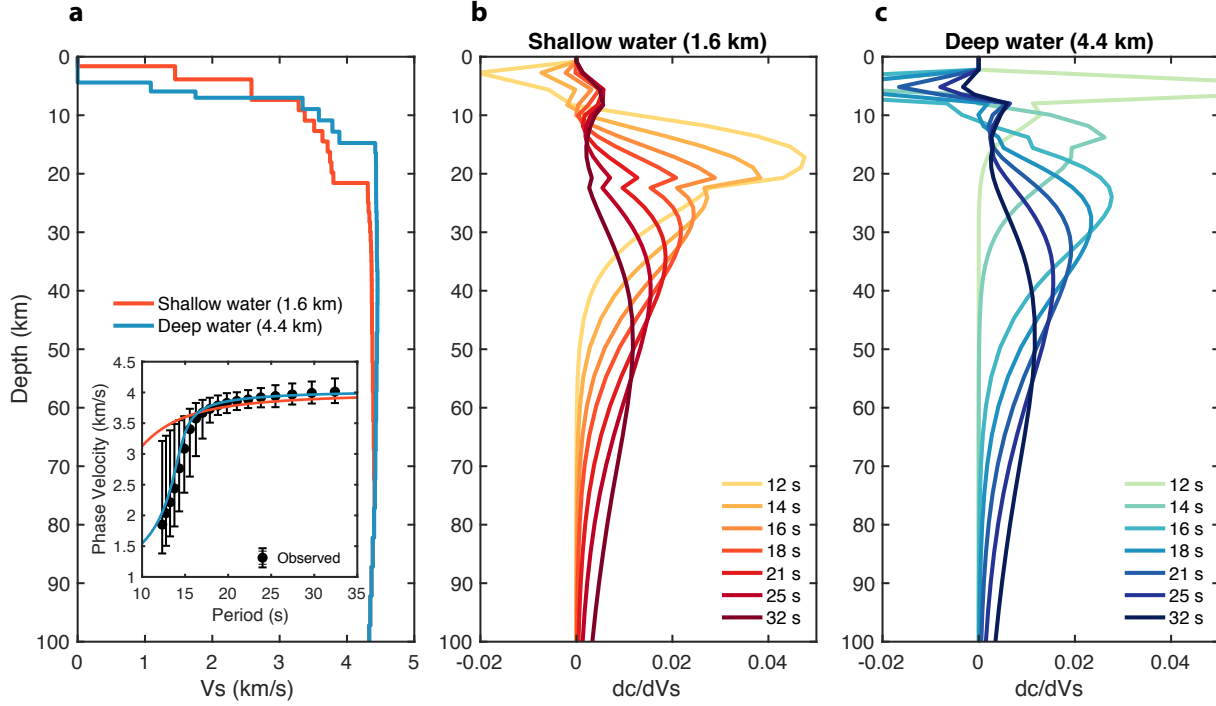


Figure 4.7: Shear velocity sensitivity kernels for end-member shallow- and deep-water structure along Line 1. (a) V_s profiles for 1.6 km *shallow* water in red (100 km along Line 1, see Figure 4.5) and 4.4 km *deep* water in blue (400 km along Line 1). The inset shows phase velocity predictions for the two models (colored lines) and the median (black circles) and range (bars) of all interstation phase velocity measurements. (c,d) Phase velocity sensitivities to shear velocity perturbations for shallow- and deep-water structure.

BSMA, although resolution is limited by modest station distribution east of the BSMA.

4.3.2 Azimuthal anisotropy

Azimuthal anisotropy of phase velocity is estimated from 17–32 s, sensitive primarily to lithospheric depths. Figure 4.9 shows 2-D maps of azimuthal anisotropy for two different choices of smoothing: (1) A smoothly parameterized inversion that seeks to minimize the second spatial derivatives $\nabla^2 A_c$ and $\nabla^2 A_s$. (2) An inversion that effectively solves for a single anisotropy fast azimuth and magnitude on either side of the BSMA by strictly enforcing $\nabla A_c = \nabla A_s = 0$ but breaking this constraint at the BSMA.

Both inversions indicate dominantly margin-parallel anisotropy across the array. In detail, the smooth model (Figure 4.9a) shows a gradual west-to-east clockwise rotation from

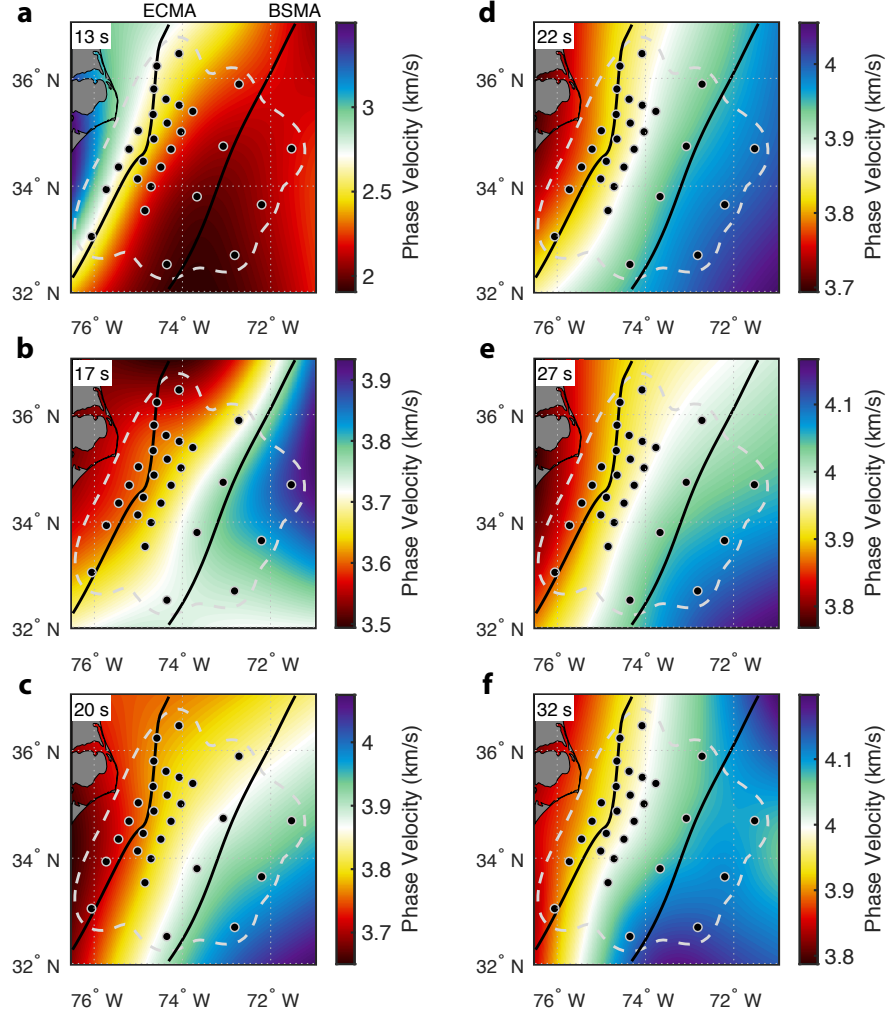


Figure 4.8: (a–f) Isotropic phase velocity maps for six periods ranging from 13–32 s. Black lines mark the East Coast Magnetic Anomaly (ECMA) and Blake Spur Magnetic Anomaly (BSMA). The dashed grey contour indicates the limit of resolution based on a value of 0.1 on the diagonals of the frequency-averaged resolution matrix.

margin-parallel. East of the BSMA and for 17–25 s period, both models indicate a $\sim 25\text{--}45^\circ$ rotation from margin-parallel towards the FSD (Figure 4.10). Neither model requires FSD-parallel anisotropy. At periods >27 s, both models indicate a reduction in anisotropy east of the BSMA. The smooth model shows evidence of NW-SE trending variations in anisotropy magnitude west of the BSMA, ranging from $\sim 3\text{--}4\%$ in the northwest to $\sim 1\text{--}2\%$ in the southeast; however, these magnitude variations may not be well resolved (see Section 4.3.2.1; Figure D.2a)

As the 2-D anisotropy maps suggest a relatively simple pattern dominated by margin-parallel anisotropy, we also solve for a 1-D array-averaged fast azimuth and magnitude for the region. Phase velocity residuals calculated relative to the 2-D path-integrated isotropic velocities are shown as a function of azimuth in Figure 4.11a–f. Azimuthal patterns are clearly dominated by a 2θ sinusoid with fast azimuth parallel to the margin and perpendicular to the FSD (Figure 4.11g,h). Anisotropy peak-to-peak magnitudes decrease slightly with increasing period from 3–4% at 17 s to \sim 2.5% at 32 s. To address potential bias caused by uneven azimuthal sampling, we also estimate anisotropy strength and fast azimuth for data averaged in 20° azimuthal bins. The fast azimuths and magnitudes obtained agree with the unbinned estimates but have uncertainties of a factor \sim 2–3 larger.

We explore whether the simpler 1-D anisotropy model can explain the data as well as the 2-D models. Phase delay residuals are compared for the three anisotropy inversions with varying degrees of freedom – the 1-D array-averaged inversion, 2-D smooth inversion, and 2-D break at the BSMA (Figure 4.12). Overall, the 2-D smooth inversion yields slightly lower root-mean-square (RMS) phase delay residuals on average, which is unsurprising as it has the most degrees of freedom. However, for most frequencies the data fits produced by each of the three inversions are nearly indistinguishable (Figure 4.12g), and therefore we favor the simplest model with 1-D margin-parallel anisotropy, though we cannot rule out a small (25 – 45°) clockwise rotation east of the BSMA.

4.3.2.1 Synthetic recovery tests: resolving anisotropy east of the BSMA

We perform synthetic tests to determine whether our dataset can resolve a 90° change in anisotropy fast direction from margin-parallel west of the BSMA to FSD-parallel east of the BSMA (Figure D.1–D.4). At each frequency, the synthetic dataset is calculated using the synthetic isotropic phase velocity maps extrapolated from Line 1 and the anisotropic model shown in Figure D.1. The input anisotropy model is characterized by a constant 2% zero-to-peak anisotropy magnitude across the array with fast azimuthal parallel to the

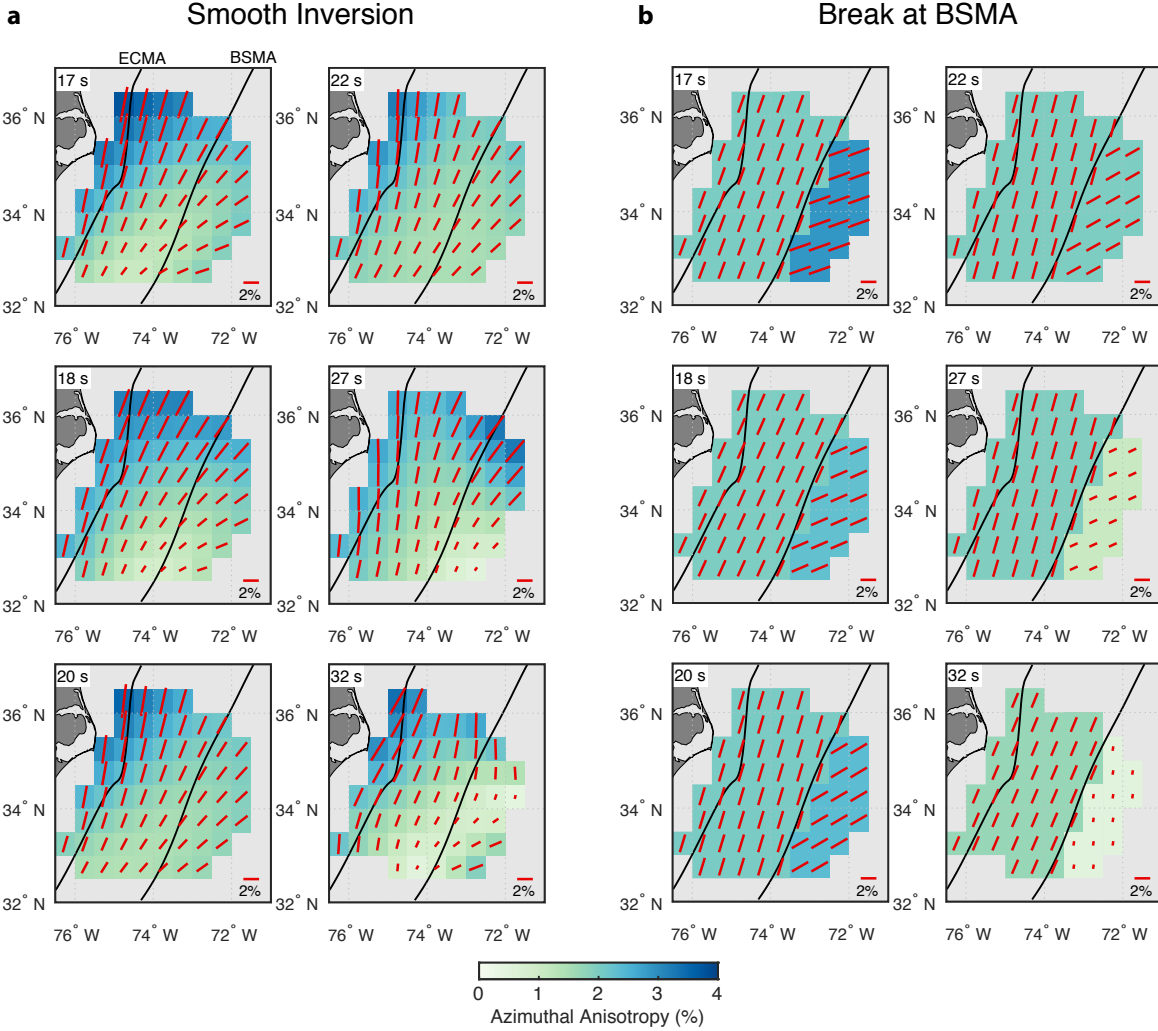


Figure 4.9: 2-D azimuthal anisotropy maps for periods ranging from 17–32 s for (a) a smoothly varying inversion and (b) an inversion that minimizes the first spatial derivative with a break at the Blake Spur Magnetic Anomaly (BSMA). Red sticks show anisotropy fast azimuths and their lengths scale with anisotropy magnitude. Black lines indicate the prominent magnetic anomalies.

margin west of the BSMA and parallel to the FSD east of the BSMA. Gaussian noise with standard deviation of 0.6 s is added to the synthetic phase delay times. We test the two different 2-D inversion strategies introduced above to evaluate their ability to recover the change in anisotropy direction across the BSMA.

We find that the smooth anisotropy inversion (Figure D.2) successfully resolves the margin-parallel anisotropy west of the BSMA and FSD-parallel anisotropy east of the BSMA

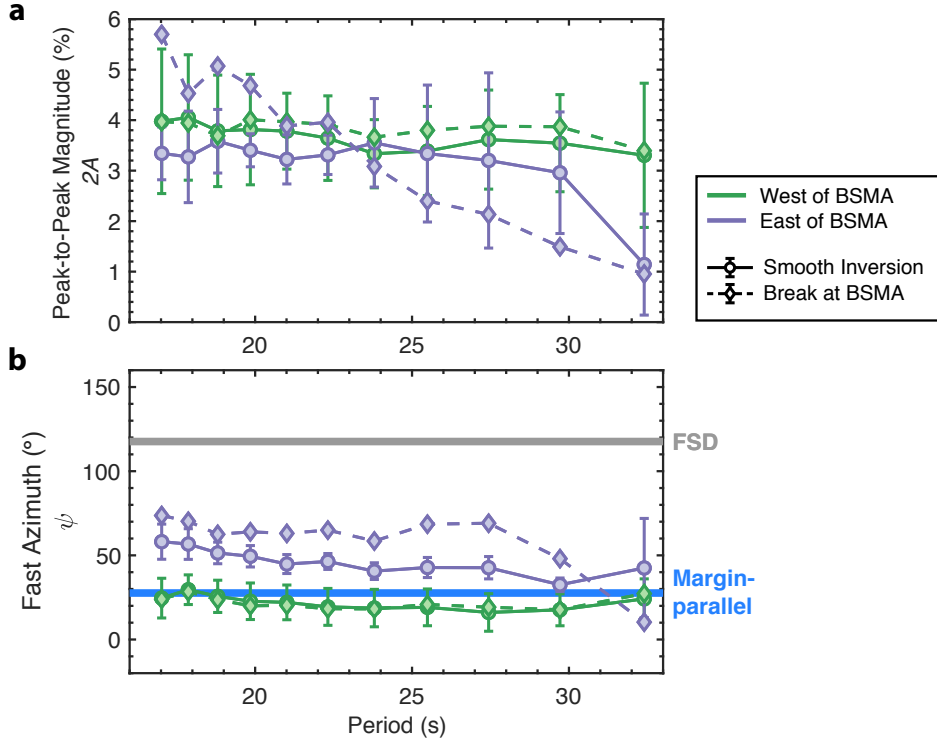


Figure 4.10: (a) Anisotropy peak-to-peak strength and (b) fast propagation azimuth for the two model solutions in Figure 4.9 for regional averages representing west of the BSMA (green) and east of the BSMA (purple). Symbols show the mean and 2σ variations for the corresponding regions. Thin solid and dashed lines correspond to Figure 4.9a and 4.9b, respectively. Thick grey and blues lines mark the fossil-spreading direction (FSD) and margin-parallel direction.

but has trouble capturing the sharp change directly at the BSMA, where recovered anisotropy magnitudes are small. Anisotropy strength is generally poorly resolved in the smooth model; it is overestimated at the westernmost edge of the array and underestimated east of the BSMA. The inversion containing the break at the BSMA (Figure D.3) more accurately captures both the anisotropy magnitude and change in direction across the BSMA. This is perhaps unsurprising given that this parameterization closely resembles the character of the input anisotropic model.

Overall, both parameterizations are able to capture a 90° change in anisotropy across the BSMA, but the parameterization that explicitly allows a break at the BSMA more accurately recovers the magnitude of anisotropy (Figure D.4). In both cases, the array-

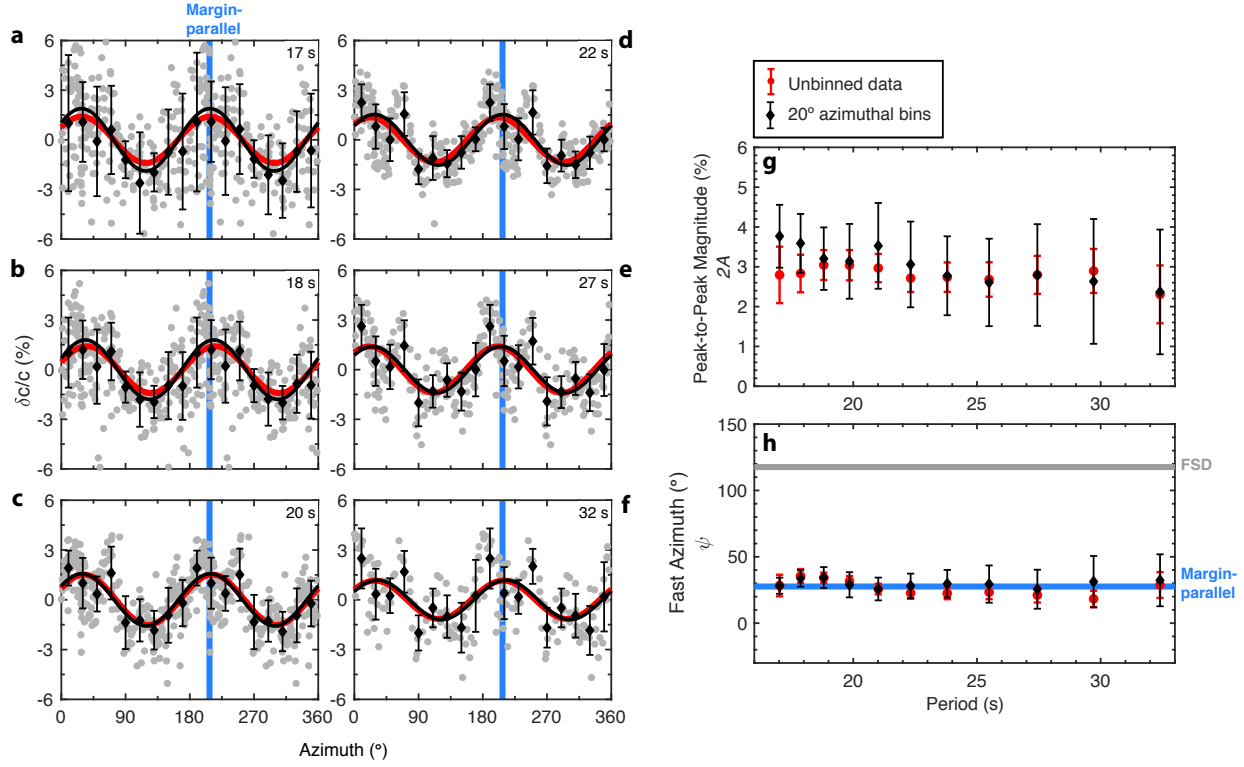


Figure 4.11: (a–f) Array-averaged 1-D azimuthal anisotropy ranging from 17–32 s period. Grey circles show interstation phase velocity deviations from the path-averaged isotropic values, and black diamonds show the mean and standard deviation for 20° azimuthal bins. The 2θ fit to the individual measurements is shown in red and the fit to the binned data is in black. The margin-parallel direction is indicated by the vertical blue dashed lines. (g) Anisotropy peak-to-peak strength and (h) fast propagation azimuth for the unbinned data in red and binned data in black. Error bars show 2σ uncertainties. Thick grey and blue dashed lines mark the fossil-spreading direction (FSD) and margin-parallel direction, respectively.

averaged anisotropy is dominated by the margin-parallel anisotropy structure west of the BSMA, due to its larger footprint and the greater number of ray paths on the western side of the array. We conclude that if a change in anisotropy direction occurs from margin-parallel west of the BSMA to FSD parallel east of the BSMA, the 2-D anisotropy inversions should recover it. However, we do not detect such FSD-parallel anisotropy east of the BSMA.

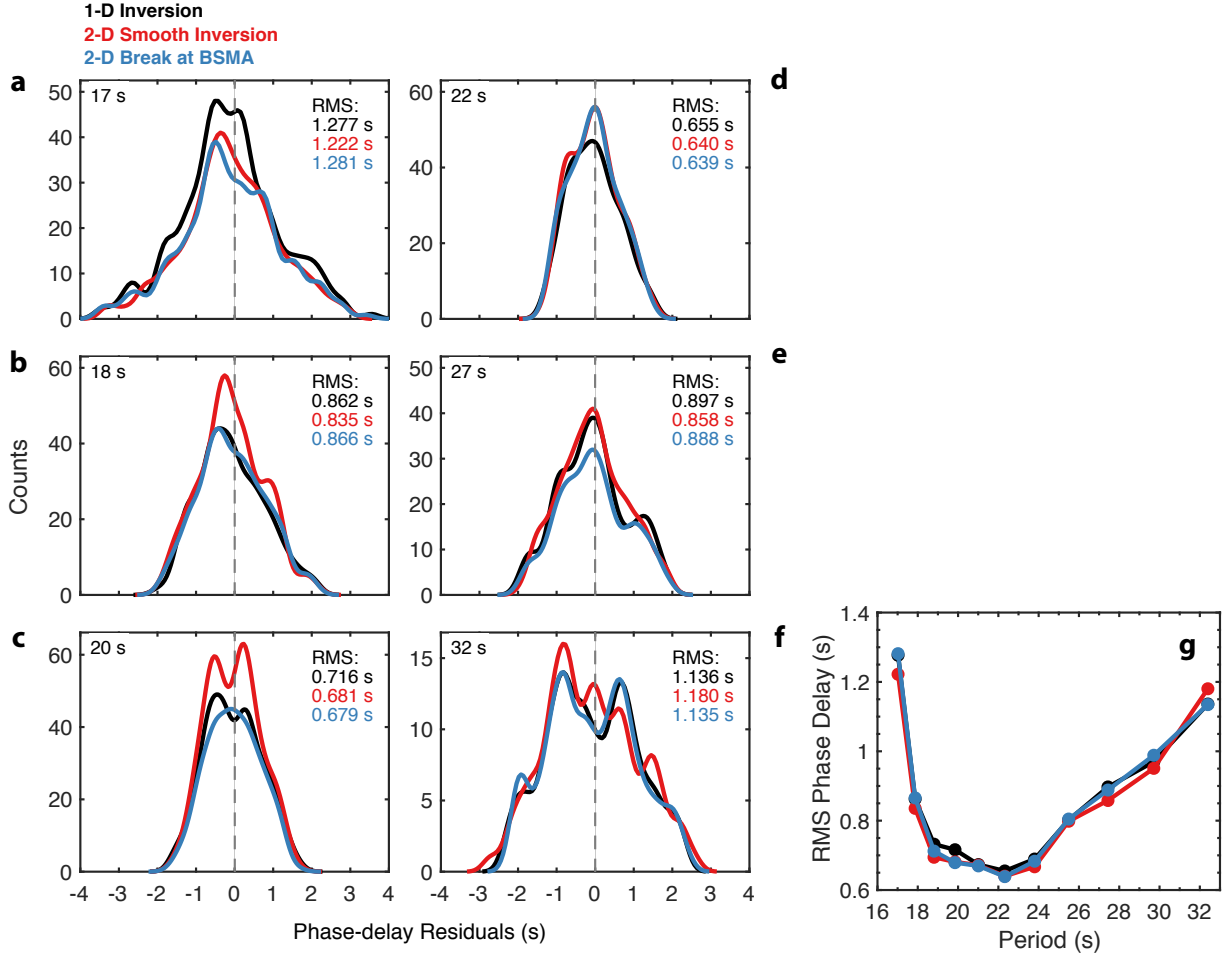


Figure 4.12: Comparison of phase-delay residuals and root-mean-square (RMS) misfits for three inversion types. (a–f) Smoothed histograms of phase-delay residuals for the 1-D inversion from Figure 4.11 (black), the 2-D smooth inversion from Figure 4.9a (red), and the 2-D inversion with the break at the BSMA Figure 4.9b (blue) for periods ranging from 17–32 s. (g) RMS phase delays for each of the three inversions.

4.3.3 3-D shear velocity model

4.3.3.1 V_S uncertainty

Example 1-D V_S profiles from the west and east are shown in Figure 4.13 with uncertainties estimated via the Monte Carlo inversion described in Section 4.2.5. Uncertainties are larger in the crust and sediments than in the mantle, particularly for the western profile (Figure 4.13a,b) where the rapid change in water depth makes resolving crustal structure more difficult. In the western profile, crustal uncertainties generally range from 0.5–0.8 km/s

compared to 0.25–0.5 km/s in the east. Mantle velocities for both the western and eastern profiles appear well resolved with uncertainties ranging from 0.1–0.3 km/s in the upper 10 km of the mantle and 0.03–0.1 km/s below (see also Figure D.7).

4.3.3.2 Crustal variations

Horizontal slices through the 3-D V_S model are shown in Figure 4.14. In the upper 4 km of the crust, velocities are slow (2–2.5 km/s) in the west corresponding to sediments and transition sharply to faster velocities (3–3.6 km/s) as the sediments thin to <4 km in the east (*Shuck et al.*, 2019). The sharpness of this basement transition is a product of the layer discontinuities built into the starting reference model (Figure D.6), which are preserved but otherwise poorly resolved by Rayleigh waves. In the lower crust (8 km), a slow velocity anomaly is observed at the BSMA near the center of the array.

A fast velocity anomaly is present in both crustal slices at the northernmost edge of the model (Figure 4.14a,b), extending beyond the resolved region. This feature may indicate anomalously fast crust that is perhaps thin relative to the surrounding crust. However, such an anomaly is not evident in the observed phase velocity maps, nor is it present in the starting V_S model (Figure D.6) or in the phase velocity maps for the starting model (Figure D.5). As the anomaly is positioned at the edge of our model where data coverage is limited, and where short period phase velocities are predicted to change rapidly (Figure D.6a) we choose not to interpret the anomaly further.

In the 4–15 km depth slices, a band of anomalously slow velocities coincides with the shelf, correlating with large gradients in seafloor depth (>2 km/°). This rapid decrease in water depth west of the shelf break is just outside the array and poorly resolved by our relatively smooth phase velocity maps. This results in slower than predicted phase velocities along the shelf that map directly into the crustal velocities. The region of the model most affected by this bias is indicated by a semi-transparent mask in Figure 4.14.

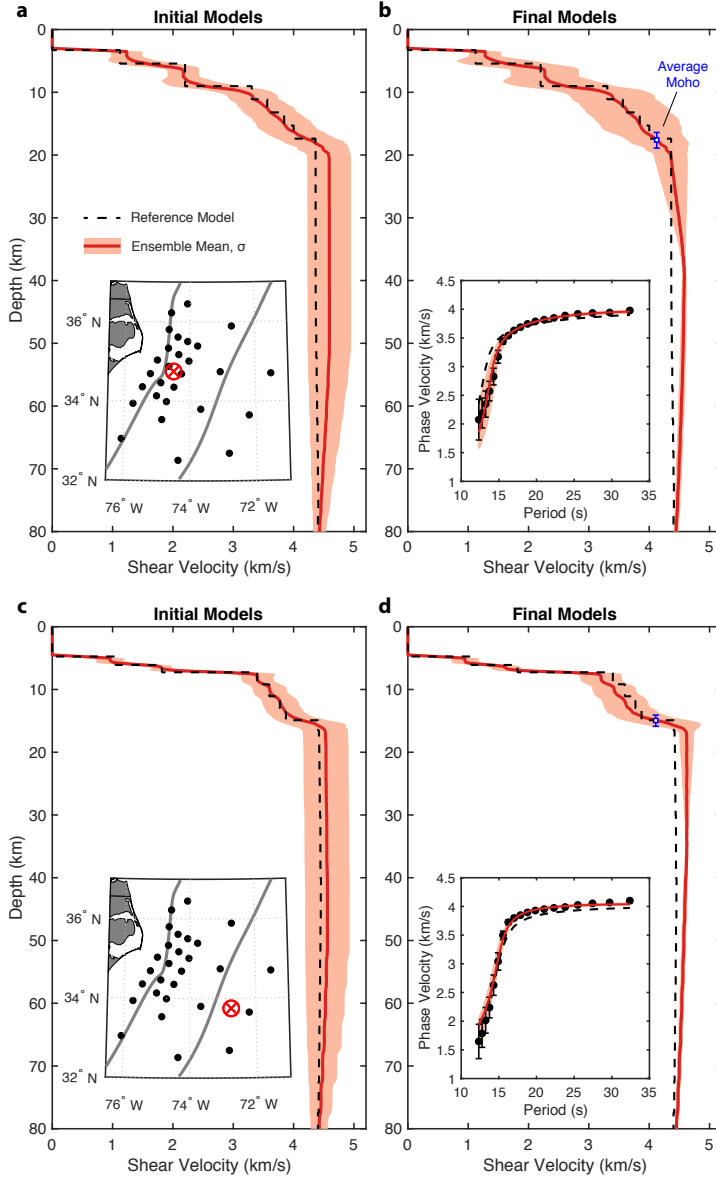


Figure 4.13: Representative 1-D V_S profiles from the Monte Carlo inversion for locations on the western and eastern edges of the array. (a) Starting model ensemble mean (red) and one standard deviation (σ , light shading). Reference model shown by black dashed line. The profile location is indicated by the red crosshair in the inset map. (b) Final model ensemble mean and standard deviation for all models with a data misfit of $\chi^2 \leq 1.25$. The mean and standard deviation Moho depth of acceptable models is shown by the blue symbol. The inset shows the dispersion data and $1-\sigma$ uncertainties in black, mean and range of model fits in red, and reference model prediction (black dashed). (c,d) Same as a), b) but for a location on the eastern edge of the array.

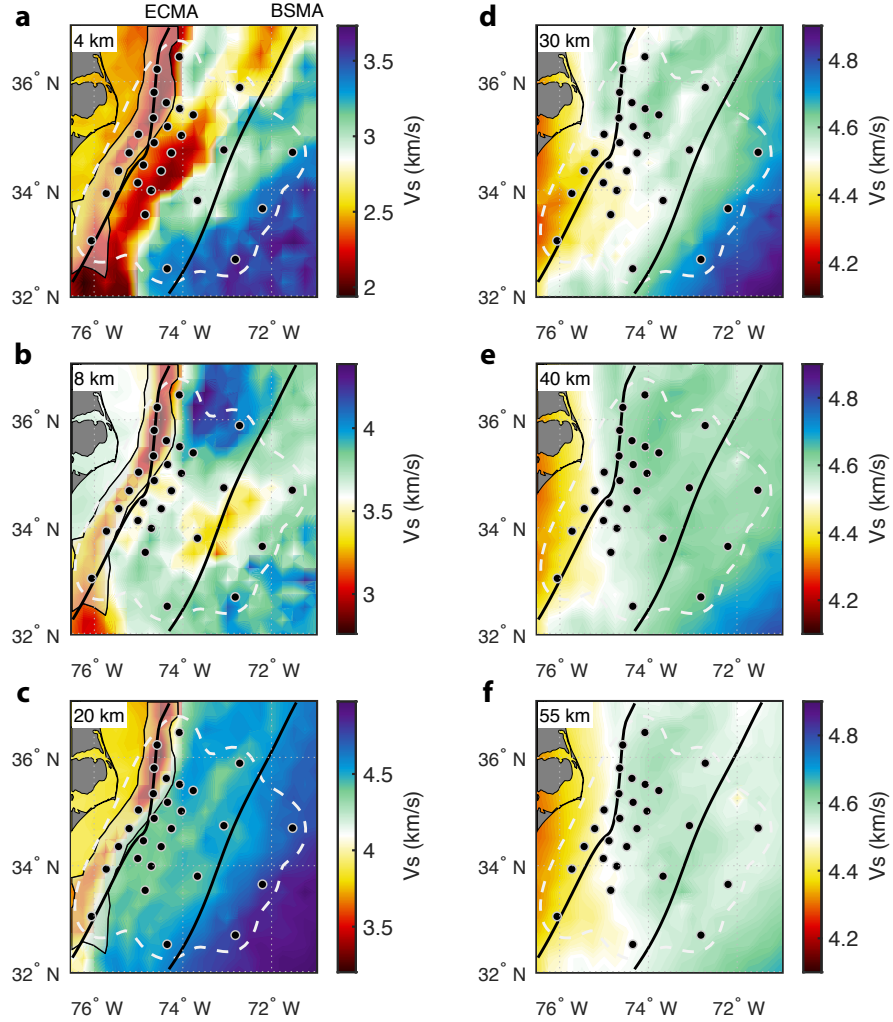


Figure 4.14: Horizontal slices through the mean 3-D shear velocity model. (a,b) Crustal slices at 4 km (upper crust) and 8 km (lower crust) below the seafloor (or free surface). (c–f) Mantle slices at 20, 30, 40, and 55 km depth. The white dashed line marks the limit of resolution. Regions of the model near the shelf where water depth changes rapidly ($>2 \text{ km/}^\circ$) are masked in grey, as these regions may contain biased slow velocity estimates (see main text). Major magnetic anomalies, ECMA and BSMA, are indicated by thick black lines.

4.3.3.3 Mantle variations

Velocities in the mantle are generally well resolved in comparison to the crust as the mantle-sensitive Rayleigh waves are not sensitive to changes in water depth. Within the array footprint, mantle velocities range from $\sim 4.4 \text{ km/s}$ in the west to $\sim 4.7 \text{ km/s}$ in the east (Figure 4.14d–e). East of the BSMA and within the array footprint, velocities peak at 4.6–

4.7 km/s in the upper 10–25 km of the mantle and decrease with depth, suggestive of thermal ocean lithosphere. At 55–60 km depth, velocities are nearly homogeneous (\sim 4.5 km/s) across the region.

4.4 Discussion

4.4.1 Margin-perpendicular structure and significance of the BSMA

The average 2-D margin-perpendicular structure of our model is shown in Figure 4.15, which shows a contrast in shallow mantle velocities that coincides approximately with the BSMA. In the upper 10–20 km of the mantle, relatively slow shear velocities (4.4–4.55 km/s) extend east of the margin \sim 200 km terminating at the BSMA. East of the BSMA, velocities are elevated ($>$ 4.6 km/s) and characteristic of depleted, cold oceanic lithosphere (e.g. *Lin et al.*, 2016, *Nishimura and Forsyth*, 1989). Below 40–50 km depth, velocities are homogeneous across the region ($<$ 4.6 km/s) east of the ECMA, and therefore we interpret that the low-velocity lid within the IMQZ is underlain by oceanic mantle lithosphere.

Velocities of the seismically slow lid west of the BSMA are similar to those just onshore (*Shen and Ritzwoller*, 2016) and may correspond to stretched and/or thermo-chemically modified continental lithosphere associated with rifting (e.g. *Hopper et al.*, 2020). This interpretation of the mantle structure is consistent with the detailed crustal structure recently imaged at the ENAM-CSE (*Bécel et al.*, 2020, *Shuck et al.*, 2019). *Shuck et al.* (2019) observe relatively thin crust (6–8 km) with fast lower crustal velocities ($V_P \sim 7.5$ km/s) on Lines 1 and 2 between the ECMA and BSMA that is best explained by deeper than usual mantle melting, which they propose resulted from a 15–20 km thick continental lithosphere that truncated the upper melting regime producing less voluminous, more mafic melts. Their prediction of the presence of a continental lithospheric lid is consistent with the slower shear velocities ($V_S < 4.55$ km/s) that we observe in the upper \sim 15 km of the mantle west of the BSMA. We also observe elevated lower crustal shear velocities within the IMQZ, though

they are present in our starting model (Figure 4.5). East of the BSMA, crustal structure is most consistent with typical seafloor spreading with melting that occurred to the base of the crust (*Shuck et al.*, 2019). In the ENAM-CSE multichannel seismic (MCS) reflection data, *Bécel et al.* (2020) observe rough basement topography between the ECMA and BSMA that transitions to smooth basement east of the BSMA, consistent with an increase in spreading rate from ultra slow (~ 0.65 cm/yr half-rate) to slow (~ 1.3 cm/yr half-rate) at the BSMA that may be explained by complete rupture of the continental lithosphere.

Alternatively, the slow lithospheric velocities could be explained by gabbroic inclusions trapped in the mantle lithosphere during ultra-slow spreading (*Lizarralde et al.*, 2004). Efficient conductive cooling at the MOR during periods of very slow spreading leads to a thicker mantle lid that could crystallize gabbroic melts and trap them in the mantle, reducing the mantle shear velocity and producing thinner crust. The crust west of the BSMA has roughness characteristics of typical ultra-slow spreading crust (*Bécel et al.*, 2020). This offers an alternative mechanism for truncating the upper melting regime from that previously proposed (*Shuck et al.*, 2019) without invoking the emplacement of proto-oceanic crust on top of continental lithosphere. However, one possible caveat is that the notion of a thicker thermal lid may be difficult to reconcile with the relatively hot mantle potential temperatures of 1395–1420°C that have been inferred based on the crustal structure in the region (*Shuck et al.*, 2019). More detailed modeling of thermal evolution of ultra-slow spreading centers in the presence of elevated mantle temperatures is required.

The average margin-perpendicular V_S structure in our model is broadly similar to the offshore structure in the previous shear velocity model of *Lynner and Porritt* (2017). However, upon closer inspection important differences do exist. Their inferred offshore crust is ~ 10 km thicker than what we observe. This is likely attributed to our differences in starting model, and in particular, that we directly incorporated the refraction tomography constraints from *Shuck et al.* (2019). They also do not observe low velocities in the uppermost mantle west of the BSMA, nor do they observe a change in mantle velocities across the BSMA. We

believe our ability to resolve these new shallow mantle features is a result of the detailed prior information incorporated into the crust.

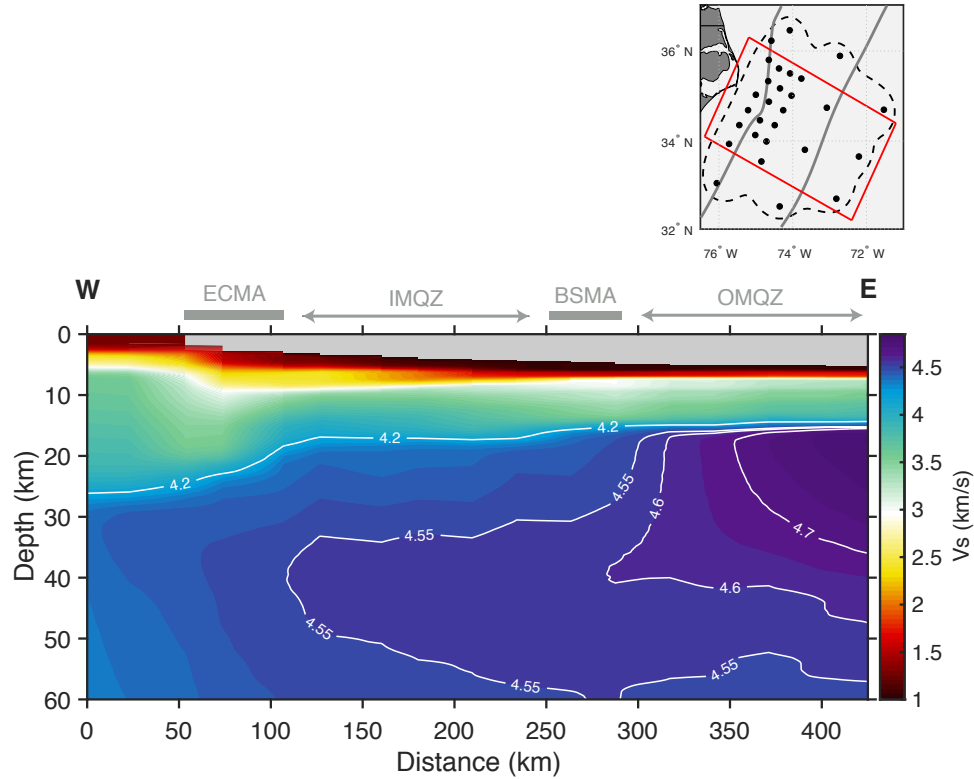


Figure 4.15: Average margin-perpendicular V_S structure. The region included in the average is shown by the red box in the upper map. The extent of the ECMA and BSMA are indicated by the grey bars. IMQZ = Inner magnetic quiet zone; OMQZ = Outer magnetic quiet zone.

4.4.2 Implications for the onset of normal seafloor spreading

If the ~ 15 km thick slow lithospheric lid that extends seaward ~ 200 km from the margin to the BSMA is attributed to thinned continental mantle lithosphere, then this would indicate that the lithosphere had not completely ruptured prior to ~ 170 Ma as suggested by *Shuck et al. (2019)* and *Bécel et al. (2020)*. This supports the notion that the complete lithospheric breakup of the ENAM from northwest Africa and the onset of normal seafloor spreading occurred at the BSMA at ~ 170 Ma, approximately 10–25 Myr after the initiation of rifting and formation of the ECMA (*Bécel et al., 2020, Shuck et al., 2019*). This is in contrast to

the previous idea that the complete breakup and onset of normal seafloor spreading took place over a relatively short-lived period that immediately followed formation of the ECMA (*Holbrook and Kelemen*, 1993, *Holbrook et al.*, 1994, *Kelemen and Holbrook*, 1995). Rather, the detailed lithospheric architecture may indicate that after formation of the ECMA and prior to the BSMA, a proto-seafloor spreading mode was active with mantle-derived melts migrating vertically through the continental lid and forming thin proto-oceanic crust (*Bécel et al.*, 2020, *Shuck et al.*, 2019).

Numerical models have shown that mantle can remain intact even after the crust has separated at rifted margins if the crust fails through brittle faulting while the underlying mantle lithosphere deforms through ductile necking (*Huismans and Beaumont*, 2011). Such ductile deformation of the lithosphere is conceivable considering the elevated mantle potential temperatures (1430–1480°C) inferred from CAMP lavas (*Callegaro et al.*, 2013) and the inferred ultra-slow extension rates (<2 cm/yr half-rate) (*Davis et al.*, 2018).

Alternatively, the slow lithospheric lid may be attributed to trapped gabbroic melts that were crystallized within the conductively cooling oceanic lithosphere (*Lizarralde et al.*, 2004). This would explain the thinner crust between the ECMA and BSMA (*Shuck et al.*, 2019) as less melt was available to form the crust. It is also consistent with the increase in spreading rate inferred at the BSMA and associated thickening of the crust (*Bécel et al.*, 2020) as well as the faster mantle velocities east of the BSMA. In this case, the implications on timing are in keeping with the more commonly held notion that breakup and the onset of normal (ultra-slow) seafloor spreading occurred immediately following formation of the ECMA. The potential for melts to become trapped in the oceanic mantle has implications for our understanding of melt extraction, crustal accretion, and thermal evolution at ultra-slow spreading centers.

4.4.3 Comparison to previous anisotropy observations

The Rayleigh-wave anisotropy that we observe in the lithosphere at the ENAM-CSE has a fast direction sub-parallel to the margin. Previous shear-wave splitting observations at the ENAM-CSE also showed margin-parallel anisotropy, but it was attributed to deeper present-day asthenospheric flow along the margin associated either large-scale density or pressure driven flow or edge-driven convection due to the large lithospheric root of the continent (*Lynner and Bodmer, 2017*). Our observations do not preclude such flow in the asthenosphere but show that strong margin-parallel anisotropy is present in the lithosphere, which likely contributed to the previous shear-wave splitting observations. A preliminary comparison of shallow mantle V_P along the margin-parallel and -perpendicular refraction lines at ENAM also indicated ($\sim 8\%$) faster velocities parallel to the margin (*Shuck and Van Avendonk, 2016*) in agreement with our observations, though spatially limited to the crossing points of the profiles.

At the Far-offset Active-source Imaging of the Mantle (FAIM) seismic refraction experiment (115–130 Ma) ~ 800 km southeast of the ENAM-CSE, *Gaherty et al. (2004)* inferred a lithospheric olivine LPO sub-parallel to the FSD (to within $\sim 15^\circ$). This implies that a rotation in lithosphere LPO from spreading-perpendicular to spreading-parallel occurred between 165–130 Ma. Observations of Love-Rayleigh scattering offshore ENAM offers evidence for such lateral gradients in anisotropy (*Servali et al., 2020*), though the frequencies considered (~ 100 s) have significant asthenospheric sensitivity, and the inferred scattering points are widely distributed throughout the western Atlantic including within the ENAM-CSE footprint. Additionally, global models show variable anisotropy at lithospheric depths in the North Atlantic that is often highly rotated from the FSD (e.g. *Becker et al., 2014, Debayle and Ricard, 2013, Schaeffer et al., 2016, Yuan and Beghein, 2013*). As significant variability in the Atlantic still exists between different global models, our high-resolution estimate provides a new benchmark for the northwest Atlantic and confirms the previous notion of variable anisotropy in the Atlantic lithosphere.

4.4.4 Interpretation of fossilized margin-parallel anisotropy

The surface-wave anisotropy that we observe is similar in strength and overall character to that observed in other oceanic regions (e.g. *Eddy et al.*, 2019, *Forsyth*, 1975, *Nishimura and Forsyth*, 1989, *Takeo et al.*, 2018), suggesting that olivine LPO is a likely mechanism for explaining the anisotropy (*Russell et al.*, 2019a). However, the margin-parallel orientation is perpendicular to what is expected for a typical seafloor spreading environment, where corner flow near the ridge generates spreading-parallel olivine LPO that is locked into the lithosphere (*Blackman and Kendall*, 2002a). Instead, our results suggest margin-parallel shear deformation during continental breakup and initial seafloor spreading. Based on recent seismic anisotropy observations in Pacific and Juan de Fuca lithosphere that deviate from the FSD by 10–70° (e.g. *Shinohara et al.*, 2008, *Shintaku et al.*, 2014, *Takeo et al.*, 2016, 2018, *Vanderbeek and Toomey*, 2017), it has been suggested that shear deformation associated with APM at the time of plate formation may dominate the spreading-related deformation if the absolute plate velocities outpace the spreading rate at the MOR (*Vanderbeek and Toomey*, 2017). This may explain the overall poor correlation between lithosphere anisotropy and FSD in the slow-spreading Atlantic (*Becker et al.*, 2014). At ENAM, estimates of spreading rate prior to the BSMA formation are ultra-slow (\sim 0.65 cm/yr half-rate), and increase to \sim 1.3 cm/yr half-rate just after BSMA formation (*Bécel et al.*, 2020).

We explore whether our observations of margin-parallel anisotropy can be explained by fast margin-parallel plate velocities at the time of ENAM formation (165–200 Ma) using four recent plate reconstruction models via the GPlates software (*Boyden et al.*, 2011): S12-ESR (*Seton et al.*, 2012); M16-AREPS (*Müller et al.*, 2016); M16-GPC (*Matthews et al.*, 2016); M19-T (*Müller et al.*, 2019) (Figure 4.16). These studies utilize continuously closing topological plate polygon networks that account for inception and cessation of plate boundaries in order to reconstruct plate motions from present day back \sim 200 Ma. Relative plate motions in these models are well constrained primarily by seafloor magnetic anomaly picks and fracture zones, particularly in the Atlantic where seafloor is preserved on both conjugate flanks of

the MOR. However, absolute plate motions are less well constrained and depend strongly on the choice of absolute reference frame (e.g. *Shephard et al.*, 2012, *Torsvik et al.*, 2008), which varies between studies. Evidence for this is seen in Figure 4.16, where North America plate motion varies strongly between the four models, particularly for ages >160 Ma. In general, the four models use hybrid reference frames with present day to 70–100 Ma described by a global moving hotspot reference frame and 100–230 Ma constrained by true-polar wander corrected paleomagnetic data. The exception is M19-T, for which authors inverted for a reference frame from 0–80 Ma that minimized trench migration velocities and global net lithospheric rotation, and this model is the only one which includes diffuse deformation along plate boundaries.

Though differences do exist between the four models, important similarities are observed. Absolute plate velocities during the ENAM breakup were variable but often fast (1.5–9 cm/yr) relative to spreading (0.5–1.5 cm/yr half-rate), especially early in the breakup (180–200 Ma). From 170–200 Ma, APM directions were significantly different from the spreading direction and often similar in azimuth to ENAM anisotropy (up to $\pm 90^\circ$ rotated from spreading) for models S12-ESR, M16-AREPS, and M16-GPC. A $\sim 180^\circ$ reversal in plate direction from approximately north along the margin to south is accompanied by a drop (and shortly followed by an increase) in plate velocity in all models except M19-T. This abrupt change in plate direction occurs at ages ranging from 170–190 Ma, depending on the model. Although its origin is not well understood, it roughly correlates in time with far-field plate reorganization processes such as opening of the Gulf of Mexico as well as the subduction polarity reversal from west-dipping to east-dipping across the Wrangellia Superterrane prior to its collision with western North America (*Shephard et al.*, 2013). As there is a 180° ambiguity in the interpretation of flow direction associated with seismic anisotropy observations, both orientations of margin-parallel plate motion are consistent with our observations.

At around the time of BSMA formation (~ 170 Ma), the spreading rate increased and plate velocities rotated closer to the FSD, on average (Figure 4.16). Therefore, fabric east of

the BSMA likely represents LPO influenced both by spreading and APM related shearing. This is consistent with the \sim 25–45° clockwise rotation in anisotropy east of the BSMA suggested by our 2-D inversions (Figure 4.9). Although the data do not strictly require

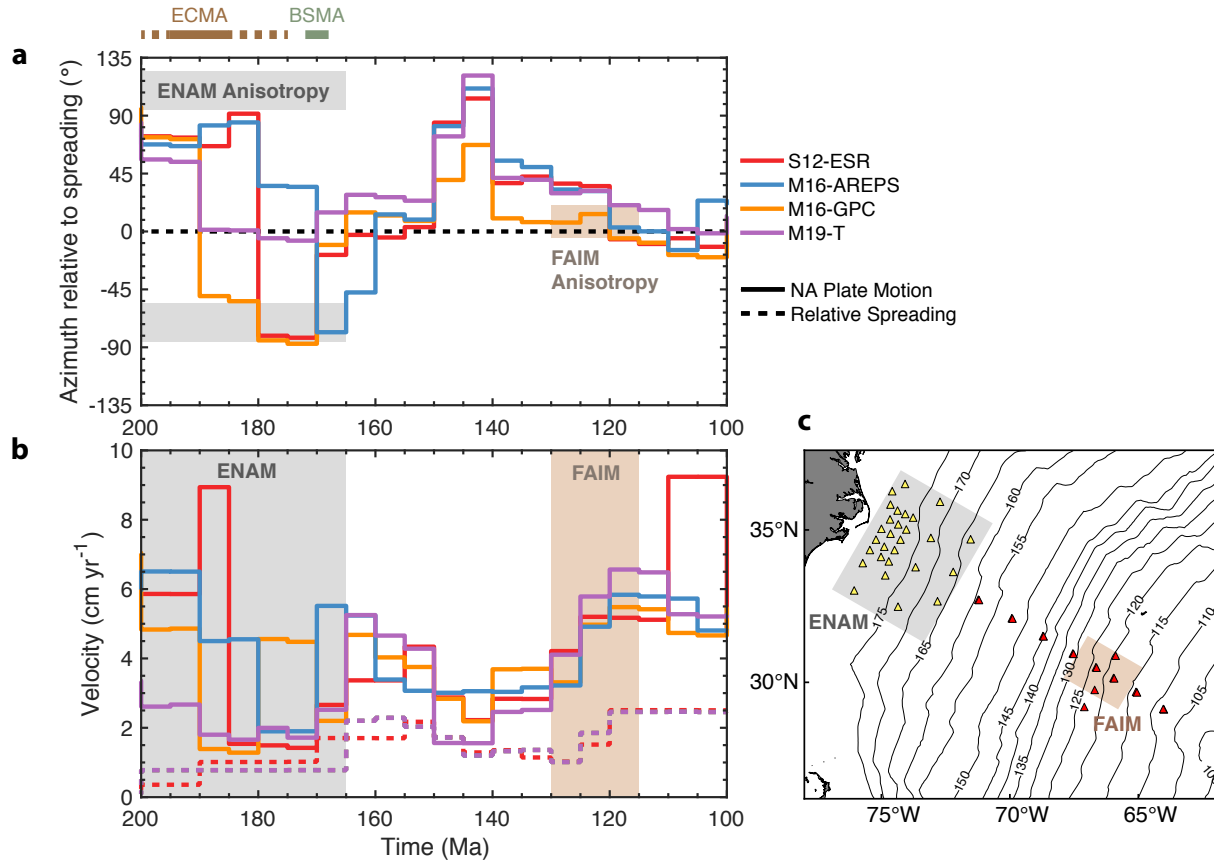


Figure 4.16: Comparison of anisotropy observations to paleo plate motions from 100–200 Ma from plate reconstruction models. Solid lines indicate absolute plate motion of North American (NA), while dashed lines indicate relative spreading motion of NA with respect to Africa. (a) Azimuth of NA plate motion relative to the spreading direction. Line colors correspond to four different plate reconstruction models (S12-ESR (*Seton et al.*, 2012); M16-AREPS (*Müller et al.*, 2016); M16-GPC (*Matthews et al.*, 2016); M19-T (*Müller et al.*, 2019)). Grey and tan regions mark the anisotropy fast azimuths at ENAM from this study and the Far-offset Active-source Imaging of the Mantle (FAIM) experiment (*Gaherty et al.*, 2004), respectively. Approximate timing of the ECMA and BSMA emplacements are indicated along the top. (b) NA plate speed (solid) and half-spreading rate of NA with respect to Africa (dashed; M16-GPC, M16-AREPS, and M19-T overlap one another). Grey and tan regions indicate the approximate range of seafloor ages at ENAM and FAIM, respectively. (c) Map of ENAM (yellow) and FAIM (red) OBS with shading that indicates approximate seafloor locations of anisotropy observations. Seafloor age contours from *Müller et al.* (2008) are shown in black in increments of 5 Myr.

this rotation of anisotropy east of the BSMA (Figure 4.12), it cannot be ruled out. That the fast azimuths east of the BSMA and within the ENAM-CSE footprint (165–170 Ma) are not FSD-parallel supports the hypothesis that the fabric is still modified by absolute plate motion even when spreading rates are on the order of APM velocities. East of the ENAM-CSE at the younger FAIM experiment (115–130 Ma), APM velocities were fast (2.5–6.5 cm/yr) relative to spreading (1–2.5 cm/yr half-rate) and approximately parallel to the FSD, in agreement with the observed FSD-parallel anisotropy from *Gaherty et al.* (2004).

An alternative explanation for margin-parallel anisotropy could be that the thin continental lid west of the BSMA consists of an accreted terrain that contains a strong relic margin-parallel LPO, similar to that inferred from shear-wave splitting studies of the eastern U.S., with splitting that largely parallels the structural grain of the Appalachians (e.g. *Barruol et al.*, 1997a,b, *Long et al.*, 2016, *Wagner et al.*, 2012). However, predominantly null shear-wave splitting observed in North Carolina directly onshore the ENAM-CSE can be interpreted as negligible (or vertical) lithospheric LPO. Furthermore, Rayleigh-wave anisotropy of the onshore region shows weak and laterally variable anisotropy in the lithosphere (*Wagner et al.*, 2018), in contrast to the regionally consistent anisotropy we observe. Olivine LPO formed during collisional orogenic processes would likely be disrupted and altered by later extensional deformation during rifting (*Barruol et al.*, 1997a), and therefore, it is unlikely that such a strong, regionally coherent LPO would remain intact at the ENAM-CSE. Finally, our inversion tests evaluating 2-D variations in anisotropy suggest a continuity in structure across the BSMA with at most a subtle rotation, arguing against a continental-lithosphere origin.

Another alternative is a shape-preferred orientation of frozen vertical melt channels in the continental lid, associated with vertical migration of melts during formation of the proto-oceanic crust (*Bécel et al.*, 2020). This idea is similar to the aligned melt-filled cracks, which have been invoked at active rifts which display rift-parallel anisotropy (e.g. *Kendall et al.*, 2005). While we cannot rule out this possibility, it is unlikely to explain all of the anisotropic

signal that we observe, especially given that the estimated thickness of the lid is only \sim 15 km, and the modest contrast between the lithified mafic channels and the surrounding ultramafic mantle would produce relatively weak anisotropy (e.g. *Gee and Jordan, 1988*).

We favor the interpretation that the lithospheric olivine LPO retains a record of strong margin-parallel APM during early ultra-slow spreading of the Atlantic. This explanation satisfies anisotropy observations at both the ENAM-CSE and FAIM experiments separated in age by \sim 50 Myr. It may also explain why we do not observe a significant rotation in anisotropy to FSD-parallel immediately east of the BSMA. It is also likely to produce anisotropy down to at least 60 km depth, which corresponds to the full depth sensitivity of the 17–32 s observations. We cannot rule out additional contributions to anisotropy from the thin continental lid between the ECMA and BSMA produced either by a relic LPO or oriented frozen melt channels, but that alone is unlikely to account for the complete anisotropic signal that we observe across the region. In conclusion, LPO fabric frozen into the lithosphere at slow spreading environments, such as in the Atlantic, is likely to retain a complex deformation signal that records the relative balance between absolute plate motion and seafloor spreading.

4.5 Conclusion

Our shear velocity model of the crust and uppermost mantle lithosphere together with observations of Rayleigh-wave anisotropy offshore the Eastern U.S. provide new constraints on the late stages of rifting and onset of seafloor spreading at the ENAM. The shear velocity model contains a proto-oceanic domain defined by oceanic crust overlying a \sim 15 km thick slow (4.4–4.55 km/s) lithospheric lid interpreted as continental mantle and/or trapped gabbroic melts extending from the margin \sim 200 km east to the BSMA. East of the BSMA, shallow mantle velocities are fast (>4.6 km/s) and indicative of more typical oceanic lithosphere, suggesting that the BSMA could mark the final breakup of the ENAM from West Africa and onset of normal seafloor spreading at \sim 170 Ma, as previously suggested (*Bécel*

et al., 2020, *Shuck et al.*, 2019). Alternatively, the region west of the BSMA may simply represent typical ultra-slow seafloor spreading with slow mantle velocities produced by frozen gabbroic melts due to less efficient melt extraction at the conductively cooling MOR.

Rayleigh-wave anisotropy is reported in the lithosphere with a fast direction parallel to the margin, correlating approximately with the APM direction at the time rather than the direction of ultra-slow spreading (2 cm/yr half-rate). Nearly 800 km southeast of ENAM at ~50 Myr younger seafloor, the FAIM experiment showed FSD-parallel anisotropy that also correlates with the fossil-APM direction (*Gaherty et al.*, 2004). We propose that lithosphere LPO formed at slow-spreading MORs, such as the Atlantic, primarily records mantle shear imparted by absolute plate motion rather than by classic corner flow.

Acknowledgements

We thank Brandon Shuck for sharing their published refraction models of the ENAM crustal velocities and Anne Bécel for insightful discussions. All broadband waveform data was accessed through the IRIS Data Management Center (www.iris.edu) under network code YO.

Concluding Remarks

This thesis represents a diverse set of observations that improve our understanding of seafloor spreading, present-day mantle dynamics, and ocean basin evolution. The NoMelt (~ 70 Ma) and YoungORCA (~ 43 Ma) OBS experiments located in the central and south Pacific, respectively, provide a detailed picture of “typical” oceanic lithosphere and asthenosphere and offer unprecedented insights into age dependence of oceanic upper mantle structure. Located just offshore the Eastern U.S., the ENAM-CSE reflects structure associated with the breakup of Pangea and onset of normal seafloor spreading, better constraining the early stages of ocean basin formation. Relatively few observations exist of lithospheric anisotropy from ultra-slow spreading environments such as the northwest Atlantic, and therefore this work informs our understanding of the spreading-rate dependence of LPO fabric.

At NoMelt, strong azimuthal anisotropy is observed in the lithosphere that correlates with corner-flow induced shear during seafloor spreading. We observe perhaps the first clear Love-wave azimuthal anisotropy that, in addition to co-located Rayleigh-wave and active source P_n constraints, provides a novel *in situ* estimate of the complete elastic tensor of the oceanic lithosphere. Comparing this observed anisotropy to a database of laboratory and naturally deformed olivine samples from the literature leads us to infer an alternative D-type LPO that has been associated with grain-size sensitive deformation, rather than the commonly assumed A-type LPO. This inferred grain-size sensitivity has implications for our understanding of grain-scale deformation mechanisms active at mid-ocean ridges and subsequent thermo-rheological evolution of the lithosphere.

At both NoMelt and YoungORCA we observe radial anisotropy in the lithosphere with $V_{SH} > V_{SV}$ indicating subhorizontal fabric, in contrast to some recent global models. We also observe azimuthal anisotropy in the lithosphere that parallels the fossil-spreading direction.

Estimates of radial anisotropy in the crust at both locations are the first of their kind and suggest horizontal layering and/or shearing associated with the crustal accretion process, consistent with previous reflection imaging.

Both NoMelt and YoungORCA show asthenospheric anisotropy that is significantly rotated from present-day APM as well as rotated from one another, deviating from the typical expectation of plate-induced shearing. This observation is consistent with small-scale density- or pressure-driven convection beneath the Pacific basin that varies in orientation over a length scale of at most \sim 2000 km and likely shorter.

By directly comparing shear velocities at YoungORCA and NoMelt, we show that the HSC model can account for most (\sim 75%) of the sublithospheric velocity difference between the two locations when anelastic effects are accounted for. The additional unaccounted for velocity reduction at YoungORCA is consistent with lithospheric reheating and potentially a small amount of melt (<0.5%), perhaps related to upwelling of hot mantle from small-scale convection and/or its proximity to the Marquesas hotspot.

While lithospheric anisotropy is parallel to the fossil-seafloor-spreading direction at both fast-spreading Pacific locations, it is perpendicular to spreading at the ENAM-CSE in the ultra-slow-spreading northwest Atlantic, which recorded fabric formed during the breakup of Pangea. Instead, anisotropy correlates with paleo APM at the time of rifting. We propose that slow-spreading environments, such as at ENAM during continental rifting, record APM-modified fabric in the lithosphere rather than typical seafloor spreading fabric.

Finally, our model of shear velocities in the lithosphere at the ENAM-CSE may indicate that normal seafloor spreading did not initiate until \sim 170 Ma, 10–25 Myr after the initiation of continental rifting, revising previous estimates. In addition, the lithospheric structure sheds new light on melt extraction processes at ultra-slow spreading environments.

Bibliography

- Abramson, E. H., J. M. Brown, L. J. Slutsky, and J. Zaug (1997), The elastic constants of San Carlos olivine to 17 GPa, *Journal of Geophysical Research*, 102(B6), 12,253–12,263, doi:10.1029/97jb00682.
- Adam, C., and A. Bonneville (2005), Extent of the South Pacific Superswell, *Journal of Geophysical Research: Solid Earth*, 110(9), 1–14, doi:10.1029/2004JB003465.
- Aki, K. (1957), Space and time spectra of stationary stochastic waves, with special reference to microtremors, doi:<http://hdl.handle.net/2261/11892>.
- Anderson, D. L. (1961), Elastic Wave Propagation in Layered Anisotropic Media, *Journal of Geophysical Research*, 66(9), 2953–2963.
- Anderson, D. L., and A. M. Dziewonski (1982), Upper mantle anisotropy: evidence from free oscillations, *Geophysical Journal of the Royal Astronomical Society*, 69, 383–404.
- Argus, D. F., and R. G. Gordon (1991), No-net-rotation of Current Plate Velocities Incorporating Plate Motion Model NUVEL-1, *Geophysical Research Letters*, 18(11), 2039–2042.
- Austin, N. J., and B. Evans (2007), Paleowattmeters: A scaling relation for dynamically recrystallized grain size, *Geology*, 35(4), 343–346, doi:10.1130/G23244A.1.
- Backus, G. E. (1962), Long-Wave Elastic Anisotropy Produced by Horizontal Layering, *Journal of Geophysical Research*, 67(11), 4427–4440.
- Barruol, G., P. G. Silver, and A. Vauchez (1997a), Seismic anisotropy in the eastern United States: Deep structure of a complex continental plate, *Journal of Geophysical Research*, 102, 8329–8348.
- Barruol, G., G. Helffrich, and A. Vauchez (1997b), Shear wave splitting around the northern Atlantic: Frozen Pangaea lithospheric anisotropy?, *Tectonophysics*, 279(1-4), 135–148, doi:10.1016/S0040-1951(97)00126-1.

Bécel, A., D. J. Shillington, M. R. Nedimovi, S. C. Webb, and H. Kuehn (2015), Origin of dipping structures in fast-spreading oceanic lower crust offshore Alaska imaged by multichannel seismic data, *Earth and Planetary Science Letters*, 424, 26–37, doi:10.1016/j.epsl.2015.05.016.

Bécel, A., J. K. Davis, B. D. Shuck, H. J. A. Van Avendonk, and J. C. Gibson (2020), Evidence for a Prolonged Continental Breakup resulting from Slow Extension Rates at the Eastern North American Volcanic Rifted Margin, *Journal of Geophysical Research: Solid Earth*, 125, 1–27, doi:10.1029/2020JB020093.

Becker, T. W., C. P. Conrad, A. J. Schaeffer, and S. Lebedev (2014), Origin of azimuthal seismic anisotropy in oceanic plates and mantle, *Earth and Planetary Science Letters*, 401, 236–250, doi:10.1016/j.epsl.2014.06.014.

Beghein, C., K. Yuan, N. Schmerr, and Z. Xing (2014), Changes in Seismic Anisotropy Shed Light on the Nature of the Gutenberg Discontinuity, *Science*, 343, 1237–1240.

Ben-Ismail, W., and D. Mainprice (1998), An olivine fabric database: An overview of upper mantle fabrics and seismic anisotropy, *Tectonophysics*, 296(1-2), 145–157, doi:10.1016/S0040-1951(98)00141-3.

Ben-Ismail, W., G. Barruol, and D. Mainprice (2001), The Kaapvaal craton seismic anisotropy: Petrophysical analyses of upper mantle kimberlite nodules, *Geophysical Research Letters*, 28(13), 2497–2500.

Bensen, G. D., M. H. Ritzwoller, M. P. Barmin, A. L. Levshin, F. Lin, M. P. Moschetti, N. M. Shapiro, and Y. Yang (2007), Processing seismic ambient noise data to obtain reliable broad-band surface wave dispersion measurements, *Geophysical Journal International*, 169(3), 1239–1260, doi:10.1111/j.1365-246X.2007.03374.x.

Benson, R. N. (2003), Age Estimates of the Seaward-Dipping Volcanic Wedge, Earliest Oceanic Crust, and Earliest Drift-Stage Sediments Along the North American Atlantic Continental Margin, in *The Central Atlantic Magmatic Province: Insights from Fragments of Pangea*, vol. 136, pp. 61–75, American Geophysical Union (AGU), doi:10.1029/136GM04.

Blackman, D. K., and J. Kendall (2002a), Seismic anisotropy in the upper mantle 2. Predictions for current plate boundary flow models, *Geochemistry, Geophysics, Geosystems*, 3, 1–26, doi:10.1029/2001GC000247.

Blackman, D. K., and J. M. Kendall (2002b), Seismic anisotropy of the upper mantle 1. Factors that affect mineral texture and effective elastic properties, *Geochemistry, Geophysics, Geosystems*, 3(9), 1–24, doi:10.1029/2001GC000248.

Blackman, D. K., J. Kendall, R. D. Paul, H. Wenk, D. Boyce, and J. P. Morgan (1996), Teleseismic imaging of subaxial flow at mid-ocean ridges : traveltimes effects of anisotropic mineral texture in the mantle, *Geophysical Journal International*, 127, 415–426.

Blackman, D. K., D. E. Boyce, O. Castelnau, P. R. Dawson, and G. Laske (2017), Effects of crystal preferred orientation on upper-mantle flow near plate boundaries: Rheologic feedbacks and seismic anisotropy, *Geophysical Journal International*, 210, 1481–1493, doi:10.1093/gji/ggx251.

Boudier, F., A. Nicolas, and B. Ildefonse (1996), Magma chambers in the Oman ophiolite: fed from the top and the bottom, *Earth and Planetary Science Letters*, 144(96), 239–250.

Bowden, D. C., M. D. Kohler, V. C. Tsai, and D. S. Weeraratne (2016), Offshore Southern California lithospheric velocity structure from noise cross-correlation functions, *Journal of Geophysical Research: Solid Earth*, 121, 1–13, doi:10.1002/2016JB012919.Received.

Boyden, J. A., D. R. Müller, M. Gurnis, T. H. Torsvik, J. A. Clark, M. Turner, H. Ivey-Law, R. J. Watson, and J. S. Cannon (2011), Next-generation plate-tectonic reconstructions using, in *Geoinformatics: Cyberinfrastructure for the Solid Earth Sciences*, pp. 95–114, Cambridge University Press, Cambridge, doi:10.1017/CBO9780511976308.008.

Braun, M. G. (2004), Petrologic and microstructural constraints on focused melt transport in dunites and the rheology of the shallow mantle, Ph.D. thesis, Massachusetts Institute of Technology.

Brocher, T. M. (2005), Empirical Relations between Elastic Wavespeeds and Density in the Earth's Crust, *Bulletin of the Seismological Society of America*, 95(6), 2081–2092, doi:10.1785/0120050077.

Burgos, G., J. P. Montagner, E. Beucler, Y. Capdeville, A. Mocquet, and M. Drilleau (2014), Oceanic lithosphere-asthenosphere boundary from surface wave dispersion data, *Journal of Geophysical Research: Solid Earth*, 119(2), 1079–1093, doi:10.1002/2013JB010528.

Bystricky, M., K. Kunze, L. Burlini, and J. P. Burg (2000), High shear strain of olivine aggregates: Rheological and seismic consequences, *Science*, 290(5496), 1564–1567, doi:10.1126/science.290.5496.1564.

Callegaro, S., A. Marzoli, H. Bertrand, M. Chiaradia, L. Reisberg, C. Meyzen, G. Bellieni, R. E. Weems, and R. Merle (2013), Upper and lower crust recycling in the source of CAMP basaltic dykes from southeastern North America, *Earth and Planetary Science Letters*, 376, 186–199, doi:10.1016/j.epsl.2013.06.023.

- Carter, N. L., and H. G. Ave'Lallmant (1970), High Temperature Flow of Dunite and Peridotite, *Geological Society of America Bulletin*, 81(9), 2181–2202, doi:10.1017/CBO9781107415324.004.
- Connolly, J. A. (2009), The geodynamic equation of state: What and how, *Geochemistry, Geophysics, Geosystems*, 10(10), doi:10.1029/2009GC002540.
- Cox, H. (1973), Spatial correlation in arbitrary noise fields with application to ambient sea noise, *The Journal of the Acoustical Society of America*, 54, 1289–1301, doi:10.1121/1.1914426.
- Crampin, S. (1977), A review of the effects of anisotropic layering, *Geophysical Journal of the Royal Astronomical Society*, 49, 9–27.
- Crampin, S. (1981), *A review of wave motion in anisotropic and cracked elastic-media*, vol. 3, 343–391 pp., North-Holland Publishing Company.
- Crawford, W. C., and S. C. Webb (2000), Identifying and Removing Tilt Noise from Low Frequency (<0.1 Hz) Seafloor Vertical Seismic Data, *Bulletin of the Seismological Society of America*, 90(4), 952–963, doi:10.1785/0119990121.
- Davis, J. K., A. Bécel, and W. R. Buck (2018), Estimating emplacement rates for seaward-dipping reflectors associated with the U.S. East Coast Magnetic Anomaly, *Geophysical Journal International*, 215(3), 1594–1603, doi:10.1093/gji/ggy360.
- Davison, A., D. Hinkley, and E. Schechtman (1986), Efficient Bootstrap Simulation, *Biometrika*, 73(3), 555–566.
- Debayle, E., and Y. Ricard (2013), Seismic observations of large-scale deformation at the bottom of fast-moving plates, *Earth and Planetary Science Letters*, 376, 165–177, doi:10.1016/j.epsl.2013.06.025.
- Delorey, A. A., R. A. Dunn, and J. B. Gaherty (2007), Surface wave tomography of the upper mantle beneath the Reykjanes Ridge with implications for ridge – hot spot interaction, *Journal of Geophysical Research*, 112, 1–16, doi:10.1029/2006JB004785.
- Dick, H., and J. Natland (1996), Late-Stage Melt Evolution and Transport in the Shallow Mantle beneath the East Pacific Rise, *Proceedings of the Ocean Drilling Program, Scientific Results*, 147, 103–134, doi:10.2973/odp.proc.sr.147.007.1996.

Doran, A. K., and G. Laske (2017), Ocean-Bottom Seismometer Instrument Orientations via Automated Rayleigh-Wave Arrival-Angle Measurements, *Bulletin of the Seismological Society of America*, 107(2), 691–708, doi:10.1785/0120160165.

Dziewonski, A. M., and D. L. Anderson (1981), Preliminary reference Earth model * Adam M., *Physics of the Earth and Planetary Interiors*, 25, 297–356.

Eddy, C. L., G. Ekström, M. Nettles, and J. B. Gaherty (2019), Age dependence and anisotropy of surface-wave phase velocities in the Pacific, *Geophysical Journal International*, 216, 640–658, doi:10.1093/gji/ggy438.

Ekström, G., and A. M. Dziewonski (1998), The unique anisotropy of the Pacific upper mantle, *Nature*, 394(6689), 168–172, doi:10.1038/28148.

Ekström, G., G. A. Abers, and S. C. Webb (2009), Determination of surface-wave phase velocities across USArray from noise and Aki's spectral formulation, *Geophysical Research Letters*, 36(18), 5–9, doi:10.1029/2009GL039131.

Faul, U., and I. Jackson (2015), Transient creep and strain energy dissipation: An experimental perspective, *Annual Review of Earth and Planetary Sciences*, 43, 541–569, doi:10.1146/annurev-earth-060313-054732.

Faul, U. H., and I. Jackson (2005), The seismological signature of temperature and grain size variations in the upper mantle, *Earth and Planetary Science Letters*, 234, 119–134, doi:10.1029/2001jb001225.

Faul, U. H., J. D. Fitz Gerald, and I. Jackson (2004), Shear wave attenuation and dispersion in melt-bearing olivine polycrystals: 2. Microstructural interpretation and seismological implications, *Journal of Geophysical Research: Solid Earth*, 109(6), 1–20, doi:10.1029/2003JB002407.

Forsyth, D. W. (1975), The Early Structural Evolution and Anisotropy of the Oceanic Upper Mantle, *Geophysical Journal of the Royal Astronomical Society*, 43(1), 103–162.

Forsyth, D. W., S. C. Webb, L. Dorman, and Y. Shen (1998), Phase velocities of Rayleigh waves across the MELT Experiment on the East Pacific Rise, *Science*, 280(5367), 1235–1238, doi:10.1016/0040-1951(70)90113-7.

French, S. W., and B. A. Romanowicz (2014), Whole-mantle radially anisotropic shear velocity structure from spectral-element waveformtomography, *Geophysical Journal International*, 199, 1303–1327, doi:10.1093/gji/ggu334.

Gaherty, J. B. (2001), Seismic Evidence for Hotspot-Induced Buoyant Flow Beneath the Reykjanes Ridge, *Science*, 293(August), 1645–1647.

Gaherty, J. B., T. H. Jordan, and L. S. Gee (1996), Seismic structure of the upper mantle in a central Pacific corridor, *Journal of Geophysical Research*, 101, 22,291–22,309.

Gaherty, J. B., M. Kato, and T. H. Jordan (1999), Seismological structure of the upper mantle: a regional comparison of seismic layering, *Physics of the Earth and Planetary Interiors*, 110, 21–41.

Gaherty, J. B., D. Lizarralde, J. A. Collins, G. Hirth, and S. Kim (2004), Mantle deformation during slow seafloor spreading constrained by observations of seismic anisotropy in the western Atlantic, *Earth and Planetary Science Letters*, 228, 255–265, doi:10.1016/j.epsl.2004.10.026.

Gee, L. S., and T. H. Jordan (1988), Polarization Anisotropy and Fine-Scale Structure of the Eurasian Upper Mantle, *Geophysical Research Letters*, 15(8), 824–827.

Greene, J. A., M. Tominaga, N. C. Miller, D. R. Hutchinson, and M. R. Karl (2017), Refining the Formation and Early Evolution of the Eastern North American Margin: New Insights From Multiscale Magnetic Anomaly Analyses, *Journal of Geophysical Research: Solid Earth*, 122(11), 8724–8748, doi: 10.1002/2017JB014308.

Hable, S., K. Sigloch, G. Barruol, S. C. Stähler, and C. Hadzioannou (2018), Clock errors in land and ocean bottom seismograms: High-accuracy estimates from multiple-component noise cross-correlations, *Geophysical Journal International*, 214, 2014–2034, doi:10.1093/GJI/GGY236.

Hacker, B. R. (2008), H₂O subduction beyond arcs, *Geochemistry, Geophysics, Geosystems*, 9(3), doi: 10.1029/2007GC001707.

Hansen, L. N., and J. M. Warren (2015), Quantifying the effect of pyroxene on deformation of peridotite in a natural shear zone, *Journal of Geophysical Research: Solid Earth*, 120, 2717–2738, doi:10.1002/2014JB011584.Received.

Hansen, L. N., M. E. Zimmerman, and D. L. Kohlstedt (2011), Grain boundary sliding in San Carlos olivine: Flow law parameters and crystallographic-preferred orientation, *Journal of Geophysical Research: Solid Earth*, 116(8), 1–16, doi:10.1029/2011JB008220.

Hansen, L. N., Y. H. Zhao, M. E. Zimmerman, and D. L. Kohlstedt (2014), Protracted fabric evolution in olivine: Implications for the relationship among strain, crystallographic fabric, and seismic anisotropy, *Earth and Planetary Science Letters*, 387, 157–168, doi:10.1016/j.epsl.2013.11.009.

Hansen, L. N., J. M. Warren, M. E. Zimmerman, and D. L. Kohlstedt (2016), Viscous anisotropy of textured olivine aggregates, Part 1: Measurement of the magnitude and evolution of anisotropy, *Earth and Planetary Science Letters*, 445, 92–103, doi:10.1016/j.epsl.2016.04.008.

Havlin, C., B. Holtzman, and E. Hopper (2020), Inference of thermodynamic state in the asthenosphere from anelastic properties, with applications to North American upper mantle, *EarthArXiv*, doi:10.31223/X5C59Z.

Haxby, W. F., and J. K. Weissel (1986), Evidence for Small-Scale Mantle Convection From Seasat Altimeter Data, *Journal of Geophysical Research*, 91(B3), 3507–3520.

Henstock, T. J., A. W. Woods, and R. S. White (1993), The accretion of oceanic crust by episodic sill intrusion, *Journal of Geophysical Research*, 98(B3), 4143–4161, doi:10.1029/92JB02661.

Herrmann, R. B. (2013), Computer programs in seismology: An evolving tool for instruction and research, *Seismological Research Letters*, 84(6), 1081–1088, doi:10.1785/0220110096.

Hess, H. (1964), Seismic Anisotropy of the Uppermost Mantle under Oceans, *Nature*, 203, 629–631.

Hiraga, T., C. Tachibana, N. Ohashi, and S. Sano (2010), Grain growth systematics for forsterite ± enstatite aggregates: Effect of lithology on grain size in the upper mantle, *Earth and Planetary Science Letters*, 291, 10–20, doi:10.1016/j.epsl.2009.12.026.

Hirth, G., and D. L. Kohlstedt (1996), Water in the oceanic upper mantle: Implications for rheology, melt extraction and the evolution of the lithosphere, *Earth and Planetary Science Letters*, 144, 93–108, doi:10.1016/0012-821x(96)00154-9.

Hirth, G., and D. L. Kohlstedt (2003), Rheology of the Upper Mantle and the Mantle Wedge: A View from the Experimentalists, in *Inside the Subduction Factory: Geophysical Monograph 138*, pp. 83–105.

Hirth, G., and D. L. Kohlstedt (2015), The stress dependence of olivine creep rate: Implications for extrapolation of lab data and interpretation of recrystallized grain size, *Earth and Planetary Science Letters*, 418, 20–26, doi:10.1016/j.epsl.2015.02.013.

Holbrook, W. S., and P. B. Kelemen (1993), Large igneous province on the US Atlantic margin and implications for magmatism during continental breakup, *Nature*, 364, 433–436, doi:10.1038/364433a0.

Holbrook, W. S., E. C. Reiter, G. M. Purdy, D. Sawyer, P. L. Stoffa, J. A. Austin, J. Oh, and J. Makris (1994), Deep structure of the US Atlantic continental margin, offshore South Carolina, from coincident

- ocean bottom and multichannel seismic data, *Journal of Geophysical Research*, 99(B5), 9155–9178, doi: 10.1029/93JB01821.
- Holtzman, B. K., and J. M. Kendall (2010), boundary lubrication, *Geochemistry Geophysics Geosystems*, 11, 1–29, doi:10.1029/2010GC003296.
- Holtzman, B. K., C. Havlin, E. Hopper, C. Bellis, J. B. Russell, H. C. P. Lau, and P.-y. P. Lin (2019), The Very Broadband Rheology Calculator: a tool for inference of thermodynamic state of the upper mantle from frequency-dependent mechanical behavior, in *AGU Fall Meeting Abstracts*, pp. S23G–0723.
- Hopper, E., J. B. Gaherty, D. J. Shillington, N. J. Accardo, A. A. Nyblade, B. K. Holtzman, C. Havlin, C. A. Scholz, P. R. Chindandali, R. W. Ferdinand, G. D. Mulibo, and G. Mbogoni (2020), Preferential localized thinning of lithospheric mantle in the melt-poor Malawi Rift, *Nature Geoscience*, 13(8), 584–589, doi:10.1038/s41561-020-0609-y.
- Huang, J., and S. Zhong (2005), Sublithospheric small-scale convection and its implications for the residual topography at old ocean basins and the plate model, *Journal of Geophysical Research: Solid Earth*, 110(5), 1–17, doi:10.1029/2004JB003153.
- Hudson, A. (1981), material containing cracks, *Geophysical Journal of the Royal Astronomical Society*, 64, 133–150.
- Huismans, R., and C. Beaumont (2011), Depth-dependent extension, two-stage breakup and cratonic underplating at rifted margins, *Nature*, 473, 74–78, doi:10.1038/nature09988.
- Hung, W. L., E. S. Lee, and S. C. Chuang (2011), Balanced bootstrap resampling method for neural model selection, *Computers and Mathematics with Applications*, 62(12), 4576–4581, doi:10.1016/j.camwa.2011.10.039.
- ichiro Karato, S. (2012), On the origin of the asthenosphere, *Earth and Planetary Science Letters*, 321–322, 95–103, doi:10.1016/j.epsl.2012.01.001.
- Jackson, I., and U. H. Faul (2010), Grainsize-sensitive viscoelastic relaxation in olivine: Towards a robust laboratory-based model for seismological application, *Physics of the Earth and Planetary Interiors*, 183, 151–163, doi:10.1016/j.pepi.2010.09.005.
- Janiszewski, H. A., J. B. Gaherty, G. A. Abers, H. Gao, and Z. C. Eilon (2019), Amphibious surface-wave phase-velocity measurements of the Cascadia subduction zone, *Geophysical Journal International*, 217(3), 1929–1948, doi:10.1093/gji/ggz051.

Jeffrey, Y., G. Æ. Mauricio, Y. J. Gu, and M. Sacchi (2009), Radon Transform Methods and Their Applications in Mapping Mantle Reflectivity Structure, *Surveys in Geophysics*, 30(4-5), 327–354, doi: 10.1007/s10712-009-9076-0.

Ji, J. (2006), CGG method for robust inversion and its application to velocity-stack inversion, *Geophysics*, 71(4), R59–R67, doi:10.1190/1.2209547.

Jin, G., and J. B. Gaherty (2015), Surface wave phase-velocity tomography based on multichannel cross-correlation, *Geophysical Journal International*, 201(3), 1383–1398, doi:10.1093/gji/ggv079.

Jung, H., and S.-i. Karato (2001), Water-Induced Fabric Transitions in Olivine, *Science*, 293, 1460–1464.

Jung, H., I. Katayama, Z. Jiang, T. Hiraga, and S.-i. Karato (2006), Effect of water and stress on the lattice-preferred orientation of olivine, *Tectonophysics*, 421, 1–22, doi:10.1016/j.tecto.2006.02.011.

Kaminski, and N. M. Ribe (2001), A kinematic model for recrystallization and texture development in olivine polycrystals, *Earth and Planetary Science Letters*, 189, 253–267, doi:10.1016/S0012-821X(01)00356-9.

Kaminski, E., and N. M. Ribe (2002), flow, *Geochemistry, Geophysics, Geosystems*, 3(8).

Karato, S.-i. (2008), Insights into the nature of plume-asthenosphere interaction from central Pacific geophysical anomalies, *Earth and Planetary Science Letters*, 274, 234–240, doi:10.1016/j.epsl.2008.07.033.

Karato, S. I., and J. Park (2019), On the origin of the upper mantle seismic discontinuities, in *Lithospheric Discontinuities, Geophysical Monograph*, edited by H. Yuan and B. Romanowicz, pp. 5–34, American Geophysical Union (AGU), doi:10.1002/9781119249740.ch1.

Karato, S.-i., and P. Wu (1993), Rheology of the upper mantle: a synthesis., doi:10.1126/science.260.5109.771.

Karato, S.-i., M. Toriumi, and T. Fujii (1980), Dynamic recrystallization of olivine single crystals during high-temperature creep, *Geophysical Research Letters*, 7(9), 649–652.

Karato, S.-i., H. Jung, I. Katayama, and P. Skemer (2008), Geodynamic Significance of Seismic Anisotropy of the Upper Mantle : New Insights from Laboratory Studies, *Annual Review Earth and Planetary Sciences*, 36, 59–95, doi:10.1146/annurev.earth.36.031207.124120.

Katayama, I., H. Jung, and S.-i. Karato (2004), New type of olivine fabric from deformation experiments at modest water content and low stress, *Geology*, 32(12), 1045–1048, doi:10.1130/G20805.1.

Katz, R. F., M. Spiegelman, and C. H. Langmuir (2003), A new parameterization of hydrous mantle melting, *Geochemistry, Geophysics, Geosystems*, 4(9), 1–19, doi:10.1029/2002GC000433.

Kawakatsu, H. (2016a), A new fifth parameter for transverse isotropy, *Geophysical Journal International*, 204(1), 682–685, doi:10.1093/gji/ggv479.

Kawakatsu, H. (2016b), A new fifth parameter for transverse isotropy II: Partial derivatives, *Geophysical Journal International*, 206(1), 360–367, doi:10.1093/gji/ggw152.

Kawakatsu, H. (2020), Unexpected Consequences of Transverse Isotropy, *Bulletin of the Seismological Society of America*, (2015), 1–10, doi:10.1785/0120200205.

Kawakatsu, H., and H. Utada (2017), Seismic and Electrical Signatures of the Lithosphere-Asthenosphere System of the Normal Oceanic Mantle, *Annual Review of Earth and Planetary Sciences*, 45, 139–167, doi:10.1146/annurev-earth-063016-020319.

Kawakatsu, H., J.-P. Montagner, and T.-R. A. Song (2015), On DLA's η , in *The Interdisciplinary Earth: A Volume in Honor of Don L. Anderson*, vol. 71, pp. 33–38, Geological Society of America Special Paper 514 and American Geophysical Union Special Publication, doi:10.1130/2015.2514(03).

Keen, C. E., and D. L. Barrett (1971), A Measurement of Seismic Anisotropy in the Northeast Pacific, *Canadian Journal of Earth Sciences*, 8(9), 1056–1064, doi:10.1139/e71-092.

Kelemen, P. B., and W. S. Holbrook (1995), Origin of thick, high-velocity igneous crust along the US east coast margin, *Journal of Geophysical Research*, 100(B6), doi:10.1029/95jb00924.

Kelemen, P. B., K. Koga, and N. Shimizu (1997), Geochemistry of gabbro sills in the crust-mantle transition zone of the Oman ophiolite: implications for the origin of the oceanic lower crust, *Earth and Planetary Science Letters*, 146, 475–488.

Kendall, J. M., G. W. Stuart, C. J. Ebinger, I. D. Bastow, and D. Keir (2005), Magma-assisted rifting in Ethiopia, *Nature*, 433, 146–148, doi:10.1038/nature03161.

Kennett, B. L., and T. Furumura (2013), High-frequency Po/So guided waves in the oceanic lithosphere: I-long-distance propagation, *Geophysical Journal International*, 195(3), 1862–1877, doi:10.1093/gji/ggt344.

Kennett, B. L., T. Furumura, and Y. Zhao (2014), High-frequency Po/So guided waves in the oceanic lithosphere: II-Heterogeneity and attenuation, *Geophysical Journal International*, 199, 614–630, doi:10.1093/gji/ggu286.

Klitgord, K. D., and H. Schouten (1986), *Plate kinematics of the North Atlantic*, vol. M, 351–378 pp., Geological Society of America, doi:10.1130/dnag-gna-m.379.

Klitgord, K. D., D. R. Hutchinson, and H. Schouten (1988), U.S. Atlantic continental margin; Structural and tectonic framework, in *The Atlantic Continental Margin*, vol. I-2, chap. 3, pp. 19–55, Geological Society of America.

Kodaira, S., G. Fujie, M. Yamashita, T. Sato, T. Takahashi, and N. Takahashi (2014), Seismological evidence of mantle flow driving plate motions at a palaeo-spreading centre, *Nature Geoscience*, 7(5), 371–375, doi: 10.1038/ngeo2121.

Korenaga, J., and P. B. Kelemen (1998), Melt migration through the oceanic lower crust: a constraint from melt percolation modeling with finite solid diffusion, *Earth and Planetary Science Letters*, 156, 1–11.

Korenaga, T., and J. Korenaga (2008), Subsidence of normal oceanic lithosphere, apparent thermal expansivity, and seafloor flattening, *Earth and Planetary Science Letters*, 268, 41–51, doi:10.1016/j.epsl.2007.12.022.

Kustowski, B., G. Ekstro, and A. M. Dziewonski (2008), Anisotropic shear-wave velocity structure of the Earth's mantle: A global model, *Journal of Geophysical Research*, 113, 1–23, doi:10.1029/2007JB005169.

Labails, C., J. L. Olivet, D. Aslanian, and W. R. Roest (2010), An alternative early opening scenario for the Central Atlantic Ocean, *Earth and Planetary Science Letters*, 297, 355–368, doi:10.1016/j.epsl.2010.06.024.

Laske, G., G. Masters, Z. Ma, and M. E. Pasyanos (2013), Update on CRUST1.0 : A 1-degree Global Model of Earth's Crust, in *The European Geophysical Union Meeting*.

Lin, F. C., and M. H. Ritzwoller (2010), Empirically determined finite frequency sensitivity kernels for surface waves, *Geophysical Journal International*, 182(2), 923–932, doi:10.1111/j.1365-246X.2010.04643.x.

Lin, P.-Y. P., J. B. Gaherty, G. Jin, J. A. Collins, D. Lizarralde, R. L. Evans, and G. Hirth (2016), High-resolution seismic constraints on flow dynamics in the oceanic asthenosphere, *Nature*, 535(7613), 1–9, doi:10.1038/nature18012.

Lizarralde, D., J. B. Gaherty, J. A. Collins, G. Hirth, and S. D. Kim (2004), Spreading-rate dependence of melt extraction at mid-ocean ridges from mantle seismic refraction data, *Nature*, 432, 744–747, doi: 10.1038/nature03140.

Lizarralde, D., J. B. Gaherty, J. A. Collins, G. Hirth, and R. L. Evans (2012), Structure of Pacific-plate upper mantle from active-source seismic measurements of the NoMelt experiment, in *The American Geophysical Union Fall Meeting*, pp. 2–3.

Long, M. D., and P. G. Silver (2009), Shear Wave Splitting and Mantle Anisotropy: Measurements, Interpretations, and New Directions, *Surveys in Geophysics*, 30, 407–461, doi:10.1007/s10712-009-9075-1.

Long, M. D., K. G. Jackson, and J. F. McNamara (2016), SKS splitting beneath Transportable Array stations in eastern North America and the signature of past lithospheric deformation, *Geochemistry, Geophysics, Geosystems*, 17, 2–15, doi:10.1002/2015GC006088.Received.

Luo, Y., J. Xia, R. D. Miller, Y. Xu, J. Liu, and Q. Liu (2008), Rayleigh-Wave Dispersive Energy Imaging Using a High-Resolution Linear Radon Transform, *Pure and Applied Geophysics*, 165(5), 903–922, doi: 10.1007/s00024-008-0338-4.

Luo, Y., Y. Yang, K. Zhao, Y. Xu, and J. Xia (2015), Unraveling overtone interferences in Love-wave phase velocity measurements by radon transform, *Geophysical Journal International*, 203(1), 327–333, doi:10.1093/gji/ggv300.

Lynner, C., and M. Bodmer (2017), Mantle flow along the eastern North American margin inferred from shear wave splitting, *Geology*, 45(10), 1–4, doi:10.1130/G38980.1.

Lynner, C., and R. W. Porritt (2017), Crustal structure across the eastern North American margin from ambient noise tomography, *Geophysical Research Letters*, 44, 6651–6657, doi:10.1002/2017GL074769.

Lynner, C., H. J. Van Avendonk, A. Bécel, G. L. Christeson, B. Dugan, J. B. Gaherty, S. Harder, M. J. Hornbach, D. Lizarralde, M. D. Long, M. B. Magnani, D. J. Shillington, K. Aderhold, Z. C. Eilon, and L. S. Wagner (2020), The eastern North American margin community seismic experiment: An amphibious active- And passive-source dataset, *Seismological Research Letters*, 91, 533–540, doi:10.1785/0220190142.

Ma, Z., C. A. Dalton, J. B. Russell, J. B. Gaherty, G. Hirth, and D. W. Forsyth (2020), Shear attenuation and anelastic mechanisms in the central Pacific upper mantle, *Earth and Planetary Science Letters*, 536, 116,148, doi:10.1016/j.epsl.2020.116148.

Mainprice, D. (2015), Seismic Anisotropy of the Deep Earth from a Mineral and Rock Physics Perspective, in *Treatise on Geophysics*, vol. 2, edited by G. Schubert and G. Price, 2 ed., pp. 487–538, Elsevier B.V., Oxford, doi:10.1016/B978-0-444-53802-4.00044-0.

Mark, H. F., D. Lizarralde, J. A. Collins, N. C. Miller, G. Hirth, J. B. Gaherty, and R. L. Evans (2019), Azimuthal Seismic Anisotropy of 70-Ma Pacific-Plate Upper Mantle, *Journal of Geophysical Research: Solid Earth*, *124*, 1889–1909, doi:10.1029/2018JB016451.

Marzoli, A., F. Jourdan, J. H. Puffer, T. Cuppone, L. H. Tanner, R. E. Weems, H. Bertrand, S. Cirilli, G. Bellieni, and A. De Min (2011), Timing and duration of the Central Atlantic magmatic province in the Newark and Culpeper basins, eastern U.S.A., *Lithos*, *122*, 175–188, doi:10.1016/j.lithos.2010.12.013.

Matthews, K. J., K. T. Maloney, S. Zahirovic, S. E. Williams, M. Seton, and R. D. Müller (2016), Global plate boundary evolution and kinematics since the late Paleozoic, *Global and Planetary Change*, *146*, 226–250, doi:10.1016/j.gloplacha.2016.10.002.

McCarthy, C., and Y. Takei (2011), Anelasticity and viscosity of partially molten rock analogue: Toward seismic detection of small quantities of melt, *Geophysical Research Letters*, *38*(18), 3–7, doi:10.1029/2011GL048776.

McCarthy, C., Y. Takei, and T. Hiraga (2011), Experimental study of attenuation and dispersion over a broad frequency range: 2. the universal scaling of polycrystalline materials, *Journal of Geophysical Research: Solid Earth*, *116*(9), 1–18, doi:10.1029/2011JB008384.

McHone, J. G. (2000), Non-plume magmatism and rifting during the opening of the central Atlantic Ocean, *Tectonophysics*, *316*(3-4), 287–296, doi:10.1016/S0040-1951(99)00260-7.

McHone, J. G. (2003), Volatile emissions from central atlantic magmatic province basalts: Mass assumptions and environmental consequences, in *The Central Atlantic Magmatic Province: Insights from Fragments of Pangea*, vol. 136, pp. 241–254, American Geophysical Union (AGU), doi:10.1029/136GM013.

McKenzie, D., J. Jackson, and K. Priestley (2005), Thermal structure of oceanic and continental lithosphere, *Earth and Planetary Science Letters*, *233*, 337–349, doi:10.1016/j.epsl.2005.02.005.

Mehl, L., B. Hacker, G. Hirth, and P. B. Kelemen (2003), Arc-parallel flow within the mantle wedge: Evidence from the accreted Talkeetna arc, south central Alaska, *Journal of Geophysical Research*, *108*(B8), doi:10.1029/2002jb002233.

Menke, W. (2012), *Geophysical Data Analysis: Discrete Inverse Theory*, 3 ed., Elsevier, doi:10.1016/B978-0-12-397160-9.00019-9.

Menke, W., and G. Jin (2015), Waveform Fitting of Cross Spectra to Determine Phase Velocity Using Aki's Formula, *Bulletin of the Seismological Society of America*, 105(3), 1619–1627, doi:10.1785/0120140245.

Michibayashi, K., T. Ina, and K. Kanagawa (2006), The effect of dynamic recrystallization on olivine fabric and seismic anisotropy: Insight from a ductile shear zone, Oman ophiolite, *Earth and Planetary Science Letters*, 244, 695–708, doi:10.1016/j.epsl.2006.02.019.

Michibayashi, K., D. Mainprice, A. Fujii, S. Uehara, Y. Shinkai, Y. Kondo, Y. Ohara, T. Ishii, P. Fryer, S. H. Bloomer, A. Ishiwatari, J. W. Hawkins, and S. Ji (2016), Natural olivine crystal-fabrics in the western Pacific convergence region : A new method to identify fabric type, *Earth and Planetary Science Letters*, 443, 70–80, doi:10.1016/j.epsl.2016.03.019.

Montagner, J. P. (2002), Upper mantle low anisotropy channels below the Pacific Plate, *Earth and Planetary Science Letters*, 202, 263–274.

Montagner, J. P., and D. L. Anderson (1989), Petrological constraints on seismic anisotropy, *Physics of the Earth and Planetary Interiors*, 54, 82–105.

Montagner, J. P., and H. C. Nataf (1986), A simple method for inverting the azimuthal anisotropy of surface waves, *Journal of Geophysical Research*, 91, 511–520.

Montagner, J. P., and T. Tanimoto (1990), Global Anisotropy in the Upper Mantle Inferred From the Regionalization of Phase Velocities, *Journal of Geophysical Research*, 95(B4), 4797–4819.

Montagner, J. P., and T. Tanimoto (1991), Global Upper Mantle Tomography of Seismic Velocities and Anisotropies, *JGR*, 96(9), 20,337–20,351.

Morgan, J. P. (1993), The Genesis of Oceanic Crust: Magma Injection, Hydrothermal Circulation, and Crustal Flow, *Journal of Geophysical Research*, 98(B4), 6283–6297.

Morgan, J. P., and Y. J. Chen (1993), The Genesis of Oceanic Crust: Magma Injection, Hydrothermal Circulation, and Crustal Flow, *Journal of Geophysical Research*, 98, 6283–6297.

Morris, G., R. W. Raitt, and G. G. Shor (1969), Velocity Anisotropy and Delay-Time Maps of the Mantle Near Hawaii, *Journal of Geophysical Research*, 74(17), 4300–4316, doi:10.1029/JB074i017p04300.

Moulik, P., and G. Ekström (2014), An anisotropic shear velocity model of the Earth's mantle using normal modes, body waves, surface waves and long-period waveforms, *Geophysical Journal International*, 199(3), 1713–1738, doi:10.1093/gji/ggu356.

Müller, R. D., M. Sdrolias, C. Gaina, and R. W. Roest (2008), Age, spreading rates, and spreading asymmetry of the world's ocean crust, *Geochemistry, Geophysics, Geosystems*, 9, 1–19, doi:10.1029/2007GC001743.

Müller, R. D., M. Seton, S. Zahirovic, S. E. Williams, K. J. Matthews, N. M. Wright, G. E. Shephard, K. T. Maloney, N. Barnett-Moore, M. Hosseinpour, D. J. Bower, and J. Cannon (2016), Ocean Basin Evolution and Global-Scale Plate Reorganization Events since Pangea Breakup, *Annual Review of Earth and Planetary Sciences*, 44, 107–138, doi:10.1146/annurev-earth-060115-012211.

Müller, R. D., S. Zahirovic, S. E. Williams, J. Cannon, M. Seton, D. J. Bower, M. G. Tetley, C. Heine, E. Le Breton, S. Liu, S. H. Russell, T. Yang, J. Leonard, and M. Gurnis (2019), A Global Plate Model Including Lithospheric Deformation Along Major Rifts and Orogenes Since the Triassic, *Tectonics*, 38(6), 1884–1907, doi:10.1029/2018TC005462.

Nettles, M., and A. M. Dziewoński (2008), Radially anisotropic shear velocity structure of the upper mantle globally and beneath North America, *Journal of Geophysical Research*, 113(B2), B02,303, doi:10.1029/2006JB004819.

Nicolas, A., and N. I. Christensen (1987), Formation of anisotropy in upper mantle peridotites - A review, in *Composition, Structure, and Dynamics of Lithosphere–Asthenosphere System*, vol. 16, edited by K. Fuchs and C. Froidevaux, pp. 111–123, AGU, Washington, DC.

Nishida, K., H. Kawakatsu, and K. Obara (2008), Three-dimensional crustal S wave velocity structure in Japan using microseismic data recorded by Hi-net tiltmeters, *Journal of Geophysical Research: Solid Earth*, 113(10), 1–22, doi:10.1029/2007JB005395.

Nishimura, C. E., and D. W. Forsyth (1989), The Anisotropic Structure of the Upper Mantle in the Pacific Ocean, *Geophysical Journal of the Royal Astronomical Society*, 96(2), 203–229.

Niu, Y., and R. Hékinian (1997), Basaltic liquids and harzburgitic residues in the Garrett Transform: A case study at fast-spreading ridges, *Earth and Planetary Science Letters*, 146, 243–258, doi:10.1016/s0012-821x(96)00218-x.

Olsen, P. E., D. V. Kent, M. Et-Touhami, and J. Puffer (2003), Cyclo-, magneto-, and bio-stratigraphic constraints on the duration of the CAMP event and its relationship to the triassic-jurassic boundary, in *The Central Atlantic Magmatic Province: Insights from Fragments of Pangea*, vol. 136, edited by W. Hames, J. McHone, P. Renne, and C. Ruppel, pp. 7–32, American Geophysical Union (AGU), doi:10.1029/136GM02.

Olugboji, T. M., S. Karato, and J. Park (2013), Structures of the oceanic lithosphere–asthenosphere boundary: Mineral-physics modeling and seismological signatures, *Geochemistry, Geophysics, Geosystems*, 14(4), 880–901, doi:10.1002/ggge.20086.

Panning, M., and B. Romanowicz (2006), A three-dimensional radially anisotropic model of shear velocity in the whole mantle, *Geophysical Journal International*, 167, 361–379, doi:10.1111/j.1365-246X.2006.03100.x.

Parker, R. L., and D. W. Oldenburg (1973), Thermal Model of Ocean Ridges, *Nature*, 242, 137–139.

Parsons, B., and D. McKenzie (1978), Mantle convection and the thermal structure of the plates, *Journal of Geophysical Research*, 83(B9), 4485, doi:10.1029/jb083ib09p04485.

Parsons, B., and J. G. Sclater (1977), An analysis of the variation of ocean floor bathymetry and heat flow with age, *Journal of Geophysical Research*, 82(5), 803–827.

Peselnick, L., and A. Nicolas (1978), Seismic Anisotropy in an Ophiolite Peridotite: Application to Oceanic Upper Mantle, *Journal of Geophysical Research*, 83(B3), 1227–1235.

Peterson, J. (1993), Observations and modeling of seismic background noise, *Tech. rep.*, U.S. Geol. Surv. Open File Report, Albuquerque, New Mexico.

Quick, J. E., and R. P. Denlinger (1993), Ductile deformation and the origin of layered gabbro in ophiolites, *Journal of Geophysical Research*, 98(B8), 14,015–14,027, doi:10.1029/93jb00698.

Raitt, R. W., G. G. Shor, T. J. G. Francis, and G. B. Morris (1969), Anisotropy of the Pacific Upper Mantle, *Journal of Geophysical Research*, 74(12), 3095–3109.

Reston, T. J., C. R. Ranero, and I. Belykh (1999), The structure of Cretaceous oceanic crust of the NW Pacific: Constraints on processes at fast spreading ridges, *Journal of Geophysical Research*, 104, 629–644.

Ribe, N. M. (1989), A continuum theory for lattice preferred orientation, *Geophysical Journal International*, 97, 199–207.

Richter, F. M., and B. Parsons (1975), On the Interaction of Two Scales of Convection in the Mantle, *Journal of Geophysical Research*, 80(17), 2529–2541.

Ruan, Y., D. W. Forsyth, and S. W. Bell (2014), Marine sediment shear velocity structure from the ratio of displacement to pressure of Rayleigh waves at seafloor, *Journal of Geophysical Research : Solid Earth*, 119, 1–15, doi:10.1002/2014JB011162.Received.

- Russell, J. B., J. B. Gaherty, P. Y. P. Lin, D. Lizarralde, J. A. Collins, G. Hirth, and R. L. Evans (2019a), High-Resolution Constraints on Pacific Upper Mantle Petrofabric Inferred From Surface-Wave Anisotropy, *Journal of Geophysical Research: Solid Earth*, 124, 631–657, doi:10.1029/2018JB016598.
- Russell, J. B., Z. Eilon, and S. Mosher (2019b), OBSrange: A New Tool for the Precise Remote Location of Ocean-Bottom Seismometers, *Seismological Research Letters*, 90(4), 1627–1641, doi:10.1785/0220180336.
- Rychert, C. a., and N. Harmon (2017), Constraints on the anisotropic contributions to velocity discontinuities at ~60 km depth beneath the Pacific, *Geochemistry, Geophysics, Geosystems*, 18(8), 1–17.
- Sahabi, M., D. Aslanian, and J. L. Olivet (2004), Un nouveau point de départ pour l'histoire de l'Atlantique central, *Comptes Rendus - Geoscience*, 336(12), 1041–1052, doi:10.1016/j.crte.2004.03.017.
- Sarafian, E., R. L. Evans, J. a. Collins, J. Elsenbeck, G. a. Gaetani, J. B. Gaherty, G. Hirth, and D. Lizarralde (2015), The electrical structure of the central Pacific upper mantle constrained by the NoMelt experiment, *G3*, 16, 1115–1132, doi:10.1002/2014GC005709. Received.
- Satsukawa, T., K. Michibayashi, U. Raye, E. Y. Anthony, J. Pulliam, and R. Stern (2010), Uppermost mantle anisotropy beneath the southern Laurentian margin: Evidence from Knippa peridotite xenoliths, Texas, *Geophysical Research Letters*, 37, L20,312, doi:10.1029/2010GL044538.
- Savage, M. K. (1999), Seismic Anisotropy and Mantle Deformation: What have we learned from shear wave splitting?, *Reviews of Geophysics*, 37(98), 65–106.
- Schaeffer, A. J., S. Lebedev, and T. W. Becker (2016), Azimuthal seismic anisotropy in the Earth's upper-mantle and the thickness of tectonic plates, *Geophysical Journal International*, 207(January), 901–933, doi:10.1093/gji/ggw309.
- Schmerr, N. (2012), The Gutenberg discontinuity: Melt at the lithosphere-asthenosphere boundary, *Science*, 335, 1480–1483, doi:10.1126/science.1215433.
- Schultz, R., and Y. Jeffrey Gu (2013), Flexible, inversion-based Matlab implementation of the Radon transform, *Computers & Geosciences*, 52, 437–442, doi:10.1016/j.cageo.2012.08.013.
- Servali, A., M. D. Long, J. Park, M. H. Benoit, and J. C. Aragon (2020), Love-to-Rayleigh scattering across the eastern North American passive margin, *Tectonophysics*, 776, 228,321, doi:10.1016/j.tecto.2020.228321.

Seton, M., R. D. Müller, S. Zahirovic, C. Gaina, T. Torsvik, G. Shephard, A. Talsma, M. Gurnis, M. Turner, S. Maus, and M. Chandler (2012), Earth-Science Reviews Global continental and ocean basin reconstructions since 200 Ma, *Earth Science Reviews*, 113, 212–270, doi:10.1016/j.earscirev.2012.03.002.

Shen, W., and M. H. Ritzwoller (2016), Crustal and uppermost mantle structure beneath the United States, *Journal of Geophysical Research: Solid Earth*, 121, 4306–4342, doi:10.1002/2015JB012608. Received.

Shephard, G. E., H. P. Bunge, B. S. Schuberth, R. D. Müller, A. S. Talsma, C. Moder, and T. C. Landgrebe (2012), Testing absolute plate reference frames and the implications for the generation of geodynamic mantle heterogeneity structure, *Earth and Planetary Science Letters*, 317–318, 204–217, doi:10.1016/j.epsl.2011.11.027.

Shephard, G. E., R. D. Müller, and M. Seton (2013), The tectonic evolution of the Arctic since Pangea breakup: Integrating constraints from surface geology and geophysics with mantle structure, *Earth-Science Reviews*, 124, 148–183, doi:10.1016/j.earscirev.2013.05.012.

Shinohara, M., T. Fukano, T. Kanazawa, E. Araki, K. Suyehiro, M. Mochizuki, K. Nakahigashi, T. Yamada, and K. Mochizuki (2008), Upper mantle and crustal seismic structure beneath the Northwestern Pacific Basin using a seafloor borehole broadband seismometer and ocean bottom seismometers, *Physics of the Earth and Planetary Interiors*, 170, 95–106, doi:10.1016/j.pepi.2008.07.039.

Shintaku, N., D. W. Forsyth, C. J. Hajewski, and D. S. Weeraratne (2014), Journal of Geophysical Research : Solid Earth, *Journal of Geophysical Research: Solid Earth*, 119, 3050–3063, doi:10.1002/2014JB011376. Received.

Shito, A., D. Suetsugu, T. Furumura, H. Sugioka, and A. Ito (2013), Small-scale heterogeneities in the oceanic lithosphere inferred from guided waves, *Geophysical Research Letters*, 40, 1708–1712, doi:10.1002/grl.50330.

Shito, A., D. Suetsugu, and T. Furumura (2015), Evolution of the oceanic lithosphere inferred from Po/So waves traveling in the Philippine Sea Plate, *Journal of Geophysical Research: Solid Earth*, 120, 5238–5248, doi:10.1002/2015JB012608. Received.

Shuck, B. D., and H. J. Van Avendonk (2016), Evolution of the Upper Lithosphere in the ENAM Area from 3-D Wide-Angle Seismic Data, in *American Geophysical Union, Fall Meeting 2016, abstract #T51G-2998*.

Shuck, B. D., H. J. Van Avendonk, and A. Bécel (2019), The role of mantle melts in the transition from rifting to seafloor spreading offshore eastern North America, *Earth and Planetary Science Letters*, 525(November), 115,756, doi:10.1016/j.epsl.2019.115756.

Sieminski, A., Q. Liu, J. Trampert, and J. Tromp (2007), Finite-frequency sensitivity of surface waves to anisotropy based upon adjoint methods, *Geophysical Journal International*, 168, 1153–1174, doi:10.1111/j.1365-246X.2006.03261.x.

Skemer, P., J. M. Warren, P. B. Kelemen, and G. Hirth (2010), Microstructural and rheological evolution of a mantle shear zone, *Journal of Petrology*, 51(1-2), 43–53, doi:10.1093/petrology/egp057.

Skemer, P., M. Sundberg, G. Hirth, and R. Cooper (2011), Torsion experiments on coarse-grained dunite: Implications for microstructural evolution when diffusion creep is suppressed, *Geological Society Special Publication*, 360(1), 211–223, doi:10.1144/SP360.12.

Skemer, P., J. M. Warren, and G. Hirth (2012), The influence of deformation history on the interpretation of seismic anisotropy, *Geochemistry, Geophysics, Geosystems*, 13(3), 1–10, doi:10.1029/2011GC003988.

Smith, D. B., M. H. Ritzwoller, and N. M. Shapiro (2004), Stratification of anisotropy in the Pacific upper mantle, *Journal of Geophysical Research*, 109(November), 1–22, doi:10.1029/2004JB003200.

Song, T. R. A., and Y. Kim (2012), Anisotropic uppermost mantle in young subducted slab underplating Central Mexico, *Nature Geoscience*, 5(1), 55–59, doi:10.1038/ngeo1342.

Stein, C. A., and S. Stein (1992), A model for the global variation in oceanic depth and heat flow with lithospheric age, *Nature*, 359, 123–129.

Stixrude, L., and C. Lithgow-Bertelloni (2011), Thermodynamics of mantle minerals - II. Phase equilibria, *Geophysical Journal International*, 184(3), 1180–1213, doi:10.1111/j.1365-246X.2010.04890.x.

Sundberg, M., and R. F. Cooper (2010), A composite viscoelastic model for incorporating grain boundary sliding and transient diffusion creep; Correlating creep and attenuation responses for materials with a fine grain size, *Philosophical Magazine*, 90(20), 2817–2840, doi:10.1080/14786431003746656.

Swift, S. A., D. Lizarralde, R. A. Stephen, and H. Hoskins (1998), Velocity structure in upper ocean crust at Hole 504B from vertical seismic profiles, *Journal of Geophysical Research*, 103, 15,361–15,376.

Takei, Y. (2017), Effects of Partial Melting on Seismic Velocity and Attenuation: A New Insight from Experiments, *Annual Review of Earth and Planetary Sciences*, 45, 447–470, doi:10.1146/annurev-earth-063016-015820.

Takeo, A., K. Nishida, T. Isse, H. Kawakatsu, H. Shiobara, and H. Sugioka (2013), Radially anisotropic structure beneath the Shikoku Basin from broadband surface wave analysis of ocean bottom seismometer records, *Journal of Geophysical Research : Solid Earth*, 118, 2878–2892, doi:10.1002/jgrb.50219.

Takeo, A., D. W. Forsyth, D. S. Weeraratne, and K. Nishida (2014), Estimation of azimuthal anisotropy in the NW Pacific from seismic ambient noise in seafloor records, *Geophysical Journal International*, 199, 11–22, doi:10.1093/gji/ggu240.

Takeo, A., H. Kawakatsu, T. Isse, K. Nishida, H. Sugioka, A. Ito, H. Shiobara, and D. Suetsugu (2016), Seismic azimuthal anisotropy in the oceanic lithosphere and asthenosphere from broadband surface wave analysis of OBS array records at 60 Ma seafloor, *Journal of Geophysical Research : Solid Earth*, 121, 1927–1947, doi:10.1002/2015JB012429. Received.

Takeo, A., H. Kawakatsu, T. Isse, K. Nishida, H. Shiobara, H. Sugioka, A. Ito, and H. Utada (2018), In Situ Characterization of the Lithosphere-Asthenosphere System beneath NW Pacific Ocean Via Broadband Dispersion Survey With Two OBS Arrays, *Geochemistry, Geophysics, Geosystems*, 19, doi: 10.1029/2018GC007588.

Takeuchi, H., and M. Saito (1972), *Seismic Surface Waves*, vol. 11, 217–295 pp., ACADEMIC PRESS, INC., doi:10.1016/B978-0-12-460811-5.50010-6.

Tan, Y., and D. V. Helmberger (2007), Trans-Pacific upper mantle shear velocity structure, *Journal of Geophysical Research: Solid Earth*, 112(8), 1–20, doi:10.1029/2006JB004853.

Thomsen, L. (1995), Elastic anisotropy due to aligned cracks in porous rock, *Geophysical Prospecting*, 43(January), 805–829.

Tian, Y., and M. H. Ritzwoller (2017), Improving ambient noise cross-correlations in the noisy ocean bottom environment of the Juan de Fuca plate, *Geophysical Journal International*, 210(3), 1787–1805, doi:10.1093/gji/ggx281.

Tommasi, A., D. Mainprice, G. Canova, and Y. Chastel (2000), Viscoplastic self-consistent and equilibrium-based modeling of olivine lattice preferred orientations: Implications for the upper mantle seismic anisotropy, *Journal of Geophysical Research*, 105, 7893–7908.

Toomey, D. R., D. Jousselin, R. A. Dunn, W. S. D. Wilcock, and R. S. Detrick (2007), Skew of mantle upwelling beneath the East Pacific Rise governs segmentation, *Nature*, *446*, 409–414, doi:10.1038/nature05679.

Torsvik, T. H., R. D. Müller, R. Van Der Voo, B. Steinberger, and C. Gaina (2008), Global plate motion frames: Toward a unified model, *Reviews of Geophysics*, *46*(3), doi:10.1029/2007RG000227.

Trampert, J., and H. J. V. Heijst (2002), Global Azimuthal Anisotropy in the Transition Zone, *Science*, *296*(May), 1297–1300.

Turcotte, D., and G. Schubert (2014), *Geodynamics*, third ed., 537–546 pp., Cambridge University Press.

Turner, A. J., R. F. Katz, and M. D. Behn (2015), Grain-size dynamics beneath mid-ocean ridges: Implications for permeability and melt extraction, *Geochemistry, Geophysics, Geosystems*, *16*, 925–946, doi:10.1002/2014GC005692. Received.

Turner, A. J., R. F. Katz, M. D. Behn, and T. Keller (2017), Magmatic Focusing to Mid-Ocean Ridges: The Role of Grain-Size Variability and Non-Newtonian Viscosity, *Geochemistry, Geophysics, Geosystems*, *18*(12), 4342–4355, doi:10.1002/2017GC007048.

Vanderbeek, B. P., and D. R. Toomey (2017), Shallow Mantle Anisotropy Beneath the Juan de Fuca Plate, *Geophysical Research Letters*, *44*, 382–389, doi:10.1002/2017GL074769.

VanTongeren, J. A., G. Hirth, and P. B. Kelemen (2015), Constraints on the accretion of the gabbroic lower oceanic crust from plagioclase lattice preferred orientation in the Samail ophiolite, *Earth and Planetary Science Letters*, *427*, 249–261, doi:10.1016/j.epsl.2015.07.001.

Visser, K., J. Trampert, and B. L. N. Kennett (2008), Global anisotropic phase velocity maps for higher mode Love and Rayleigh waves, *Geophysical Journal International*, *172*, 1016–1032, doi:10.1111/j.1365-246X.2007.03685.x.

Wagner, L. S., M. D. Long, M. D. Johnston, and M. H. Benoit (2012), Lithospheric and asthenospheric contributions to shear-wave splitting observations in the southeastern United States, *Earth and Planetary Science Letters*, *341-344*, 128–138, doi:10.1016/j.epsl.2012.06.020.

Wagner, L. S., K. M. Fischer, R. Hawman, E. Hopper, and D. Howell (2018), The relative roles of inheritance and long-term passive margin lithospheric evolution on the modern structure and tectonic activity in the southeastern United States, *Geosphere*, *14*(4), 1385–1410, doi:10.1130/GES01593.1.

Warren, J. M. (2016), Global variations in abyssal peridotite compositions, *Lithos*, 248-251, 193–219, doi: 10.1016/j.lithos.2015.12.023.

Warren, J. M., G. Hirth, and P. B. Kelemen (2008), Evolution of olivine lattice preferred orientation during simple shear in the mantle, *Earth and Planetary Science Letters*, 272(3-4), 501–512, doi:10.1016/j.epsl.2008.03.063.

Webber, C., J. Newman, C. W. Holyoke, T. Little, and B. Tikoff (2010), Fabric development in cm-scale shear zones in ultramafic rocks, Red Hills, New Zealand, *Tectonophysics*, 489, 55–75, doi:10.1016/j.tecto.2010.04.001.

Weeraratne, D. S., D. W. Forsyth, Y. Yang, and S. C. Webb (2007), Rayleigh wave tomography beneath intraplate volcanic ridges in the South Pacific, *Journal of Geophysical Research*, 112, 1–18, doi:10.1029/2006JB004403.

Withjack, M. O., R. W. Schlische, and P. E. Olsen (1998), Diachronous rifting, drifting, and inversion on the passive margin of central eastern North America: an analog for other passive margins, *AAPG Bulletin*, 82(5A), 817–835, doi:10.1306/1d9bc60b-172d-11d7-8645000102c1865d.

Withjack, M. O., R. W. Schlische, and P. E. Olsen (2012), Development of the passive margin of Eastern North America: Mesozoic rifting, igneous activity, and breakup, in *Regional Geology and Tectonics: Phanerozoic Rift Systems and Sedimentary Basins*, chap. 13, pp. 300–335, Elsevier B.V., doi:10.1016/B978-0-444-56356-9.00012-2.

Yamauchi, H., and Y. Takei (2016), Polycrystal anelasticity at near-solidus temperatures, *Journal of Geophysical Research: Solid Earth*, 121, 7790–7820, doi:10.1002/2016JB013316.

Yang, X., Y. Luo, H. Xu, and K. Zhao (2020), Shear wave velocity and radial anisotropy structures beneath the central Pacific from surface wave analysis of OBS records, *Earth and Planetary Science Letters*, 534, 116,086, doi:10.1016/j.epsl.2020.116086.

Yuan, K., and C. Beghein (2013), Seismic anisotropy changes across upper mantle phase transitions, *Earth and Planetary Science Letters*, 374, 132–144, doi:10.1016/j.epsl.2013.05.031.

Yuan, K., and C. Beghein (2014), Three-dimensional variations in Love and Rayleigh wave azimuthal anisotropy for the upper 800km of the mantle, *Journal of Geophysical Research : Solid Earth*, 119, 3232–3255, doi:10.1002/2013JB010853.Received.

Zhang, S., and S.-i. Karato (1995), Lattice preferred orientation of olivine aggregates deformed in simple shear, *Nature*, 375, 774–777.

Zhang, S., S. ichiro Karato, J. Fitz Gerald, U. H. Faul, and Y. Zhou (2000), Simple shear deformation of olivine aggregates, *Tectonophysics*, 316, 133–152, doi:10.1016/S0040-1951(99)00229-2.

Appendices

A.1 Seismic anisotropy parameterization

The full anisotropic complexity of surface waves traveling through a weakly anisotropic medium can be described by 13 independent elastic parameters, composing the elastic stiffness tensor C_{ij} . In practice, this elastic tensor can be divided into two parts:

$$C_{ij} = C_{ij}^{TI} + \delta C_{ij}, \quad (\text{A.1})$$

where C_{ij}^{TI} consists of 5 independent parameters describing the transversely isotropic part that satisfies the azimuthally averaged Rayleigh- and Love-wave phase velocities, and δC_{ij} consists of 8 independent parameters describing the azimuthally anisotropic part that captures the 2θ and 4θ azimuthal variations of surface waves. In this study, we constrain the full elastic tensor by solving separately for C_{ij}^{TI} and δC_{ij} .

The azimuthally averaged transversely isotropic part, C_{ij}^{TI} , is parameterized by horizontally propagating vertically and horizontally polarized S-wave speeds (V_{SV} , V_{SH}); vertically and horizontally propagating P-wave speeds (V_{PV} , V_{PH}); the parameter η , which influences waves traveling at angles intermediate to the symmetry axis but lacks a clear physical meaning (Kawakatsu, 2016a,b); and density ρ (or equivalently, Love's parameters A , C , L , N , and F). These moduli can be written in terms of the full elastic tensor in equation (A.1)

(Montagner and Nataf, 1986):

$$A = \rho V_{PH}^2 = \frac{3}{8}(C_{11} + C_{22}) + \frac{1}{4}C_{12} + \frac{1}{2}C_{66}, \quad (\text{A.2})$$

$$C = \rho V_{PV}^2 = C_{33}, \quad (\text{A.3})$$

$$L = \rho V_{SV}^2 = \frac{1}{2}(C_{55} + C_{44}), \quad (\text{A.4})$$

$$N = \rho V_{SH}^2 = \frac{1}{8}(C_{11} + C_{22}) - \frac{1}{4}C_{12} + \frac{1}{2}C_{66}, \quad (\text{A.5})$$

$$F = \rho\eta(V_{PH}^2 - 2V_{SV}^2) = \frac{1}{2}(C_{13} + C_{23}), \quad (\text{A.6})$$

$$\xi = \left(\frac{V_{SH}}{V_{SV}}\right)^2 = \frac{N}{L}, \quad (\text{A.7})$$

where radial anisotropy, ξ , is a proxy for vertical ($\xi < 1$) or horizontal ($\xi > 1$) flow in the mantle when produced by the lattice-preferred orientation (LPO) of olivine. The transversely isotropic earth defined in this way is equivalent to a hexagonal crystal with a vertical symmetry axis and sufficiently describes average global body- and surface-wave datasets (*Anderson and Dziewonski, 1982, Dziewonski and Anderson, 1981*).

If olivine LPO is coherent at the local or regional scale, A , L , N , and F will also vary with propagation azimuth, resulting in a lower symmetry system that exhibits azimuthal anisotropy (Montagner, 2002). The azimuthal variation of each elastic moduli around its average value, δC_{ij} , is described by a magnitude (G , B , H , and E) and corresponding

direction (Ψ_G , Ψ_B , Ψ_H , and Ψ_E) of anisotropy:

2θ :

$$G = \delta L = \sqrt{G_c^2 + G_s^2}, \quad \Psi_G = \frac{1}{2} \arctan \left(\frac{G_s}{G_c} \right); \quad (\text{A.8})$$

$$B = \delta A = \sqrt{B_c^2 + B_s^2}, \quad \Psi_B = \frac{1}{2} \arctan \left(\frac{B_s}{B_c} \right); \quad (\text{A.9})$$

$$H = \delta F = \sqrt{H_c^2 + H_s^2}, \quad \Psi_H = \frac{1}{2} \arctan \left(\frac{H_s}{H_c} \right); \quad (\text{A.10})$$

4θ :

$$E = \delta N = \sqrt{E_c^2 + E_s^2}, \quad \Psi_E = \frac{1}{4} \arctan \left(\frac{-E_s}{-E_c} \right); \quad (\text{A.11})$$

$$G_c = \frac{1}{2}(C_{55} - C_{44}), \quad (\text{A.12})$$

$$G_s = C_{54}, \quad (\text{A.13})$$

$$B_c = \frac{1}{2}(C_{11} - C_{22}), \quad (\text{A.14})$$

$$B_s = C_{16} + C_{26}, \quad (\text{A.15})$$

$$H_c = \frac{1}{2}(C_{13} - C_{23}), \quad (\text{A.16})$$

$$H_s = C_{36}, \quad (\text{A.17})$$

$$E_c = \frac{1}{8}(C_{11} + C_{22}) - \frac{1}{4}C_{12} - \frac{1}{2}C_{66}, \quad (\text{A.18})$$

$$E_s = \frac{1}{2}(C_{16} - C_{26}), \quad (\text{A.19})$$

In this case, the direction and strength of anisotropy depend on the bulk orientation and degree of organization of olivine [100] axes within the horizontal plane. The azimuthal variation of body-wave velocities are a direct function of these elastic parameters (*Crampin*,

1977):

$$\rho V_{qP}(\theta)^2 = A + B_c \cos(2\theta) + B_s \sin(2\theta) + E_c \cos(4\theta) + E_s \sin(4\theta), \quad (\text{A.20})$$

$$\rho V_{qSV}(\theta)^2 = L + G_c \cos(2\theta) + G_s \sin(2\theta), \quad (\text{A.21})$$

$$\rho V_{qSH}(\theta)^2 = N - E_c \cos(4\theta) - E_s \sin(4\theta), \quad (\text{A.22})$$

where θ is the propagation azimuth and V_{qP} , V_{qSV} , and V_{qSH} are the velocities of quasi compressional- and shear-waves propagating along the horizontal plane. The azimuthal anisotropy of surface waves is more complex; Rayleigh waves propagate with a 2θ azimuthal dependence controlled by G , B , and H with a fast direction parallel to the horizontal [100] axis of olivine, and Love waves exhibit both a 2θ and 4θ azimuthal dependence controlled by G and E , respectively (*Montagner and Nataf*, 1986). Love-wave azimuthal anisotropy has remained poorly constrained owing to a lack of azimuthal coverage and the high noise-levels typically observed on the horizontal components.

The complete C_{ij} can be constructed from the transversely isotropic and azimuthal terms

by rearranging equations (A.2–A.6; A.12–A.19):

$$C_{ij} = \begin{pmatrix} A + B_c + E_c & A - 2N - E_c & F + H_c & 0 & 0 & \frac{1}{2}B_s + E_s \\ & & & & & \\ & A - B_c + E_c & F - H_c & 0 & 0 & \frac{1}{2}B_s - E_s \\ & & & & & \\ & & C & 0 & 0 & H_s \\ & & & & & \\ & & & L - G_c & G_s & 0 \\ & & & & & \\ & & & & L + G_c & 0 \\ & & & & & \\ & & & & & N - E_c \end{pmatrix} \quad (\text{A.23})$$

Of the 13 parameters, only 6 (primarily shear) parameters are well-resolved by Rayleigh (L or V_{SV} ; $G_{c,s}$) and Love waves (N or V_{SH} ; $E_{c,s}$) and therefore, symmetry relations and a priori information must be used to constrain the remaining 7 parameters. In this study, we apply such constraints to account for all 13 elastic parameters, focusing our interpretations primarily on the most well-resolved ones: ξ , G , Ψ_G , E , and Ψ_E .

A.2 Effect of lateral variations on azimuthal anisotropy estimates

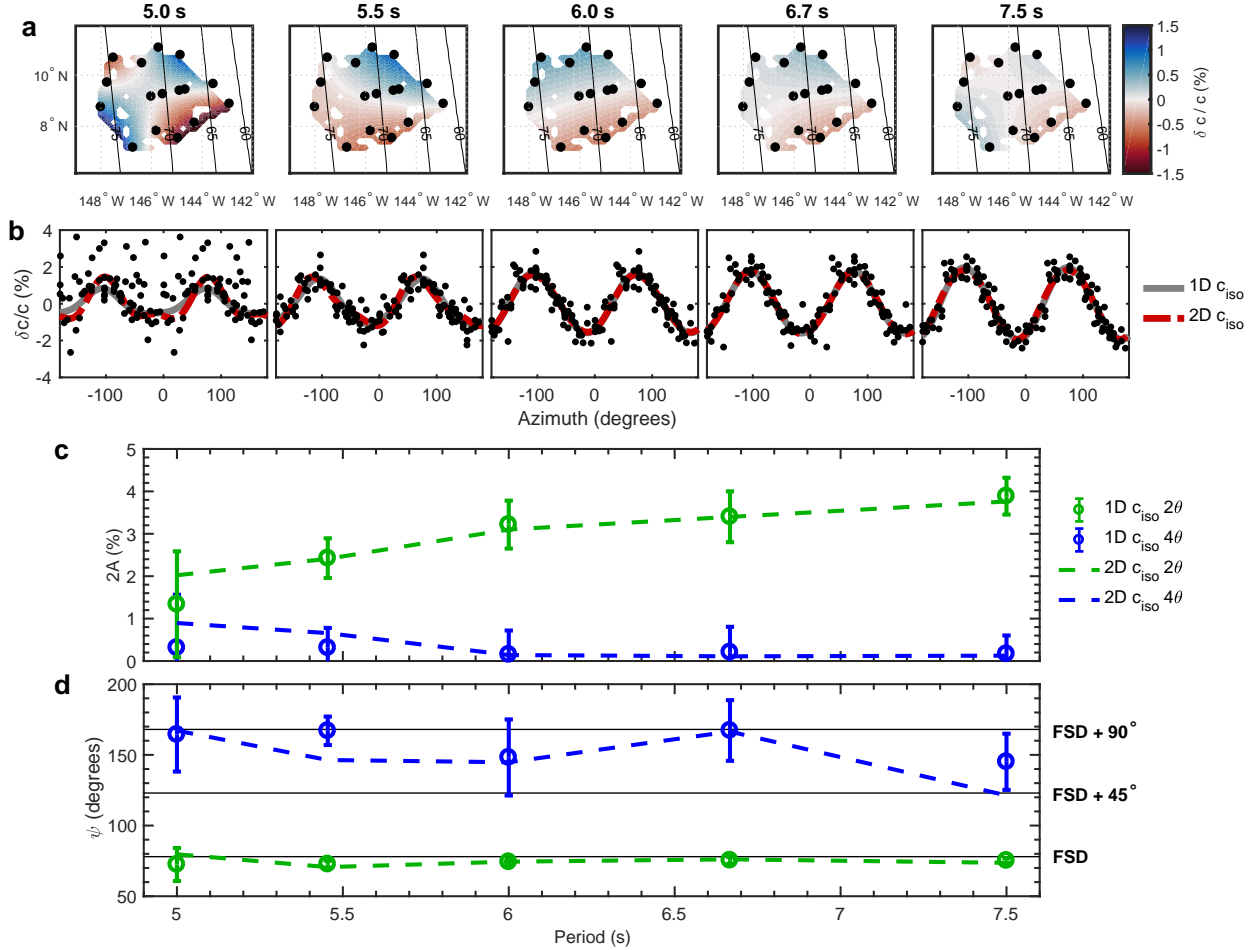


Figure A.1: Comparison of Rayleigh 2θ and 4θ azimuthal parameters for 1D and 2D isotropic phase velocities. (a) 2D isotropic phase velocity maps with seafloor isochrons in black. (b) Azimuthal variation in phase velocity (2θ and 4θ) with 1D (solid grey) and 2D (dashed red) isotropic velocities. (c) Amplitude and (d) direction of 2θ and 4θ anisotropic parameters modeled with 1D (symbols) and 2D (dashed line) isotropic models. Rayleigh 4θ is indistinguishable from zero in both cases, and therefore we neglect it from the modeling. Furthermore, the anisotropic parameters do not change when introducing 2D isotropic structure, suggesting that our simplifying assumption of 1D isotropic structure does not bias the results.

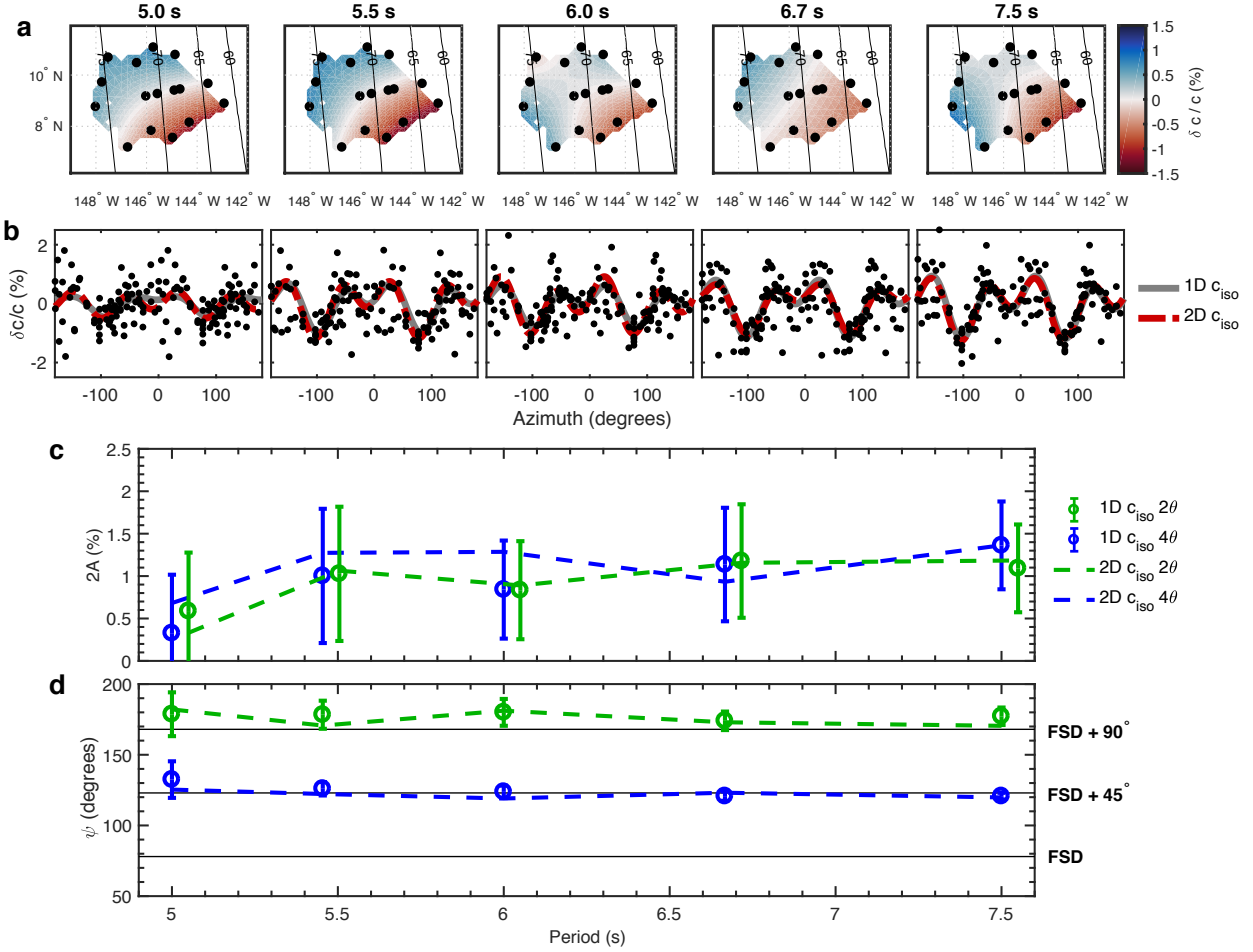


Figure A.2: Same as Figure A.1 but for Love waves. The grey curve in (b) is the same as Figure 4b in the main text. Again, the anisotropic parameters are not biased by assuming a 1D isotropic structure. Even when accounting for the 2D isotropic structure, the Love 2θ signal is as strong as (or in some cases stronger than) the 4θ signal, suggesting that the unusually strong 2θ signal is not due to unaccounted-for 2D isotropic variations.

A.3 Enforcing layers of constant ξ

We enforce layers of constant ξ in the lower crust and mantle, separately. Since ξ is not an explicit parameter in the inversion, this constraint is achieved by scaling the normalized vertical gradients of V_{SV} and V_{SH} (as well as V_{PV} and V_{PH}) by the corresponding gradients of the previous model iteration. In particular, for a previous model iteration m_0 , the desired constraint between neighboring nodes k and $k + 1$ of the updated model parameter m is:

$$\frac{m^k - m^{k+1}}{m^k + m^{k+1}} = \frac{m_0^k - m_0^{k+1}}{m_0^k + m_0^{k+1}}. \quad (\text{A.24})$$

By isolating m^k and m^{k+1} , the constraint equation becomes:

$$m^k \left(1 - \frac{m_0^k - m_0^{k+1}}{m_0^k + m_0^{k+1}} \right) - m^{k+1} \left(1 + \frac{m_0^k - m_0^{k+1}}{m_0^k + m_0^{k+1}} \right) = 0. \quad (\text{A.25})$$

When applied simultaneously to V_{SV} and V_{SH} , equation (A.25) enforces constant ξ throughout the desired portion of the model. This constraint greatly stabilizes the inversion such that additional smoothing is not required and, in combination with other a priori constraints discussed in the main text, effectively reduces the number of model parameters.

A.4 Additional radial anisotropy squeeze tests

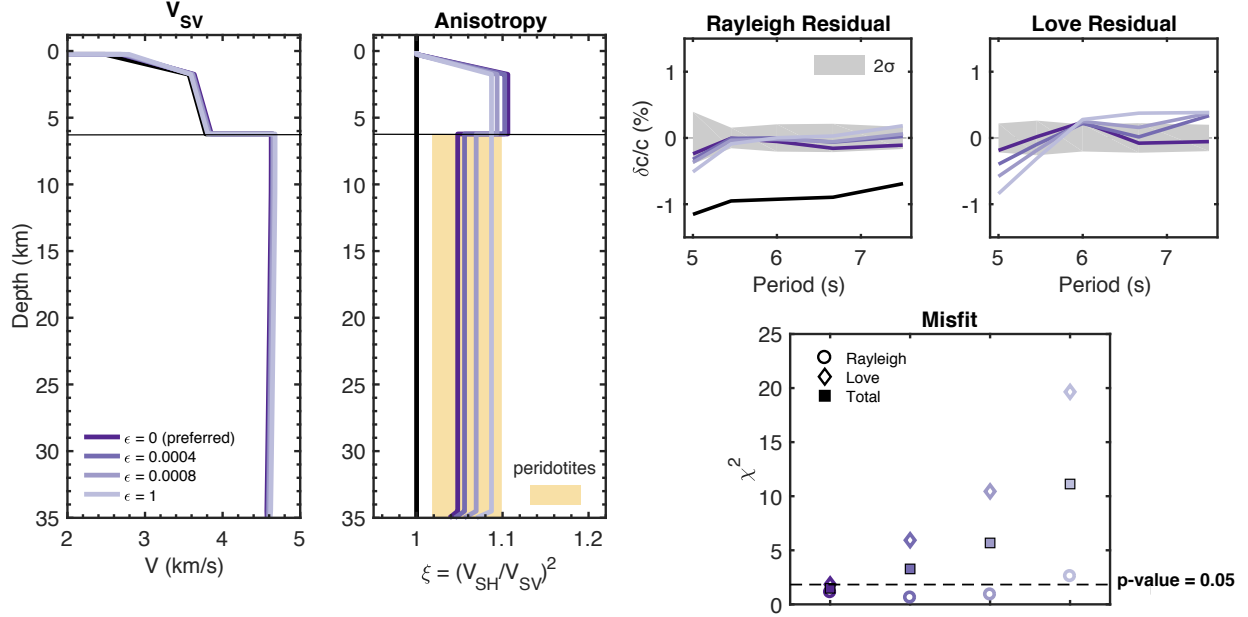


Figure A.3: Results of minimizing the change in radial anisotropy across the Moho, where ϵ is the weight applied to the new constraint equation ($\epsilon = 0$ is the same as model 3 from Figure 8 in the main text). Misfit increases with increasing ϵ , due mostly to increased Love-wave misfit, suggesting that the jump in ξ across the Moho is required by the data. See Figure 8 for detailed figure caption.

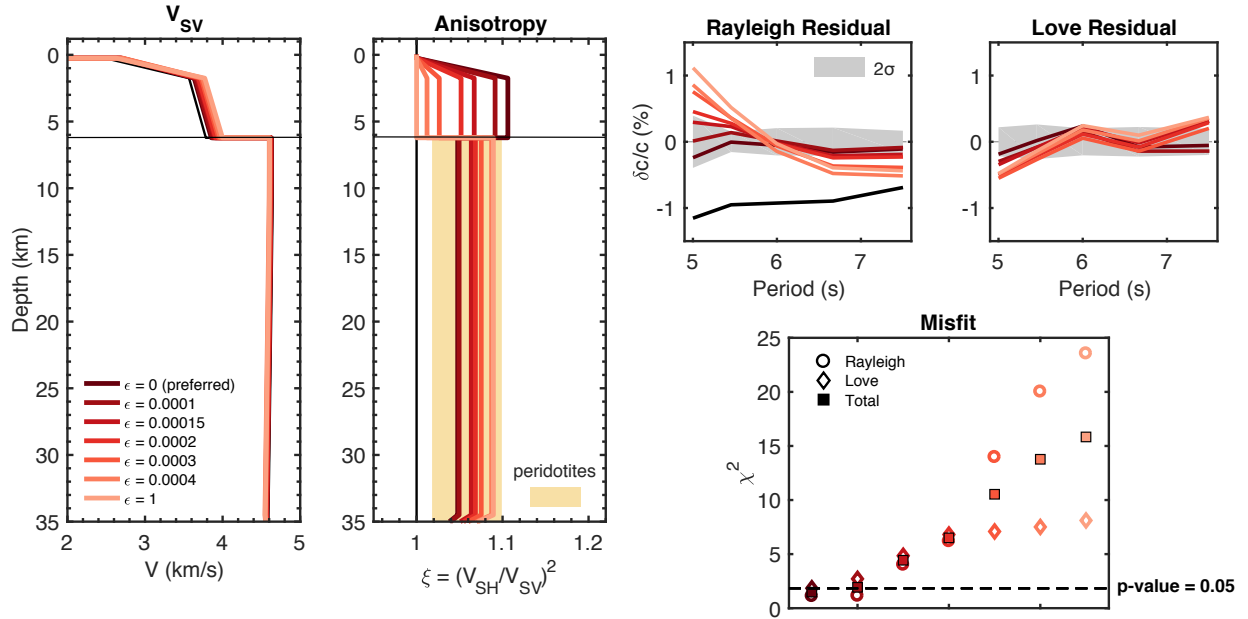


Figure A.4: Results of incrementally minimizing radial anisotropy in the lower crust, where ϵ is the weight applied to the constraint ($\epsilon = 0$ is model 3 and $\epsilon = 1$ is model 2 from Figure 8 in the main text). Misfit increases with increasing ϵ , suggesting that strong ξ in the crust (~ 1.1) is required by the data. The model with $\epsilon = 0.0001$ has slightly weaker crustal anisotropy ($\xi \sim 1.09$) and still fits the data well with $\chi^2 \sim 1.9$, plotting just beyond the 95% confidence level. See Figure 8 for detailed figure caption.

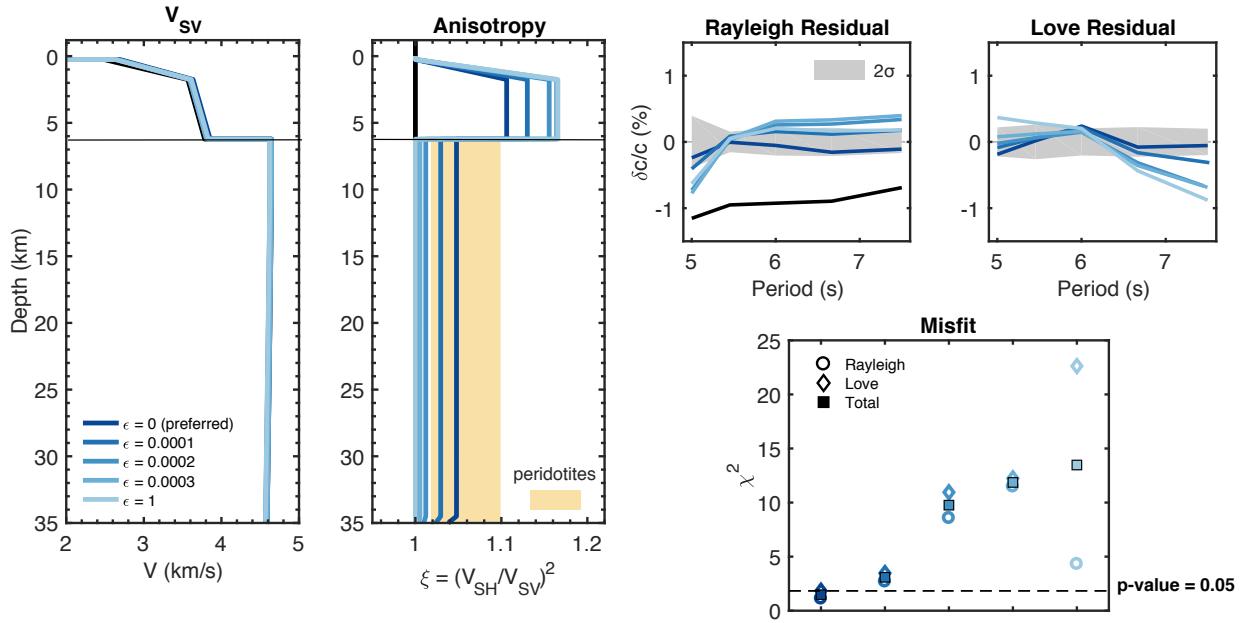


Figure A.5: Results of incrementally minimizing radial anisotropy in the mantle, where ϵ is the weight applied to the constraint ($\epsilon = 0$ is model 3 and $\epsilon = 1$ is model 1 from Figure 8 in the main text). Misfit increases with increasing ϵ , suggesting that ξ in the mantle with fast V_{SH} (~ 1.05) is required by the data. See Figure 8 for detailed figure caption.

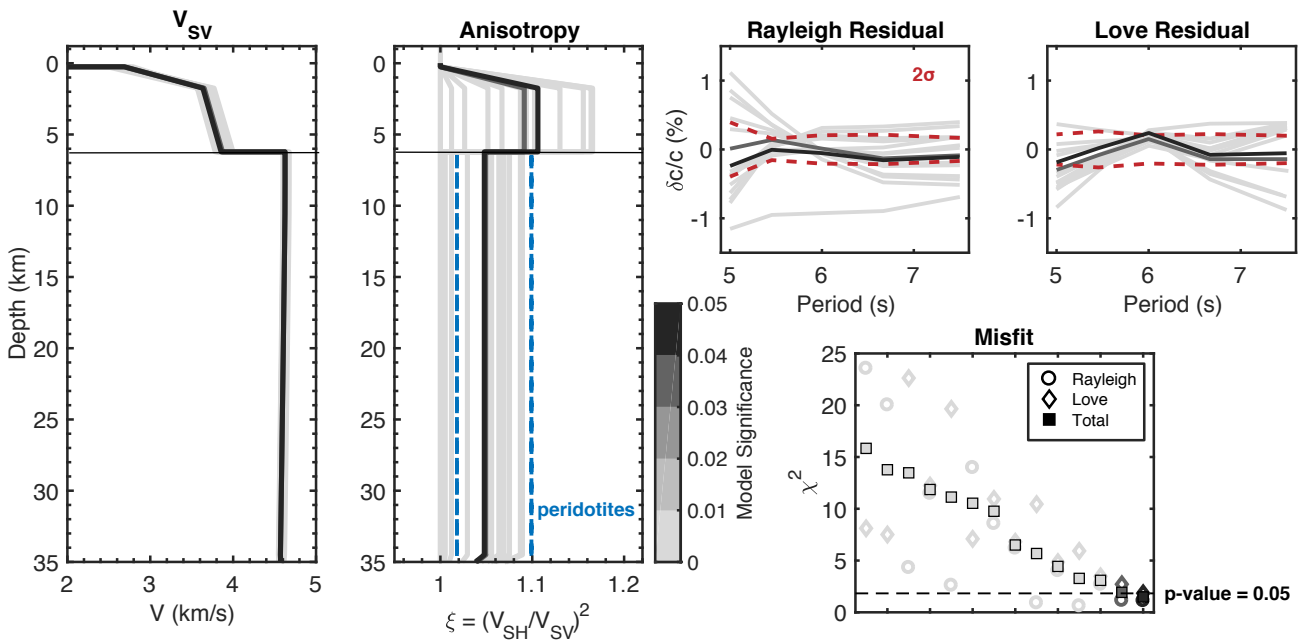


Figure A.6: Comparison of all 14 models from Figures A.3–A.5 colored by model significance level (p -value). Our preferred model is the only one which has a significance greater than 0.05, the 95% confidence level. The model from Figure A.4 with $\epsilon = 0.0001$ is similar to our preferred model but with slightly weaker crustal anisotropy ($\xi \sim 1.09$) and $p = 0.037$.

A.5 NoMelt OBS orientations

Table A.1: NoMelt OBS orientations displayed as the mean H1-azimuth ($\bar{\theta}$) measured clockwise from north and the 4σ uncertainties. Due to poor data quality, orientations could not be determined for 6 of the 22 stations in the IRIS DMC.

Station	θ (°)	4σ (°)
B01	281.07	3.77
B02	119.15	2.95
B04	20.43	3.57
B05	28.99	2.73
B06	32.62	2.56
B07	—	—
B08	174.69	2.51
B11	282.98	3.11
B13	101.43	2.63
B14	—	—
B15	—	—
B16	244.89	2.15
B17	340.40	2.23
B18	—	—
B19	59.80	2.89
B20	—	—
B21	—	—
B22	98.11	3.07
B23	4.17	2.53
B24	94.47	2.88
B25	196.29	2.34
B26	166.71	2.46

B

Chapter 2 Supplementary Material

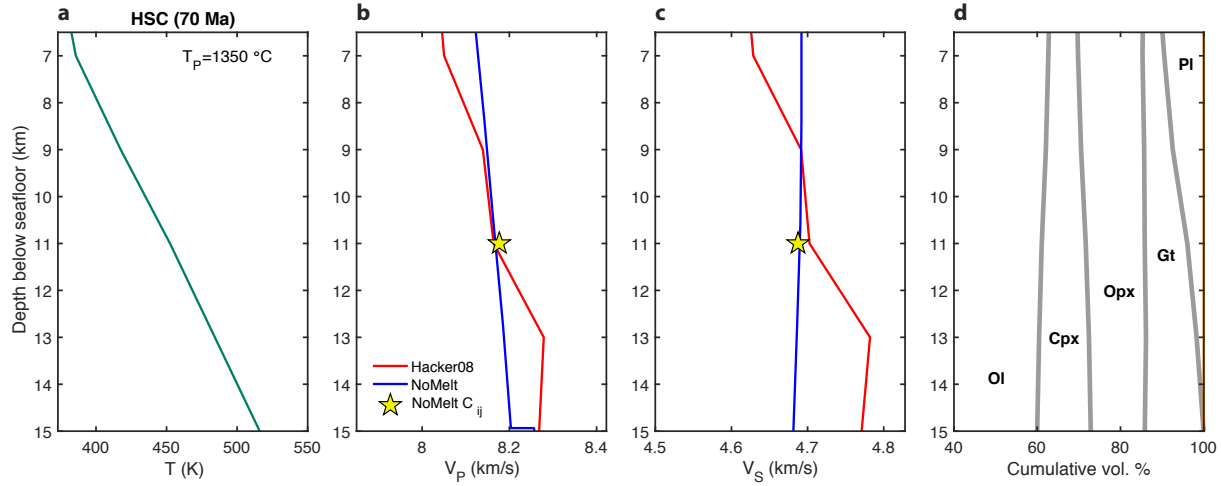


Figure B.1: **Estimating V_P , V_S , and olivine content.** **a** 70 Ma half-space cooling (HSC) geotherm with mantle potential temperature $T_P = 1350^\circ\text{C}$. **b, c** Mineral physics calculations of Voigt average V_P and V_S (red solid lines) and **d** mineral abundance from Perple_X (Connolly, 2009), using the solution models of Stixrude and Lithgow-Bertelloni (2011) and assuming a depleted mid-ocean ridge basalt (MORB) mantle composition (Hacker, 2008). The NoMelt elastic tensor averaged over the plotted depth range is indicated by the yellow star. Although the predicted velocity gradients are less steep for both V_P and V_S (and for V_P , opposite in sign), there is fair agreement with the depth averaged NoMelt velocities. Modal estimates yield $\sim 60\%$ olivine. Ol = olivine; Cpx = clinopyroxene; Opx = orthopyroxene; Gt = garnet; Pl = plagioclase

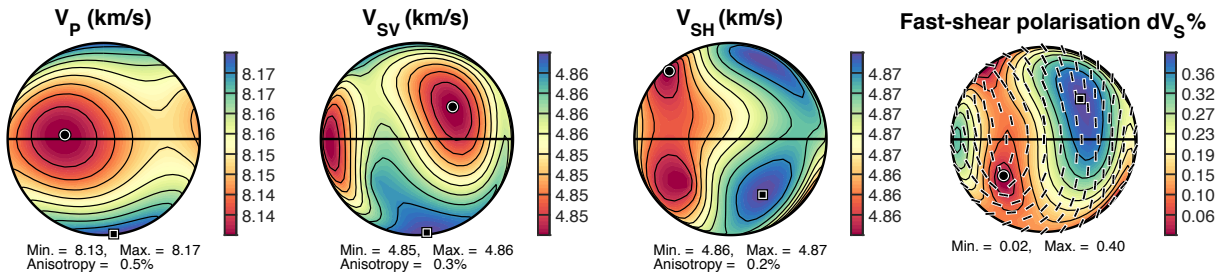


Figure B.2: Orthopyroxene texture used in calculations. A generic orthopyroxene texture from the torsion experiments of Hansen *et al.* (2014). The fabric is extremely weak ($\sim 0.4\%$ V_P anisotropy) and oriented with its [100] crystallographic axis perpendicular to the shear plane, [001] sub-parallel to the shear direction, and [010] perpendicular to shear and in the shear plane. $dV_S = 200(V_{SH} - V_{SV})/(V_{SH} + V_{SV})$

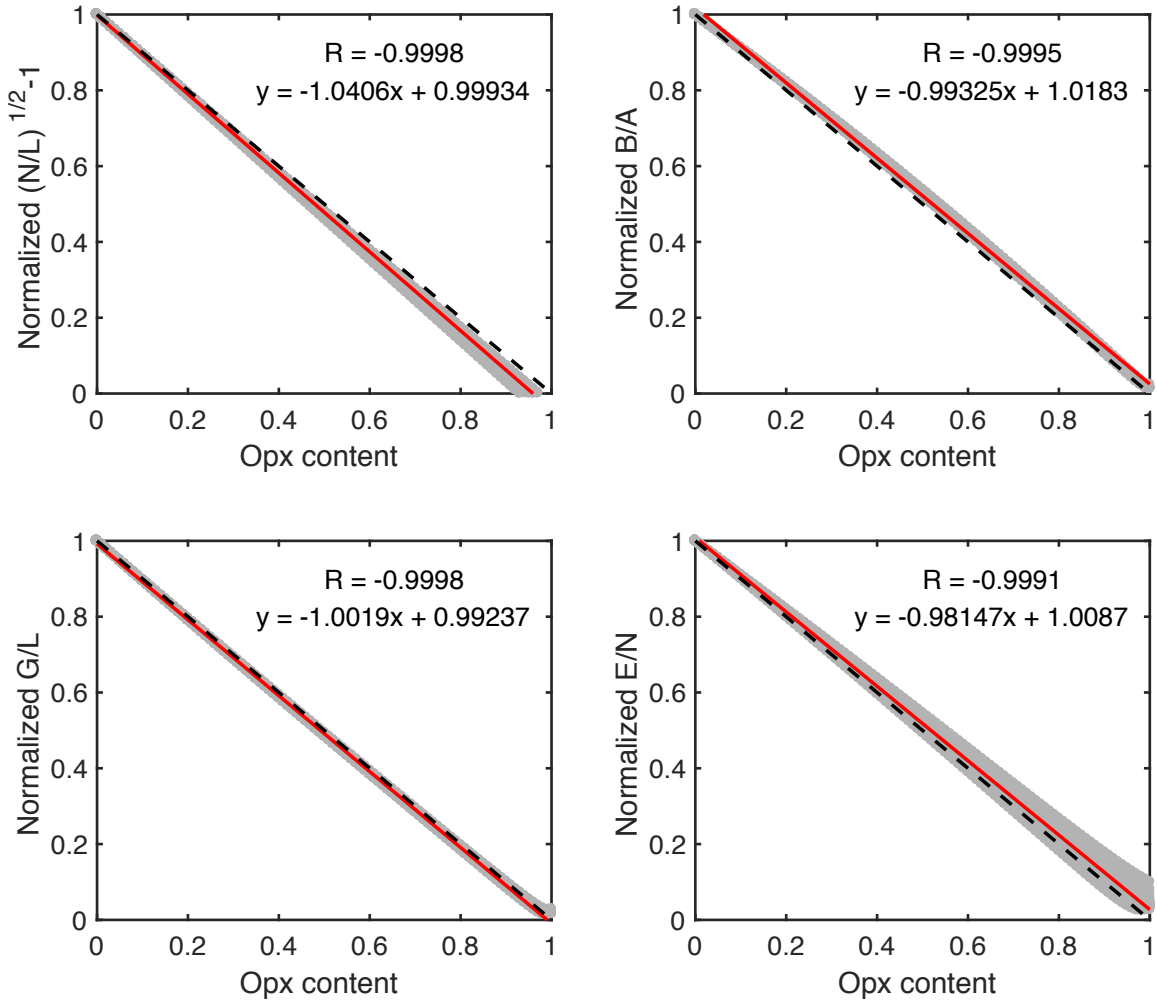


Figure B.3: Reduction in anisotropy strength with increasing orthopyroxene content. Using well-developed laboratory olivine samples from Hansen *et al.* (2014, 2016) with shear strains of $\gamma > 2$, shown in grey, scaling relationships are found between orthopyroxene content and anisotropy strength (using the orthopyroxene fabric in Figure B.2; see methods for details). Anisotropy values for each sample are normalized by the pure olivine estimate in order to determine a single scaling relation for all samples. The best fit line that describes anisotropy reduction with increasing orthopyroxene is shown in red, and nearly falls along the -1:1 line dashed in black.

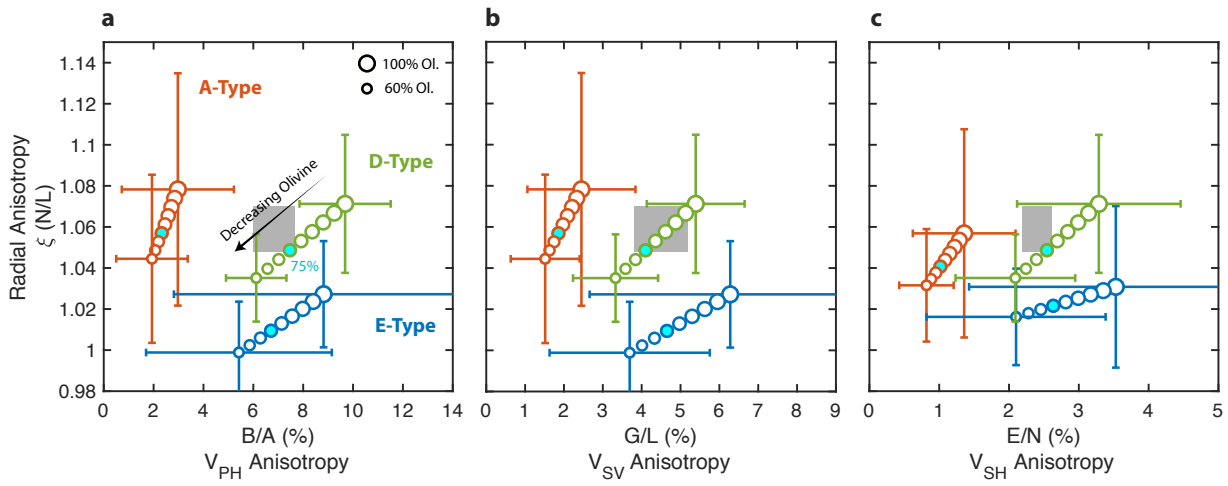


Figure B.4: **Effect of assumed olivine content on LPO-type comparison.** a–c, As in Figure 2.4 in the main text. Circles show anisotropy averages assuming varying ratios of olivine and pyroxene content, where symbol size scales with the amount of olivine ranging from 60% to 100% in increments of 5%, and color denotes fabric type. Anisotropy strength decreases with decreasing olivine content. The best fitting composition of 75% olivine and 25% is shown in cyan.

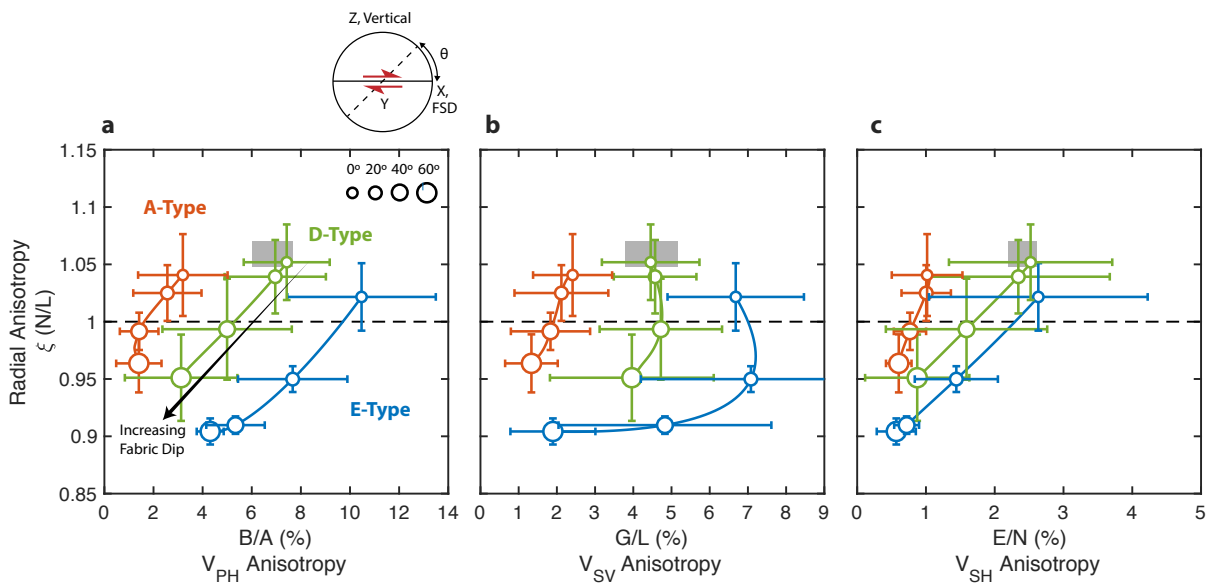


Figure B.5: **Effect of fabric dip on LPO-type comparison.** **a–c**, As in Figure 2.4 in the main text. Symbols show anisotropy averages and one standard deviation after rotating samples about the Y axis by an angle θ , effectively rotating [100] out of the shear plane. Symbol size scales with introduced fabric dip ranging from 0° to 60°, and color denotes fabric type. A composition of 75% olivine and 25% orthopyroxene is assumed. Radial and azimuthal anisotropy generally decreases with increasing fabric dip. In detail, V_{VS} anisotropy in **b** shows a more complex behavior, in particular for samples with strong azimuthal anisotropy, where an initial slight increase with dip to 20–40° is followed by a nonlinear decrease.

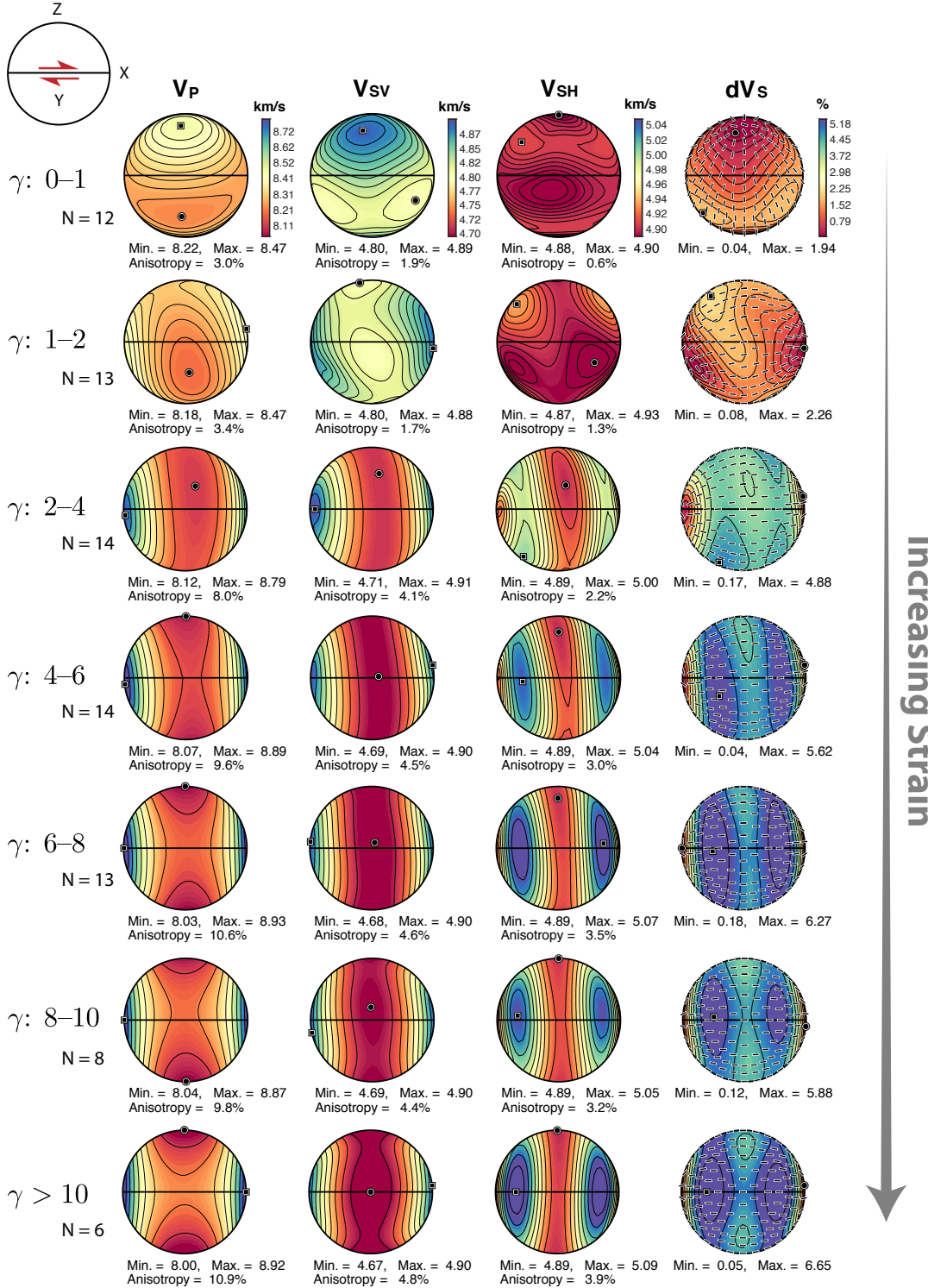


Figure B.6: **Strain evolution of anisotropy for laboratory samples shown in Figure 2.3.** (left to right) Columns show V_P , V_{SV} , V_{SH} , and dV_S anisotropy for laboratory samples from Hansen et al. (2014, 2016) grouped and averaged by shear strain for 60% olivine and 40% pyroxene. (top to bottom) Each row represents an average of all samples within the range of γ indicated at the left of each row. Strain increases from top to bottom. A common color scale is used for each column. $dV_S = 200(V_{SH} - V_{SV})/(V_{SH} + V_{SV})$

Table B.1: NoMelt elasticity tensor, C_{ij} , averaged over the upper 7km of the mantle.

i	j	1	2	3	4	5	6
1		264.7677	89.3975	90.5184	0	0	-0.8534
2		—	222.5967	91.6841	0	0	0.0550
3		—	—	228.1420	0	0	0.0209
4		—	—	—	66.8637	-0.1482	0
5		—	—	—	—	75.1225	0
6		—	—	—	—	—	73.3499

C | Chapter 3 Supplementary Material

C.1 Clock drift corrections

Unlike land-based seismometers, OBS are unable to synchronize their clocks to a GPS in real time while on the seafloor. Total clock drift over the course of the deployment is typically determined upon recovery and distributed across each day of the deployment assuming a linear drift. However, of the 30 YoungORCA stations, 8 were recovered with a dead battery, and no drift correction could be determined.

For the 8 instruments for which clock drift was unknown, we used daily ambient-noise cross-correlation functions (CCFs) to determine drift following *Hable et al.* (2018). Under the assumption that there is no temporal change in instrument response or in velocity structure between the two stations, any shift in the ambient-noise Rayleigh arrival with time indicates a drift in the instrument clock. For each instrument without timing, we calculate daily DPG CCFs with a neighboring instrument with valid timing. A reference CCF is constructed by stacking CCFs for the first 30 days of the deployment and filtering to 3–8 s period. Cross-correlation between the reference CCF and a 7-day moving average CCF provides a measure of the relative daily clock drift (dt) at the maximum coherence value (CC_{max}) for each day of the deployment. Only dts for $CC_{max} > 0.2$ were considered. Finally, the daily drift rate is determined by the slope of the linear fit to the variation in dt with time. The daily time vector, T^k , on day k of the deployment is then corrected via

$$T_{corr}^k = T_{raw}^k - k \left(\frac{\Delta T}{\Delta t} \right) \quad (\text{C.1})$$

where $\Delta T/\Delta t$ is the drift correction in ms day $^{-1}$ in table C.2. We find that the assumption of linear drift is valid, and clock drifts range from 0–10 ms/day (Figures C.1,C.2).

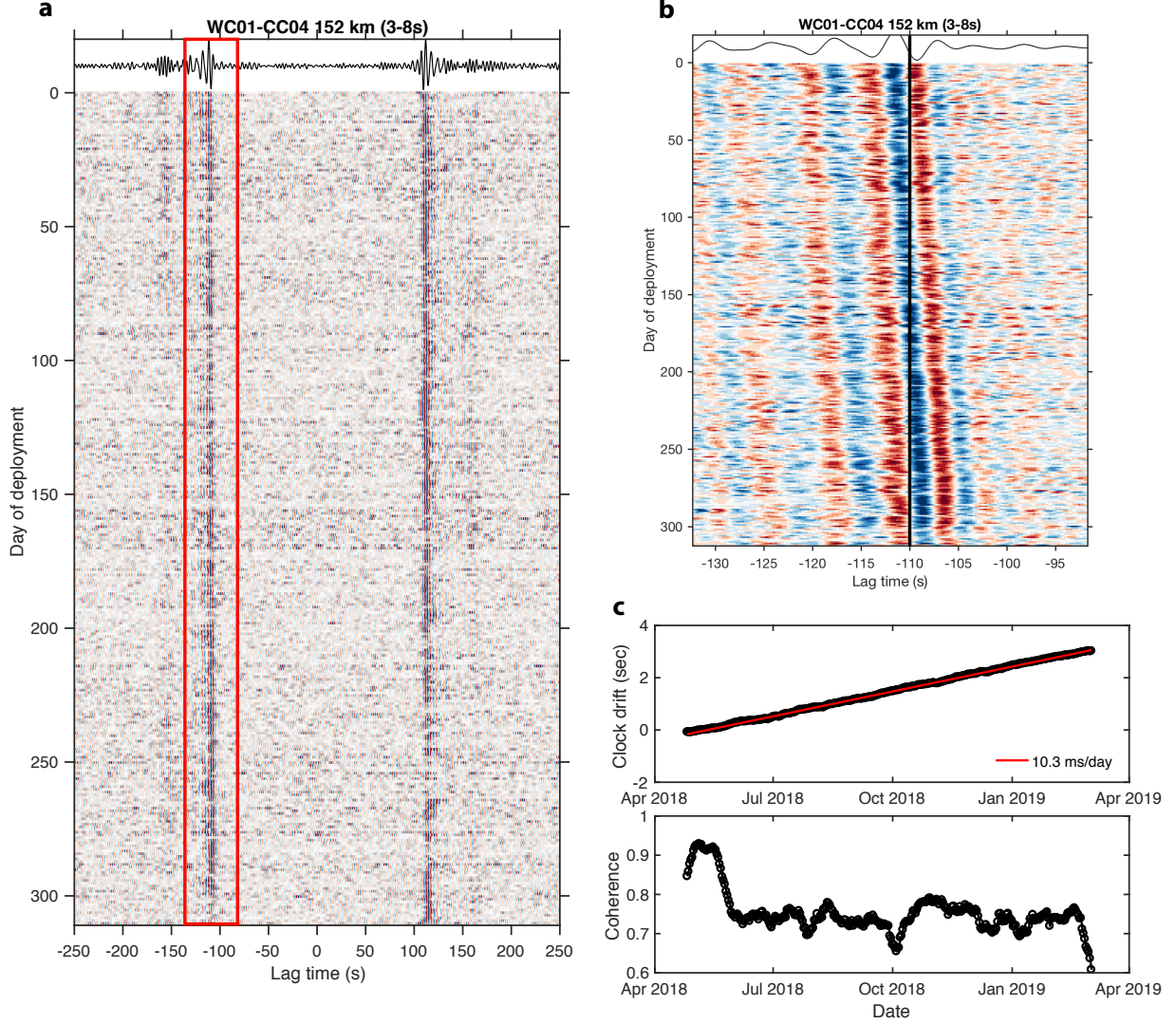


Figure C.1: Example daily cross-correlation functions (CCFs) and clock drift measurement for station pair WC01-CC01 with interstation distance 152 km filtered from 3–8 s period. (a) Daily DPG CCFs for the duration of the deployment. The 30-day reference trace is shown at the top in black. The red box indicates the time range displayed in panel b). (b) Zoom in time of the negative branch of the daily CCFs, where a clear time drift is observed. A vertical black line is shown for reference. (c) Clock drift (top) and corresponding maximum coherence (bottom) for the central day of each 7-day average moving window over the course of the deployment. The red line shows the linear fit that defines the drift rate of 10.3 ms/day.

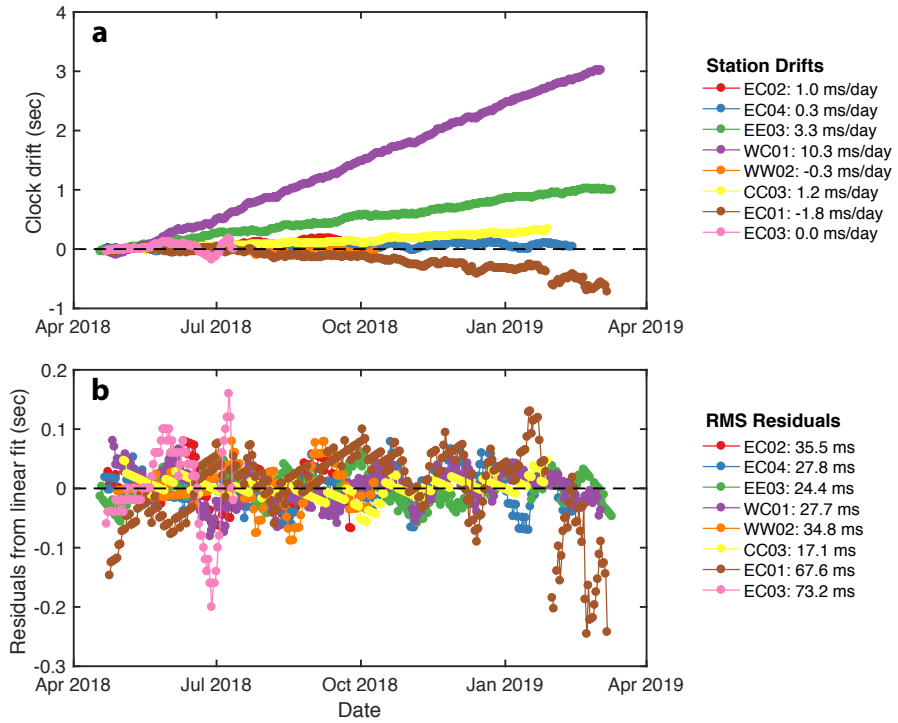


Figure C.2: Summary of clock drift measurements for all 8 stations. (a) Clock drift as in Figure C.1c for each station. Measured drift for each station is shown to the right of the legend. (b) Clock drift residuals after removing the linear fits to the data in a). Root mean squared (RMS) residuals are shown for each station to the right of the legend. Most of the RMS values are on the order of one sample (20 ms).

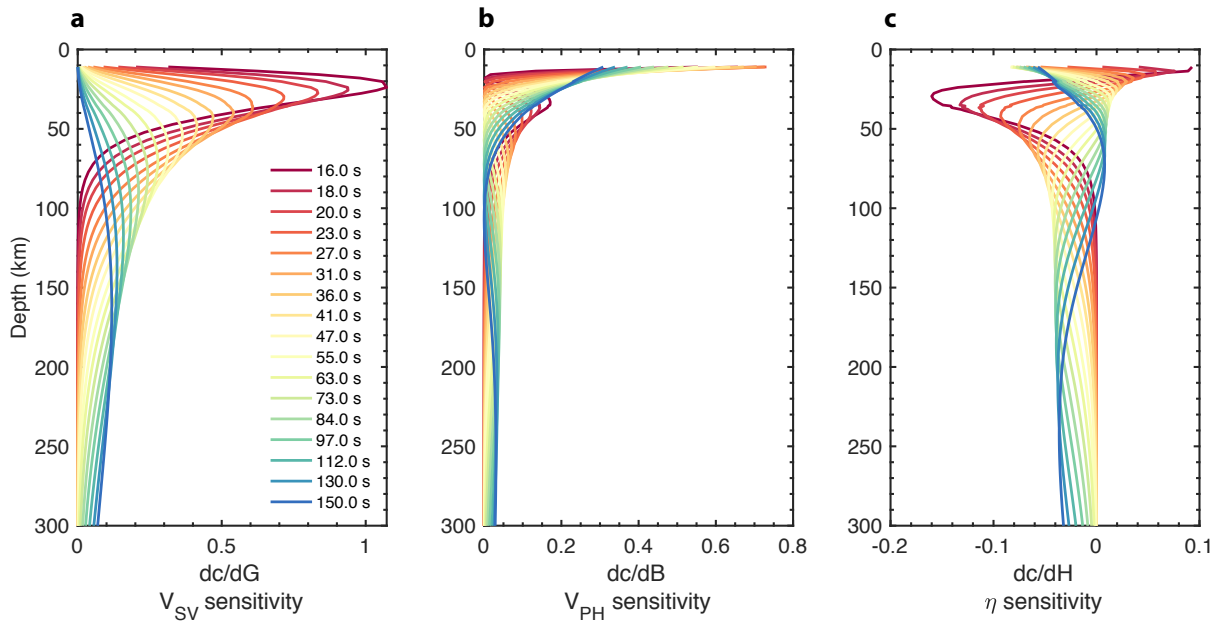


Figure C.3: Azimuthal anisotropy sensitivity kernels for fundamental mode Rayleigh-waves from 16–150 s for (a) G , (b) B , (c) H . Note the strong sensitivity to V_P anisotropy (B) in lithosphere, even for the 150 s Rayleigh waves.

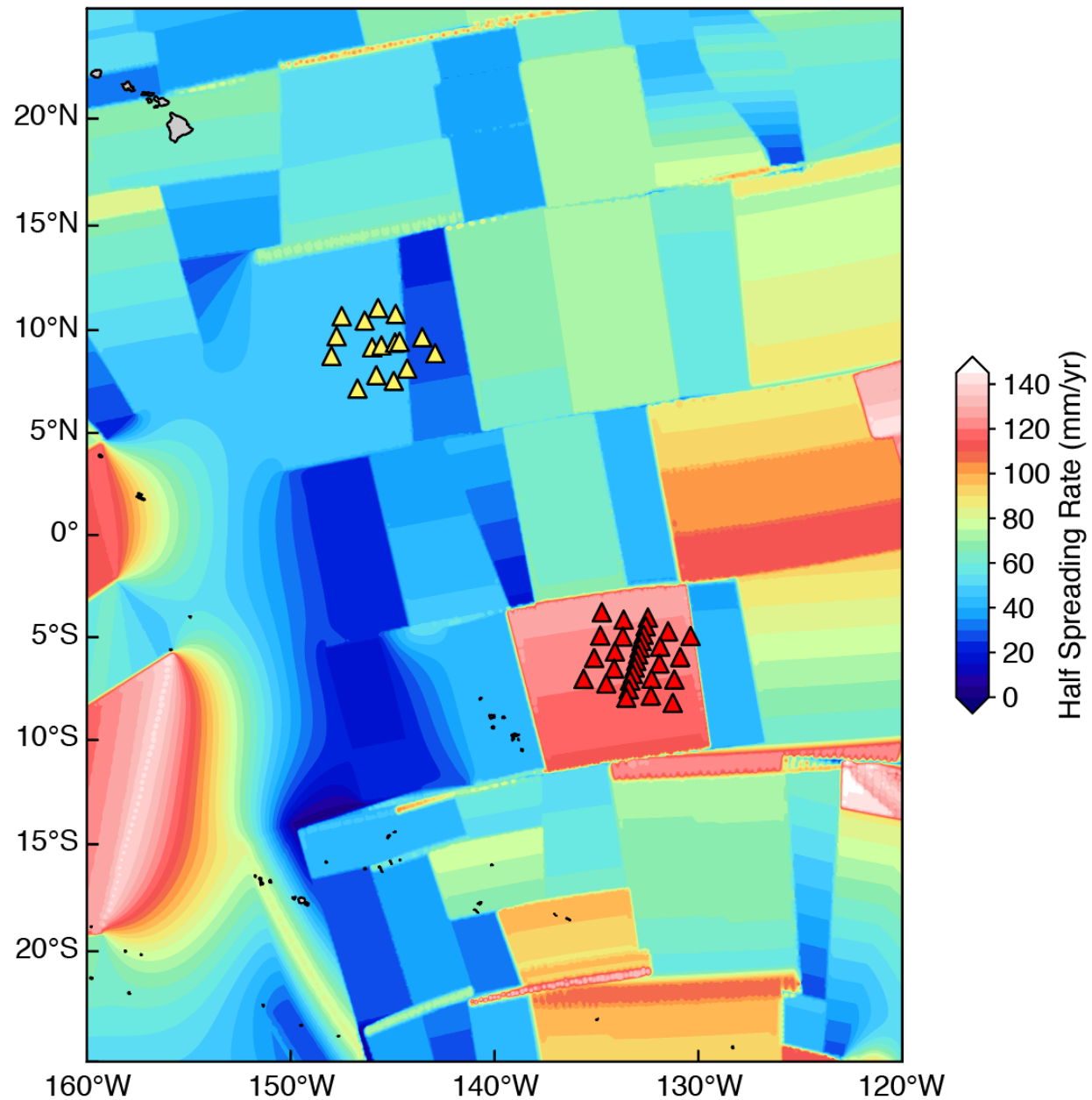


Figure C.4: Map of seafloor spreading rates from (Müller *et al.*, 2008). Triangles show broadband OBS at the YoungORCA (red) and NoMelt (yellow) experiments.

Table C.1: OBS orientations displayed as the mean H1-azimuth ($\bar{\theta}$) measured clockwise from north and the 4σ uncertainties. Due to poor data quality, orientations could not be determined for 10 of the 30 instruments. The average 4σ orientation uncertainty for successfully oriented stations is $\sim 6^\circ$.

Station	θ (°)	4σ (°)
CC01	335.63	11.72
CC02	87.61	3.91
CC03	124.24	9.27
CC04	357.49	3.80
CC05	123.27	4.94
CC06	51.26	4.36
CC07	106.02	5.10
CC08	148.80	5.61
CC09	53.93	10.71
CC10	—	—
CC11	223.89	5.79
CC12	—	—
EC01	—	—
EC02	—	—
EC03	—	—
EC04	—	—
EC05	37.50	7.72
EE01	84.50	3.88
EE02	8.02	4.62
EE03	—	—
EE04	23.28	4.38
WC01	—	—
WC02	30.53	3.55
WC03	128.02	4.64
WC04	117.61	8.35
WC05	102.40	3.10
WW01	—	—
WW02	—	—
WW03	302.68	8.36
WW04	256.13	4.28

Table C.2: YoungORCA OBS clock drift corrections

Station	Drift (ms day^{-1})
CC03	1.184550
EC01	-1.780495
EC02	1.003335
EC03	0.005442
EC04	0.329250
EE03	3.293424
WC01	10.344895
WW02	-0.328534

D | Chapter 4 Supplementary Material

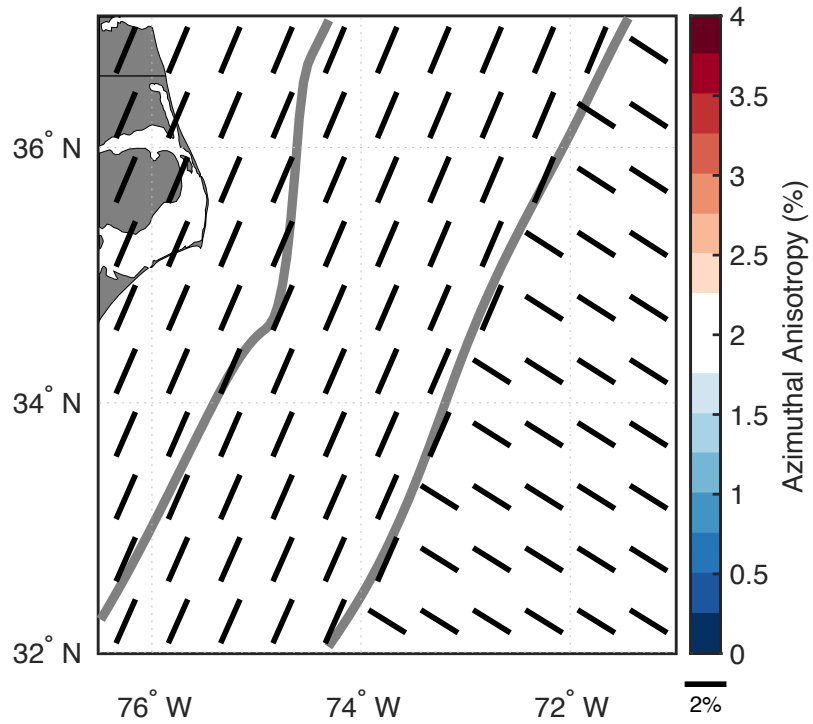


Figure D.1: Input anisotropy model used in the synthetic tests in Figures D.2–D.4. Black sticks show the anisotropy directions and their lengths scale with anisotropy magnitude. Anisotropy strength is held constant at 2% across the model. West of the BSMA anisotropy is margin-parallel, and east of the BSMA it abruptly rotates 90° to FSD-parallel.

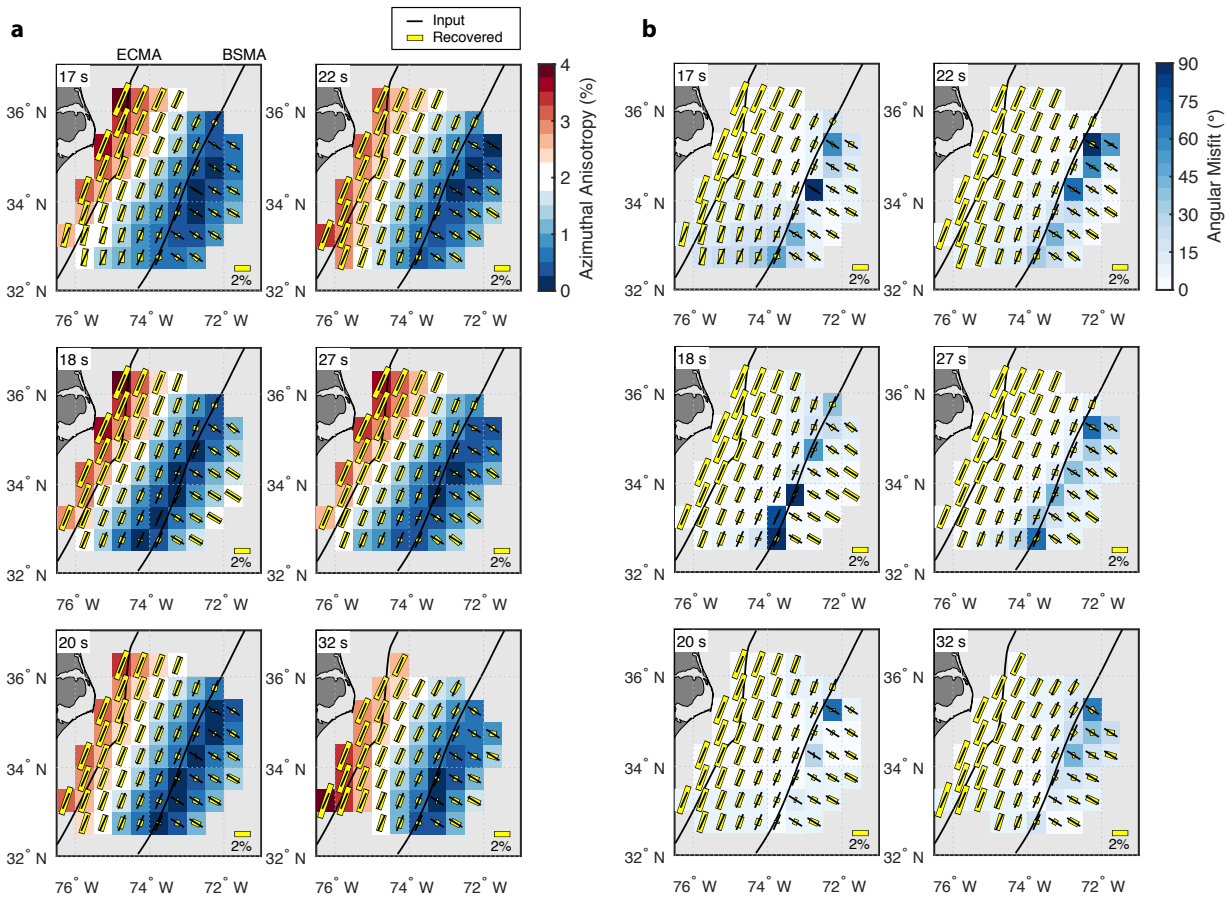


Figure D.2: Synthetic anisotropy test results for the smooth anisotropy model parameterization. (a) Maps of recovered anisotropy magnitudes, where deviations from white indicate overshoot (red) and undershoot (blue) relative to the input model. (b) Absolute angular misfit between fast azimuths of the input and recovered model. Deviations from white indicate poor fast azimuth recovery. Black sticks represent in the input model and yellow bars indicate the recovered model at each frequency.

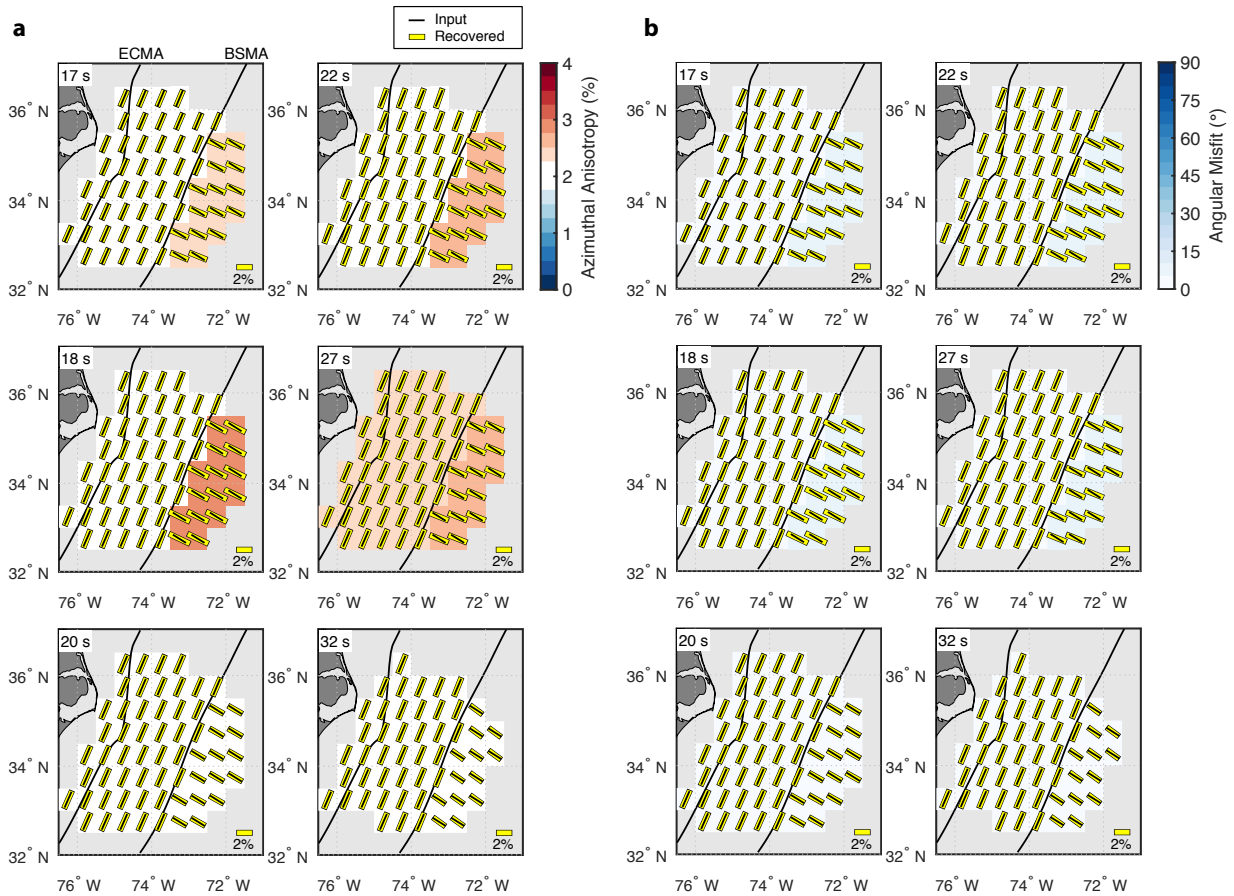


Figure D.3: Same as Figure D.2 but for the model parameterization with a break at the BSMA.

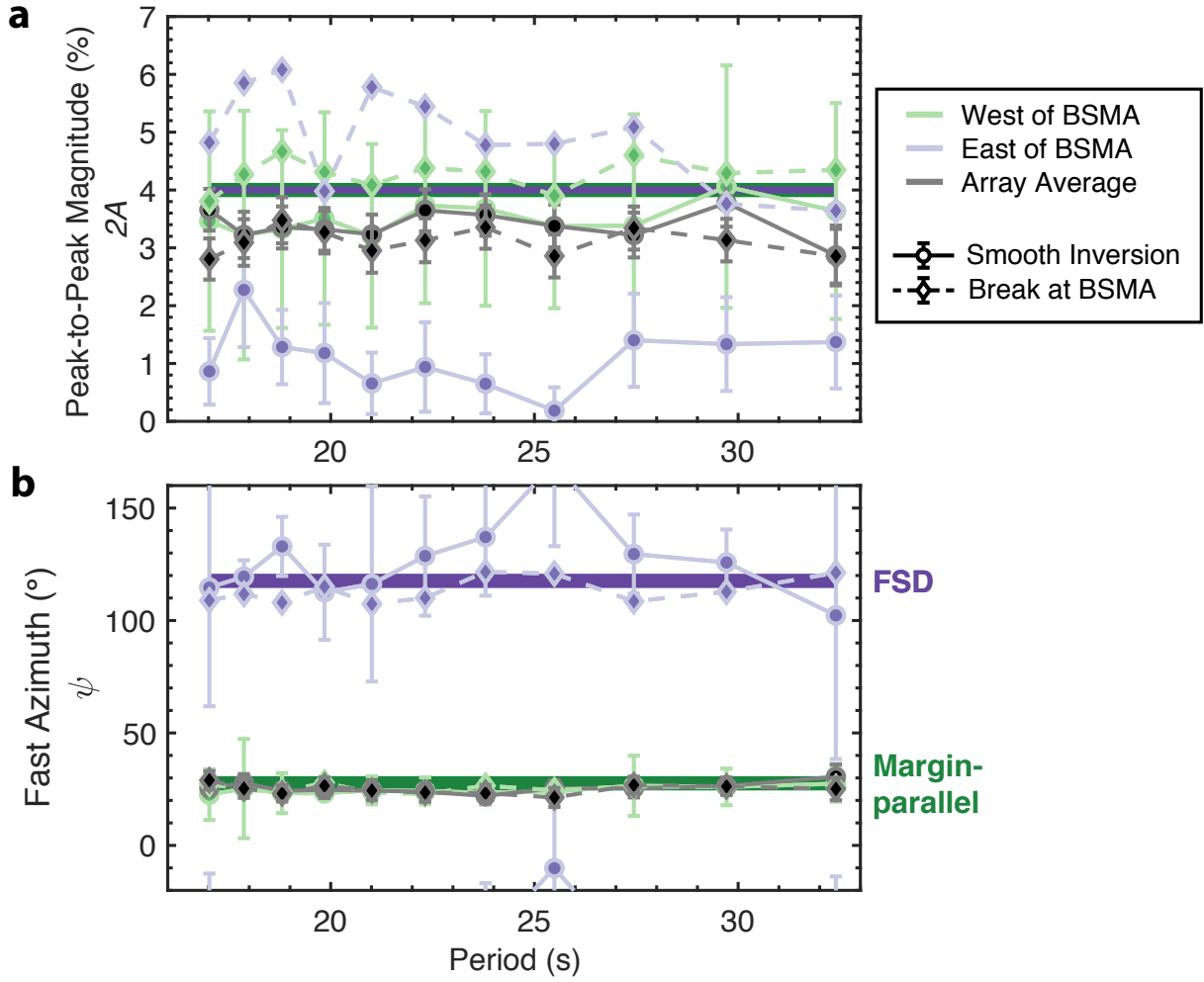


Figure D.4: Summary of synthetic recovery tests. (a) Peak-to-peak anisotropy magnitude and (b) fast azimuths recovered from 17–32 s period. Thick bars indicate the input model values. Results for the smooth parameterization and break at BSMA are shown by solid and dashed lines, respectively. Regional averages for the recovered models are indicated by color: west of the BSMA (green), east of the BSMA (purple), and array average (grey).

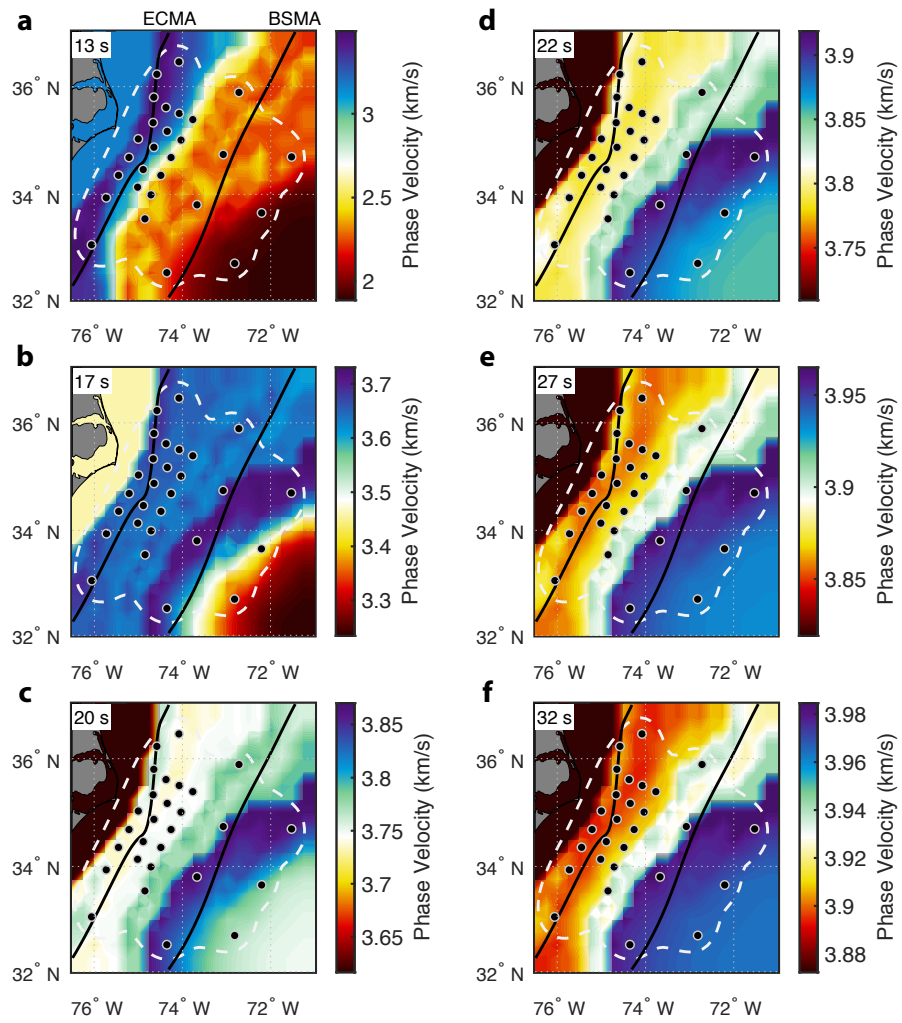


Figure D.5: Starting model phase velocity maps for the same frequencies as in Figure 4.8 in the main text.

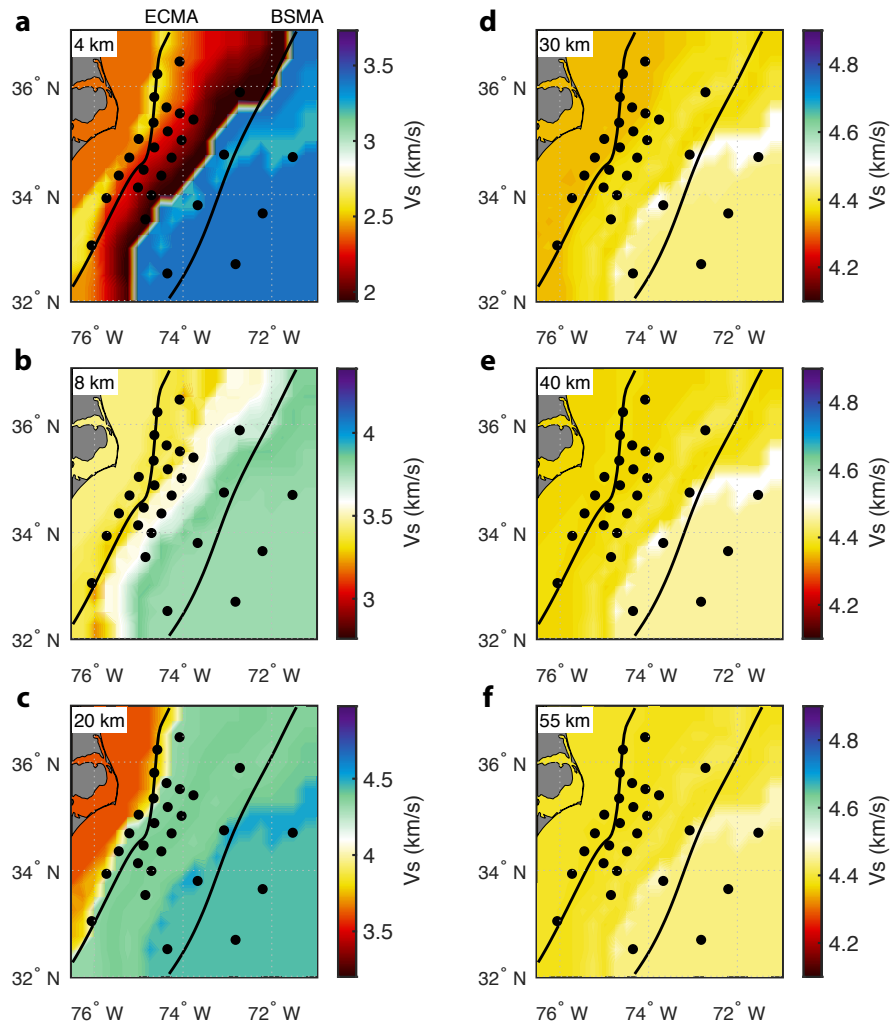


Figure D.6: Horizontal slices through the reference V_S model, as in Figure 4.14 in the main text.

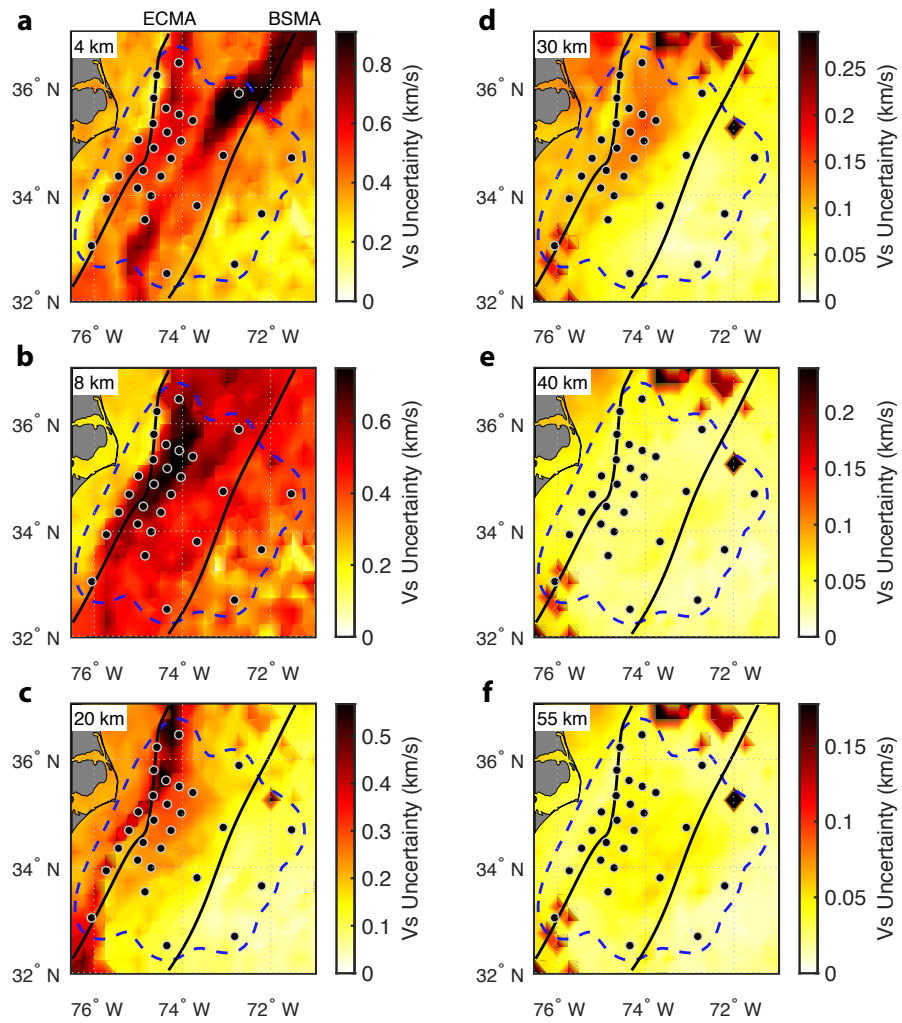


Figure D.7: One standard deviation of the final V_S model ensemble with data misfit $\chi^2 < 1.25$ for the depth slices shown in Figure 4.14 in the main text.

E | Sensitivity kernels

Rayleigh and Love phase velocity sensitivity kernels are calculated using the normal-mode based code, MINEOS. Given an input 1-D transversely isotropic Earth model described by (V_{SV} , V_{SH} , V_{PV} , V_{PH} , η , ρ) MINEOS outputs phase velocity dispersion sensitivity kernels following *Dziewonski and Anderson* (1981). Sensitivity kernels are first calculated for the Love parameters (A , C , F , L , N), related to the velocities by equations A.7.

For spheroidal modes (Rayleigh waves):

$$\begin{aligned}
 K_A &= \left[2U - \sqrt{l(l+1)}V \right]^2 \\
 &\approx \left[\sqrt{l(l+1)}V \right]^2 \\
 K_C &= \left[r\dot{U} \right]^2 \\
 K_F &= 2r\dot{U} \left[2U - \sqrt{l(l+1)}V \right] \\
 &\approx -2r\dot{U}\sqrt{l(l+1)}V \\
 K_L &= \left[r\dot{V} + \sqrt{l(l+1)}U - V \right]^2 \\
 &\approx \left[r\dot{V} + \sqrt{l(l+1)}U \right]^2 \\
 K_N &= (l-1)(l+2)V^2 - \left[2U - \sqrt{l(l+1)}V \right]^2
 \end{aligned} \tag{E.1}$$

where l is angular order, U and V are vertical and radial spheroidal eigenfunctions with normalization:

$$\omega^2 \int_0^\infty \rho (U^2 + V^2) r^2 dr = 1 \tag{E.2}$$

for eigenfrequency ω . \dot{U} and \dot{V} represent radial derivatives. For toroidal modes (Love waves):

$$\begin{aligned} K_L &= \left[r\dot{W} - W \right]^2 \\ &\approx \left[r\dot{W} \right]^2 \\ K_N &= (l-1)(l+2)W^2 \\ &\approx \left[\sqrt{l(l+1)}W \right]^2 \end{aligned} \tag{E.3}$$

$$K_A = K_C = K_F = 0$$

where W is the tangential eigenfunction with normalization:

$$\omega^2 \int_0^\infty \rho W^2 r^2 dr = 1 \tag{E.4}$$

These kernels are used to build the velocity kernels as follows:

$$K_{SV} = \frac{1}{\omega} \frac{\partial \omega}{\partial V_{SV}} = 2\rho V_{SV} (K_L - 2\eta K_F) \tag{E.5}$$

$$K_{SH} = \frac{1}{\omega} \frac{\partial \omega}{\partial V_{SH}} = 2\rho V_{SH} K_N \tag{E.6}$$

$$K_{PV} = \frac{1}{\omega} \frac{\partial \omega}{\partial V_{PV}} = 2\rho V_{PV} K_C \tag{E.7}$$

$$K_{PH} = \frac{1}{\omega} \frac{\partial \omega}{\partial V_{PH}} = 2\rho V_{PH} (K_A + \eta K_F) \tag{E.8}$$

$$K_\eta = \frac{1}{\omega} \frac{\partial \omega}{\partial \eta} = \rho (V_{PH}^2 - 2V_{SV}^2) K_F \tag{E.9}$$

E.1 Note on eigenfunction normalization output from MINEOS

The eigenfunctions, U , V , and W output directly from MINEOS are lacking a normalization factor and must be multiplied by a scale factor:

$$scale = \left[\bar{\rho} R \sqrt{R \pi G'} \right]^{-1} \quad (\text{E.10})$$

where $R = 6371000$ m, $G' = 6.6723 \times 10^{-11}$ m kg $^{-1}$ s $^{-2}$, and $\bar{\rho} = 5515$ kg m $^{-3}$.

This can always be checked by ensuring:

$$1 = \omega^2 \int_0^\infty \rho \left((scale \cdot U)^2 + (scale \cdot V)^2 \right) r^2 dr \quad (\text{E.11})$$

$$1 = \omega^2 \int_0^\infty \rho (scale \cdot W)^2 r^2 dr \quad (\text{E.12})$$

E.2 Derivation of η_κ kernels in terms of A , C , F , L , N kernels

Kawakatsu et al. (2015) introduce a new fifth parameter, η_κ , to be used in place of η as originally defined by *Anderson* (1961). This alternate formulation is associated with modified sensitivity kernels described in *Kawakatsu* (2016b) using the notation of *Takeuchi and Saito* (1972); however, we would like to obtain the modified sensitivities in terms of the A , C , F , L , and N kernels as in equations (E.5–E.9) to facilitate their calculation using MINEOS. This section outlines their derivation.

Following *Dziewonski and Anderson* (1981) a perturbation to phase velocity can be described by a perturbation to the Love parameters by (ignoring density and discontinuity terms)

$$\frac{\delta c}{c} = \frac{c}{U} \int_0^a \left(K_A \delta A(r) + K_C \delta C(r) + K_L \delta L(r) + K_N \delta N(r) + K_F \delta F(r) \right) dr \quad (\text{E.13})$$

where K_A , K_C , K_F , K_L , and K_N are the eigenfrequency Frechet derivatives given by equations (E.1,E.3). We would instead like to rewrite this expression in terms of V_{SV} , V_{SH} , V_{PV} , V_{PH} , and η_κ where

$$\eta_\kappa = \frac{F + L}{\sqrt{(A - L)(C - L)}} \quad (\text{E.14})$$

and therefore, $F = \eta_\kappa \sqrt{(A - L)(C - L)} - L$. The Love parameters are then expressed as:

$$\begin{aligned} A &= \rho V_{PH}^2 \\ C &= \rho V_{PV}^2 \\ L &= \rho V_{SV}^2 \\ N &= \rho V_{SH}^2 \\ F &= \rho \eta_\kappa \sqrt{(V_{PH}^2 - V_{SV}^2)(V_{PV}^2 - V_{SV}^2)} - \rho V_{SV}^2 \end{aligned} \quad (\text{E.15})$$

where F is the only term that changes under the new definition. We can now calculate perturbations to each of the old parameters in terms of the new using the chain rule (i.e. $\delta x \approx (\partial x / \partial y) \cdot \delta y$). This gives:

$$\begin{aligned} \delta A &= 2\rho V_{PH} \delta V_{PH} \\ \delta C &= 2\rho V_{PV} \delta V_{PV} \\ \delta N &= 2\rho V_{SH} \delta V_{SH} \\ \delta L &= 2\rho V_{SV} \delta V_{SV} \\ \delta F &= \frac{\partial F}{\partial V_{SV}} \delta V_{SV} + \frac{\partial F}{\partial V_{PH}} \delta V_{PH} + \frac{\partial F}{\partial V_{PV}} \delta V_{PV} + \frac{\partial F}{\partial \eta_\kappa} \delta \eta_\kappa \end{aligned} \quad (\text{E.16})$$

The expanded partial derivatives for F are cumbersome, so we omit them here. All terms are then grouped separately by δV_{PH} , δV_{PV} , δV_{SH} , δV_{SV} , and $\delta \eta_\kappa$ yielding the desired equation for phase velocity perturbations in terms of the new parameters:

$$\frac{\delta c}{c} = \frac{c}{U} \int_0^a \left(K_{V_{PH}} \delta V_{PH}(r) + K_{V_{PV}} \delta V_{PV}(r) + K_{V_{SV}} \delta V_{SV}(r) + K_{V_{SH}} \delta V_{SH}(r) + K_{\eta_\kappa} \delta \eta_\kappa(r) \right) dr \quad (\text{E.17})$$

where the desired sensitivity kernels are given by

$$K_{PV} = \rho V_{PV} \left(2 K_C + \eta_\kappa \sqrt{\frac{V_{PH}^2 - V_{SV}^2}{V_{PV}^2 - V_{SV}^2}} K_F \right) \quad (\text{E.18})$$

$$K_{PH} = \rho V_{PH} \left(2 K_A + \eta_\kappa \sqrt{\frac{V_{PV}^2 - V_{SV}^2}{V_{PH}^2 - V_{SV}^2}} K_F \right) \quad (\text{E.19})$$

$$K_{SV} = \rho V_{SV} \left[2 K_L - \left(2 + \eta_\kappa \sqrt{\frac{V_{PH}^2 - V_{SV}^2}{V_{PV}^2 - V_{SV}^2}} + \eta_\kappa \sqrt{\frac{V_{PV}^2 - V_{SV}^2}{V_{PH}^2 - V_{SV}^2}} \right) K_F \right] \quad (\text{E.20})$$

$$K_{SH} = 2\rho V_{SH} K_N \quad (\text{E.21})$$

$$K_{\eta_\kappa} = \rho \sqrt{(V_{PH}^2 - V_{SV}^2)(V_{PV}^2 - V_{SV}^2)} K_F \quad (\text{E.22})$$

F

Equivalence of (G, B, H, E) and $(\delta V_{SV}, \delta V_{SH}, \delta V_{PH})$

Throughout this dissertation we choose to solve for azimuthal anisotropy in terms of Love parameters (G, B, H, E) rather than the equivalent velocity perturbations (δV_{SV} , δV_{SH} , δV_{PH}). In this section, I demonstrate that the parameterizations are equivalent: $G/L = 2\delta V_{SV}/V_{SV}$, $E/N = 2\delta V_{SH}/V_{SH}$, and $B/A = 2\delta V_{PH}/V_{PH}$.

This leads to the following equation for inverting Rayleigh-wave phase velocities for depth-dependent azimuthal anisotropy:

$$\begin{aligned} \left(\frac{\delta c}{c} \right)_{c,s} &= \frac{c}{U} \int_0^a \left[L K_L \frac{G_{c,s}}{L}(r) + A K_A \frac{B_{c,s}}{A}(r) + F K_F \frac{H_{c,s}}{F}(r) \right] dr \\ &= \frac{c}{U} \int_0^a \left[V_{SV} K_{SV} \left(\frac{\delta V_{SV}}{V_{SV}}(r) \right)_{c,s} + V_{PH} K_{PH} \left(\frac{\delta V_{PH}}{V_{PH}}(r) \right)_{c,s} \right] dr \end{aligned} \quad (\text{F.1})$$

A corollary is that inverting Rayleigh-wave anisotropy for G (or B) alone is not strictly equivalent to inverting for its respective velocity perturbation δV_{SV} (or δV_{PH}).

Finally, an analytical scaling for H arises under the assumption that azimuthal variations in η are small:

$$\frac{H}{F} = \frac{B - 2G}{A - 2L} \quad (\text{F.2})$$

which may be used as a prior constraint when other information about the character of H is unavailable.

F.1 Solving for (G, B, H, E) in terms of VTI parameters

We define $G = \delta L$, $B = \delta A$, $H = \delta F$, and $E = \delta N$. Using equations (A.2–A.7) we have

$$G = \delta L = \frac{\partial L}{\partial V_{SV}} \delta V_{SV} = 2\rho V_{SV} \delta V_{SV} \quad (\text{F.3})$$

$$B = \delta A = \frac{\partial B}{\partial V_{PH}} \delta V_{PH} = 2\rho V_{PH} \delta V_{PH} \quad (\text{F.4})$$

$$E = \delta N = \frac{\partial E}{\partial V_{SH}} \delta V_{SH} = 2\rho V_{SH} \delta V_{SH} \quad (\text{F.5})$$

$$\begin{aligned} H = \delta F &= \frac{\partial F}{\partial V_{SV}} \delta V_{SV} + \frac{\partial F}{\partial V_{PH}} \delta V_{PH} + \frac{\partial F}{\partial \eta} \delta \eta \\ &= 2\rho \eta \left[V_{PH}^2 \left(\frac{\delta V_{PH}}{V_{PH}} + \frac{\delta \eta}{2\eta} \right) - 2V_{SV}^2 \left(\frac{\delta V_{SV}}{V_{SV}} + \frac{\delta \eta}{2\eta} \right) \right] \end{aligned} \quad (\text{F.6})$$

We can divide by the respective Love parameters in order to get perturbations in percent:

$$\begin{aligned} \frac{G}{L} &= 2 \frac{\delta V_{SV}}{V_{SV}}; & \frac{B}{A} &= 2 \frac{\delta V_{PH}}{V_{PH}}; & \frac{E}{N} &= 2 \frac{\delta V_{SH}}{V_{SH}} \\ \frac{H}{F} &= \frac{2(V_{PH}\delta V_{PH} - 2V_{SV}\delta V_{SV})}{V_{PH}^2 - 2V_{SV}^2} + \frac{\delta \eta}{\eta} \end{aligned} \quad (\text{F.7})$$

If we assume that the azimuthal dependence of η is negligible, $\delta\eta/\eta \approx 0$ and

$$\begin{aligned} H &= 2\rho \eta (V_{PH}\delta V_{PH} - 2V_{SV}\delta V_{SV}) \\ &= \eta (B - 2G) \end{aligned} \quad (\text{F.8})$$

or

$$\frac{H}{F} = \frac{B - 2G}{A - 2L} \quad (\text{F.9})$$

Equation (F.9) provides an analytical scaling that may be used to enforce the character of H when other *a priori* information is unavailable.

F.2 Rayleigh-wave inversion

Plugging equations (E.5–E.9) and (F.7) into equation (1.11) for the perturbation to Rayleigh wave phase velocities gives:

$$\begin{aligned} \left(\frac{\delta c}{c}\right)_{c,s} &= \frac{c}{U} \int_0^a \left[L K_L \frac{G_{c,s}}{L}(r) + A K_A \frac{B_{c,s}}{A}(r) + F K_F \frac{H_{c,s}}{F}(r) \right] dr \\ &= \frac{c}{U} \int_0^a \left[V_{SV} K_{SV} \left(\frac{\delta V_{SV}}{V_{SV}}(r) \right)_{c,s} + V_{PH} K_{PH} \left(\frac{\delta V_{PH}}{V_{PH}}(r) \right)_{c,s} \right] dr \end{aligned} \quad (\text{F.10})$$

Importantly, given their definitions in (F.7) the two parameterizations result in answers that are different by a factor of two. The Love parameterization gives peak-to-peak anisotropy magnitudes while the velocity parameterization gives zero-to-peak magnitudes.

Additionally, it can be shown that

$$\int_0^a L K_L \frac{G_{c,s}}{L}(r) dr \neq \int_0^a V_{SV} K_{SV} \left(\frac{\delta V_{SV}}{V_{SV}}(r) \right)_{c,s} dr \quad (\text{F.11})$$

$$\int_0^a A K_A \frac{B_{c,s}}{A}(r) dr \neq \int_0^a V_{PH} K_{PH} \left(\frac{\delta V_{PH}}{V_{PH}}(r) \right)_{c,s} dr \quad (\text{F.12})$$

Therefore, solving for $\delta V_{SV}/V_{SV}$ (or $\delta V_{PH}/V_{PH}$) on its own is not equivalent to solving for G/L (or B/A). All anisotropy terms must be solved for simultaneously.

F.3 Love-wave inversion

We carry out the same exercise for Love waves. For the 2θ azimuthal variations we have

$$\begin{aligned} \left(\frac{\delta c}{c}\right)_{c,s} &= \frac{c}{U} \int_0^a -L K_L \frac{G_{c,s}}{L}(r) dr \\ &= \frac{c}{U} \int_0^a -V_{SV} K_{SV} \left(\frac{\delta V_{SV}}{V_{SV}}(r) \right)_{c,s} dr \end{aligned} \quad (\text{F.13})$$

Similarly, for the 4θ component of Love waves

$$\begin{aligned} \left(\frac{\delta c}{c}\right)_{c,s} &= \frac{c}{U} \int_0^a -N K_E \frac{E_{c,s}}{N}(r) dr \\ &= \frac{c}{U} \int_0^a -V_{SH} K_{SH} \left(\frac{\delta V_{SH}}{V_{SH}}(r) \right)_{c,s} dr \end{aligned} \quad (\text{F.14})$$

F.4 Numerical demonstration

Here, we numerically demonstrate the validity of equations (F.7) by solving the Christoffel equation for an elastic tensor C_{ij} of the form (A.23) for all azimuths in the horizontal $x1$ - $x2$ plane. The resulting phase velocities for each of the three orthogonal waves provide estimates of V_{SV} , V_{SH} , and V_{PH} as a function of azimuth. We compare their peak-to-peak values to the anisotropy strength calculated using equations (A.12–A.19) and find excellent agreement.

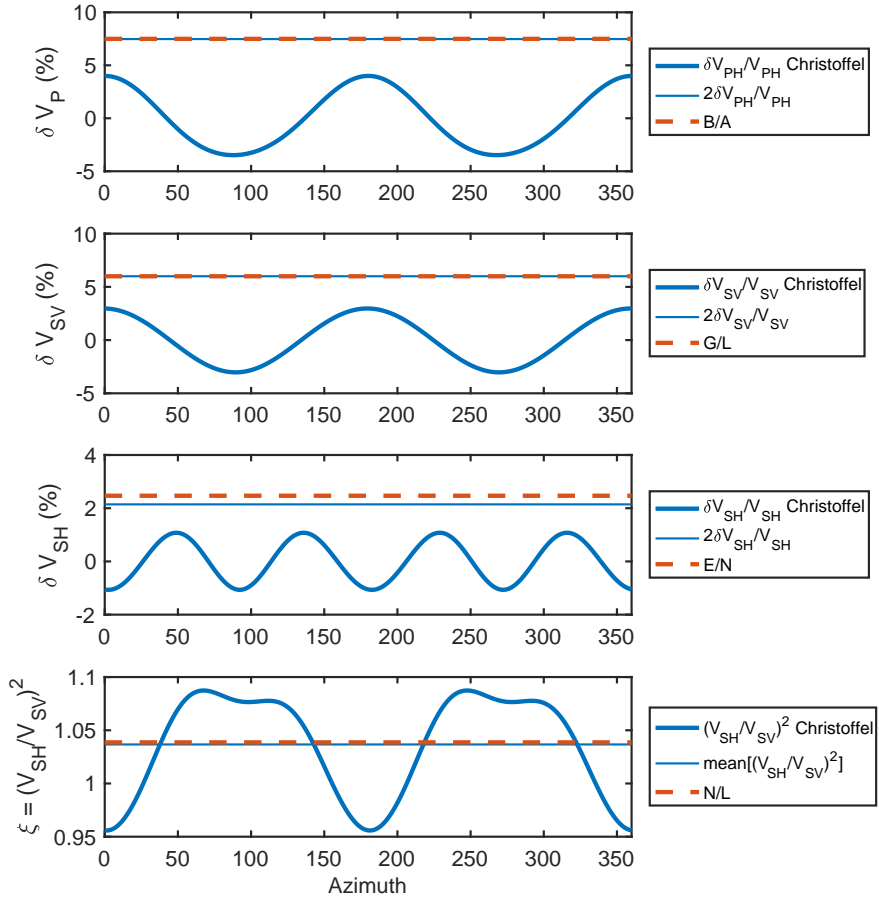


Figure F.1: Plots showing the validity of equations (F.7). Anisotropy is calculated for an elastic tensor C_{ij} of the form (A.23) by solving the Christoffel equation (thick blue) in the horizontal $x1$ - $x2$ plane and perpendicular to vertical $x3$ direction. The peak-to-peak value of the Christoffel solution is shown by the thin blue line. The values B/A , G/L , E/N , and N/L are calculated from equations (A.12–A.19).

G | Error propagation from (A, ψ) to (A_c, A_s)

We must convert our uncertainties of azimuthal anisotropy strength and azimuth (A, ψ) to uncertainties in (A_c, A_s) . This is achieved using the standard error propagation procedure. In general, if $F = F(x, y, \dots)$, then propagation of errors in $\delta x, \delta y, \dots$ through to δF is given by

$$\delta F = \sqrt{\left(\frac{\partial F}{\partial x} \delta x\right)^2 + \left(\frac{\partial F}{\partial y} \delta y\right)^2 + \dots} \quad (\text{G.1})$$

In our case, we have functions

$$A_c = A \cos(2\psi), \quad A_s = A \sin(2\psi) \quad (\text{G.2})$$

Plugging these into equation G.1 above, we have

$$\delta A_c = \sqrt{\left(\cos(2\psi) \delta A\right)^2 + \left(-2A \sin(2\psi) \delta \psi\right)^2} \quad (\text{G.3})$$

$$\delta A_s = \sqrt{\left(\sin(2\psi) \delta A\right)^2 + \left(2A \cos(2\psi) \delta \psi\right)^2} \quad (\text{G.4})$$

H | Linear Radon Transform

We utilize the Linear Radon Transform (LRT) to measure the average surface-wave dispersion across the seismic array following (*Luo et al.*, 2008, 2015). For a given slowness p and zero offset intercept time τ , the Radon transform maps data from the Radon domain $m(p, \tau)$ to the data space $d(\Delta, t)$ as follows (*Jeffrey et al.*, 2009, *Luo et al.*, 2008)

$$d(\Delta, t) = \sum_{p=p_{min}}^{p_{max}} m(p, \tau = t - p\Delta) \quad (\text{H.1})$$

The adjoint transform is given by

$$m(p, \tau) = \sum_{\Delta=\Delta_{min}}^{\Delta_{max}} d(\Delta, t = \tau + p\Delta) \quad (\text{H.2})$$

where $d(\Delta, t)$ is the observed seismogram for a time t and source-receiver separation Δ . The Fourier transform of equations (H.1) and (H.2) at frequency f_j is given by

$$d(\Delta, f_j) = \sum_{p=p_{min}}^{p_{max}} m(p, f_j) e^{-i2\pi f_j p\Delta} \quad (\text{H.3})$$

and

$$m(p, f_j) = \sum_{\Delta=\Delta_{min}}^{\Delta_{max}} d(\Delta, f_j) e^{i2\pi f_j p\Delta} \quad (\text{H.4})$$

We can write equation (H.3) in matrix form as

$$\begin{pmatrix} d(\Delta_1, f_j) \\ d(\Delta_2, f_j) \\ \vdots \\ d(\Delta_N, f_j) \end{pmatrix} = \begin{pmatrix} e^{-i2\pi f_j p_1 \Delta_1} & e^{-i2\pi f_j p_2 \Delta_1} & \dots & e^{-i2\pi f_j p_M \Delta_1} \\ e^{-i2\pi f_j p_1 \Delta_2} & e^{-i2\pi f_j p_2 \Delta_2} & \dots & e^{-i2\pi f_j p_M \Delta_2} \\ \vdots & \vdots & \vdots & \vdots \\ e^{-i2\pi f_j p_1 \Delta_N} & e^{-i2\pi f_j p_2 \Delta_N} & \dots & e^{-i2\pi f_j p_M \Delta_N} \end{pmatrix} \begin{pmatrix} m(p_1, f_j) \\ m(p_2, f_j) \\ \vdots \\ m(p_M, f_j) \end{pmatrix} \quad (\text{H.5})$$

which can be written simply as

$$\mathbf{d}(f_j) = \mathbf{L}(f_j) \mathbf{m}(f_j) \quad (\text{H.6})$$

where $\mathbf{L}(f_j) = e^{-i2\pi f_j p \Delta}$ is the forward LRT operator. This matrix equation must be solved separately for each frequency component of interest. We use a conjugate guided gradient approach with model and residual weighting as described by *Ji* (2006) (their Algorithm 5) to solve equation H.5. The advantage of this method is that regularization parameters do not need to be specified ahead of time, and instead are determined by the data.